

AFIT/DS/ENY/99-02

EFFECTS OF FOREIGN OBJECT DAMAGE  
FROM SMALL HARD PARTICLES ON THE  
HIGH-CYCLE FATIGUE LIFE OF Ti-6Al-4V

DISSERTATION

Joseph L. Hamrick, II, B.S., M.S.  
Major, USAF

Sponsored by the Air Force Research Laboratory, WPAFB, OH

September 1999

Approved for public release; distribution unlimited

19991115 056

The views expressed in this dissertation are those of the author and do not reflect the official policy or position of the Department of Defense or the U.S. Government.

This work was supported in part by a grant of high performance computer time from the DoD High Performance Computer Center (Aeronautical Systems Center - Major Shared Resource Center, Wright-Patterson Air Force Base, OH).

AFIT/DS/ENY/99-02

EFFECTS OF FOREIGN OBJECT DAMAGE FROM SMALL HARD  
PARTICLES ON THE HIGH-CYCLE FATIGUE LIFE OF Ti-6Al-4V

DISSERTATION

Presented to the Faculty of the School of Engineering  
of the Air Force Institute of Technology  
Air University in Partial Fulfillment of the  
Requirements for the Degree of  
Doctor of Philosophy

Joseph L. Hamrick, II, B.S., M.S.

Major, USAF


September 1999

Approved for public release; distribution unlimited

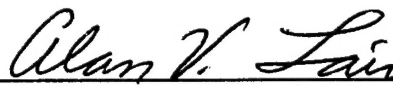
EFFECTS OF FOREIGN OBJECT DAMAGE FROM SMALL HARD  
PARTICLES ON THE HIGH-CYCLE FATIGUE LIFE OF Ti-6Al-4V

Joseph L. Hamrick, II, B.S., M.S.  
Major, USAF


Approved:

  
\_\_\_\_\_  
Dr. Shankar Mall  
Committee Chairman


29 Sept 99  
Date

  
\_\_\_\_\_  
Dr. Alan V. Lair  
Committee Member


9/29/99  
Date

  
\_\_\_\_\_  
Lt. Col. Jeffery S. Turcotte  
Committee Member

30 Sep 99  
Date


  
\_\_\_\_\_  
Dr. Theodore Nicholas  
Committee Member

29 Sept 99  
Date

  
\_\_\_\_\_  
Dr. Kenneth W. Bauer, Jr.  
Dean's Representative

30 SEPT 99  
Date

Accepted:

  
\_\_\_\_\_  
Robert A. Calico  
Dean, Graduate School of Engineering



## ***ACKNOWLEDGMENTS***

First, I wish to thank my Lord Jesus Christ for the great blessing of being allowed to attend AFIT for this program, and the strength and ability to complete it. Also, many thanks and much gratitude to my wonderful wife Sharon for her immense patience, sacrifice and encouragement over the last three years. I'm deeply indebted to my advisor, Dr Shankar Mall for his patience and sage guidance about many things beyond this research, namely how to think logically and get that logic across on paper. To AFRL/MLLN for sponsoring my work and giving me such neat toys to play with, especially Dr Ted Nicholas, for his many key insights into fatigue and strategic injections of humor into the process. Thanks also to the rest of my committee, Lt Col Jeff Turcotte, Dr Alan Lair and Dr Kenneth Bauer for encouragement and extra effort in making this a far better document than I could myself.

This work would have been much harder without skillful support from many people: Rick Goodman, Bob Lewis, Luann Piazza and Scott Apt were particularly vital, both by their support and for sharing their knowledge. Joe, Alisha, Vanessa, Larry, Jay, Eric and the whole MLL family were great help and encouragement. Thanks to Bob Brockman and Craig Weeks for their insight into dynamic modeling. Thanks also to Gary Meyer, Dan Schornak, CJ, Bobbi and everyone at the MSRC for keeping the computers crunching.

Joe Hamrick

## **TABLE OF CONTENTS**

	<b>Page</b>
ACKNOWLEDGMENTS .....	iii
LIST OF FIGURES .....	viii
LIST OF TABLES .....	xvi
ABSTRACT .....	xvii
I. INTRODUCTION .....	1
II. BACKGROUND .....	7
Fracture and Fatigue .....	7
<i>Cyclic Loading</i> .....	8
<i>Fatigue Life / Fatigue Limit</i> .....	10
Stress-life Methods .....	11
Factors Affecting Fatigue .....	13
Stress Concentration .....	14
Linear Elastic Fracture Mechanics .....	19
Strain Amplitude Life .....	22
Influence of Cycle Asymmetry (Mean Stress Effects) .....	26
Constant Life Diagrams .....	28
Numerical Modeling of Stress States .....	31
Previous Studies .....	34
III. EXPERIMENTAL PROCEDURE .....	41
Specimen Preparation .....	41

	<b>Page</b>
<i>Material details</i> .....	41
<i>Test specimens</i> .....	42
<i>Simulated airfoil leading edge cross section</i> .....	42
<i>Rectangular cross section</i> .....	43
<i>FOD Simulation Techniques</i> .....	45
<i>Gas Gun Impact</i> .....	46
<i>Chisel Indentation</i> .....	51
<i>Sheared Chisel Notches</i> .....	57
<i>Fatigue Test Procedure</i> .....	58
<i>High Frequency Tensile Machine</i> .....	61
<i>Sample Alignment and Test Procedure</i> .....	63
<b>IV. DAMAGE QUANTIFICATION</b> .....	<b>72</b>
Optical Observation of Plastic Deformation .....	72
Grain Size Measurement .....	85
Finite Element Modeling .....	94
Damage Mechanisms .....	101
<i>Glass Sphere Impacts Without Erosion</i> .....	101
<i>Glass Sphere Impacts Causing Erosion</i> .....	102
<i>Chisel Indentations Without Chipping</i> .....	110
<i>Chisel Indentations Causing Chipping</i> .....	116
<i>Steel sphere impacts without chipping</i> .....	123

	<b>Page</b>
<i>Steel sphere impacts causing chipping</i> .....	127
<i>Sheared notches using chisel in transverse direction</i> .....	130
Summary .....	133
V. FINITE ELEMENT ANALYSIS .....	139
Material Models and Boundary Conditions .....	140
Quasi-static Model .....	143
Dynamic Model .....	152
Quasi-static Results .....	159
Dynamic Results .....	166
VI. FATIGUE STRENGTH OF SIMULATED FOD SPECIMENS .....	178
Fatigue Strength Reduction. ....	178
<i>Undamaged Fatigue Strength</i> .....	179
<i>Effect of Chisel Indentation Damage</i> .....	179
<i>Effect of Glass Sphere Damage</i> .....	183
<i>Effect of Steel Sphere Indentation Damage</i> .....	184
<i>Effect of Chisel Sheared Notches</i> .....	185
Analysis of Simulated FOD Effects .....	186
VII. SUMMARY .....	197
Damage Quantification .....	199
Finite Element Analysis .....	202
Fatigue Strength .....	203

	<b>Page</b>
APPENDIX A: Processing of the HCF Program Ti-6Al-4V .....	208
APPENDIX B: Gas Gun Impacting Procedure .....	215
APPENDIX C: Approximate Crack Growth Rate .....	218
APPENDIX D: Verification of the Step Loading Technique .....	219
APPENDIX E: Example HCF Testing Machine Output .....	223
APPENDIX F: Mesh Refinement Analysis .....	225
APPENDIX G: Calculation of Damping for Dynamic Model .....	227
APPENDIX H: Fatigue Strength versus Indent Depth .....	229
APPENDIX I. Fatigue Strength Data .....	230
APPENDIX J. Fatigue Crack Initiation Sites .....	233
BIBLIOGRAPHY .....	237
VITA .....	245

## ***LIST OF FIGURES***

<b>#</b>	<b>Title</b>	<b>Page</b>
1	Cyclic Stress Parameters .....	9
2	Typical S-N Curves .....	12
3	Plastic Zone Near Notch Root with Small Crack .....	16
4	Stresses Near the Plastic Zone Behind Notch Root .....	17
5	Crack Opening Modes .....	20
6	Stresses Around a Mode I Crack Tip .....	21
7	Stress- and Strain-Life Curves .....	24
8	Mean Stress Effects on Typical S-N Curves .....	26
9	Constant Life Curves .....	30
10	Typical Microstructure of AFRL HCF Program Ti-6Al-4V .....	43
11	Airfoil-shaped Ti-6Al-4V Test Samples .....	44
12	Flat Ti-6Al-4V Test Samples .....	45
13	Specimen Damage Parameters .....	47
14	Specimen Damage Parameters - cont'd .....	48
15	Plastic Damage Zone Parameter .....	49
16	High Speed Film of 2 mm Diameter Glass Sphere Impact .....	53
17	High Speed Film of 5 mm Diameter Glass Sphere Impact .....	54
18	Chisel Indentation Tool .....	54
19	Chisel Indentation Fixture .....	55

### ***LIST OF FIGURES (cont'd)***

<b>#</b>	<b>Title</b>	<b>Page</b>
20	Static Chisel Displacement Parameters .....	56
21	Perpendicular Shearing Chisel .....	57
22	Sheared Chisel Notching Fixture .....	58
23	Illustration of Accelerated Fatigue Strength Testing .....	61
24	Schematic of High Frequency Tensile Machine .....	62
25	High Frequency Tensile Machine .....	63
26	Grip Fixtures for HCF#6 .....	65
27	Sample Alignment Gage Block .....	66
28	MathCad Worksheet for Test Condition Preparation .....	67
29	Control Panel for HCF #6 .....	70
30	Nikon Upright Microscope with X-Y Translation Stage .....	73
31	Close-up View of Fracture Surface on Specimen 98-B18 .....	74
32	Measurement of Deformation Bands on Fracture Surface .....	76
33	Typical Deformation Band Shapes .....	76
34	Deformation Band on Specimen 98-J52 .....	78
35	Asymmetric Crater Optical Measurements .....	79
36	SEM of Fracture Surface .....	80
37	Close-up Views of Fracture Surface .....	81
38	Shear Bands on Polished Fracture Surface .....	83

## ***LIST OF FIGURES (cont'd)***

<b>#</b>	<b>Title</b>	<b>Page</b>
39	FEM Model of Plastic Strain Magnitude .....	84
40	Grain Deformation Due to Plastic Straining .....	87
41	Grain Size Sectioning .....	90
42	Cross Sectioning of Damage Site .....	90
43	Grain Size Distribution Near Crater .....	91
44	Grain Size as Function of Distance from Indent .....	92
45	Nominal Strain as Function of Distance from Indent .....	93
46	Deformed Shape of 1 mm Diameter Chisel Indent .....	96
47	Plastic Strain vs. Depth into Specimen from ABAQUS Model .....	97
48	Plastic Strain vs. Depth into Specimen from Dytran Model .....	98
49	Comparison of Damage Quantification Techniques .....	100
50	Surface of Glass Impact Crater without Erosion .....	102
51	Crater from Glass Sphere Impacts with Erosion .....	105
52	Crater from Glass Sphere Impact with Erosion - cont'd .....	106
53	Deformation Patterns for Glass Sphere Impacts .....	107
54	Plastic Zone Size for 2 mm Glass Sphere .....	108
55	Plastic Zone Size for 5 mm Glass Sphere .....	109
56	Glass Sphere Damage Depth .....	110
57	98-J78 Indentation from 2 mm Chisel without Chipping .....	112



## ***LIST OF FIGURES (cont'd)***

<b>#</b>	<b>Title</b>	<b>Page</b>
58	Deformation Band Shape for Chisel Indentations without Chipping .	113
59	Highly Developed Shear Cracking .....	113
60	Ductile Fracture in Opposite Notch .....	114
61	$D_p$ vs. $D_i$ for Chisel Indentation without Chipping .....	116
62	FEM Simulation of Chipped Region .....	118
63	Chipped Region from 5 mm Chisel Indentation .....	119
64	Chipped Region from 5 mm Chisel Indentation - Close-up .....	120
65	Edge View of Chipped Specimen .....	121
66	Indentation from 5 mm Chisel with Chipping .....	121
67	Deformation Band Shape for Chisel Indentations with Chipping ....	122
68	Chisel Indentation with Chipping Damage Depth .....	123
69	Steel Sphere Impact without Chipping .....	124
70	Deformation Band Shape for Steel Sphere Impacts without Chipping	126
71	Steel Sphere Impacts without Chipping Damage Depth .....	126
72	Deformation Band Shape for Steel Sphere Impacts with Chipping ...	127
73	Steel Sphere Impacts with Chipping .....	128
74	Steel Sphere Impacts with Chipping Damage Depth .....	130
75	Deformation Band Shape for Chisel Sheared Notches .....	131
76	Chisel Sheared Notch .....	132

# ***LIST OF FIGURES (cont'd)***

<b>#</b>	<b>Title</b>	<b>Page</b>
77	Chisel Sheared Notches Damage Depth .....	133
78	Plastic Zone Size as a Function of Indent Depth .....	137
79	Stress-Strain Curve for Ti-6Al-4V .....	142
80	Finite Element Model of Ti-6Al-4V Specimens .....	143
81	FEM Model of 5 mm Chisel Indentor .....	144
82	FEM Model of 2 mm Chisel Indentor .....	145
83	FEM Model of 1 mm Chisel Indentor .....	145
84	Displacement and Contact for Quasi-static Model .....	147
85	Load Application Steps for Chisel Models .....	149
86	Selection of Tension Loads During FEM .....	150
87	Quasi-static Crater Dimensions .....	151
88	Dytran Mesh - 5 mm Glass Sphere .....	152
89	Dytran Mesh- 2 mm Sphere .....	153
90	Interior of Dytran Mesh- 2 mm Sphere .....	154
91	Damping and Loading Applied - 2 mm Glass Sphere .....	156
92	Damping and Loading Applied - 5 mm Glass Sphere .....	157
93	Damping and Loading Applied - 2 mm Steel Sphere .....	157
94	Dynamic Crater Dimensions .....	158
95	ABAQUS Prediction of Tensile Stress; 1 mm Chisel Indent .....	160

### ***LIST OF FIGURES (cont'd)***

<b>#</b>	<b>Title</b>	<b>Page</b>
96	ABAQUS Prediction of Tensile Stress; 2 mm Chisel Indent .....	161
97	ABAQUS Prediction of Tensile Stress; 5 mm Chisel Indent .....	162
98	Stress Distribution Due to Tensile Load; 1 mm Chisel Indent .....	163
99	Stress Distribution Due to Tensile Load; 2 mm Chisel Indent .....	164
100	Stress Distribution Due to Tensile Load; 5 mm Chisel Indent .....	165
101	Plastic Strain from 5 mm Glass Sphere Impact .....	168
102	Tensile Stress from 5 mm Glass Sphere Impact .....	168
103	Plastic Strain from 2 mm Glass Sphere Impact .....	169
104	Tensile Stress from 2 mm Glass Sphere Impact .....	169
105	Plastic Strain from 2 mm Steel Sphere Impact .....	170
106	Tensile Stress from 2 mm Steel Sphere Impact .....	170
107	Von Mises' Plastic Strain vs. Time; 5 mm Glass Sphere .....	171
108	Tensile Stress vs. Time; 5 mm Glass Sphere .....	171
109	Stress Distribution Due to Tensile Load; 5 mm Glass Sphere .....	172
110	Von Mises' Plastic Strain vs. Time; 2 mm Glass Sphere .....	173
111	Tensile Stress vs. Time; 2 mm Glass Sphere .....	173
112	Stress Distribution Due to Tensile Load; 2 mm Glass Sphere .....	174
113	Von Mises' Plastic Strain vs. Time; 2 mm Steel Sphere .....	175
114	Tensile Stress vs. Time; 2 mm Steel Sphere .....	175

### ***LIST OF FIGURES (cont'd)***

<b>#</b>	<b>Title</b>	<b>Page</b>
115	Stress Distribution Due to Tensile Load; 2 mm Steel Sphere . . . . .	176
116	Nicholas-Haigh Life Diagram - Undamaged Ti-6Al-4V . . . . .	180
117	Undamaged Ti-6Al-4V - 99% Prediction Interval . . . . .	181
118	Fatigue Strength vs. $D_d$ for Chisel Indentations . . . . .	182
119	Fatigue Strength vs. $D_d$ for Glass Sphere Impacts . . . . .	183
120	Fatigue Strength vs. $D_d$ for Steel Sphere Impacts . . . . .	184
121	Fatigue Strength vs. $D_d$ for Chisel Sheared Notches . . . . .	185
122	2 mm Chisel Profile . . . . .	186
123	Fatigue Strength vs. $D_d$ for All Samples . . . . .	187
124	Fatigue Strength Data Sorted by Stress Ratio . . . . .	189
125	Elastic SCF Measured from Notch Dimensions . . . . .	191
126	Fatigue Strength vs. $D_i$ with SCF - $R = 0.1$ . . . . .	192
127	Fatigue Strength vs. $D_i$ with SCF - $R = 0.5$ . . . . .	193
128	Actual Tensile Stress State Shift - Chisel Indents. . . . .	195
129	Actual Tensile Stress State Shift - Sphere Impacts . . . . .	196
130	Schematic of Gas Gun Used for Sphere Impact Tests . . . . .	215
131	Step Loading Variation Results . . . . .	220
132	S-N Data and Step Loading Comparison . . . . .	222
133	ABAQUS Predicted Stresses for Notch with SCF of 2.00 . . . . .	226

***LIST OF FIGURES (cont'd)***

<b>#</b>	<b>Title</b>	<b>Page</b>
134	ABAQUS Predicted Stresses for Notch with SCF of 2.45 .....	226
135	Fatigue Strength vs. $D_i$ and $D_d$ .....	229
136	Stress Amplitude vs. Mean Stress - Chisel Indentations .....	230
137	Stress Amplitude vs. Mean Stress - Spheres and Sheared Notches ...	231
138	Peak Tensile Stress Locations .....	233
139	Fatigue Crack Initiation Sites .....	234

## ***LIST OF TABLES***

<b>#</b>	<b>Title</b>	<b>Page</b>
1	Ti-6Al-4V Mechanical Properties .....	42
2	Tested Damage Conditions .....	46
3	Glass Sphere Impact Details .....	50
4	Steel Sphere Impact Details .....	51
5	FOD Details .....	93
6	Material Property Inputs to FEM Codes .....	141
7	Quasi-static FEM Notch Predictions .....	151
8	Dynamic FEM Notch Predictions .....	158
9	Effective Stress States from Chisel Indentations .....	166
10	Effective Stress States from Sphere Impacts .....	177
11	Damage Quantities Tested .....	178
12	Glass Sphere Impact Raw Data .....	216
13	Variations Between Step Loading Techniques (Notched Specimens) .	221
14	Stress Concentration Factors .....	225
15	Fatigue Strength of Simulated FOD Specimens .....	231
16	Locations of Crack Initiation Sites .....	235

## ***ABSTRACT***

High cycle fatigue (HCF) related failures are currently the largest single cause of major engine failures experienced by the Air Force and Navy. Of particular concern in turbine engines is the interaction of HCF and foreign object damage (FOD) to the blades from the impact of small hard particles. The present design methodology for fan and compressor blades is lacking sufficient understanding and information to predict their life after suffering FOD, especially under HCF conditions.

The goal of this research was, therefore, to develop a scientific knowledge of the HCF behavior of fan and compressor blades when subjected to FOD. To do this, laboratory specimens were made from the titanium alloy Ti-6Al-4V, which is currently used as the material for blades in many military engines. The specimens were damaged by four different techniques to simulate the actual FOD seen on turbine blades: 1) impact with glass spheres of different diameters at a velocity representative of actual FOD impact conditions, 2) impact with steel spheres of different diameters at the same velocity as the glass spheres, 3) quasi-static displacement controlled indentation using steel chisels with different radii and 4) shearing notches with a constant radius chisel point under a quasi-static loading condition. The damaged specimens, and undamaged specimens, were fatigue tested in uniaxial tension at 350 Hz to determine their fatigue strength at a life of  $10^7$

cycles. The fatigue testing was conducted at stress ratios of 0.1 and 0.5 using the step loading technique.

The damage mechanisms in the specimens were investigated by microscopic and numerical techniques. The extent of the plastically deformed zone in several specimens was deduced by measuring the changes in grain size through the damaged region. Finite element analysis was conducted to model the damage process from the quasi-static chisel indentations and the glass and steel sphere impacts. The computed strain field around the damaged zone was compared to that obtained by measuring the grain sizes. Microscopic examination of the fatigue fractured surfaces under polarized light revealed visible bands created by shear strain at the periphery of the plastically deformed zone. The location of these bands was used as a measure of the damaged zone size.

The fatigue strength required for crack initiation at  $10^7$  cycles was found to be a function of the total damage depth into a specimen to which the damage zone encroaches, i.e., total depth up to the plastically deformed zone from the edge of the undeformed specimen. A simple relation can be seen to describe this effect in all cases except for two of the FOD simulations. For damage depths less than 1750  $\mu\text{m}$ , the reduction in fatigue strength is proportional to the depth of total damage. For more than 1750  $\mu\text{m}$ , there appears to be a threshold value of fatigue strength.

The finite element models also provided the stress distribution through the damaged zone and surrounding area. The residual stresses in the damaged zone caused the



peak tensile stresses in the specimen to change from the nominal values applied. The percentage of stress increase changed, however, with the amount of tension applied. This caused the effective stress ratio seen in the specimen at the point of peak tensile stress to be different than that applied to the specimen. These effective stress states met the fatigue failure criteria for undamaged Ti-6Al-4V developed from undamaged specimens. It was determined that the cause of HCF failure in specimens, damaged by simulated FOD, is the enhanced stress values due to the residual stresses in the damaged region around the notch.

Glass sphere impacts are the best representation of the actual FOD, but it is difficult to obtain reproducible damage this way. It is also expensive, while the static indentation and shearing methods are much easier and cost effective. This study determined that any of these methods can be used to simulate FOD in the laboratory so long as the damage is measured by the depth from the original edge of the specimen in to the position where the plastic damage zone ends. Simulating FOD cannot reliably be accomplished simply by matching the physical dimensions of the notch. Correlation of one damage technique with another requires matching the total depth of the notch plus the plastic zone. The quasi-static indentations and sheared notches were created with damage depths from 492  $\mu\text{m}$  to 2817  $\mu\text{m}$ , while the glass sphere impacts had damage depths from 1154  $\mu\text{m}$  to 1615  $\mu\text{m}$ . At the damage depths seen by the glass spheres, their fatigue strength reduction was the same as the fatigue strength reduction in specimens damaged by the other methods when damage depth was the same. This similarity shows that damage created by repeatable, inexpensive

quasi-static chisel indentation or shearing can be used to create simulated FOD for laboratory testing purposes more economically than the expensive glass sphere damage technique.

EFFECTS OF FOREIGN OBJECT DAMAGE FROM SMALL HARD PARTICLES  
ON THE HIGH-CYCLE FATIGUE LIFE OF Ti-6AL-4V

*I. INTRODUCTION*

Since the advent of jet aircraft engine technology, increasingly stringent demands have been placed upon jet engine components. As engine design has evolved in order to increase their performance, new failure modes have appeared. In the 1950's, creep of engine turbine blades was a major problem. As creep resistant alloys became available, low cycle fatigue (LCF) - the accumulation of incremental damage under cyclic forces such that the failure occurs in less than  $10^5$  cycles - became a new cause of failure. The Air Force's Engine Structural Integrity Program (ENSIP) brought about design changes that resulted in engines that were more resistant to LCF (16). The resulting decrease in LCF failures has brought increased attention to high cycle fatigue (HCF) related failures - failure under cyclic loading at  $10^6$  or more cycles - as they become a larger and larger percentage of the total number of engine failures (54; 52).

Presently, HCF related failures have become the primary cause of major engine failures experienced by the Air Force and Navy (52; 58). Because HCF conditions are leading to unpredicted and often catastrophic failures, it is currently a major

safety risk, especially in single engine fighters. This prompted then Chief of Staff of the Air Force, General Fogelman to state on 1 November 1995

Part of the problem is the workload on (sic) flightline troops and our engine shops are experiencing due to new inspection requirements to combat high cycle fatigue. We are working this problem hard but still don't know the root cause. It's a big problem-although the number of Class A accidents has decreased between FY 89 and FY 95, the percentage caused by engine material failure has increased. AFMC is working with the using commands, AF/LG, and SAF/AQ to find a solution. (25)

A national HCF Science and Technology program was therefore created to investigate this problem in 1996. Consisting of experts in HCF from the Air Force, Navy, industry and academia, its main purpose is to reduce HCF related mishaps by 50 percent by 2002 (12).

There is a particular HCF concern in aircraft engines which involves the impact of small foreign object damage (FOD) on the turbine blades. This FOD commonly occurs due to impact of debris, sand particles, etc., while taxiing on runways and during flight. This FOD combined with HCF is of extreme importance to the designers and maintenance crews of aircraft engines. The design methodology of blades is at present lacking sufficient understanding to predict the HCF life of a turbine blade after suffering FOD. A number of fan blades have been found to have failed from the fatigue initiated in regions of small FOD. Current fatigue design criteria are unable to predict the reduction in life of these damaged blades (rather current design would have predicted these flaws to be too small to cause any failure),

and many flaws are too small to be reliably detected by inspection. This clearly indicates that the ability to predict blade life in the presence of these small flaws is currently inadequate (54; 58).

When small FOD sites are discovered, a decision must be made to either repair the damage or replace the entire blade. If a repair is attempted, it is usually made by smoothing the damage site by grinding and polishing a groove of a much larger radius in place of the FOD. Estimates of the allowable radii for blending out the defects are based upon safe limits for edge notches in the blade. These estimates are presently largely empirical. Engineering criteria for determining which FOD areas need to be repaired, what those repair procedures should be, or alternatively when blades with FOD should be replaced, are still lacking (54).

To establish these engineering based criteria (instead of experience based criteria as currently being used) a scientific knowledge is needed to establish the relationship between FOD in a material and the material's life under HCF situations. To achieve this, this study used a hybrid experimental-numerical approach. The experimental part involved the testing of laboratory specimens to establish the HCF response after suffering initial damage representative of the types of FOD experienced by aircraft engine turbine blades in actual applications. The numerical part modeled the experimental conditions mathematically.

Two types of laboratory specimens were tested. The first type was a specimen of uniform rectangular cross-section. This simple geometry made it easier to measure

the dimensions of the damage inflicted upon these specimens. It also simplified the numerical modeling of the damaged state. The second type of specimen had a cross-section with tapers on both sides and rounded edges to simulate the geometry of an airfoil's leading edge. This geometry was chosen to be representative of typical turbine engine fan blades in service. The dimensions of this leading edge specimen were selected to correspond to other HCF testing being conducted under the HCF S&T program (12).

The material of all specimens in this study was the titanium alloy Ti-6Al-4V, which is currently being used as the material for fan blades in many military engines, and also in the HCF S&T program. Specimens were given various levels of initial damage by four FOD-simulating techniques to investigate their effects on the HCF behavior. These four techniques were selected because they are considered to span the extremes of the several possible methods to simulate FOD. Specimens without FOD were also tested to characterize their HCF resistance in an undamaged state.

The primary damage simulation technique was to impact the specimen with glass spheres with different diameters at a velocity representative of FOD impact. This is considered to be the most accurate simulation of actual field FOD events; it is also the most expensive and hardest to control from repeatability considerations. Because of the expense and complexity, cheaper and easier methods would be beneficial for FOD testing purposes. Some specimens were impacted by steel spheres also. This

was done to provide an additional check on the ability of finite element methods to model the sphere impact events.

A simpler chisel indentation method was also used, in order to determine its ability to faithfully simulate FOD effects on HCF behavior. This involved a quasi-static, displacement controlled indentation of the samples with chisel-pointed tools. These tools were made with various profiles to create different shapes of damage. This indentation was performed by loading the tool perpendicular to the edge. This technique has advantages in its cost and ability to control the depth and shape of damage. Finally, some specimens had a notch sheared from them by a chisel-pointed tool being moved across their thickness, i.e., in a direction transverse to the displacement used in the third method.

The high cycle fatigue behavior of the damaged specimens was established by testing the specimens in cyclic uniaxial tension loading. The fatigue stress needed to cause failure at a life of  $10^7$  cycles was established by the step testing method of Maxwell and Nicholas (45). An electromagnetic shaker was used to load the specimens at 350 Hz to reduce the time needed to accumulate the  $10^7$  cycles at each load step. These HCF tests were used to develop Haigh diagrams for a fatigue life of  $10^7$  cycles. Since in HCF the total life is dominated by the crack initiation time (40; 69), the cycles to failure were assumed to be the same as the crack initiation life (26).

The specimens were examined by various fractographic and microscopic techniques to record the size and shape of the damaged region and the location of the crack

initiation sites. Further, two novel techniques were developed to measure the plastic zone sizes. Three-dimensional nonlinear finite element modeling (FEM) of the damage imparted to the specimens was conducted to estimate the plastic zone and residual stresses around the FOD. Commercial FEM codes (both static and dynamic) were used to conduct this analysis. The computed results also validated the two novel measurement techniques used to measure the plastic zone size. These measurements of the plastic zone and the computed stress and strain fields in the vicinity of the FOD were used to explain the reduction in the fatigue life.

The specific objectives of this study can be summarized as:

- Conduct experiments to investigate the nature of the damage caused to Ti-6Al-4V by four different methods of FOD simulation:
  - impact by glass spheres
  - impact by steel spheres
  - indentation by a steel chisel perpendicular to the edge of the specimen
  - shearing notches by transverse motion of a steel chisel
- Determine the means by which the amount of damage imparted to a specimen can be quantified
- Measure the fatigue strength due to these different simulated FOD sites for a life of  $10^7$  cycles
- Analyze the FOD damage and fatigue loading using numerical methods to comprehend the mechanism by which FOD reduces high cycle fatigue strength

The next chapter provides some background material on pertinent fatigue topics and a review of the literature applicable to this study.



## ***II. BACKGROUND***

This chapter will present background information related to this study of FOD effects on the HCF behavior of Ti-6Al-4V. The first part concerns the engineering principles describing fatigue and damage phenomena under conditions being explored in this study. The second part discusses some broad classes of finite element analysis. The third will summarize previous studies performed in areas pertinent to this effort.

### **Fracture and Fatigue**

Fracture, the cracking, breaking or rupturing of an object, can be caused in metal components by various stress states which exceed the metal's ability to carry the load that causes the stresses. In the past, designing machine parts to resist stress only considered the application of static forces, and the part's resistance was only characterized by static properties such as the ultimate strength or the yield strength (85:45).

Over time it was observed that a part that could withstand a high static load would fail if the load fluctuated and that safe design limits for fluctuating loads had to be below the static limits. Thus the fatigue concept, with historical beginnings from the 19th century, was developed to account for this decreased resistance to fluctuating load (85).

We can say today, then, that fracture of metals by fatigue occurs when repeated loading over time causes failure. This can occur at stress levels which would not cause failure if applied in a steady manner or for shorter periods of time. The consideration of fatigue is essential to the design of components which undergo cyclic load variations, such as those in aircraft turbine engines. Various sources conclude that most machine parts fail from fatigue. Estimates of the number of parts range from 50% to 90% (26) to as high as 80 % to 100% (85). Since many of these failures cause financial loss or even loss of life, accurately predicting the behavior of machine parts subject to fatigue loading is very important.

The usual goal of this prediction is to determine the useful life of the part, i.e. number of cycles to failure ( $N_f$ ). However, for parts subjected to large numbers of cycles under the conditions which cause HCF, the goal is to determine the endurance limit stress - that stress below which failure will never occur during the design life of the part. To explore these concepts further requires some nomenclature to describe two important concepts: cyclic loading and fatigue life (85).

*Cyclic Loading.* The fluctuating load on a part can be random or periodic in nature. Random fluctuating loads will not be addressed in this work, and the periodic fluctuations considered here will have constant amplitude. The parameters describing this constant amplitude loading are described in Figure 1.

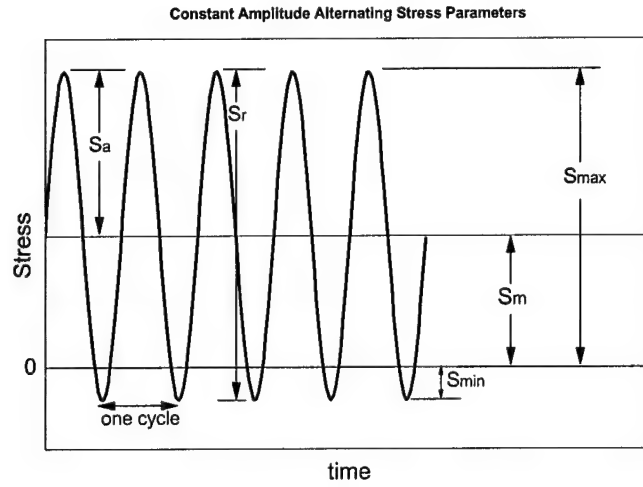


**Figure 1. Cyclic Stress Parameters**

We define

$S$  = nominal stress (*load / undeformed area;  $P/A$* )

$\sigma$  = true stress (uniaxial)

$\sigma_{ij}$  = tensorial stress

and for the special case of constant amplitude loading

$S_{\max}$  = numerically largest stress

$S_{\min}$  = numerically smallest stress (tension positive)

$$S_m = \frac{S_{\max} + S_{\min}}{2} \quad \text{mean stress}$$

$$S_a = \frac{S_{\max} - S_{\min}}{2} \quad \text{alternating stress}$$

$$S_r = S_{\max} - S_{\min} \quad \text{stress range}$$

$$R = \frac{S_{\min}}{S_{\max}} \quad \text{stress ratio}$$

$$A = \frac{S_a}{S_{\max}} \quad \text{amplitude ratio}$$

and note the useful relations  $A = \frac{1-R}{1+R}$  and  $R = \frac{1-A}{1+A}$ .

*Fatigue Life / Fatigue Limit.* Fatigue life ( $N$ ) is the number of loading cycles (of a specified type) a given specimen can tolerate before failure (of a specific nature). Fatigue strength is the stress required to cause failure at a specified fatigue life,  $N$ . Fatigue limit ( $S_f$ ) is the limiting value of fatigue strength as  $N$  becomes arbitrarily large, or in the case of materials which have no definable limit, the fatigue strength for a specified large  $N$  (this will usually be  $10^7$  in this effort). We can equally well define the fatigue limit in terms of plastic-strain amplitude, or for initially cracked bodies, in terms of the stress-intensity-factor (SIF) amplitude (32).

Fracture requires both the nucleation and propagation of cracks. The fatigue limit can be seen as a critical condition for nucleation of cracks or as critical circumstances for propagation of cracks of critical size. Real materials always have local inhomogeneities in stress distribution, so it isn't surprising that microcracks can be observed at nominal stress levels slightly below the fatigue limit. The micromechanics of persistent slip band (PSB) formation and the creation of microcracks, even in nominally smooth specimens, involves details of crystallographic dislocation movement (14; 38; 39; 40; 73). At the larger scale of the damage to be investigated in this effort, crack initiation criteria based upon the continuum mechanics of the bulk material near the damage site will apply.

Critical conditions for crack propagation can be expressed in terms of crack length and stress intensity factor (SIF). Stress amplitude and plastic strain amplitude are factors more suited for predicting initiation. Fatigue crack initiation occurs at stress

levels above and just below the fatigue limit. Above the limit, the crack will grow to failure. Below the limit, the crack will initiate, grow to some non-critical value, and stop (32).

It isn't often easy to tell whether the critical conditions for crack initiation or crack propagation are dominant, although it can be shown that for very long lives as in HCF, crack initiation life is nearly equal to the total fatigue life (38; 69).

### **Stress-life Methods**

The stress method of predicting fatigue life provides the number of cycles before failure ( $N_f$ ) as a function of the applied stress ( $S$ ). According to Zahavi, it assumes the material behaves elastically, ignoring plastic deformation (85:42). The relation between  $S$  and  $N_f$  is called the S-N curve (or Wohler curve). Defined as the dependence of the stress amplitude on the number of cycles to fracture, it has for many years been the only fatigue characteristic used for evaluation of basic fatigue strength, and was sufficient for this purpose until recently. Most metals exhibit S-N curves shaped like those in Figure 2.

Many equations have been proposed to describe the S-N curve. One of the simplest and most accepted is based upon the nearly linear relationship between these two parameters when  $N$  is plotted on a logarithmic axis (32:156):

$$\sigma_a = \sigma'_f (2 N_f)^b \quad (1)$$

where  $\sigma_a$  is the stress amplitude (here being true stress),  $\sigma'_f$  is the fatigue-strength coefficient (an empirical constant picked to fit experimental data to the equation), and  $b$  is the exponent of the S-N curve. Note the use of  $2N_f$  as the independent variable. This allows the fatigue strength coefficient to be computed by extrapolating the data back to the first log cycle, where  $N_f$  is  $\frac{1}{2}$ . This corresponds to failure after only one-half stress cycle, or loading from minimum to maximum load, prompting an analogy between fatigue-strength coefficient and the true fracture stress  $\sigma_f$ . Various relations have been proposed to relate the two. These relations vary from  $\sigma'_f = 0.92 \sigma_f$  to  $\sigma'_f = 1.15 \sigma_f$ . However, considering the poor agreement with test data referenced by Klesnil (32), any relation proposed for relating these two can only serve as a rough estimate of the true fatigue strength coefficient.

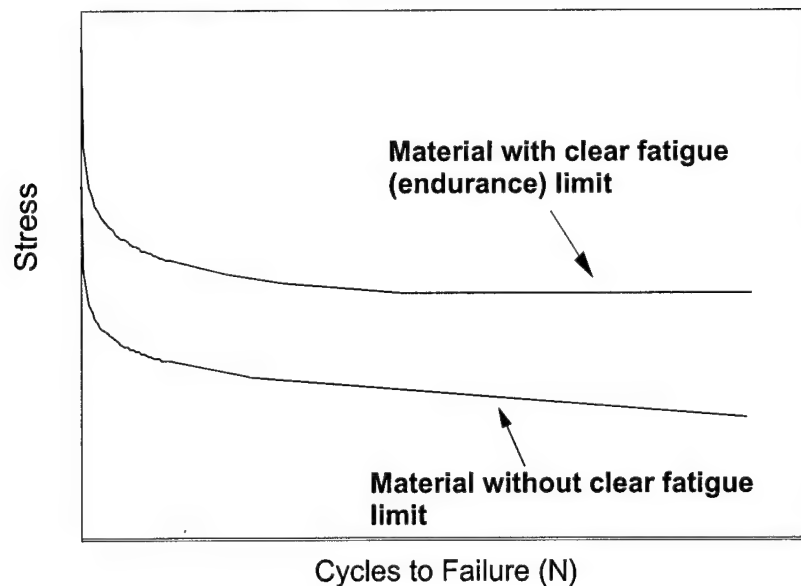


**Figure 2. Typical S-N Curves**

The Wohler curves are most often generated from stress controlled tests. The other procedure is strain control testing (32). They are important because in designing for finite life, not only is the resistance of the material to cyclic stress important, but the resistance to cyclic plastic strain can also be important, as will be discussed later.

### **Factors Affecting Fatigue**

When using data from a standard rotating-beam fatigue test, allowances must be made for differences between this standard specimen and the component whose fatigue resistance is being estimated (85). The empirical correlation describing these differences is given as

$$S_f = S'_f k_a k_b k_c \quad (2)$$

where

$S_f$  = fatigue limit for component

$S'_f$  = fatigue limit for standard test

$k_a$  = loading mode factor

$k_b$  = size effect factor

$k_c$  = surface roughness factor

The loading mode factor correcting rotating-beam test data for axial conditions is usually taken to be about 0.9. The size effect factor is 1.0 for axial loading (85:59).

Surface roughness can greatly affect the fatigue life of a part. Typically reported S-N curves use the nominal stress  $S$ , which is computed based upon the overall geometry, and surface roughness features and other irregularities act as stress concentration

points. As reported in (85:60), for steel this factor can vary from 0.9-0.95 for grinding operations to as low as 0.8 to 0.2 for forging. The lower factors usually coincide with higher tensile strength.

In addition to simple surface roughness, fatigue life depends strongly on the general state of the surface layer. This dependence is mainly due to influence on crack nucleation (32; 56; 70). While stress concentrations due to surface roughness can be detrimental, residual stresses and work hardening of the surface can improve the fatigue life.

### **Stress Concentration**

The most important factor affecting fatigue life is the rise in local stress due to stress concentrations. These can come from notches, initial cracks or other damage, or particles in the microstructure. At these concentrations, the peak stresses will be greater than the nominal stresses.

An important way to describe this rise in stress is the stress concentration factor,  $K_t$ . It is defined from elasticity theory as the ratio of the theoretical peak stress at a notch or other geometry to the nominal stress in the specimen containing the geometry:

$$K_t = \frac{\text{theoretical peak stress}}{\text{nominal stress}} \quad (3)$$



As the geometry of a notch becomes sharper, the stress concentration factor (SCF) rises, as can be seen from the formula for the SCF of an elliptical notch:

$$K_t = 1 + 2\sqrt{A/r} \quad (4)$$

where A is the semi major axis or depth of the notch and r is the notch root radius.

As used here,  $K_t$  is an elastic stress concentration, applicable only as long as no yielding occurs in the zone near the notch root. If yielding occurs, as it easily may in many notches, the actual stress will no longer be  $K_t S$ . This yielded zone near the notch root both lowers the stresses and the gradient of the stress as it decays to the nominal stress away from the notch zone (Figs. 3,4).

As a result of this changed stress gradient, it is found that the true fatigue life of many notched specimens is not exactly predicted by  $K_t$  (17:401). To get better agreement with experimental data, a fatigue notch factor,  $K_f$ , is used instead. By assuming the notched specimen fails when the peak stress applied to it equals the peak stress applied to a smooth specimen, then the fatigue notch factor is the ratio of the two fatigue limits  $K_f = (\text{fatigue limit}_{\text{smooth}})/(\text{fatigue limit}_{\text{notched}})$ .

$K_f$  can also be thought of as the ratio of the true peak stress in a notched specimen to the nominal stress in the specimen. In general,  $K_f$  is less than or equal to  $K_t$  (17; 85).

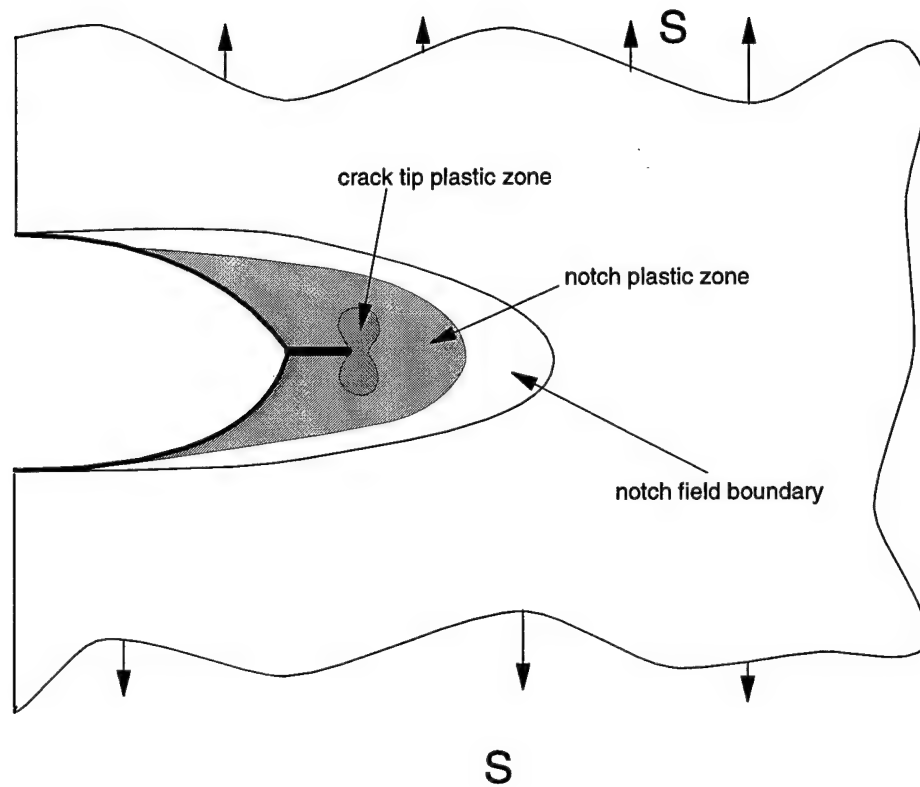


**Figure 3. Plastic Zone Near Notch Root with Small Crack.** The notch field boundary is an area where stresses created by the notch can be expected to affect the structure's strength. The notch plastic zone is the region plastically deformed due to overload from the notch (or possibly from the event which created the notch). The crack tip plastic zone is that region which flows due to stress overloading caused by the small crack emanating from the notch root.

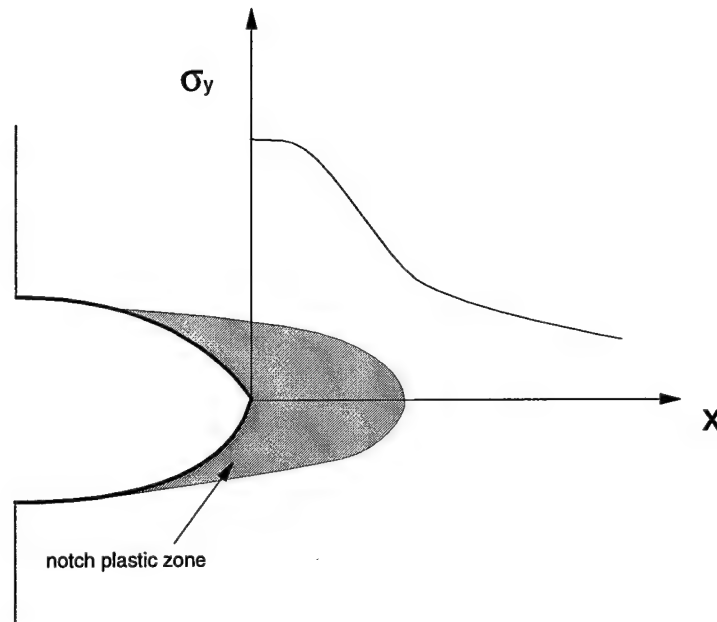


**Figure 4. Stresses Near the Plastic Zone Behind Notch Root.** In the case of the notch plastic zone, the stresses will rise as the notch is approached, but taper off to a maximum due to the plastic yield of material, which cannot support higher stresses than those at which it flows plastically.

This inequality is due to the notch root plasticity. An empirical relation between the two is known as Nueber's equation<sup>1</sup> (85)

$$K_f = 1 + \frac{(K_t - 1)}{1 + \sqrt{\frac{a}{r}}} \quad (5)$$

where  $r$  is the notch radius and  $a$  is a material property with dimensions of length.

Another widely used equation is by Peterson (46), which contains  $a/r$  raised to the unitary power.

---

<sup>1</sup> Referred to as Nueber's formula in the reference, this equation can be confused with a relationship between the nominal SCF,  $K_t$ , and the SCF and strain concentration factors,  $K_\sigma$  and  $K_\epsilon$ , at the notch root.

The relationship between  $K_f$  and  $K_t$  can alternately be described in terms of a notch

sensitivity factor,  $q$ , as  $q \doteq \frac{\text{effective stress rise due to notch}}{\text{theoretical stress rise due to notch}}$  or  $q = \frac{(K_f-1)}{(K_t-1)}$ . Use of

Nueber's equation for the fatigue notch factor would show the notch sensitivity to be

$$q = 1/(1 + \sqrt{a/r}).$$

$K_t$  is only a function of the loading mode and specimen geometry, while  $K_f$  is an empirically derived quantity. This makes the stress-life approach - estimating  $q$  and  $K_f$  by picking material constants (like  $a$  above) to fit the equation to test data and then simply reducing the fatigue life by  $K_f$  - a useful estimate where little plastic deformation is created. However, as noted in (68), it is unsuitable for situations where large plastic deformation occurs ahead of the notch root.

Other approaches to express  $K_f$  as a function of  $K_t$  and other material parameters have been tried which take into account the notch plasticity (19; 42; 63; 79; 86). Most invoke Nueber's formula (as distinct from Nueber's equation above) when the SCF and strain concentration factors in the notch root are different. Nueber's formula in this case is

$$K_t = \sqrt{K_\sigma K_\epsilon} \quad (6)$$

where  $K_t$  is the nominal SCF and  $K_\sigma$  and  $K_\epsilon$  are the SCF and strain concentration factors, respectively, at the notch root (17).

The use of  $q$  is best applied to smooth notches such as those deliberately machined into a part as a design feature. If the notch is very sharp, it may be more conservative

to assume it as a sharp crack and apply linear elastic fracture mechanics (LEFM) (17).

### **Linear Elastic Fracture Mechanics**

Fracture mechanics application to fatigue crack growth requires similitude. That is, if the growth of the fatigue crack can be characterized by a similitude parameter such as  $K$ , then similar values of  $K$  will yield similar fatigue behavior, regardless of the actual length of the crack. Stresses in a cracked body can prompt the crack to grow in three basic modes, as shown in Figure 5.

The stress state at the crack tip in Mode I (the only one to be discussed here) of a body loaded by a remote stress  $S$  can be expressed in the coordinate system described in Figure 6 as

$$\sigma_{ij} = \frac{K_I}{\sqrt{2\pi r}} f_{ij}(\theta) \quad (7)$$

where  $\sigma_{ij}$  is the stress at a point a distance  $r$  away from the crack tip at an angle  $\theta$  to the plane of the crack, and the  $f_{ij}$  are known functions.

$K_I$ , the similitude parameter, is the previously mentioned SIF which completely describes the stress intensity in the region of the crack.  $K_I$  is determined from considerations of the loading and crack geometry. It is distinct from the SCF, which remains continuous in the region of the notches they describe, in that expressions for  $K_I$  become singular (tending toward infinity) at the tip of the crack. Since real metals

cannot support infinite stress,  $K_I$  only approximates the stress state away from some (possibly vanishingly small) plastic zone. So long as the region of interest near the crack tip remains elastic,  $K_I$  adequately describes the stress state, and cracks with similar  $K_I$  will behave similarly (11).

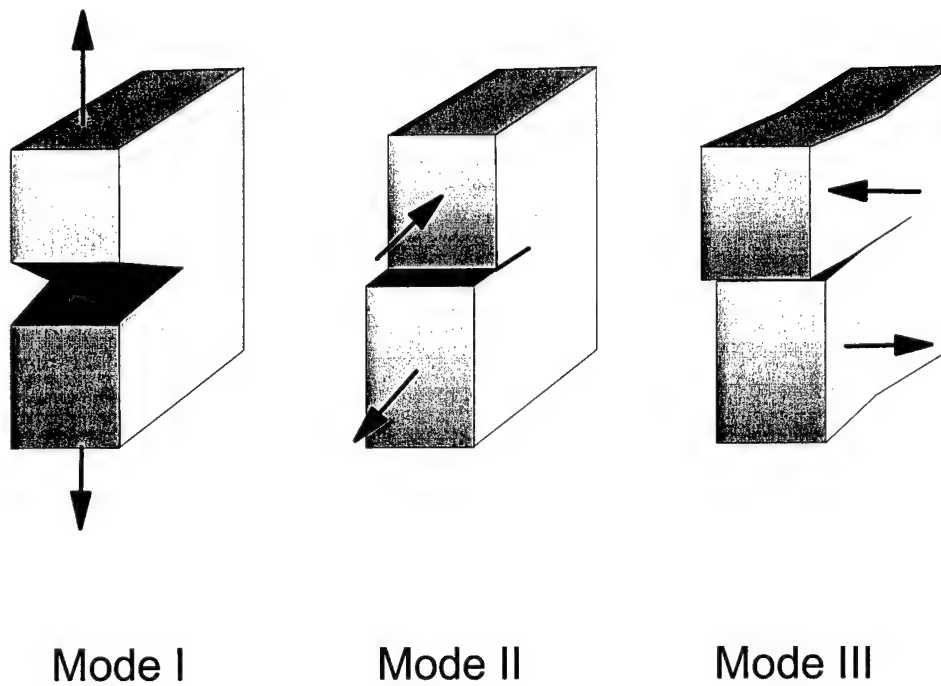


**Figure 5. Crack Opening Modes**

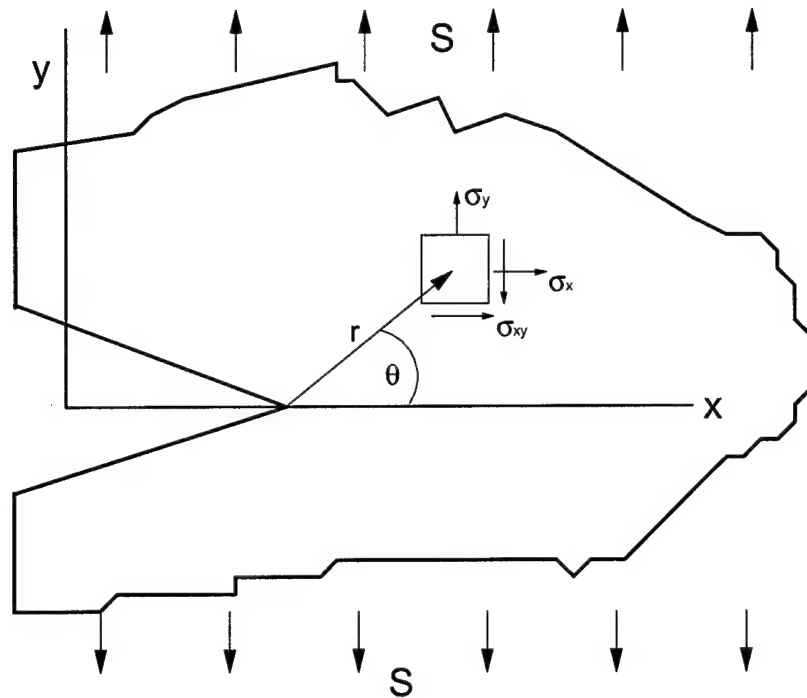


**Figure 6. Stresses Around a Mode I Crack Tip**

Crack propagation studies, where an initial crack size is assumed or present, frequently use  $K_I$  as the independent variable (2; 9; 18; 28; 36; 72). But LEFM is based upon elastic behavior at the crack tip, and even elastic-plastic fracture mechanics only accounts for a plastic zone created near the crack tip. Various means to adjust  $K_I$  for the effects of a finite plastic zone near the crack tip have been devised (9; 18; 20; 28; 30; 65; 75; 84). Most of these involve various estimations of the size and shape of the plastic zone. However, when the crack is still nucleating or is so small it lies wholly within the plastic zone, its behavior is markedly different from large crack behavior at similar values of  $K_I$ , and LEFM fails to adequately describe the crack growth (68:294).

Because much of the HCF life is consumed in crack initiation (38; 69), the regime where LEFM applies to the crack growth is expected to be insignificant. At best if a significant portion of the total fatigue life is consumed in growing a small crack through the plastic zone near the FOD damage, small crack anomalous growth would apply (20; 22; 30; 34; 41; 71; 76; 80). Small crack anomalous growth refers to the tendency of some materials to show crack growth rates which cannot be described by LEFM when the crack sizes are very small (58).

Neither simple adjustment of smooth specimen fatigue data for elastic SCFs (which is usually only concerned with a notch root radius) nor elastic-plastic fracture mechanics (which assumes the plastic zone is created only by yield due to remote stress) should be expected to include everything that affects fatigue crack initiation in and propagation from a FOD-created plastic zone. Stress concentration due to changed geometry, as well as plasticity and residual stresses created from the impact may all play important roles and should be considered. Approaches which account for these factors have been tried by Sheppard and Xin-lu (63; 83). In these approaches, FEM techniques are used to evaluate the stress field in a finite area around the notch. The fatigue notch factor is evaluated as the ratio of the weighted average stress in the zone around the notch root to the nominal stress.

### **Strain Amplitude Life**

Fatigue life data presented in terms of strain amplitude first appeared in the 1950's. Manson and Coffin presented the plastic strain amplitude versus cycles to failure for



low-cycle fatigue data. Twenty years later the first papers showing this approach used to represent high-cycle fatigue data appeared (32). The Manson-Coffin relation between plastic-strain amplitude and cycles to failure can be written as

$$\varepsilon_{ap} = \varepsilon'_f (2N_f)^c \quad (8)$$

where  $\varepsilon'_f$  is the fatigue-ductility coefficient and  $c$  is the Manson-Coffin exponent.

The close fit to many experimental data justifies the power-law relationship in (8). However, some experimental data indicate that this power-law relation may not always give the best fit to the data. For those cases where the simpler relation in (8) is appropriate, the relationship between the fatigue-ductility coefficient and the true fracture strain cannot be given by a single formula. Measurement of the fatigue-ductility coefficient is thus based upon actual measurements of the Manson-Coffin curve (32:158).

Many real components operate under conditions of constant total-strain amplitude. Total strain amplitude is the sum of plastic-strain amplitude and elastic-strain amplitude, which can be related to stress amplitude by Hooke's law ( $\varepsilon_{ae} = \sigma_a/E$ ). This gives a form for the fatigue life curve in terms of total-strain

$$\varepsilon_{at} = \varepsilon_{ae} + \varepsilon_{ap} = \frac{\sigma'_f}{E} (2N_f)^b + \varepsilon'_f (2N_f)^c \quad (9)$$

where the constants  $\sigma'_f$ ,  $b$ ,  $\varepsilon'_f$  and  $c$  are considered to be material properties (17; 32).

Superposition of the S-N curve and the Manson-Coffin curves shows that, in the region of high-cycle fatigue, elastic-strain amplitude dominates the total strain amplitude (Fig. 7).

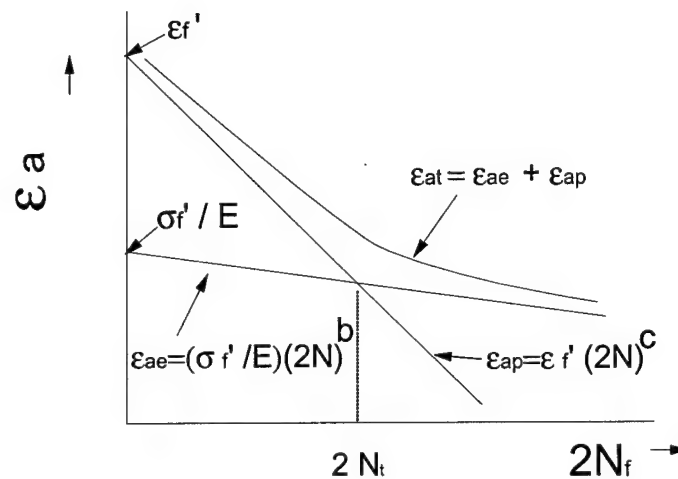


**Figure 7. Stress- and Strain-Life Curves**

Langer (32:161) proposed an estimation of the total-strain versus cycles to failure curve by a technique called the *fictive stress*, which is defined as  $\sigma_{aF} = E\epsilon_{at}$ .

Expressing the plastic strain amplitude in terms of the fictive stress and choosing values for the constants appropriately yields  $\epsilon_{at} = \epsilon_f / (4\sqrt{N_f}) + S_f / E$ .

Manson and Hirschberg (32:162) proposed the method of a "Universal slopes equation." In it they assumed the slopes of the two straight lines in Figure 7 are the

same for all materials. Equation (9) is then applied to experimental data and the constants that give the best fit are determined. The result of this approach is

$$\varepsilon_{at} = 0.585 \left( \frac{\sigma_{UTS}}{E} \right)^{0.832} N_f^{-0.09} + 0.0133 \varepsilon_f^{0.155} \left( \frac{\sigma_{UTS}}{E} \right)^{-0.53} N_f^{-0.56} \quad (10)$$

where  $\varepsilon_{at}$  is the total strain amplitude  
 $\sigma_{UTS}$  is the ultimate tensile strength  
 $E$  is the elastic (Young's) modulus  
 $\varepsilon_f$  is the true strain at fracture  
 $N_f$  is the cycles to failure

Equation (10) includes data for 47 materials, including steels, aluminum and titanium (32:162). Unfortunately, this procedure can differ from actual data by as much as an order of magnitude. Thus this equation, and the Langer method also, are good for crude estimation only.

The difficulties in estimating fatigue life curves by these methods led Klesnil and Lukas to conclude

Since experimental techniques today enable the fatigue life curve to be determined relatively quickly, it is advisable even in engineering practice to choose direct experimental determination of the strain verses N curve, and not the crude estimation offered by the procedures presented. (32)

### Influence of Cycle Asymmetry (Mean Stress Effects)

Nearly all the discussion above has been concerned with cyclic loading where the mean stress was zero or  $R = -1$ . However engine blades, and many other practical components, have a significant tensile mean stress. This mean stress shortens fatigue life as illustrated in Figure 8 (68; 82).

A majority of the procedures for describing the effects of mean stress on fatigue life can be found in the paper by Nihei et al. (55). The most promising approach for this work seems to be the Smith-Watson-Topper (SWT) procedure based upon the parameter  $\sigma_{\max} \epsilon_{at}$ , where  $\sigma_{\max}$  is the maximum cyclic stress and  $\epsilon_{at}$  the total strain amplitude. In the SWT approach, it is assumed that fatigue life curves expressed as this parameter versus cycles to failure are independent of the mean stress.

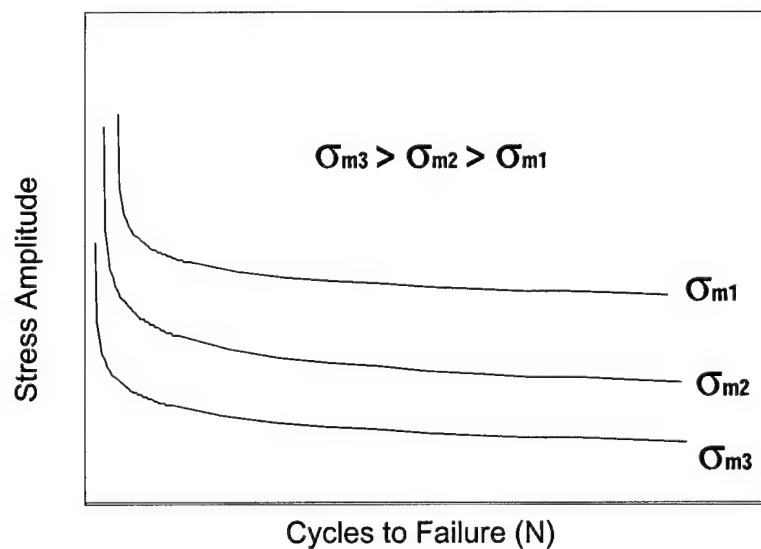


**Figure 8. Mean Stress Effects on Typical S-N Curves**

Another way to state this is to say that the SWT parameter is a function only of the fatigue life, i.e.  $\sigma_{\max} \epsilon_{at} = f(N_f)$ . Since the SWT parameter is assumed to be identical for any state of mean stress and for the completely reversed loading case, it can be written as  $\sigma_{\max} \epsilon_{at} = \sigma_{\max(\text{fully reversed})} \epsilon_{at(\text{fully reversed})}$ . Using Equations (1) and (9) for stress and strain, we obtain  $\sigma_{\max} \epsilon_{at} = \sigma'_f (2N_f)^b \left[ \frac{\sigma'_f}{E} (2N_f)^b + \epsilon'_f (2N_f)^c \right]$ . This can be rearranged to

$$\sigma_{\max} \epsilon_{at} = \frac{\sigma'^2_f}{E} (2N_f)^{2b} + [\sigma'_f \epsilon'_f (2N_f)^{b+c}] \quad (11)$$

Klesnil states that for data taken on copper, a stress-strain parameter based upon plastic strain is better than one based upon total strain. He asserts that it is probably true for all ductile materials (32).

Landgraf proposed another mean stress relationship  $\sigma_a = (\sigma'_f - \sigma_m)(2N_f)^b$ , and verified it for steel (17; 32). This form has the advantage of needing only stress data for estimation of fatigue life. Dowling shows how this form is derived from Morrow's approach of defining an equivalent completely reversed stress amplitude (17):

$$\sigma_{ar} = \sigma_a / \left(1 - \frac{\sigma_m}{\sigma'_f}\right) \quad (12)$$

### Constant Life Diagrams

Constant life diagrams are another way to present mean stress effects. In this approach, curves that represent combinations of states which yield a constant value of fatigue life are plotted with axes representing two of the cyclic stress parameters.

The oldest relationships are those attributed to Goodman and Gerber (32). Along with the Soderberg relation, they are the most well known of the constant life diagrams (68). These empirical relations are obtained by expressing the dependent variable (here stress amplitude) in terms of the independent variable (ratio of mean stress to UTS or yield strength) (13):

$$\sigma_a = \sigma_f \left\{ 1 - \frac{\sigma_m}{\sigma_{UTS}} \right\} \quad \text{Goodman} \quad (13a)$$

$$\sigma_a = \sigma_f \left\{ 1 - \left( \frac{\sigma_m}{\sigma_{UTS}} \right)^2 \right\} \quad \text{Gerber} \quad (13b)$$

$$\sigma_a = \sigma_f \left\{ 1 - \frac{\sigma_m}{\sigma_{yield}} \right\} \quad \text{Soderberg} \quad (13c)$$

where  $\sigma_f$  is the fatigue strength for the fixed life plotted at zero mean stress ( $R = -1$ ).

Note that some sources in the fatigue literature call the first relation a *modified Goodman equation* (17; 26). These three equations are shown schematically in Figure 9. Most of these equations require vast amounts of experimental data in order to determine fatigue limit values.

Accelerated means to acquire fatigue data, especially high-cycle fatigue data have been sought. In the accelerated technique proposed by Maxwell and Nicholas, the

stress conditions which result in a fatigue life of a given number of cycles are plotted on axes of stress amplitude versus mean stress, as in the constant life axes in Figure 9 (45). The key differences are that no attempt is made to relate the x- or y-axis intercepts to static material properties in this 'Nicholas-Haigh' (N-H) diagram<sup>2</sup>. To collect life data in an accelerated manner, a single specimen is subjected to  $10^7$  cycles of loading (or other appropriate value of fatigue life) at a value of stress that is not expected to cause failure. If the specimen survives this block of loading, the stress level is increased by a small amount (5% is suggested) and the test repeated. This continues until the specimen fails in less than  $10^7$  cycles. Assuming the damage accumulates linearly, the maximum stress plotted on the ordinate is

$$\sigma_{N-H} = \sigma_{pr} + \frac{N_f}{10^7}(\sigma_f - \sigma_{pr}) \quad (14)$$

where

$\sigma_{N-H}$  is the maximum stress to be plotted on the N-H diagram

$\sigma_{pr}$  is the maximum stress level of the previous block of loading

$N_f$  is the number of cycles to failure during the last block of loading

$\sigma_f$  is the maximum stress level of the final block of loading

Note that the denominator of  $N_f$  in Equation (14) should be changed if a fatigue life other than  $10^7$  is chosen.

---

<sup>2</sup> In reference 45, the historical accuracy of referring to constant life plots on stress amplitude/ mean stress coordinates by various names is discussed. Here we will refer to these plots as Haigh diagrams.

This method of adding damage from different test conditions keeps all variables the same except the maximum stress. Other methods of adding damage from different conditions are used to account for variable amplitude and random loadings. The most well known of these is the Palmgren-Miner linear damage accumulation rule (13; 17; 35; 62; 68).

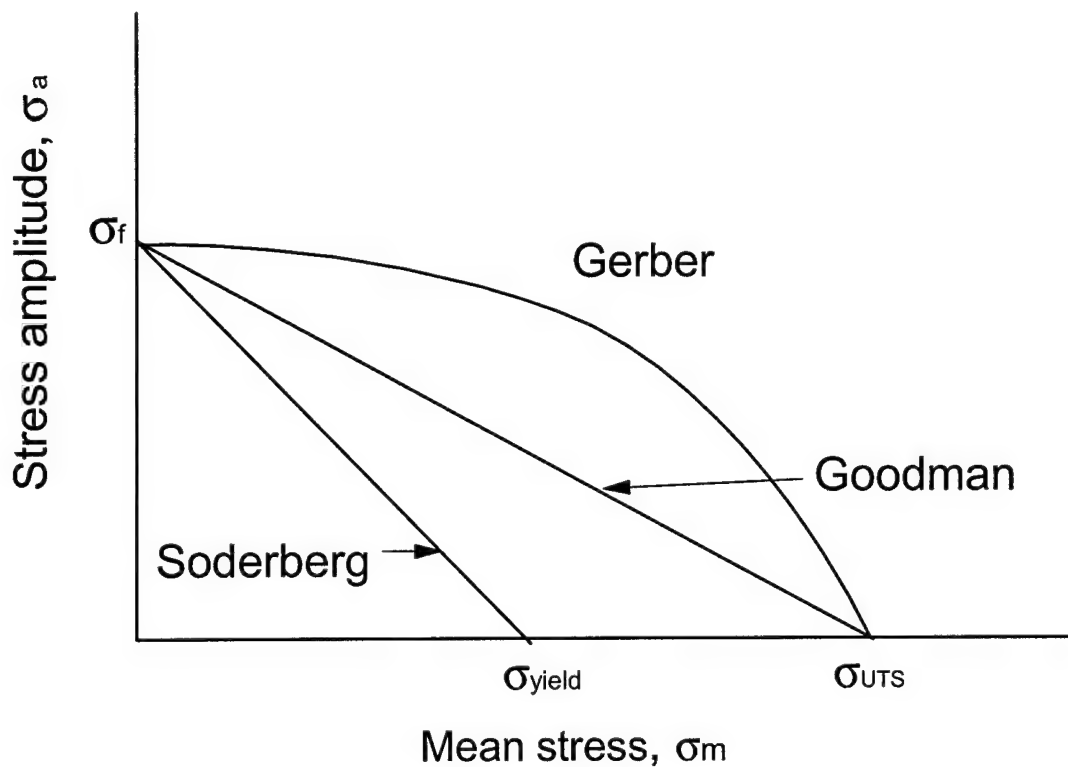


**Figure 9. Constant Life Curves**

The Palmgren-Miner rule assumes that the percentage of total fatigue life of a specimen expended during cycling at one stress condition can be added to the percentages expended at other stress conditions. If a specimen is cycled for  $n_1$  cycles at a stress amplitude  $\sigma_{a1}$  which corresponds to a fatigue life  $N_{f1}$ , and then is



cycled for  $n_2$  cycles at a stress amplitude  $\sigma_{a2}$  which corresponds to a fatigue life  $N_{f2}$ , then failure will occur if the percentages of fatigue life sum to unity,

$$\frac{n_1}{N_{f1}} + \frac{n_2}{N_{f2}} = 1 \quad (15)$$

Palmgren-Miner's rule is based upon the assumption that total hysteresis losses are independent of stress amplitude. Feltner and Morrow further assume the energy to fracture in cyclic and monotonic loading are identical (32). If this is correct, it suggests a way to relate FOD damage and subsequent HCF failure. Feltner and Morrow's expression for the total deformation energy  $U$  in monotonic fracture is given by

$$U = \int_0^{\varepsilon_f} \sigma_f \left( \frac{\varepsilon}{\varepsilon_f} \right)^n d\varepsilon = \frac{\sigma_f \varepsilon_f}{1+n} \quad (16)$$

where  $\sigma_f$  and  $\varepsilon_f$  are the true fracture stress and strain, respectively, and  $n$  is the monotonic strain hardening exponent (32:173).

### **Numerical Modeling of Stress States**

Most of the approaches for predicting crack initiation life mentioned above have required knowing or estimating the stress and/or strain states in the region around the crack. For simple geometries of notches, there are many closed form analytical solutions to achieve this (5; 6; 23; 24; 37; 42; 43; 81). These geometries are often

studied because of their ease of analysis, or because they are representative of deliberately machined features needed in actual applications. For arbitrarily shaped damage, as will be expected in the case of FOD, the damaged zone is more complex and finite element modeling is required (18; 35; 63; 69; 77; 83).

If an initial defect is created by the impact of a hard object into a specimen, the resulting stress and strain distribution may be complex, even for relatively simple defect geometry. The FEM analysis of the damage site is needed to predict the final shape of defect (hereafter also referred to as a notch) as well as to predict the residual stress/strain in the damage zone. The shape and size of plastic deformation is essential for an accurate understanding of the role of the plastic zone in the initiation or propagation of fatigue cracks in the vicinity of a damage site (34; 44). FEM methods can be also be used to predict the stress concentration at the notch root after the damage has been created.

A proper application of finite element methods to model a damage event and subsequent tension loading due to fatigue begins with understanding how the finite element method works. The finite element method is a numerical scheme to approximate the solution ( $\phi$ ) to an equation defined over a continuum, such as a structural body. The body is divided into smaller regions (elements) and  $\phi$  is approximated by simple equations in terms of the values of  $\phi$  at discrete locations within the element (nodes). In the case studied in this effort, elasticity theory is used to derive the relationship  $\mathbf{F} = \mathbf{k} \mathbf{x}$  where  $\mathbf{F}$  is a vector of forces applied to each node

and  $\mathbf{k}$  is a square matrix of stiffness coefficients which relate the forces  $\mathbf{F}$  to the displacements of the nodes,  $\mathbf{x}$ . If  $\mathbf{F}$  and  $\mathbf{k}$  are independent of time,  $\mathbf{x}$  can be solved by inverting  $\mathbf{k}$ ,  $\mathbf{x} = \mathbf{k}^{-1} \mathbf{F}$ . For details of how these forces, displacements and stiffnesses are defined, the reader is referred to the excellent text by Cook et al. (15).

When the forces or stiffnesses are dependent upon the displacements (as they are when the material yields plastically or the deformations grow so large that the deformed positions of the material cause the force application directions to change) the total response of the system is modeled as a series of smaller steps, during each of which a linear approximation to the stiffness matrix is used to solve for the state of the body at the end of the step. This state is used as the initial input to another small step, where a new approximation to the stiffness matrix is made which agrees with the state of the displacements at that particular step. Various means to accomplish these approximation steps have been developed and are available in commercial FEM codes such as ABAQUS (1; 15; 47).

When the inertia of a structure is significant, as it would be during a time history analysis of the response of the rectangular specimen to the impact of the glass or steel spheres, the equations to be solved become

$$\mathbf{M}\ddot{\mathbf{x}} + \mathbf{C}\dot{\mathbf{x}} + \mathbf{k}\mathbf{x} = \mathbf{F} \quad (17)$$

where  $\mathbf{M}$  is a matrix of nodal masses  
 $\mathbf{C}$  is a matrix of damping coefficients  
 $\dot{\mathbf{x}}, \ddot{\mathbf{x}}$  are the first and second time derivatives of the displacements

If the stiffness and/or damping matrices are nonlinear (functions of displacements), the preferred method of solving this set of equations is to integrate them directly over time (that is, create a time-history solution). To do this, the time derivatives  $\dot{x}$  and  $\ddot{x}$  are replaced by finite-difference representations. If the finite-difference discretization of the displacements and their derivatives yields a formula for the displacement at a given time step in terms of the displacements at previous time steps (so that they will be explicitly known before the calculation is needed) the solution is known as an explicit direct integration time history. Explicit methods are only conditionally stable; if the time step chosen for the discretization is too large, the method will not converge to a solution (15:395-398). Commercial applications like MSC/Dytran have the option of choosing a suitable time step automatically (48). The present effort used both ABAQUS and MSC/Dytran finite element codes to analyze the FOD in the specimens, as discussed in Chapter V.

### **Previous Studies**

There are many studies available in fatigue literature which describe related topics applicable to the present study. These include earlier referenced topics such as fatigue notch sensitivity studies (2; 5; 6; 18-20; 28; 30; 37; 46; 65; 72; 75; 76; 79; 84; 86), HCF crack initiation (9; 14; 20; 34; 38; 40; 62), FEM studies of the stress field around notches (63; 80; 83), fatigue response of metals with non-FOD types of

damage (8; 43-45; 55; 58; 69; 74), and similar studies concerned with pieces of the FOD/HCF interaction process, as opposed to the entire combined phenomena.

Although there has been some interest in FOD/fatigue interactions for at least two decades, almost no previous studies were found by the author where FOD was investigated under HCF conditions. A 1980 study of FOD effects on fatigue by Nicholas et al. studied the LCF strength reduction due to steel, glass and sand pellet impacts (53).

The complex phenomena of impact damage and HCF historically have been studied separately, not together. Since the need to study the combination of FOD and HCF has only recently become important, the majority of FOD/HCF efforts exist as unpublished preliminary studies, especially within the engine industry (66; 29; 60). A presentation by Gravett et al. at the 4th National Turbine Engine High Cycle Fatigue Conference (HCF '99) describes the recent efforts funded by the USAF to investigate various HCF performance issues, including HCF/FOD interaction (27).

One of the earlier studies into this area was presented by Roder, Thompson and Ritchie at the 3rd National Turbine Engine High Cycle Fatigue Conference (HCF '98) (60). In it, they investigated combined FOD/HCF effects using a single size of chrome-hardened steel sphere which impacted the face of tension specimens made from the same lot of Ti-6Al-4V used in this study. The damage characterization methods described in Reference 60 were limited to optical measurements of physical

notch size, although plans were described for future work measuring the residual stresses in the damaged region.

Besides Roder's paper (60), seven other papers on HCF/FOD interaction were presented at HCF '99. Each included an important part of the study of the FOD/HCF problem. Hudak et al. applied a fracture mechanics approach to account for the worst possible cracks that may grow from a damaged region, and predicted the conditions under which these cracks would arrest or else grow to failure (31). They applied this approach to data collected on HCF/LCF interaction experiments conducted on specimens with machined notches. The residual stress field created by FOD could be accommodated in this approach, although no attempt was made in Reference 31 to assess these complex stresses.

Lanning et al. presented work on the LCF/HCF interaction of notches machined around the circumference of a round tension specimen and V-shaped notches machined at opposite edges of a flat dogbone specimen (33). FEM predictions of the actual stress states in the notches were plotted on Haigh diagrams for lives of  $10^6$  cycles. The finite element modeling included three-dimensional elastic models, and two-dimensional plane strain elastic-perfectly plastic models. There was some indication that the FEM-predicted actual stress states might explain the HCF behavior of the specimens damaged by prior LCF loading.

Boyce et al. described efforts to develop an X-ray diffraction technique for measuring the residual stresses in very small areas, like those around the FOD damage site (7).

While this technique will be very useful when perfected, it is currently unavailable due to many experimental difficulties.

In Reference 59, Roder et al. described further study on the steel sphere impact damage reported in Ref. 60. Additional specimens were tested at one angle (perpendicular to the face of the specimens) and a velocity range between 200 and 300 m/s. The fatigue loading was applied at 20 Hz and crack propagation was measured. The fatigue life curves were generated but the residual stresses were not assessed. No crack propagation through the damaged zone was observed when the stress intensity factor range was less than  $2.9 \text{ MPa}\sqrt{\text{m}}$ .

Stewart et al. conducted steel sphere impacts on actual engine blades (67). Impacts were on the face of the blades, near the leading edges. The details of fatigue testing of these blades is not provided. Dyna3D was used for FEM analysis of the impact damage. The sphere was modeled as an elastic body, using steel material values from handbooks. The blade was described by an elastic-perfectly plastic model. An effort to model the material failure by a more complex criterion dependent upon several variables was described.

Finally, Ruschau et al. described their experimental work on HCF effects from 1 mm diameter glass sphere impacts on the edges of specimens (61). A dogbone specimen was used, which was tapered to a radius at the edges. Two radii, representative of engine blade leading edges, were tested. The glass spheres were impacted directly onto the tip of the edges at various angles from  $0^\circ$  to  $60^\circ$ . Specimens were made from

the same batch of Ti-6Al-4V plates as used in this study and also from an ingot forged into a round bar. The specimens that were made from the plates were tested to a life of  $10^7$  cycles using an electromagnetic shaker identical to the one used in this study. The marked decrease in fatigue strength at  $10^7$  cycles from the glass spheres, especially those fired at  $30^\circ$  into the edges, is documented. No effect on the fatigue strength reduction from the leading edge radius was apparent. Further, analysis of the damage created at the FOD is limited to visible and scanning electron microscope observations.

From the above mentioned previous studies, even though of limited amount, it is obvious that useful insight into the actual process of HCF failure in materials damaged by foreign objects would require a unique combination of many approaches simultaneously. A thorough understanding of the damage created by FOD-like mechanisms must include the residual stresses. From Ref. (7), it is clear that residual stress is important to the FOD/HCF interaction, although Refs. (59) and (60) indicate how difficult it is to include residual stress effects.

An actual mechanism for the initiation of fatigue cracks in the damaged regions and a criterion for predicting HCF life after FOD damage must be identified. An appropriate numerical model, if it could accurately represent the damage mechanism, could be used to compute the residual stress field in the damaged region. This field's effects on the HCF behavior of Ti-6Al-4V could then be determined. This will require a more complex model than any described in the works referenced above.



Finally, a comparison should be made among the several means of simulating FOD currently in use, in order to establish what methods are best for laboratory evaluation of the HCF properties of FOD damaged turbine engine materials and structures.

To accomplish these requirements, this study has:

- Investigated damage in flat rectangular specimens of Ti-6Al-4V by four different means of simulating FOD:
  - ♦ from impact by 1 mm, 2 mm and 5 mm diameter glass spheres at 305 m/s (which has been considered the most faithful representation of real FOD from sand or gravel).
  - ♦ from impact by 2 mm and 4 mm diameter steel spheres at 305 m/s (a good simulation of damage from rivets or other metallic objects).
  - ♦ by quasi-statically indenting the specimen edges with steel chisels having tip radii of 0.5 mm, 1 mm and 2.5 mm.
  - ♦ by shearing a notch from the specimen edges with a 1 mm radius chisel.
- Quantified the damage by three different techniques, including one easy to apply optical criterion which has not been previously reported.
- Tested these specimens at 350 Hz to determine their fatigue strength at  $10^7$  cycles and determined a stress threshold below which no fatigue fracture was observed. The total depth into a specimen to which the plastically deformed zone extends was found to be a damage quantification parameter which yields a simple empirical relationship with the reduction in fatigue strength. Using this parameter, the damage created by all techniques studied produced identical

reductions in fatigue strength, within the statistical variation in the fatigue strength.

- Analyzed the glass and steel sphere impacts and chisel indentations with more complex three-dimensional elastic-plastic finite element models than previously applied and verified the ability of these models to accurately describe the FOD event.
- Used these finite element models to simulate the HCF loading levels in order to understand the effect of the residual stress state on the failure of the damaged specimens and determined a criterion to predict HCF failure of Ti-6Al-4V after damage by simulated FOD.

This study contributed to four major aspects of the high cycle fatigue community's recent research into the effects of FOD on HCF. The suspected importance of residual stresses on FOD/HCF interaction has been confirmed. The validity of numerical modeling to compute the residual stress field created by FOD and that field's effects on the fatigue strength of Ti-6Al-4V has been demonstrated. The existence of a threshold strength for Ti-6Al-4V which has suffered large amounts of damage is indicated - a potentially very useful result for engine design. A damage parameter which can be used to equate damage amounts from four different FOD simulation techniques has been determined. This will allow the use of inexpensive and easily controlled methods of FOD simulation to replace more difficult and expensive means.

### ***III. EXPERIMENTAL PROCEDURE***

This chapter will describe the material from which the specimens were made and the configuration in which they were tested. It will then describe the four means by which the specimens were damaged and present the details of how the fatigue testing was conducted.

#### **Specimen Preparation**

*Material details.* All specimens were taken from the material prepared especially for the Air Force Research Laboratory's HCF program (21). The material is a titanium alloy containing 6% aluminum and 4% vanadium (Ti-6Al-4V). It was cast as a 63.5 mm (2.5") diameter bar and cut into 406 mm (16") lengths which were then forged into flat plates approximately 406 mm x 150 mm x 20 mm. These forged plates were solution heat treated and vacuum annealed. A complete description is given in Appendix A.

The material has been characterized for tensile properties extensively by several organizations under the AFRL HCF program (3; 4; 21). A summary of these results is shown in Table 1 and a depiction of the typical microstructure is in Figure 10. The averages of these properties at the slowest strain rate are:

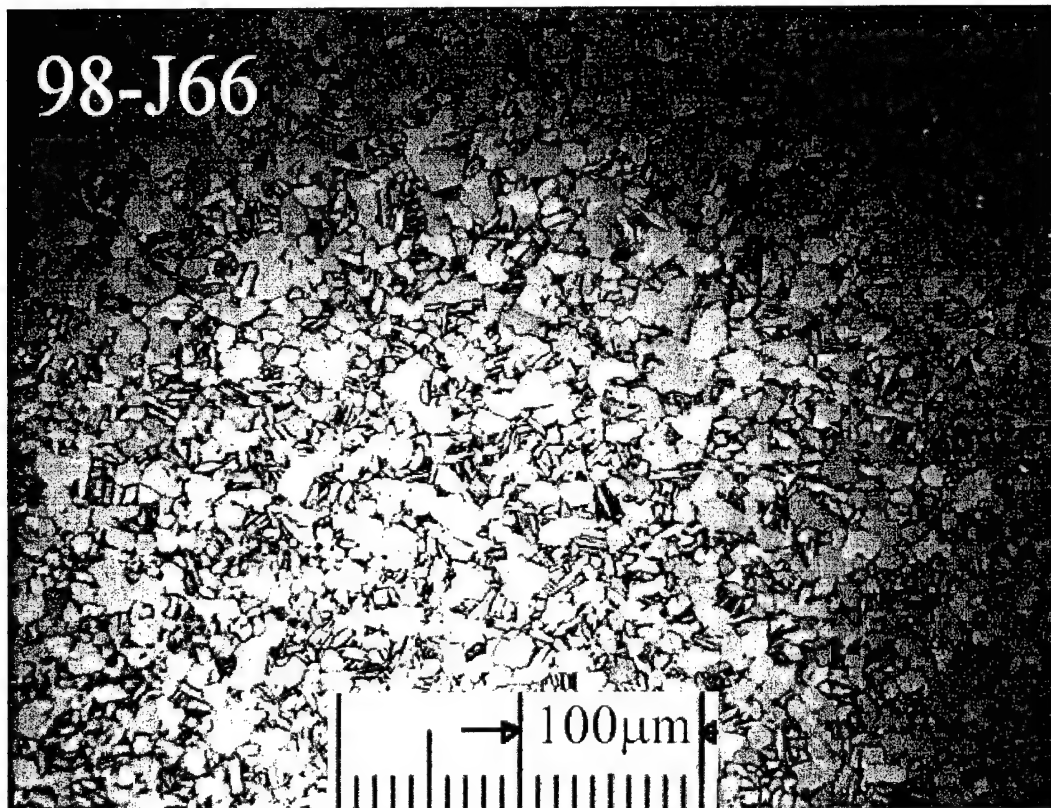
Yield Stress: 930 MPa (134.9 ksi)  
Ultimate Tensile Stress: 978 MPa (141.8 ksi)  
Young's Modulus: 118 GPa (17,100 ksi)

Table 1. Ti-6Al-4V Mechanical Properties (21)

Sample	Location*	Orient.	Strain Rate (s <sup>-1</sup> )	UTS (MPa)	YS (MPa)	EI (%)	Modulus (GPa)
97-H86	edge	L	5X10 <sup>-4</sup>	970	926	19.9	116
97-H98	edge	L	5X10 <sup>-4</sup>	985	935	20.0	115
97-H90	center	L	5X10 <sup>-4</sup>	976	929	21.2	116
97-H91	center	L	5X10 <sup>-4</sup>	981	931	19.0	124
97-J02	center-tran	T	5X10 <sup>-4</sup>	997	947	21.0	121
97-J03	center-tran	T	5X10 <sup>-4</sup>	993	937	19.2	134
97-H92	center	L	5X10 <sup>-2</sup>	1008	998	18.1	128
97-H93	center	L	5X10 <sup>-2</sup>	1019	1007	18.4	125
97-H94	center	L	5X10 <sup>0</sup>	1075	na	15.5	na
* location refers to the position within the forged plates, as summarized in Appendix A and described in Ref. 21.							

*Test specimens.* Two different types of specimens were tested, as discussed in the following sections.

*Simulated airfoil leading edge cross section.* Figure 11 shows the specimen with a simulated airfoil leading edge cross section. This specimen configuration was developed under an Air Force Research Laboratory program to study other aspects of FOD/HCF interaction. In this effort, this specimen was used only to establish the undamaged HCF properties of Ti-6Al-4V. The specimens were cut from the rolled plates with the specimen longitudinal axis aligned with the rolling direction.



**Figure 10. Typical Microstructure of AFRL HCF Program Ti-6Al-4V.** This sample came from Specimen 98-J66. The surface was polished and etched as described in Chapter IV in the section on grain counting. The location shown here is in an undamaged region far from any damage sites and represents the undamaged microstructure of all specimens in the X-Y plane of the specimen (see Figure 12).

*Rectangular cross section.* Figure 12 shows the uniform rectangular cross section samples. This configuration was chosen for the FOD samples because it can be machined less expensively and it can be analyzed easily. The lack of a thicker section at the grip ends was not expected to cause any difficulty during fatigue testing due to the anticipated stress concentration which would be created in the center of the sample by the simulated FOD.

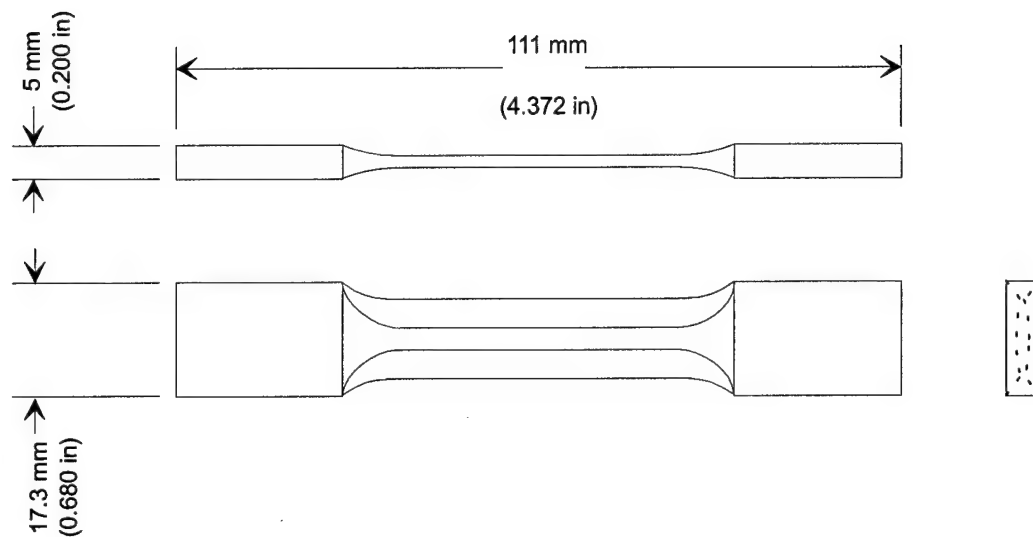


**Figure 11. Airfoil-shaped Ti-6Al-4V Test Samples.** Note the English units in the drawing. The original specifications to the machine shop preparing the specimens were given in English units.

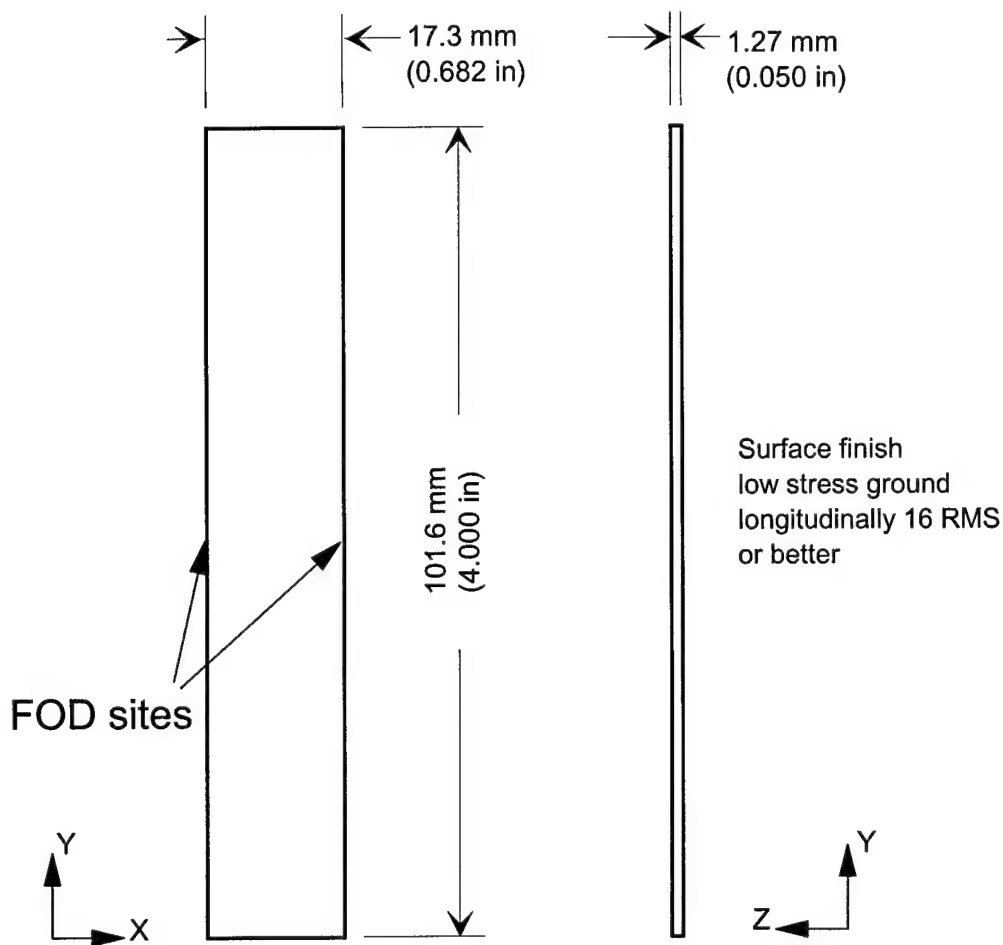


**Figure 12. Flat Ti-6Al-4V Test Samples.** Note the English units in the drawing. The original specifications to the machine shop preparing the specimens were given in English units. The simulated FOD sites are shown in the left-hand view. The direction of sphere impact and chisel indentations is into the page in the right-hand view. This direction is referred to as 'perpendicular to the edge' in this text. An xyz coordinate reference which will be used throughout this study is introduced here.

*FOD Simulation Techniques.* Four damage techniques were chosen which represent the extremes of various methods to simulate the real world FOD. These damage conditions are shown in Table 2. To establish the relationship between the glass and steel spheres, and the chisel indentation, the sizes of both the spheres and the chisels

will be described by their diameters, e.g. the chisel with a 1 mm tip radius will be referred to as the 2 mm diameter chisel. Figures 13 through 15 show the parameters used to refer to the damage locations and specimen orientations. The regions surrounding the notches contain various amounts of damage. Figure 15 shows the nomenclature used to describe the damage amount.

Table 2. Tested Damage Conditions

<b>Glass sphere impact</b>	<b>Steel sphere impact</b>	<b>Steel chisel indentation</b>	<b>Sheared notch</b>
<i>1.0 mm diameter*</i>		1.0 mm diameter	
2.0 mm diameter	2.0 mm diameter	2.0 mm diameter	2.0 mm diameter
	4.0 mm diameter		
5.0 mm diameter		5.0 mm diameter	

*\*not HCF tested*

*Gas Gun Impact.* The most accurate representation of FOD which can be reasonably achieved in the laboratory is to fire a projectile of FOD material into a specimen at a velocity representative of actual FOD events in the real world. Since rocks and sand are typical items causing damage when ingested into an engine compressor, spherical projectiles of ordinary soda glass were chosen for this effort. To have an additional condition to compare, and for computational simplicity in the FEM analysis, steel spheres were also used. Due to limitations on the availability of the steel spheres used for projectiles, the largest size was 4 mm in diameter, not 5 mm like the largest glass spheres.



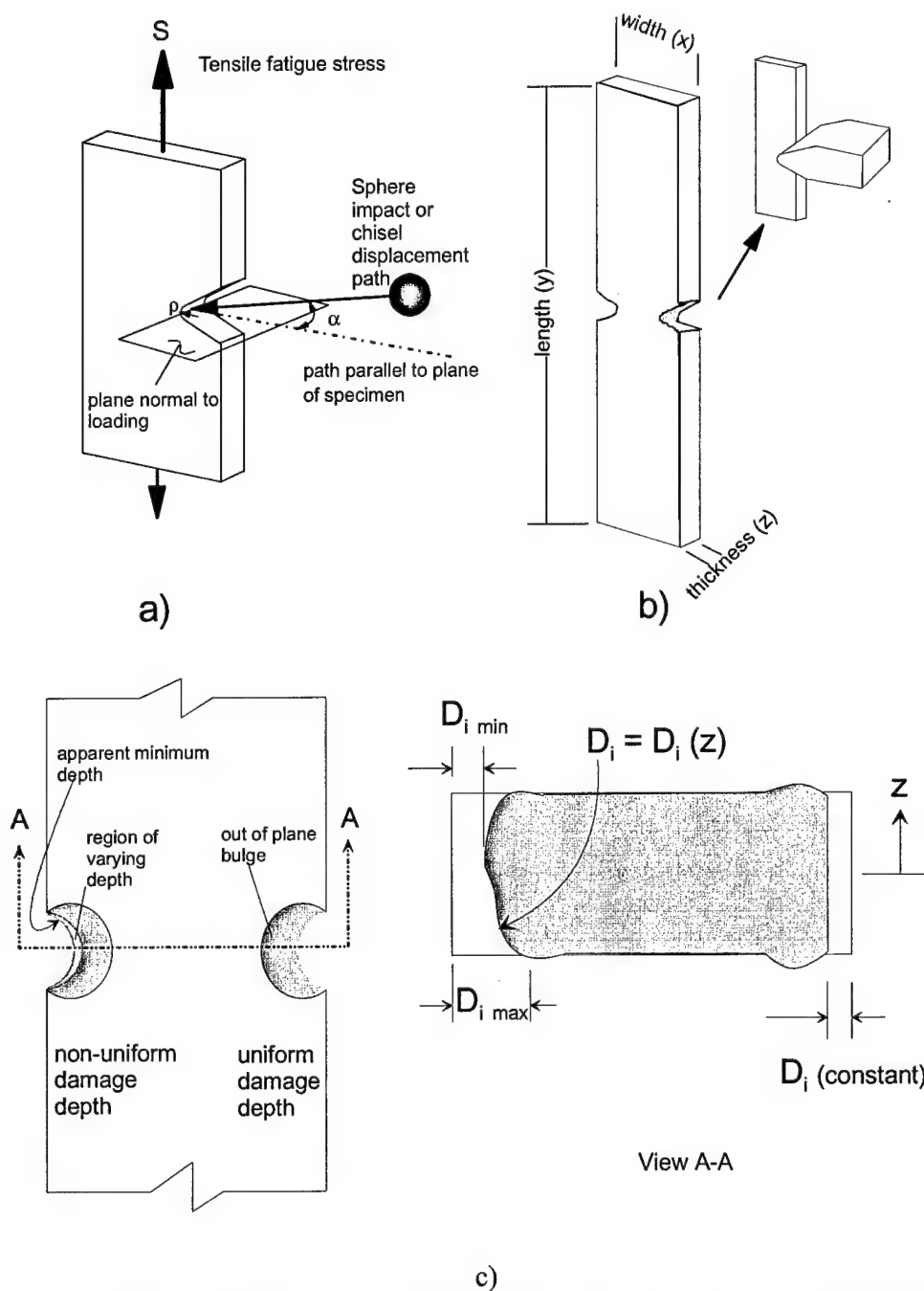


**Figure 13. Specimen Damage Parameters.** In a) the damage orientation with respect to the specimen is shown. In b) the double edge damage on a single specimen is shown, along with an inset depicting a chisel indenting the sample. c) shows the variation in the indent damage depth through the thickness of the specimen,  $D_i$ . On specimens where  $D_i$  is not uniform, but is symmetric, the minimum depth is the value used. In the case of highly asymmetric craters, the minimum depth can be zero. The maximum depth is used in this case.

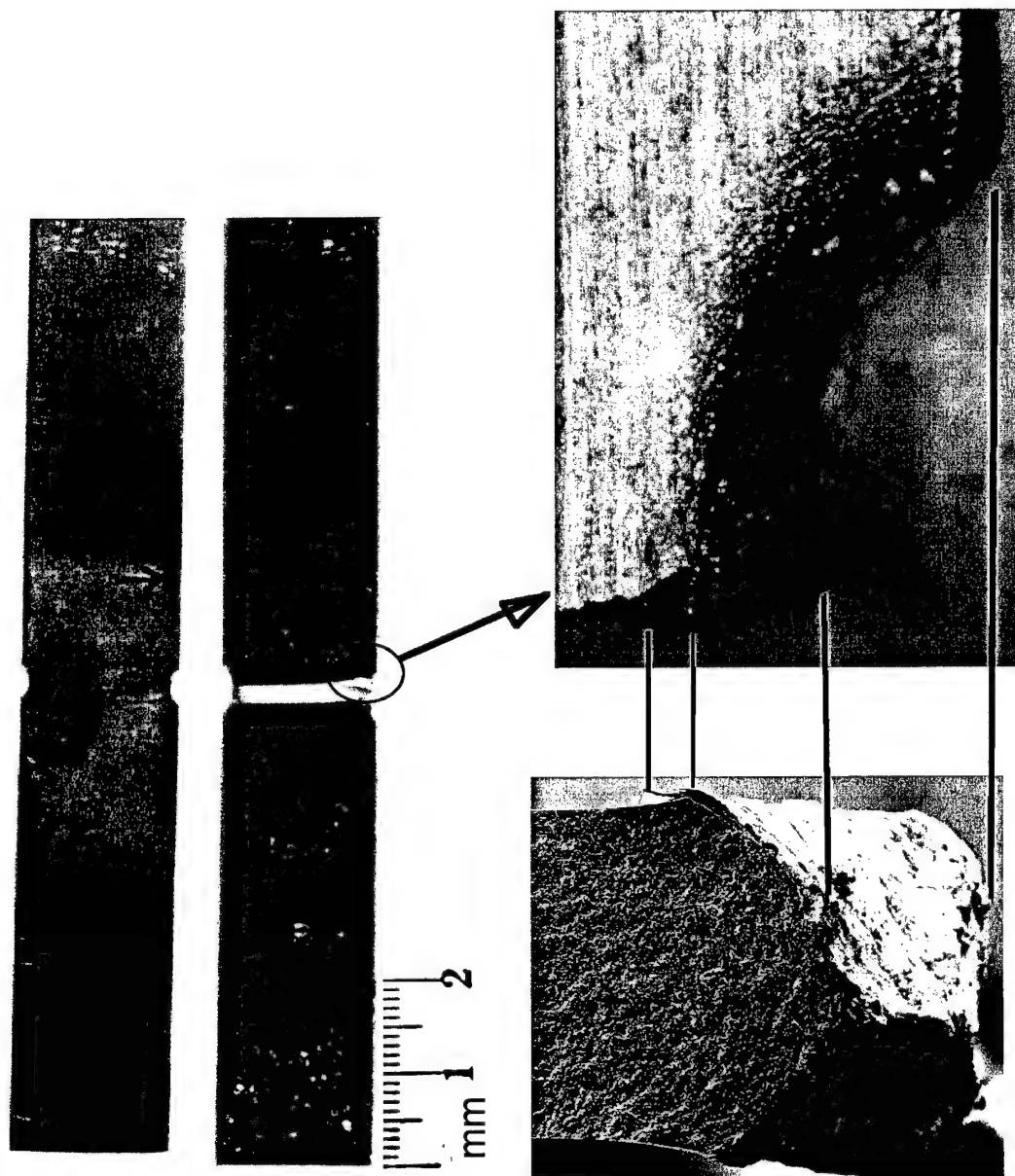


**Figure 14. Specimen Damage Parameters - cont'd.** Photographs depict the views diagrammed in Figure 13 a) & b).

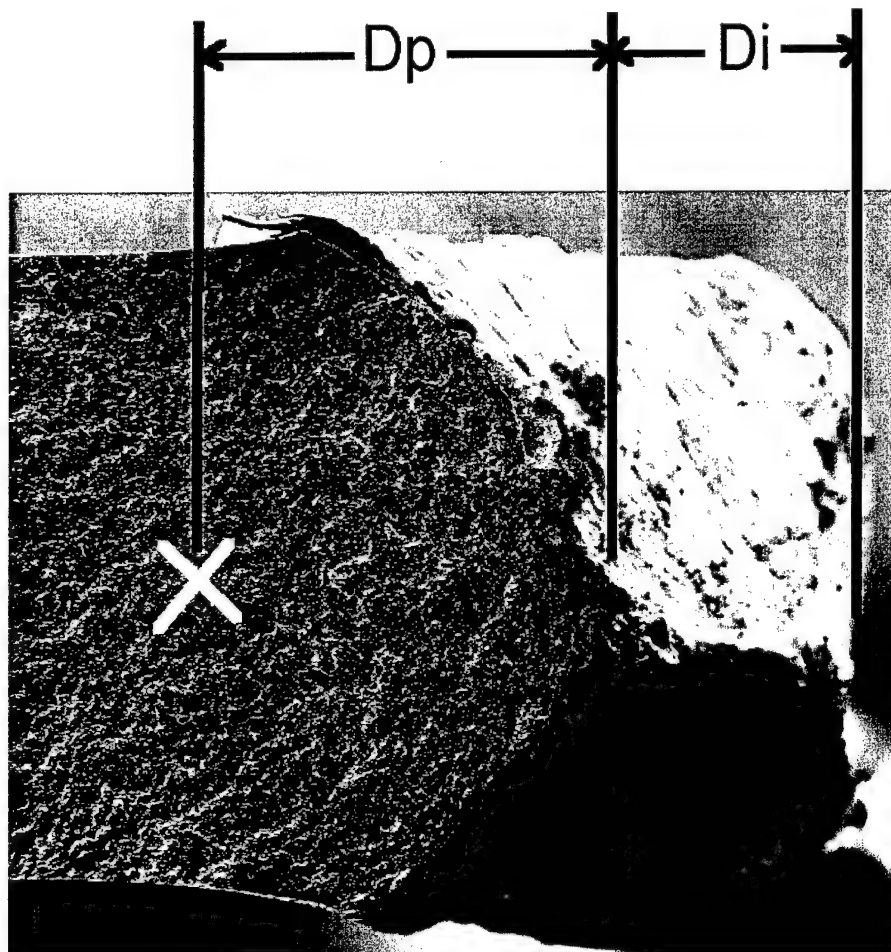


**Figure 15. Plastic Damage Zone Parameter.** The inset from Figure 14 is repeated here, illustrating the depth of the plastic zone,  $D_p$ . The extent of the plastic zone (depicted by the white X) is determined by the techniques described in Chapter IV. The depth to which material is removed or displaced is the indent depth,  $D_i$ . The total damage size is  $D_t = D_p + D_i$ .

Discussions with the engine companies indicated that impact angles of approximately  $15^\circ$  to  $60^\circ$  with respect to the leading edge of a fan blade were most representative of damage seen in the actual application of the engine blades. Analysis of the dynamics of the rotating blades indicated that the relative impact velocity was about 305 m/s (1000 fps) (12; 60). To try to represent these conditions while also maintaining an

analytically tractable experimental condition, sphere impact conditions of velocity equal to 305 m/s (1000 fps) and an impact angle of zero degrees were enforced<sup>3</sup>.

The sphere impacts were performed by the University of Dayton Research Institute (UDRI) under contract from the AFRL Systems Support Division (AFRL/MLS).

Each specimen was damaged in two locations. These locations were on either edge across the width of the specimen as shown in Figures 13 and 14. Each impact location was centered with respect to the specimen's long axis and its thickness. Complete details of the impact procedure and results are found in Appendix B. The conditions of the glass and steel sphere impacts and their indent depths are summarized in Tables 3 and 4, respectively.

Table 3. Glass Sphere Impact Details

Projectile diameter (mm)	Projectile Weight (g)		Impact Velocity (m/s)		Crater Depth (μm)	
	Average	Std Dev	Average	Std Dev	Average	Std Dev
1.0	0.00177	0.00032	309.7	10.4	NA*	NA*
2.0	0.00980	Not recorded	304.8	6.7	598	183
5.0	0.16000	Not recorded	295.7	6.7	745	107

\* The 1 mm diameter glass sphere craters did not create sufficient damage to cause reliable fracture in the area of the crater and will not be analyzed here.

<sup>3</sup> All quantities will be reported in the text in SI units or their derivative units. The inputs to the finite element codes mentioned in this and later chapters were made in English units. Likewise, most specimen measurements were made with instruments calibrated in English units.

Table 4. Steel Sphere Impact Details

Projectile diameter (mm)	Projectile Weight (g)		Impact Velocity (m/s)		Crater Depth ( $\mu\text{m}$ )	
	Average	Std Dev	Average	Std Dev	Average	Std Dev
2.0	0.0342	Not recorded	310.9	4.3	716	108
4.0	0.2740*	Not recorded	306.5	9.2	1868	315

\*weight of 4 mm diameter steel spheres inferred from density of 2 mm steel spheres.

Figures 16 and 17 show high speed film taken of glass sphere impact tests. The film was exposed at 100,000 frames per second. The frame in the lower left corner is the first one exposed. The frame above it is next. The frame on the bottom to the right of the first frame is next, and so on. Note how the opacity of the sphere changes in the frame in which the sphere contacts the specimen. This is due to the nearly instantaneous shattering of the glass. The damage to the sample is created by impact from a cloud of tiny glass fragments flowing over the sample. The fragments both displace the material and erode part of it away. This mechanism creates a smaller plastic zone than a chisel indentation of comparable overall crater size, and leaves glass fragments embedded in the surface of the crater. Detailed photographs of this damage are presented in Chapter IV, Damage Quantification.

*Chisel Indentation.* High-strength steel chisel-tipped tools were made with a 45° angle with a tip of smooth radius (Fig. 18). The radii of the chisel tips were chosen to coincide with the radii of the spheres used to impact specimens.

The chisel was gripped in the upper grip of a tensile testing machine made by the MTS company. A flat steel plate was gripped in the lower grip. The samples were laid with their transverse width direction vertical and held between two steel bars with a pair of spring loaded clips. This assembly was placed on the steel plate and positioned directly beneath the chisel tip. A mirror placed on the plate was used to ensure that the indent location was placed in the center of the specimen in both directions. Figure 19 shows a schematic diagram of this arrangement. The crossheads were moved together until a force of approximately 10 pounds (44.5 N) was read by the test machine load cell.

At this point a digital data acquisition system was started. It recorded the displacement of the crosshead and the force on the load cell. The crossheads were moved manually by increasing the desired offset via a rotary knob on the test machine control panel. The amount of displacement necessary to achieve a given depth of indent was determined by trial and error using a sacrificial specimen which had several indents made of various depths in order to calibrate the amount of compliance in the test machine system. Figure 20 shows the indent depths recorded and the applied crosshead displacement necessary to achieve these depths, as well as the relationship between load and displacement as they changed with time during the indenting process. Note the force drop in Figure 20b associated with the 5 mm diameter damage mechanism described in Chapter IV.

Simulated FOD sites were created on several specimens with various damage depths and radii from this technique. Chisel damage depths were initially chosen to match the depths ( $D_i$ ) of the craters made by the glass spheres of equal diameter. This was done in the expectation that specimens thus damaged would exhibit similar fatigue strength reduction. When initial fatigue testing indicated that this was not the case, subsequent chisel indentation depths were varied to give a range of damage depths.

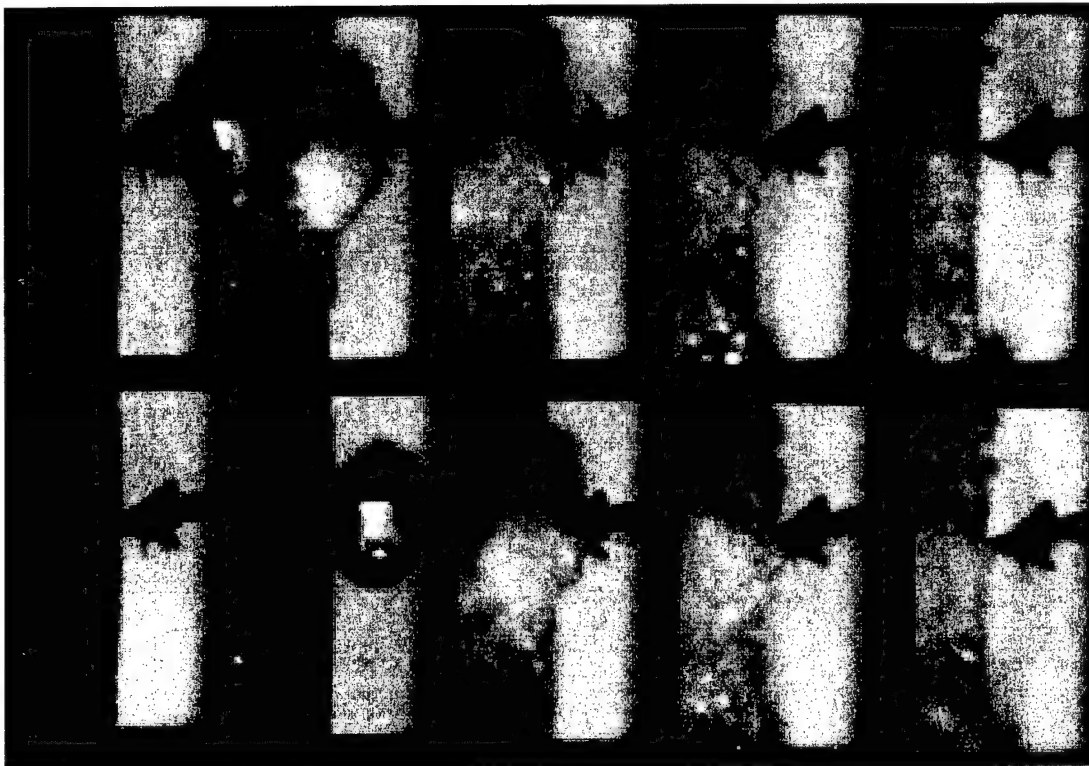


**Figure 16. High Speed Film of 2 mm Diameter Glass Sphere Impact.** The frames are exposed at 100,000 frames per second, and the sequence begins with the lower left corner frame. The frame above it is next. The frame on the bottom just to the right of the first frame is next, and so on.



**Figure 17. High Speed Film of 5 mm Diameter Glass Sphere Impact.** The exposure rate and sequencing is identical to that described for Figure 13.

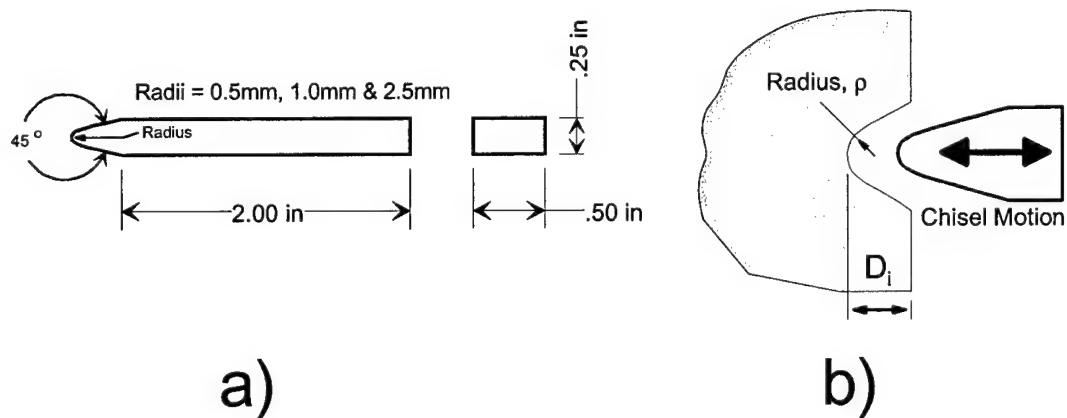


**Figure 18. Chisel Indentation Tool.** In a) the drawing used to fabricate the chisel indentation tools is shown. b) depicts the tool's motion relative to the specimens.



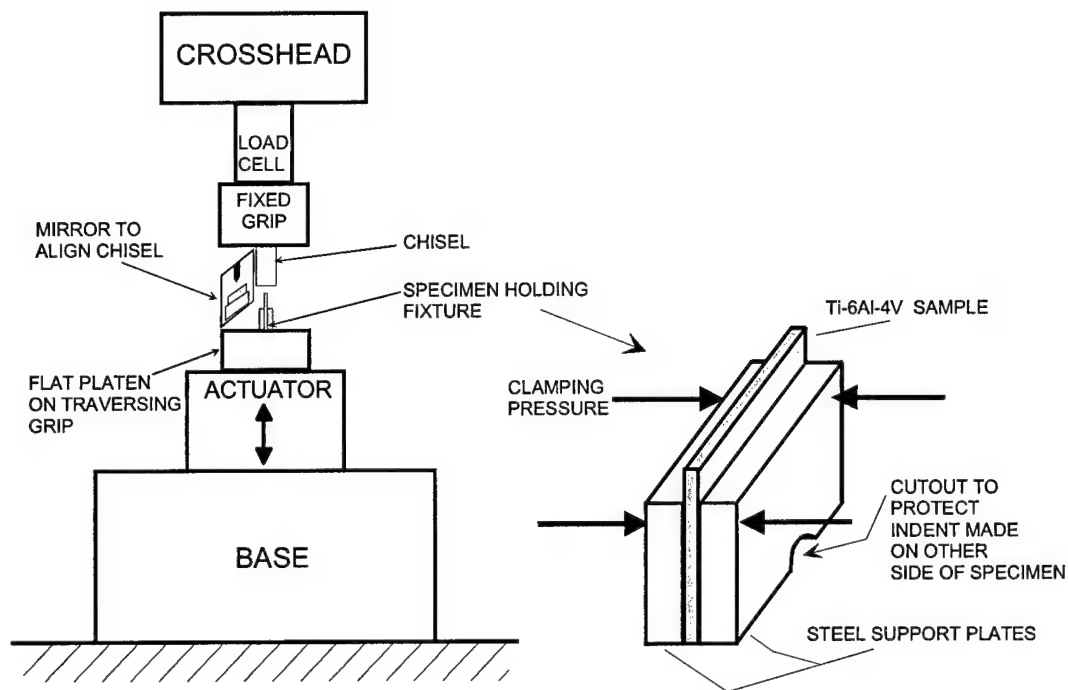


**Figure 19. Chisel Indentation Fixture.** The fixture on the right is set on the platen atop the lower grip. The lower grip is traversed up, driving the sample into the fixed chisel.

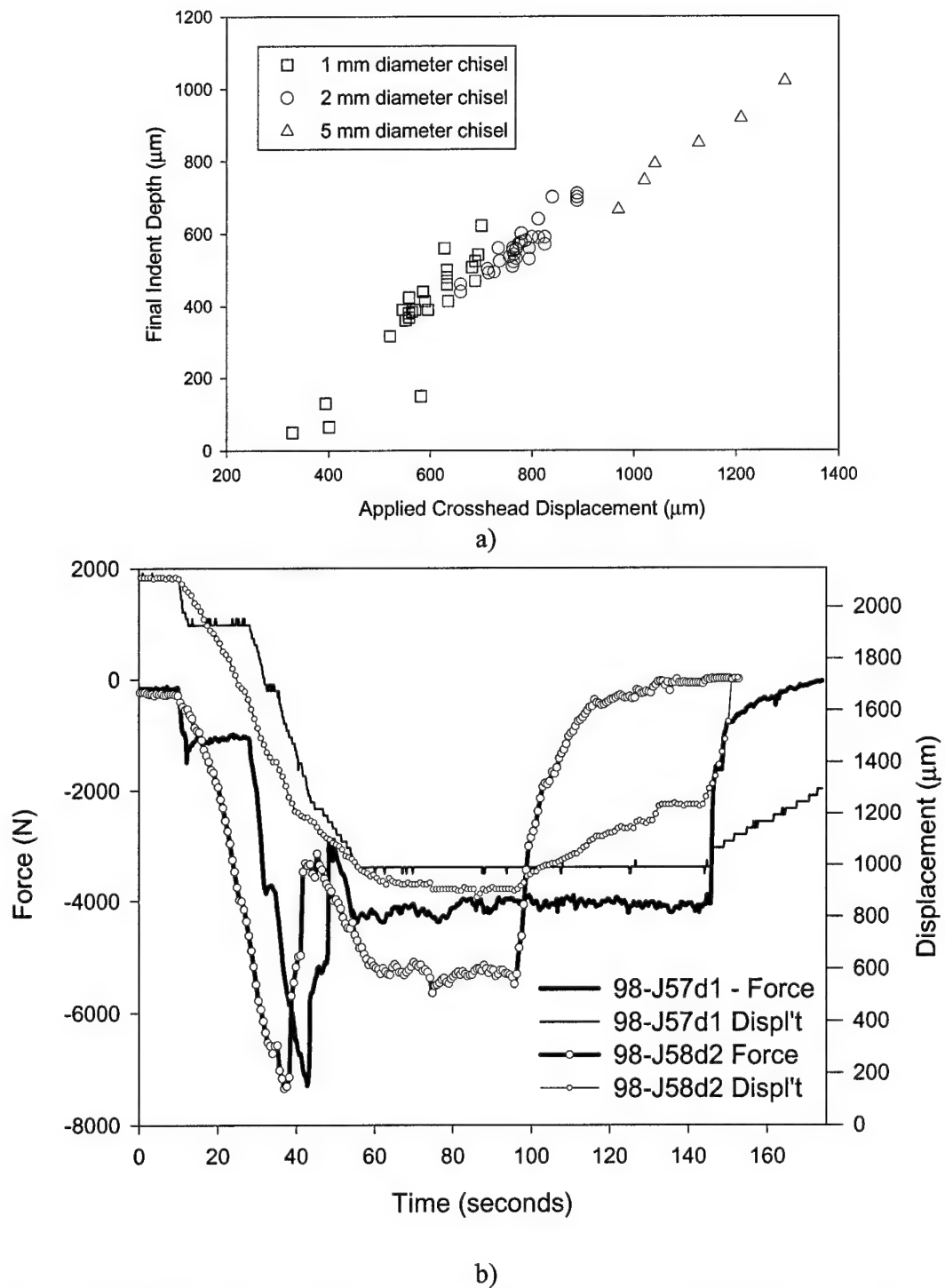


**Figure 20. Static Chisel Displacement Parameters.** a) The crosshead motion required to create indentations of desired depth. b) Force and displacement histories of indents made with a 5 mm diameter chisel. Note how the force required drops sharply when the shear chipped material is cleaved from the specimen.

*Sheared Chisel Notches.* A special 2 mm diameter chisel was made with its axis perpendicular to the chisel used in the previous method. The chisel was passed through the thickness of the specimens as shown in Figure 21. This caused the chisel to shear a notch from the specimens as they were held in a special fixture designed to support them everywhere except under the portion to be sheared away as shown in Figure 22. This fixture also provided an easy way to control the depth of the simulated FOD. Samples were prepared with notch depths between 400  $\mu\text{m}$  and 1015  $\mu\text{m}$ .

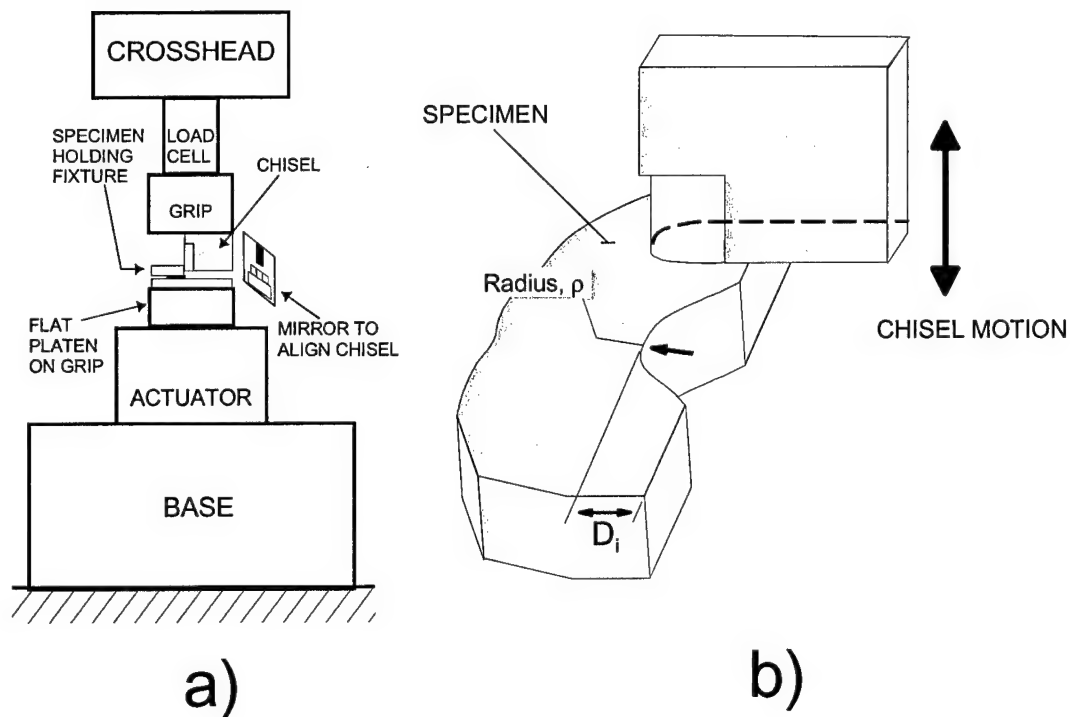


**Figure 21. Perpendicular Shearing Chisel.** a) shows a schematic of the placement of the shear notching fixture in the test machine. In b) the shearing chisel's motion relative to the specimen is depicted.

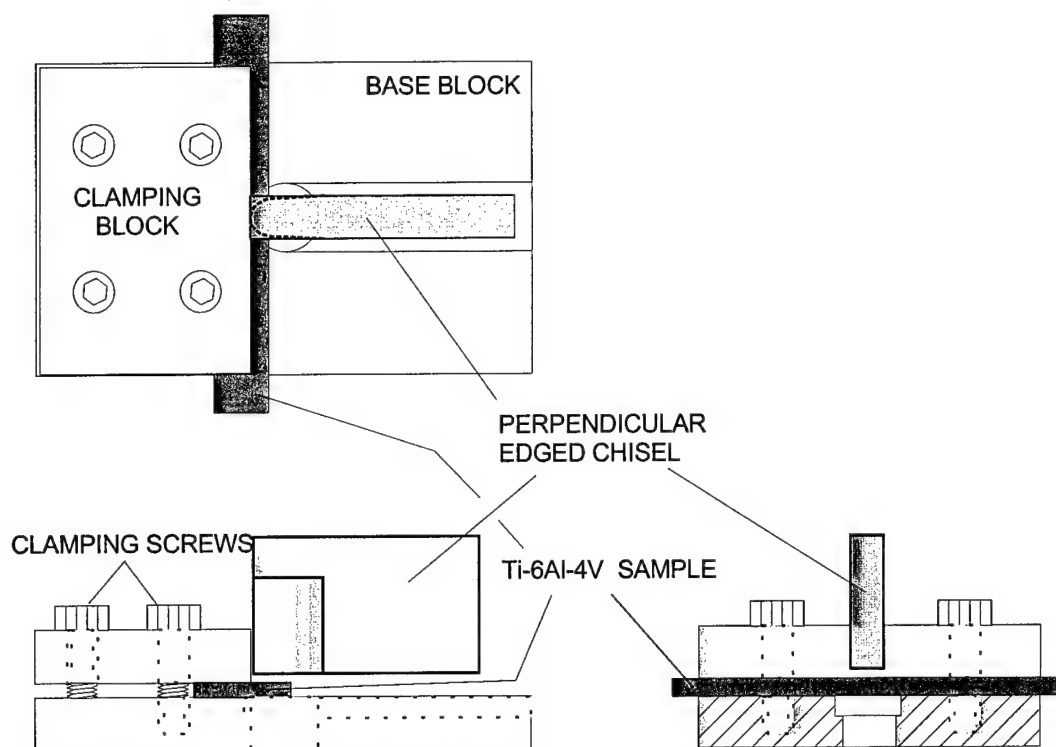


**Figure 22. Sheared Chisel Notching Fixture.** Note the holes drilled through the bottom plate directly underneath the portion of the specimen to be sheared away. The rim of this hole provides the edge against which the chisel tip shears the specimen.

### Fatigue Test Procedure

The objective of this research is to understand the factors related to FOD damage which effect fatigue life and fatigue strength. The measurement of fatigue life and/or strength is thus vital to this goal. Although actual engine blades are subjected to a complex stress state, data taken from simple uniaxial tension tests are traditionally used to determine material properties like fatigue strength. It was assumed in this study that uniaxial tension fatigue testing of damaged Ti-6Al-4V would provide

understanding of its response to HCF conditions. This understanding could then be applied to specific structural analysis situations in the future.

The FOD damaged samples were therefore fatigue tested to determine their strength. The fatigue strength at a life of  $10^7$  cycles was chosen as the property to be measured. This life was picked because it is a reasonable compromise between the actual lives to which an engine part would be designed and a number of cycles which could be achieved in a laboratory in a reasonable period of time. Also, due to a number of previous and ongoing research efforts presenting findings as fatigue strength at  $10^7$  cycles, the ability to compare results with these efforts existed.

The objective of fatigue tests was to determine the stress required to initiate a crack in  $10^7$  cycles under HCF conditions in the damaged samples. The number of cycles to crack initiation was taken to be the same as the number required for sample failure. This is a valid assumption since the number of cycles to which the samples were tested ( $10^7$ ) is very much larger than the cycles required to propagate the crack for total specimen failure (38; 69). See Appendix C for details on the validation of this assertion.

For both damaged and undamaged (baseline) specimens, the HCF stress corresponding to  $10^7$  cycles was obtained by a step-loading technique (45). To collect fatigue life data with this technique, a single specimen was subjected to  $10^7$  cycles of loading (although any other appropriate number of cycles for fatigue life could be chosen) at a value of stress that was not expected to cause failure. If the

specimen survived this step of loading, the stress level was increased by 5% and the test was repeated. This continued until the specimen failed in less than  $10^7$  cycles. Figure 23 illustrates this schematically.

The damage is assumed to accumulate linearly in the last step in which the specimen fails, and the maximum stress is calculated from Eqn. (14) which is repeated here:

$$\sigma_{\max} = \sigma_{pr} + \frac{N_f}{10^7}(\sigma_f - \sigma_{pr}) \quad (14)$$

where

$\sigma_{\max}$  is the maximum stress

$\sigma_{pr}$  is the maximum stress level of the previous block of loading

$N_f$  is the number of cycles to failure during the last block of loading

$\sigma_f$  is the maximum stress level of the last block of loading

Note that the denominator of  $N_f$  in Equation (14) should be changed if a fatigue life other than  $10^7$  is chosen. This method of adding damage from different test conditions keeps the stress ratio  $R$  the same and increments the maximum stress (causing an increase in the minimum stress to maintain constant  $R$ ). An alternative to this would be to hold the maximum stress constant and increasing the minimum stress so that the stress ratio increases. Data collected in this manner are presented in Appendix D. These data indicate that this alternative approach yields values for the maximum fatigue strength which are within 12% of data collected by the constant  $R$ , increasing maximum stress method used in this study.

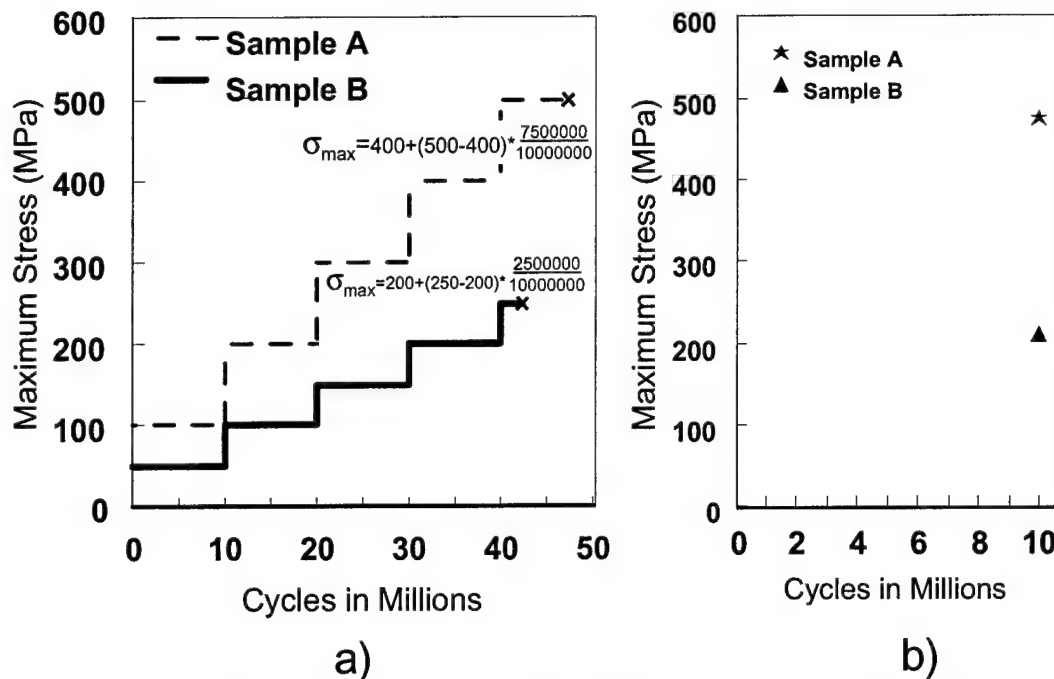


**Figure 23. Illustration of Accelerated Fatigue Strength Testing.** a) Stress vs. cycles histories are shown for two typical specimens. b) The positions on a stress-life curve where the data points would be plotted.

The step loading technique was developed as an alternative to collecting a number of data points for an S-N (Wohler) curve and extrapolating them to the number of cycles of interest (e.g.,  $10^7$  in this study). S-N testing is an old and accepted method for determining the fatigue strength of a material at a given life, while the accelerated step testing technique is recent. To confirm the step testing technique's applicability to this study, S-N data was collected for several test conditions. Appendix D presents this data for a comparison of the constant maximum stress step loading test and typical S-N testing.

*High Frequency Tensile Machine.* The samples were fatigued using an electromagnetic shaker-based high cycle fatigue testing machine designed by the

University of Dayton Research Institute under contract to AFRL/MLLN. Being the 6th machine designed for use in MLLN's HCF laboratory, it was named HCF#6. A schematic and photograph of HCF#6 are shown in Figures 24 and 25. In this device, a lower grip holds the specimen while attached to a high frequency load cell. A pneumatic actuator pulls the other grip in tension to apply mean loading. In addition to being attached to the pneumatic actuator, the upper grip is also attached to the armature of the electromagnetic shaker. When driven by a signal generator through a high power amplifier, the shaker applies the alternating load.

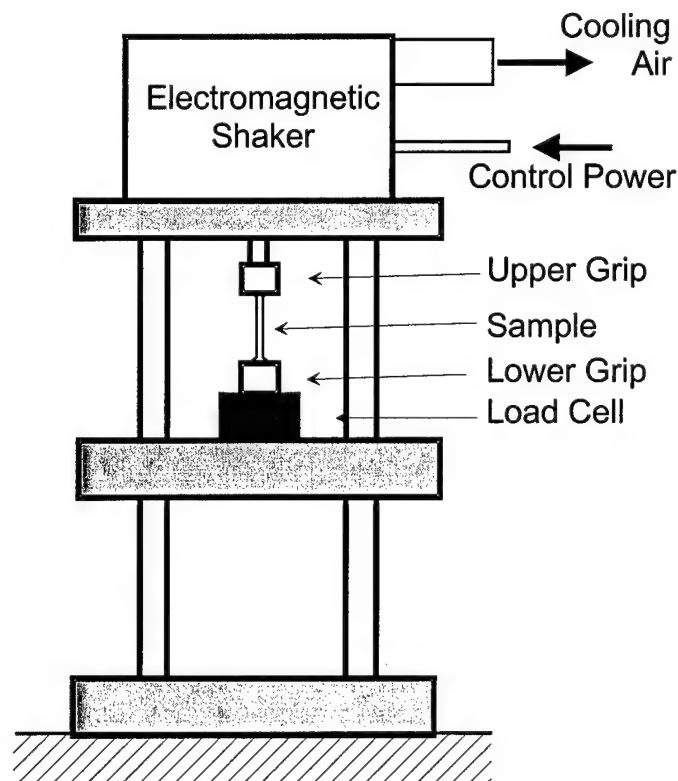


**Figure 24. Schematic of High Frequency Tensile Machine**



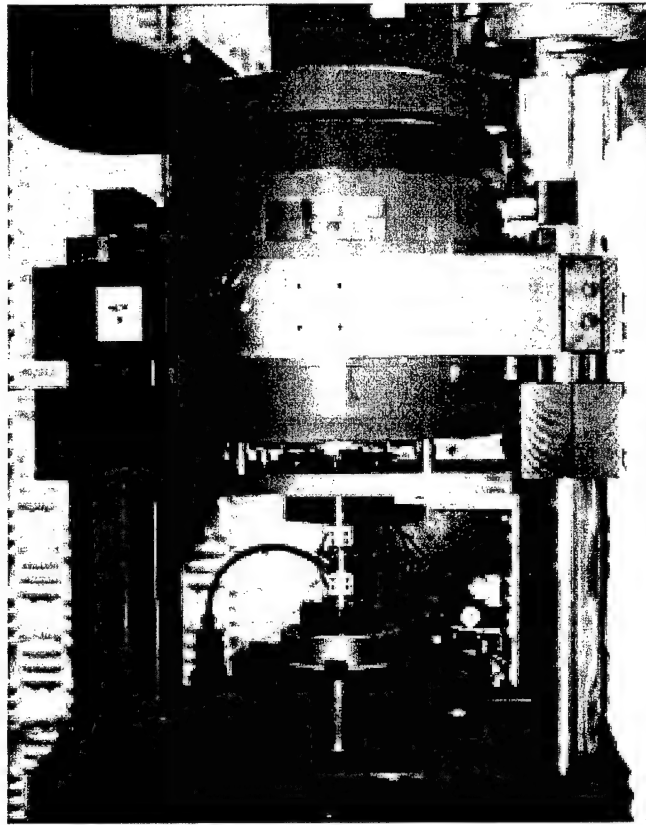


**Figure 25. High Frequency Tensile Machine.** The 6th machine built for MLLN's HCF laboratory, it is known as HCF#6.

*Sample Alignment and Test Procedure.* To use the machine, a specimen is placed between the grips. The grips are aligned for co-linearity and evenness front to back by clamping thick precision machined angle irons to the top and bottom grips holding them apart the desired amount. The top grip is attached to the armature of the shaker. The bottom grip is attached to a disk which is free to float in a cavity slightly larger than the disk. When the clamping force is applied, a solder-like metal known as 'Wood's metal' is melted into the small space between the disk and cavity and allowed to cool. This fixes the bottom grip in alignment with the top grip, and attaches the grip to the load cell.

The grips are simple aluminum blocks machined with a slot to allow the specimen to be inserted. The slot is oversized to allow multiple sizes of specimen, and spacer inserts are stacked symmetrically around the specimen. The spacers touching the specimen are roughened with a commercially available coating to ensure the specimen remains fixed during testing as shown in Figure 26.

The left to right alignment of the specimen is checked with fixture blocks built for that purpose (Fig. 27). The machine screws are extended an amount equal to the distance from the edge of the sample to the edge of the grip when centered. This distance is checked with a Brown and Sharpe Model 599-571-3 (s/n950245) dial caliper to  $\pm 0.0127$  mm (in actuality  $\pm 0.0005$ "). Since the top and bottom grips are not exactly the same width, one block is set to the distance of the top grip, and one to the distance of the bottom grip. A MathCad worksheet was prepared for every specimen to facilitate these settings. A typical worksheet is shown in Figure 28. The blocks are set on the grips and the specimen is held against them while cap screws which have been placed through the grip fixture are tightened by hand. When the screws are tight enough to prevent movement of the specimen, the blocks are slid across the opposite side of the grips to ensure the specimen is centered. When this is correct, the screws are tightened to uniform torque with a torque wrench (CDI model 6002LDIN). In all experiments (after a few initial tests to check the machine) the torque applied was 13.5 N-m (120 in-lbs).

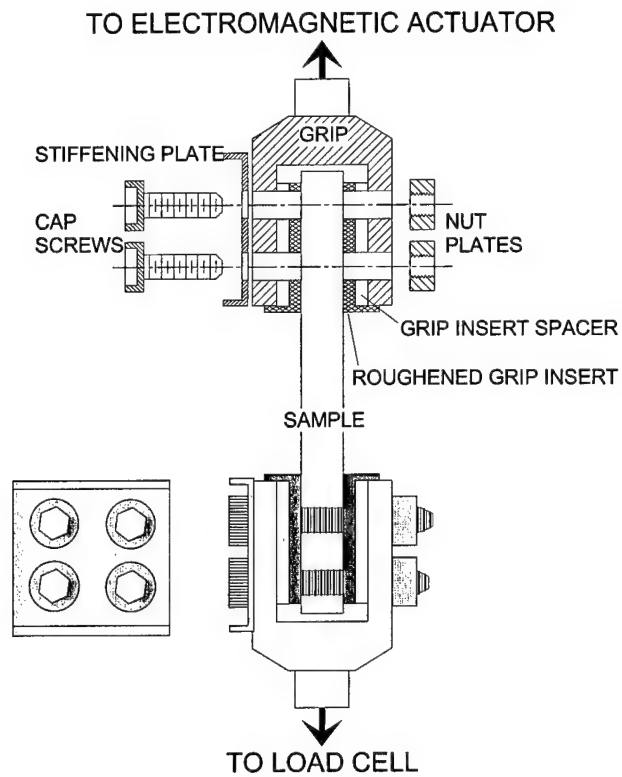


**Figure 26. Grip Fixtures for HCF#6.** The drawing of the bottom grip shows a left hand side view of the stiffening plate. The top grip is shown as a section drawn through the screw centerlines.

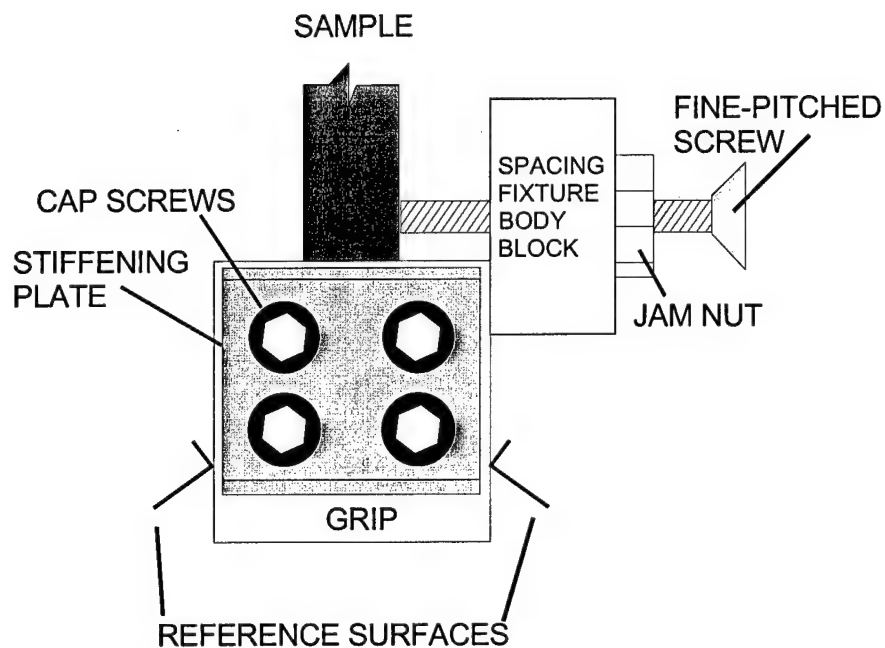


**Figure 27. Sample Alignment Gage Block.** Two blocks were made. One was held against the side of the top and bottom grips simultaneously while the cap screws were tightened. The opposite sides of the grips were then checked to ensure the screw tip barely passed the sample without touching.

**Desired Stress Ratio**  $R := 0.5$

2mm steel ball

$$l := .0505 \text{ in}$$
$$l = 1.28270 \cdot \text{mm}$$
$$w := .6836 \cdot i$$
$$w = 17.36344 \cdot \text{mm}$$
$$d_j := \frac{1.650 \cdot \text{in} - w}{2}$$
$$\text{adj} = 0.4832 \cdot \text{in}$$
$$\text{adj} := \frac{1.650 \cdot \ln - w}{2}$$
$$\text{adj} = 0.4832 \cdot \text{in}$$

**NOTE: ALL CALCULATIONS ON THIS PAGE BASED ON UNDAMAGED AREA!!**

From previous tests on 2mm ball indents, we estimate an endurance limit between 200 and 246 MPa  $S_{endur} \approx 200 \text{ MPa}$

```
perc := 0.%
```

$$S_1 := \frac{S_{\text{endur}}}{\text{perc} + 1}$$

we define a **percentage increase** in each step

$$S_{\max} := S_1, 1.05 \cdot S_1 \dots \text{over } S_{\text{endur}}$$

	$S_{\max}$	$P_{\max}(S_{\max})$	$P_{pp}(S_{\max})$	$S_m(S_{\max})$	$P_m(S_{\max})$
block	MPa	kN	kN	MPa	kN
1	200	4.4544	2.2272	150	3.3408
2	210	4.6771	2.3386	157.5	3.5079
3	220	4.8999	2.4499	165	3.6749
4	230	5.1226	2.5613	172.5	3.8419
5	240	5.3453	2.6727	180	4.009
6	250	5.568	2.784	187.5	4.176
7	260	5.7907	2.8954	195	4.3431
8	270	6.0135	3.0067	202.5	4.5101
9	280	6.2362	3.1181	210	4.6771
10	290	6.4589	3.2295	217.5	4.8442
11	300	6.6816	3.3408	225	5.0112

Failure cycles:  $N_{\text{fail}} := 1533512$

**Bolt Torques: upper: 120 in\*lb lower: 120 in\*lb**

**Figure 28. MathCad Worksheet for Test Condition Preparation**

The signal generator was driven via a GPIB connection to a 486 PC controlled by a FORTRAN program written by UDRI. This allowed the user to specify various parameters of the test. In this research, the parameters were controlled as follows:

Upon initialization of the control program, the user is prompted to read test parameters from a previous file saved for this purpose. If no file is selected, or to change the parameters which are different from those of the last test, an interactive mode is selected. Test sample description data such as sample number, material properties, etc. are entered or corrected.

The specimen's geometry description is chosen from a menu. Rectangular geometry was always chosen, and the user is then prompted for the width and thickness of the specimen. (This was true even for the airfoil shaped specimens, since no general shape choice was available. In these cases, the measured cross section area was divided by 2.54 mm (0.1 inch) and the quotient and 2.54 mm were entered as the dimensions.) These data were used to convert requested stresses into applied loads in the program.

The user next chooses the loading waveform. The choices are pure HCF and combined LCF/HCF. In all cases reported here, HCF was chosen. The desired frequency (350 Hz), stress ratio (0.1 or 0.5 typically) and initial maximum stress are all entered. The next choices concern how to increment the loading after the first step. For all but a few of the cases considered here (see Appendix D), this was to increase the maximum stress by 5% of the initial stress every  $10^7$  cycles, while

keeping R constant. After all these parameters are entered, the user is prompted for file names and locations to store the data and the parameters just entered. The stored parameters go into a file called a 'restart file', since in addition to the parameters, the restart file is updated periodically (this period having been entered by the user) with the status of the test. This allows the test to be continued with minimal interruption if it is aborted for some reason.

Periodically through the data entry process the user is prompted to check several conditions on the control electronics equipment rack which contains the PC-controlled transducers which connect to the shaker, amplifier and pneumatic actuator (Fig. 29). These prompts ensure that several switches which could be set in multiple positions are actually in the positions assumed by the control program. When all this is set to the user's preferences, the testing is initiated.

The first task taken by the controller program is to increase the mean load to 10% (user input) of the desired mean. This is the value at which an unbroken specimen will be loaded in the event of a test being interrupted by the user, or aborting (this is a requirement for crack growth tests, where an initiated crack would be damaged by any compressive loading). The output of the load cell is read to provide this feedback. Once the hold load is established, the full mean load is applied. At this point the electromagnetic shaker is driven to applied alternating load. A graphic window displays a sampling of the load cell voltage to provide a visual check that the correct waveform is applied. To avoid egregious amounts of data being stored,

extreme fluctuations of the stress and load values are kept in memory, and every 600 seconds (another user selected quantity), the data file has one instance of the average test conditions written to it. The extreme fluctuations seen above and below these average values are also recorded, allowing the user to confirm after the test is completed that the desired nominal conditions were applied to the specimen throughout the test period. The output of a typical file can be seen in Appendix E.

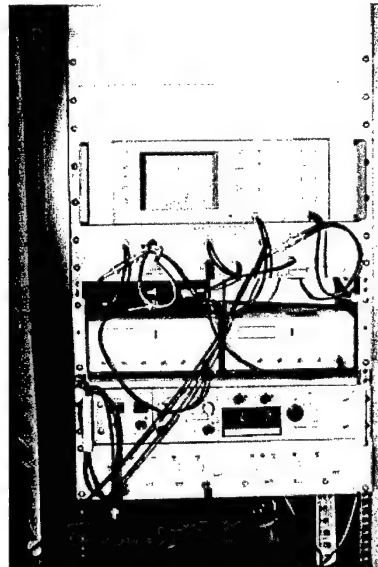


**Figure 29. Control Panel for HCF #6.** This panel sits between the machine shown in Figure 25 and the PC which sends the control signals. The 3rd panel from the top contains two GPIB driven waveform generators; one for the low frequency signal (in this case a DC offset for the mean stresses) and one for the high frequency signal.

When a test finished successfully, the primary data needed for analysis were usually written down from the PC screen. These were the number of cycles to failure and the maximum stress applied in the last load step. The MathCad worksheet created to



calculate alignment fixture block settings also calculated the stress and loading parameters at each step for each test sample, so the stress at the next-to-last step was known. The fatigue strength was calculated from these data using Equation (14).

#### ***IV. DAMAGE QUANTIFICATION***

One of the vital components towards the understanding of FOD/HCF interaction is an assessment of the actual amount of the damage. For this purpose, the size of the damaged region was quantified in this study. This consisted of two parts (see Figure 15): the depth of the indentation caused by the removal of material,  $D_i$  and the extent of the material into the specimen that is plastically deformed,  $D_p$ . This quantification was achieved by a combination of the following three methods.

##### **Optical Observation of Plastic Deformation**

After being fatigue tested, the samples were examined under an optical microscope. A Nikon upright microscope with a polarizing filter and micrometer-actuated x-y stage was used to observe the fracture surfaces (Fig. 30).

One half of the fractured specimen was placed in a paper binder clip to hold it upright and placed under the microscope. The microscope was focused on the fracture surface, and the light polarizing filter was adjusted to allow the minimum possible amount of light to go through. This means that only those light rays which were polarized in a specific direction were visible. Under these conditions, a region of the fractured specimen appeared as dark bands under polarized light, which could not be seen under ordinary white light (Figure 31). As will be shown later in this chapter, the location of these bands was found to correlate to a certain amount of

plastic strain in the specimen. This darker region can be seen in Figure 31. The dark band which follows the shape of the eroded crater will be referred to as the deformation band in this study. The dark fan-shaped region to the left of the deformation band is the 'river pattern' which is seen on all fatigue fractured Ti-6Al-4V specimens. Under polarized light as described above, the river marks are typically invisible and the deformation bands are much clearer.

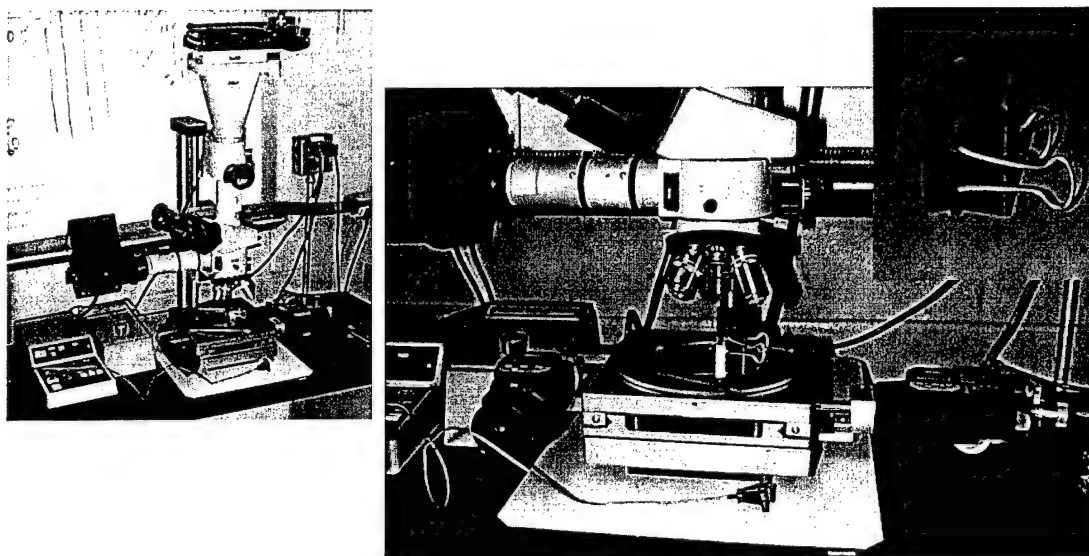


**Figure 30. Nikon Upright Microscope with X-Y Translation Stage.** In the inset a fractured specimen is shown being held upright in a binder clip.

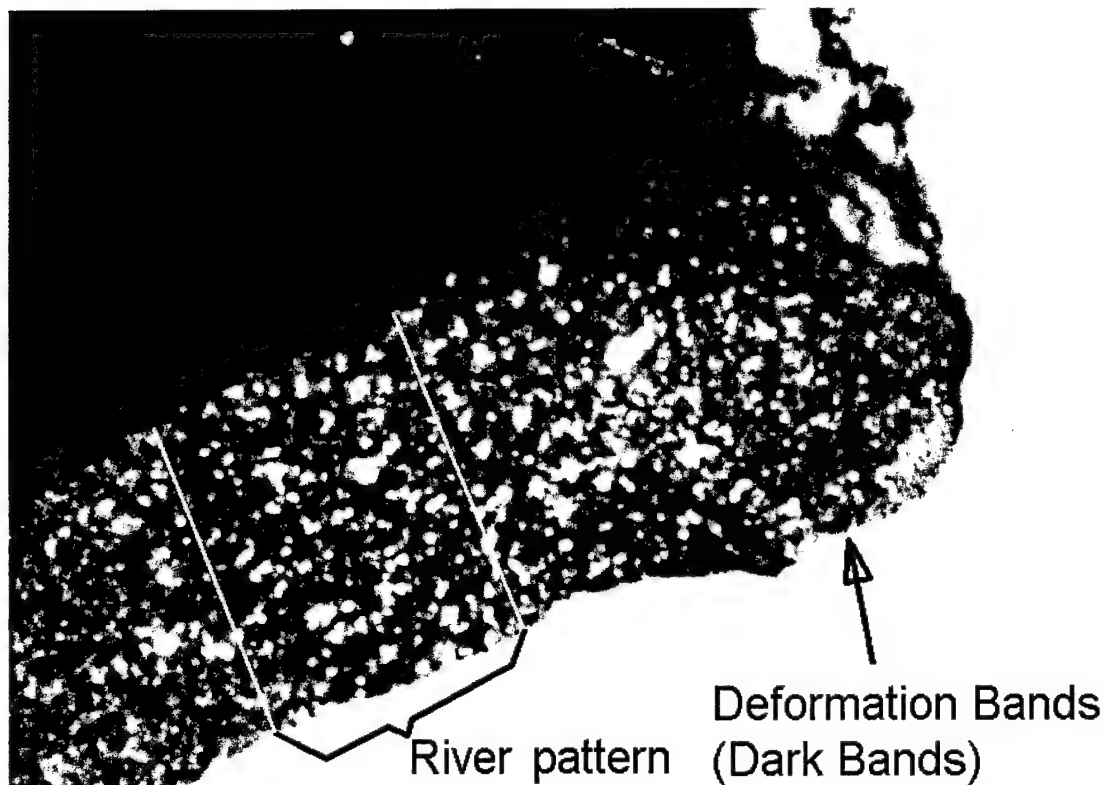
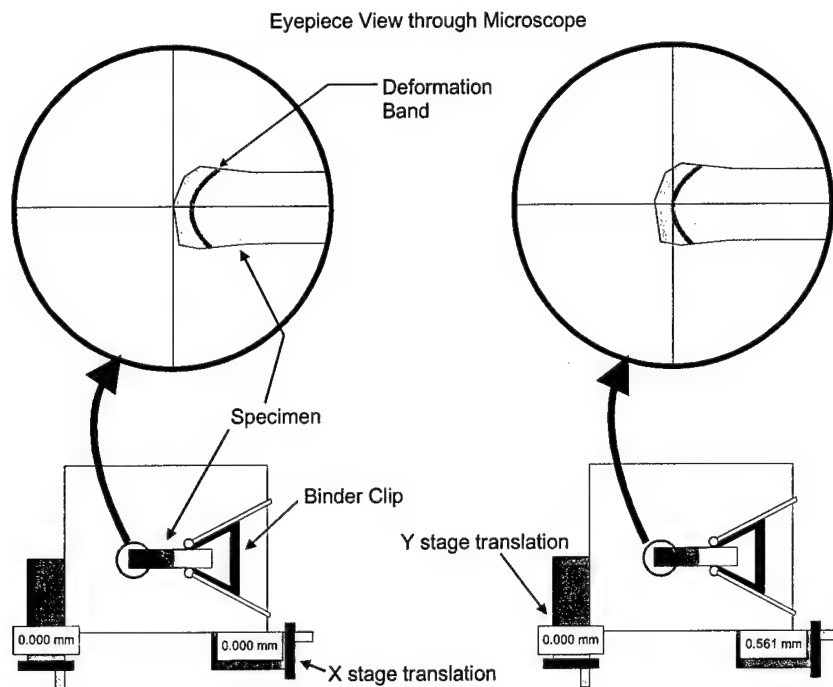


**Figure 31. Close-up View of Fracture Surface on Specimen 98-B18.**  
Note the deformation band which follows the contour of the eroded surface. The dark pattern at the left of the image is the 'river pattern' created by propagation of the fatigue crack.

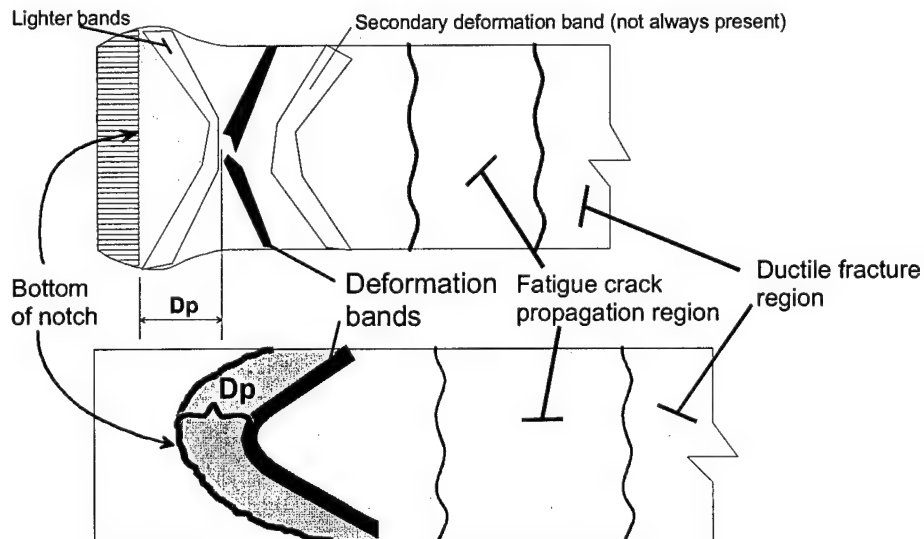
To measure the locations of these deformation bands, a crosshair located in the microscope eyepiece was located at the edge of the fracture surface. The micrometer was zeroed and the stage moved to the intersection of the visible deformation bands and the centerline of the fracture surface as shown in Figure 32. These bands were visible as dark regions approximately 75  $\mu\text{m}$  to 150  $\mu\text{m}$  thick. As shown in Figure

33, the region between the notch or crater root and the band was a uniform dark gray color. The beginning of the darker deformation band was not easily seen with precision, but the center of the region could be determined, therefore the distance from the edge of the fracture surface to the center of the thickness of the deformation band was recorded. The region past the deformation band was another, lighter, uniform gray. In this region, there may or may not be visible a secondary deformation band. Typically chisel indented specimens had deformation bands that appeared as the right-hand half ( $\frac{1}{2}$ ) of an 'X' pattern (as shown in Figure 33), the left part of which was described as a lighter band which began at the intersections of the notch root and the free faces of the specimen. In the sphere impacted specimens, the band followed the contour of the eroded crater surface (Fig. 34). This was generally true whether the eroded crater was symmetrically centered on the specimen or not (Fig. 35).

The other half of the specimen was also used for this measurement. Usually one half or the other would reveal a better view of the deformation zone. Figure 34 shows the other half of the specimen shown in Figure 32. Because this optical measurement could be taken on every specimen tested with great ease, it was the primary method by which the extent of damage on all specimens was analyzed. However, damage was also obtained by two other techniques with a few specimens as discussed later.

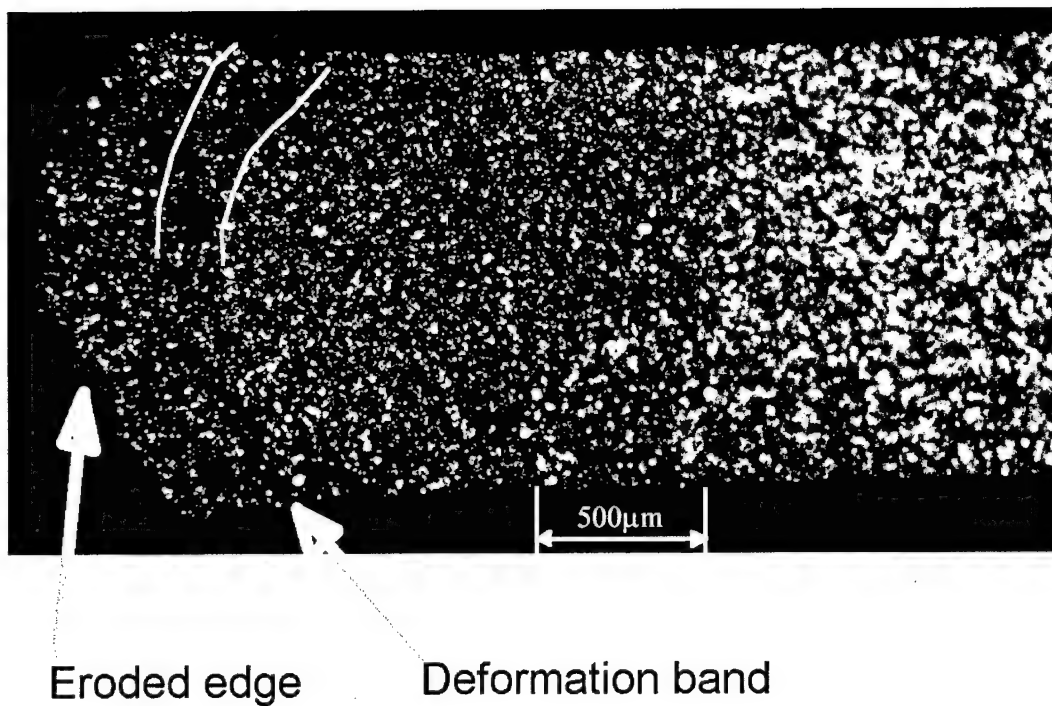


**Figure 32. Measurement of Deformation Bands on Fracture Surface.** The specimen is held in a binder clip as shown in Figure 30. The readouts on the stage are zeroed with the crosshairs at the indentation (left). The X translation stage is moved to place the crosshairs in the center of the dark band, and the distance is read from the micrometer (right).



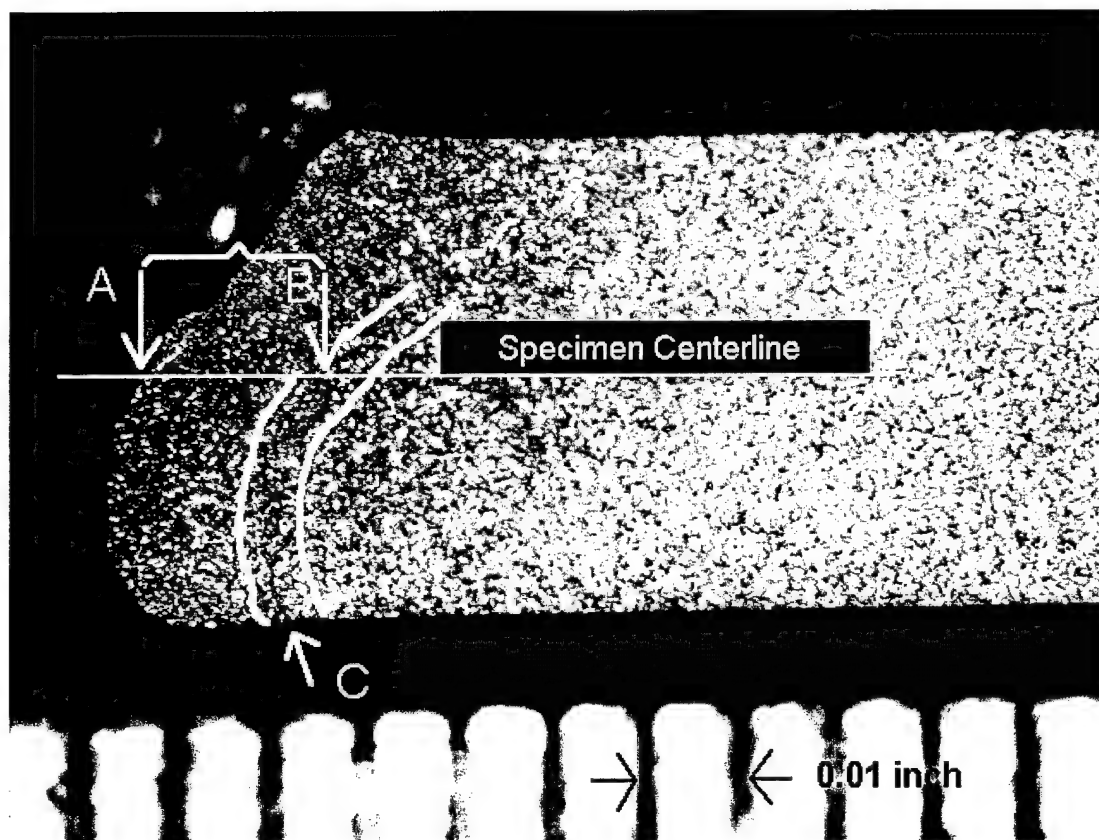
**Figure 33. Typical Deformation Band Shapes.** The major features of the fractured surface visible under polarized light are shown.

Figure 36 shows an SEM photograph of a specimen damaged by a 5 mm chisel. Four locations at different locations in the deformation band are marked, as well as a location well away from the deformed zone, where the surface is created by fatigue crack propagation through undeformed material. In the close-up view of the fractured surfaces at these locations in Figures 37a and 37b, note that the fractured grains seem somewhat smooth, and there appears to be no preferred direction in which the grain boundaries are exposed in the fatigue crack propagation region. In other words, the fracture surface texture is dominated by a flat, transgranular cleavage appearance across both the primary  $\alpha$  grains and the Widmanstätten  $\alpha+\beta$  grains. The fracture morphology remains the same regardless of the microstructure encountered by the crack front. This is in contrast to the surfaces shown in Figures 37c through 37f, which show close-up views of the deformation band, where the local direction of the deformation band is depicted on each photograph. Note that the grain surface texture is sharper, somewhat smaller, and a preferred direction can be detected. The fracture surface has become dominated by a tortuosity (noticeable change in orientations of the planes along which the advancing crack fractures individual grains). This is an indication of the propagating crack's sensitivity to the microstructure, which is caused by a combination of the local grain orientation, slip availability and the residual stresses in the material. This different texture is the cause due to which the polarized light reflected differently, which caused this region to appear darker, or as a deformation band.



**Figure 34. Deformation Band on Specimen 98-J52.** This photograph was taken in the orientation described in Figure 33. The arrow pointing to the deformation band shows the extent of the plastic deformation due to FOD. In the upper half of the photo the deformation band is outlined by gray lines.





**Figure 35. Asymmetric Crater Optical Measurements.** This view shows how the plastic zone size was defined on specimens where the damaged region was not symmetric with respect to the centerline of the fracture surface. The distance A-B from the eroded edge to the center of the band is measured along the fracture surface centerline. Since the deformation band approximately follows the contour of the eroded edge,  $D_p$  is approximately the same anywhere along the deformation band (which intersects the bottom face of this specimen at C). This is the opposite half of the specimen shown in Figure 34.

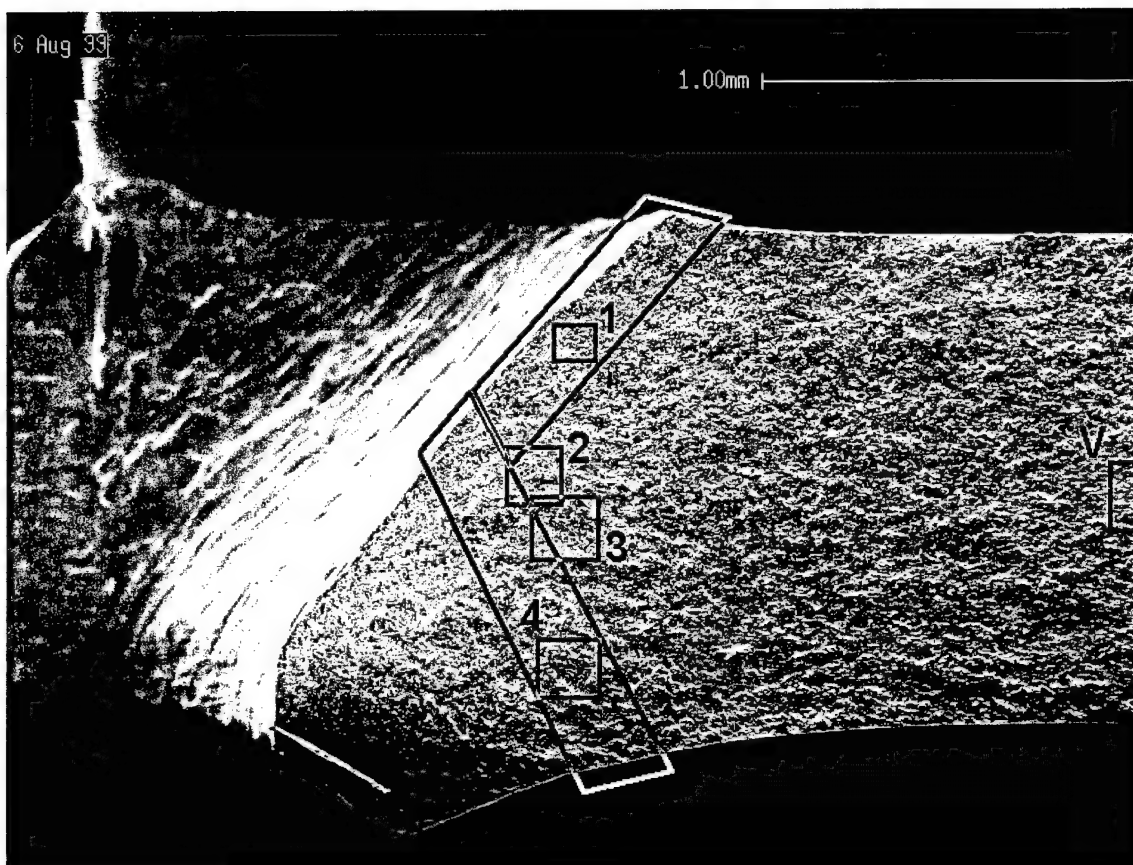


**Figure 36. SEM of Fracture Surface.** In this overview, the locations of the deformation bands visible under polarized light are marked by large boxes. The smaller boxes (labeled '1' through '4' and 'V') indicate the approximate location of the close-up photographs shown in Figure 37 a) through f).

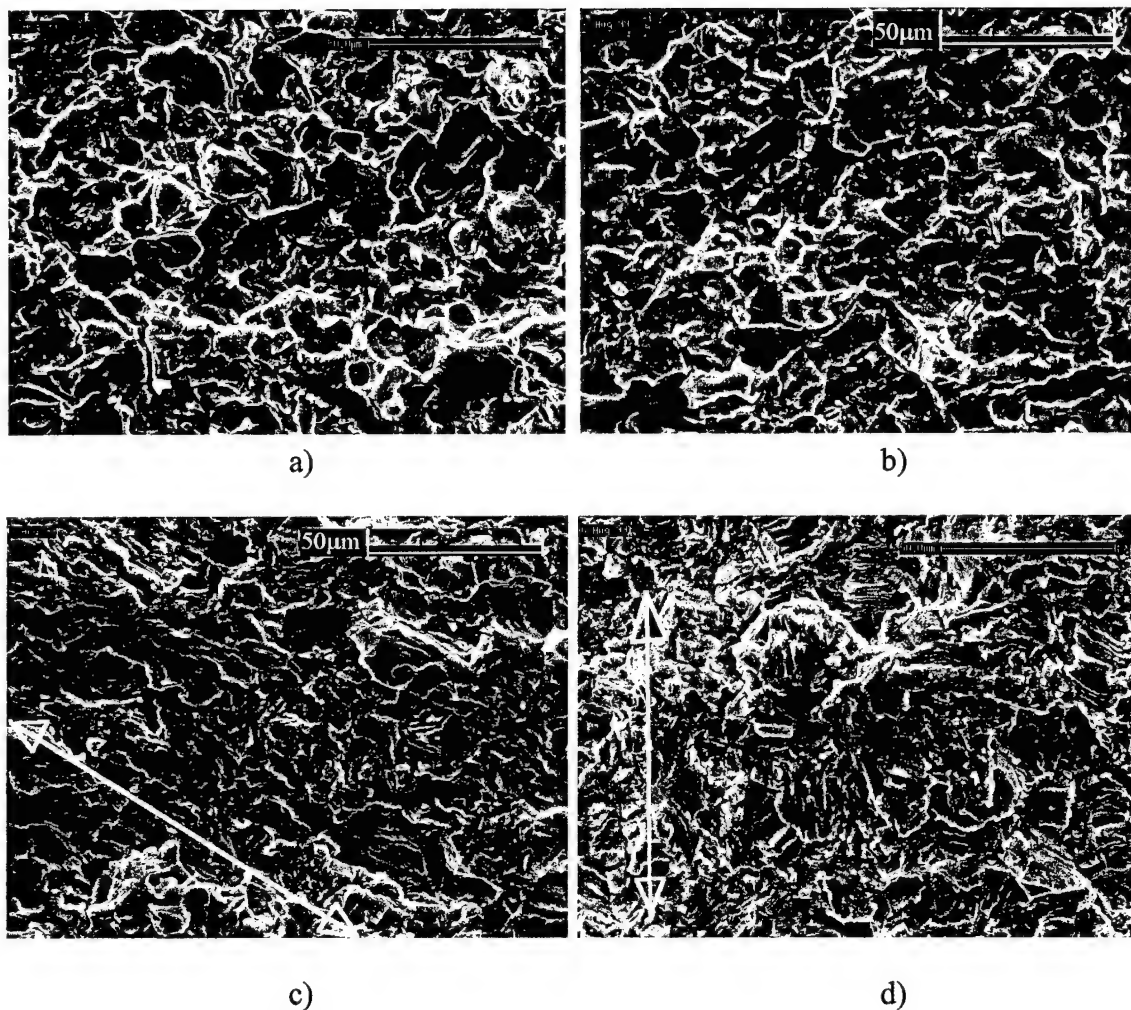


**Figure 37. Close-up Views of Fracture Surface.** a) and b) show the fracture surface in the virgin Ti-6Al-4V, location marked with 'V' in Figure 36. Note the fracture morphology remains the same regardless of the microstructure encountered by the crack front. This is in contrast to the surfaces shown in c) through f). c) Close-up of location 3. d) Location 2. In c) and d), the orientation of the deformation band in that region is shown by a white arrow. Note the preferred fracture of the grains along these directions.

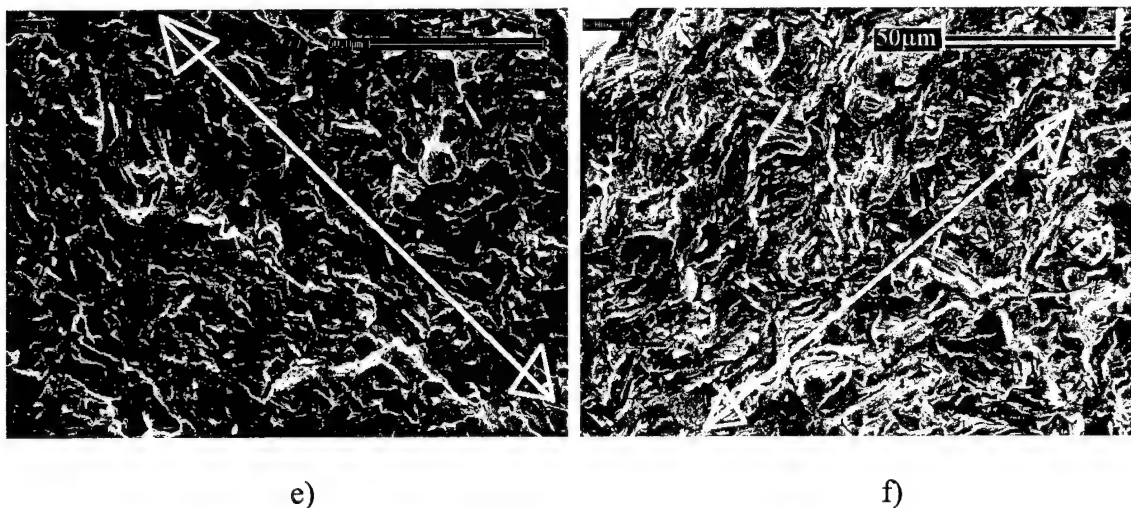


**Figure 37 (continued).** e) Location 4. Here the orientation of the grains along the local direction of the deformation band can again be clearly seen. f) Location 1. Here the preferential surface texture is less visible, but present.

Figure 38 shows this same region in a sample which was not fractured by fatigue after being indented with a 1 mm diameter chisel. Instead, this specimen was cut through the center with a diamond surfaced saw blade, mounted, polished and etched as described in Chapter III. The region that coincides with the deformation bands on the fatigued specimens can be clearly seen to be the location of severe shear banding and cracking. Figure 39 shows the residual strains after static indentation from the finite element analysis. The details of these results will be discussed in Chapter V. However, it can be seen that they show a similar pattern to that seen in the deformation bands.

These evidences indicate that the deformation bands are the visible manifestations of shear bands and high strains. They exist because the region of high shear strain damage created by the simulated FOD causes the grains of Ti-6Al-4V to fracture

under fatigue loading with a preferred directional texture, which became evident under the polarized light.

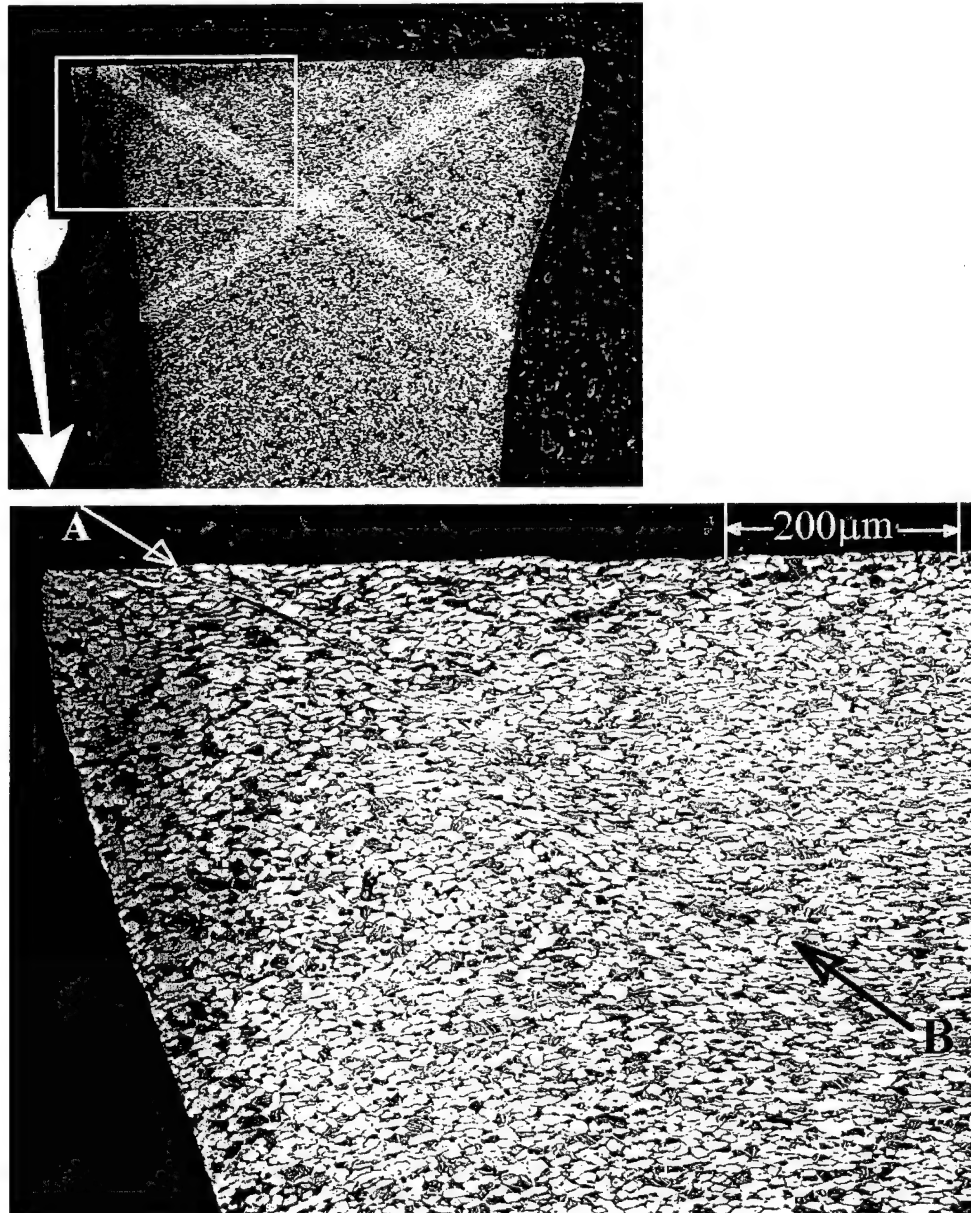
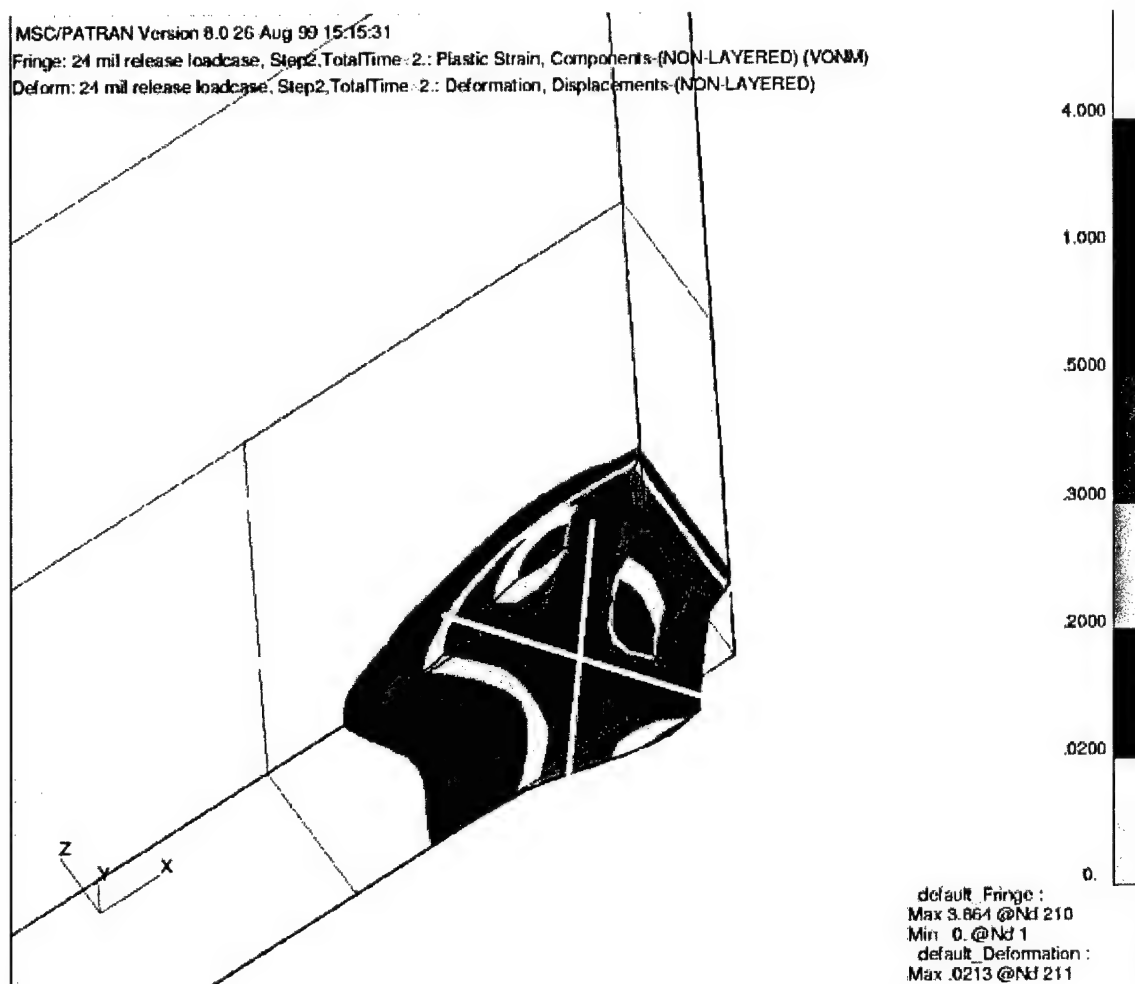
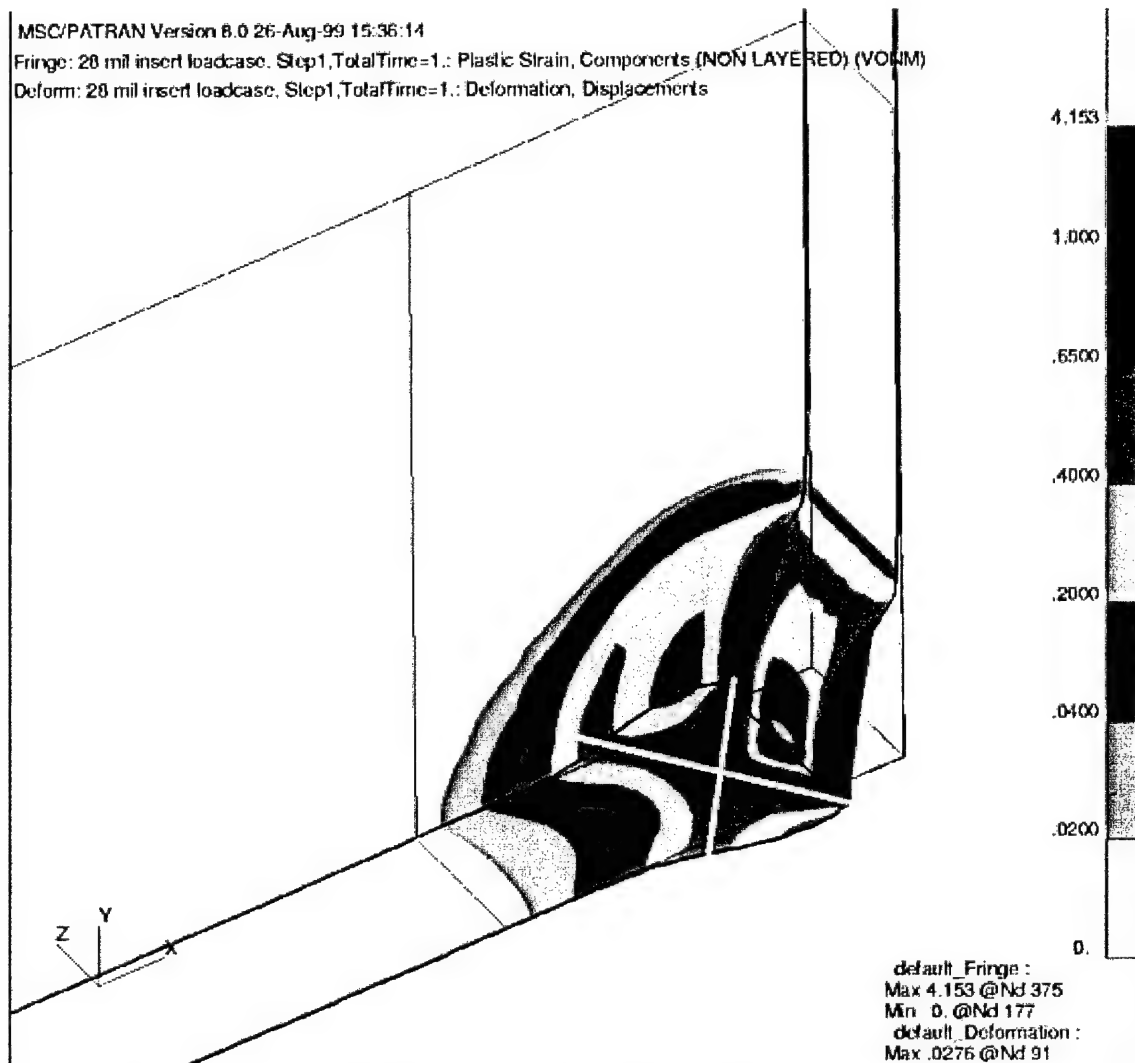


**Figure 38. Shear Bands on Polished Fracture Surface.** A sample damaged by a 1 mm diameter chisel has been cut through the plane in which fatigue fracture occurs. This specimen has been polished and etched to reveal grain structures. The usual location of deformation bands is highlighted in the inset. The close-up shows the distinct shear band running along the line from A to B. This band coincides with the deformation band location. An open crack caused by the shearing can be seen near 'A'.



a)

**Figure 39. FEM Model of Plastic Strain Magnitude.** a) Contours of equal plastic strain magnitude are plotted in this view for a specimen subjected to an indent from a 2 mm diameter chisel. The fracture surface at the bottom of this view shows an 'X' shaped region (highlighted by white lines) defined by those elements where the von Mises effective strain exceeds 20%.



b)

**Figure 39. FEM Model of Plastic Strain Magnitude (cont'd).** b) This shows the plastic strain for the case of indentation with a 5 mm chisel, where the 'X' pattern is again seen to coincide with high strain values ( $> 20\%$ ).

### Grain Size Measurement

The concept of measuring plastic strain from grain information is based on the assumption that the distribution of grain sizes is uniform throughout the undamaged

sample. In other words, if many measurements were made of the average grain dimensions in a given cross section of a specimen, they would be the same.

This means that if large plastic deformation occurs, the average grain size in the deformed material will change also. This can qualitatively be seen in Figure 40 where the cross-section of a rectangular specimen has been deformed due to indentation with a chisel. The grain structure can be seen to be shortened in the direction of chisel displacement into the sample. The grains are elongated in the direction perpendicular to the displacement, and also a radial flow of the deformed grains' long axes can be also seen.

To quantify this deformation pattern, the actual grain sizes must be measured. This was done by grinding a sample to reveal a plane in which the grain size measurements are to be taken (Figs. 41-42). The region containing the deformation is cut from a sample and mounted for metallographic preparation. The surface of the sample is flattened with 600 grit abrasive paper to remove any out-of-plane deformation due to Poisson's effects. Next, the surface is diamond-grit lapped and polished, finishing with 0.02  $\mu\text{m}$  abrasive. This surface is etched in a solution known as Kroll's etchant. It is a mixture of 20 parts nitric acid, 30 parts hydrofluoric acid and 200 parts distilled water. Samples are immersed for 25 to 30 seconds in this solution, then removed and the etchant neutralized in a saturated solution of sodium bicarbonate. This selectively erodes the two phases within the Ti-6Al-4V, making them visible to microscopic observation.



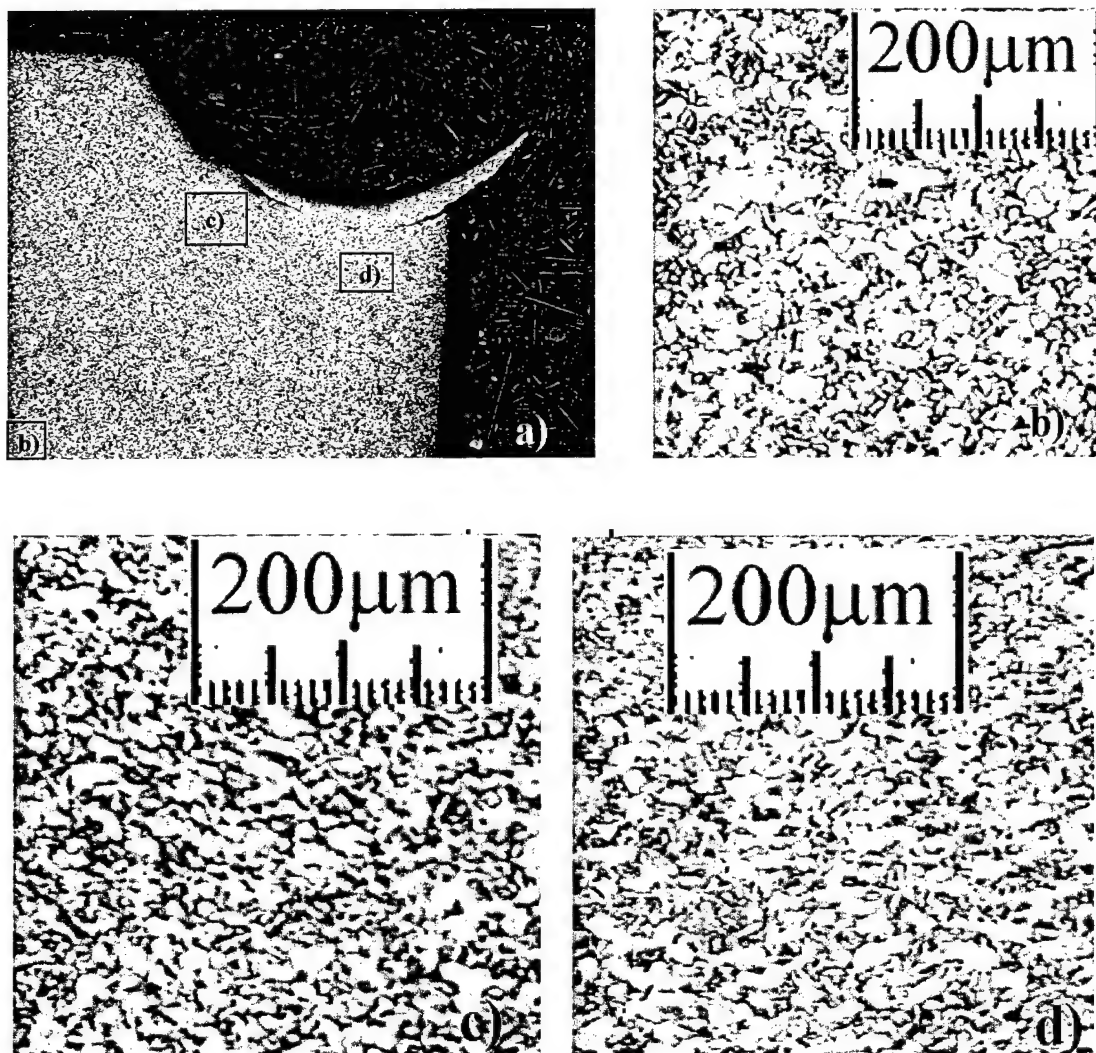


**Figure 40. Grain Deformation Due to Plastic Straining.** a) a 5 mm chisel indent in specimen 98-J66 showing the locations of the next three photographs. b) the undeformed structure (compare Figure 10). c) Grains near the 7 o'clock position of the chisel indentation. The grains can be seen to be visibly stretched and skewed in the same manner as the notch. d) The grains immediately behind the notch. Here the stretching runs left to right, since the compression is straight down in this view.

Microphotographs are taken of the area around the indentation and assembled into a montage (Fig. 43a). A microphotograph of a precision scale is also taken at the same magnification. This scale is used to calibrate measurements of grain boundary

location made on the montage. A reference line is drawn on the montage in the direction in which the strain measurement is desired (Fig 43b). An origin is chosen, usually at the bottom center of the indentation projection into the plane of observation. Note that the coordinates of this line increase in the direction of the negative x axis shown in Figure 12. The distance at which each grain boundary is crossed is recorded in a spreadsheet program. From the second boundary on, each boundary distance is subtracted from the one previous, creating a column of grain sizes as measured in the direction of the reference line. As the reference line goes farther away from the origin of the damage, the average grain size grows, until it reaches a maximum value (Fig. 44). The average was computed from the measurement of the present and previous 40 grains, and it will be referred to as a 40 per moving average<sup>4</sup>. This value is the average grain size at that location. In some cases, the moving average varied enough that the proper distance at which to evaluate the undeformed average was not obvious. In these cases, several lines were drawn on the montage at the maximum possible distance away from the indentation. The number of grains crossing these lines were counted, and a single average over the line's distance (typically 300  $\mu\text{m}$ ) was computed. The values were then averaged among each other, and this was taken as the average grain size.

Each individual grain's size is subtracted from this average grain size, then divided by the average grain size, yielding an approximation to the strain value:

---

<sup>4</sup> This average could be taken over any number,  $n$ , of grains, and would be called an ' $n$ ' per moving average. On some plots, the value of  $n$  was chosen adaptively by a MathCad routine; these plots are referred to as 'adaptively smoothed'

$$e_i \cong \frac{h_i - \bar{h}}{\bar{h}} \quad (18)$$

where  $e_i$  is the approximate nominal strain of the  $i^{\text{th}}$  grain  
 $h_i$  is the size of the  $i^{\text{th}}$  grain  
 $\bar{h}$  is the average grain size

This procedure is repeated for each grain size measurement taken (Fig. 45). Note that the wide range of grain sizes in the undamaged section yields very high standard deviations of the undeformed grain size. While Figure 44 shows how the grain sizes decrease due to the deformation, strain values obtained this way are not of high precision. The only potentially useful information from strain measured this way is an approximation to the distance at which the plastic strain has essentially disappeared, and even that is difficult to determine with any precision because of the large variation in undeformed grain sizes. Data from the samples which had grain size measurements taken on them are shown in Table 5 as the range of approximate strain at the distance to the optical deformation bands. Further details of the glass sphere impacted specimens subjected to grain size measurement, including the strain distributions, are in the section describing damage mechanisms.

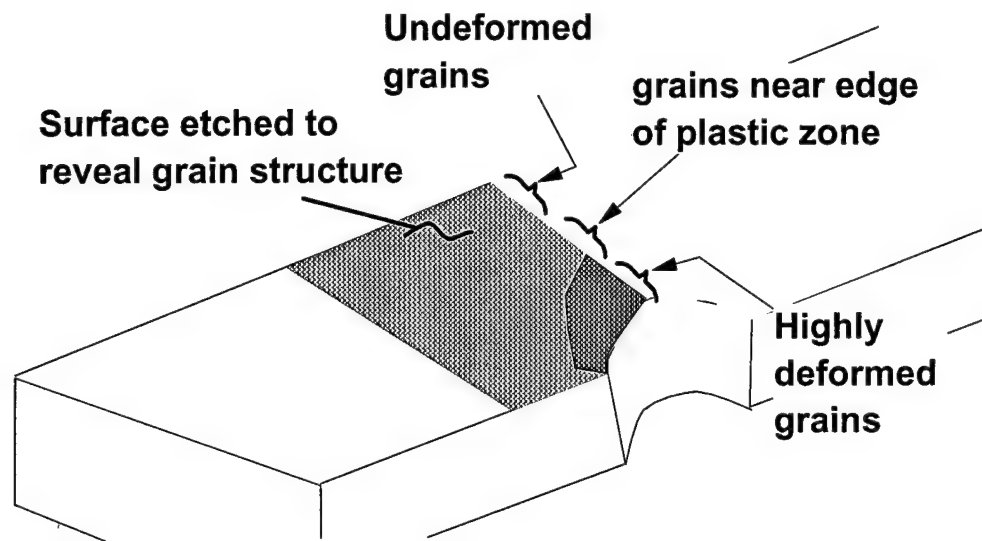


**Figure 41. Grain Size Sectioning.** This illustrates the types of regions seen when using grain size measurement technique.

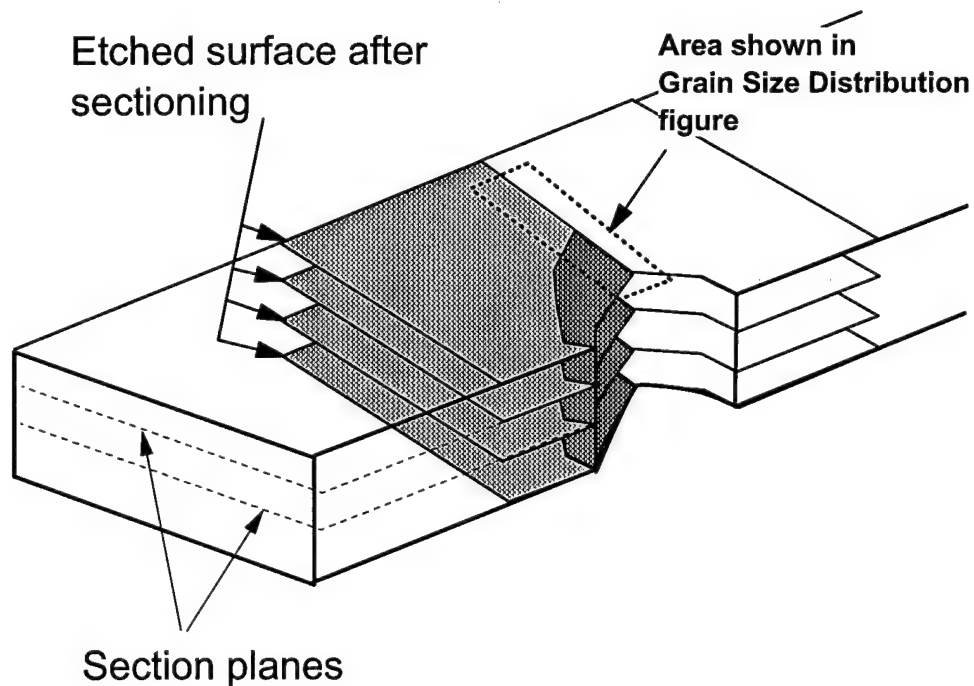
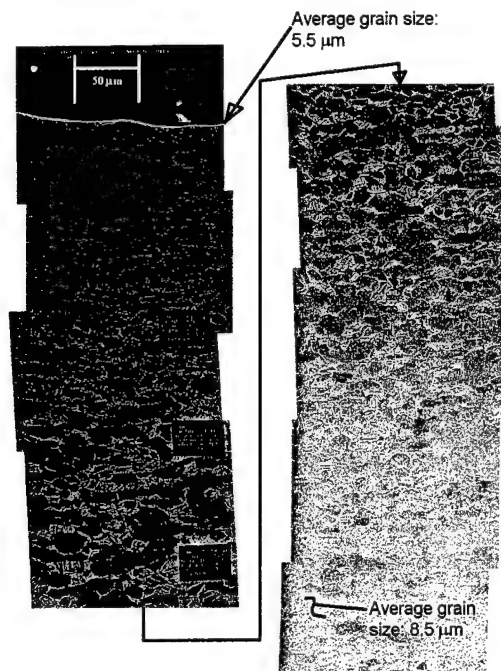
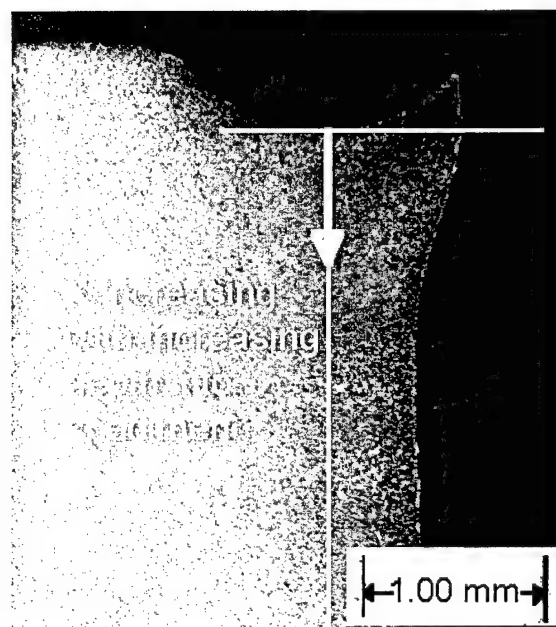


**Figure 42. Cross Sectioning of Damage Site.** Some specimens were examined by grain size measurement at multiple planes to evaluate the change in plastic zone through the thickness.



a)



b)

**Figure 43. Grain Size Distribution Near Crater.** a) The montage of multiple photographs allows the size of a grain to be associated with that grain's location from the bottom of the indent. b) The origin and reference line mentioned in text.

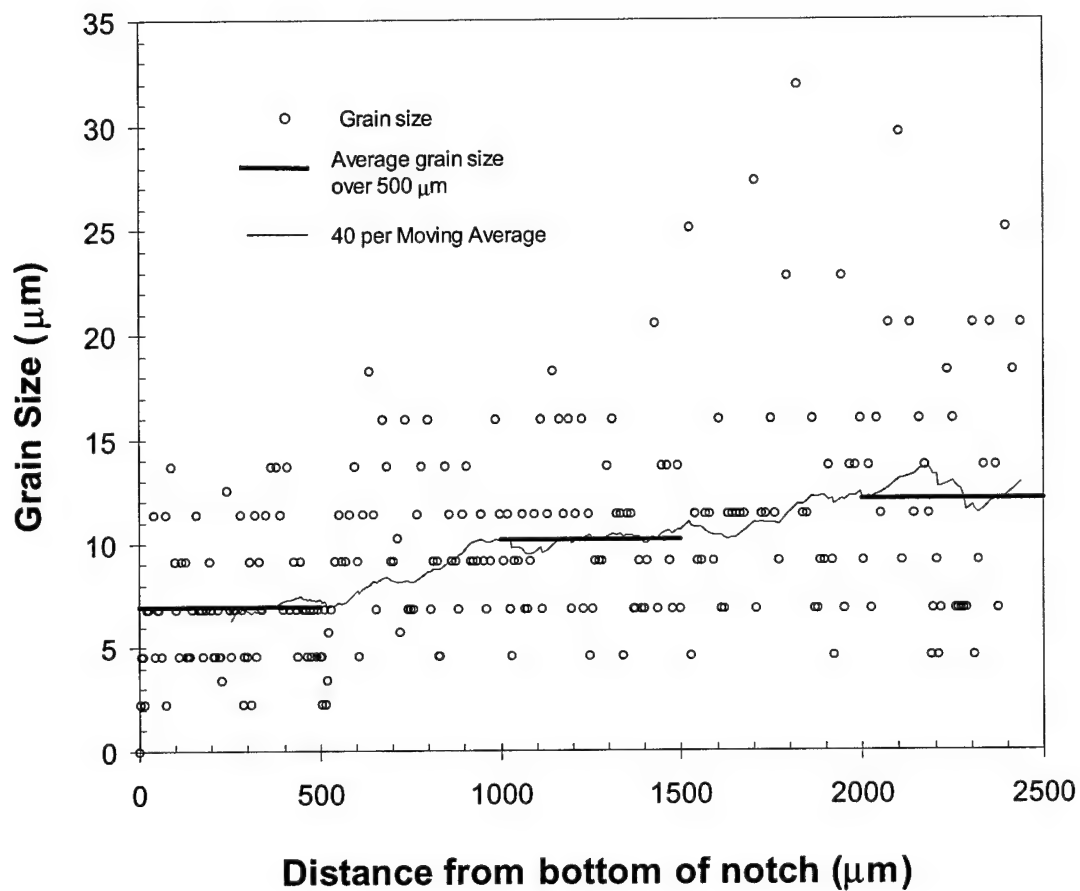


**Figure 44. Grain Size as Function of Distance from Indent.** This is from specimen 98-J66, which was damaged by a 2 mm diameter chisel, and is typical of the grain size measurement procedure.

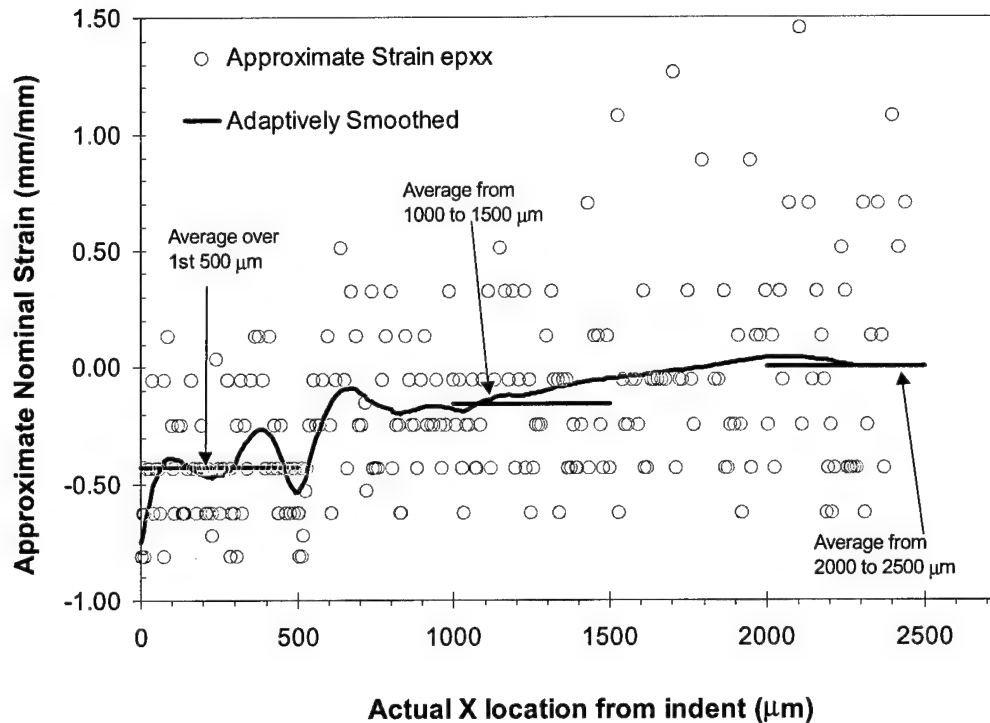


**Figure 45. Nominal Strain as Function of Distance from Indent.** The grain size data from Figure 44 are used to calculate strains from Eqn. 18.

Table 5. FOD Details

Sample	Damage Type	Indent Depth $D_i$ ( $\mu\text{m}$ )	$D_p$ from Optical Method ( $\mu\text{m}$ )	Approximate Grain Size strain at $D_p$ (optical)	FEM Plastic Strain at $D_p$ (optical)*
98-B12 d301**	5 mm glass sphere	901	790	9% - 2%	0.6% - 0.2%
98-B18	2 mm glass sphere	676	363	20% - 0%	0.5% - 0.3%
98-J54	5 mm chisel	640	1,750	8% - 6%	4% - 2%
98-J66	2 mm chisel	587	1,170	12% - 10%	12% - 9%
* von Mises plastic strain was used for the dynamic models; normal plastic strain for the quasi-static models.					
** d301 indicates the last three digits of the number assigned to the individual gas gun shot by UDRI contractor (see Appendix B). This specimen was not fatigue tested, and direct optical measurements were not taken; $D_p$ (optical) was interpolated from optical measurement data.					

## **Finite Element Modeling**

The complete details of the finite element modeling (FEM) methods used in this study to numerically simulate the test conditions are discussed in Chapter V. In this section a description of these methods sufficient to understand the results of strain and deformation calculations will be presented.

For the purpose of FEM analysis, the damage techniques described in Chapter III can be divided into two classes; dynamic and quasi-static events. The damage from the sphere impacts occurred so suddenly that it was assumed that modeling of the dynamic behavior of the FOD event would be required to model all variables that would influence the specimen's response. In other words, inertia effects were assumed to be significant. To model this, the commercial FEM code MSC/Dytran was used (48).

In the chisel indentation method, specimens were indented so slowly that inertia effects could be ignored. Hence ABAQUS, the FEM code used to model the chisel indentations, assumed that the specimen was in static equilibrium at all times (1; 47). This is often referred to as 'quasi-static' analysis (15:367).

In both FEM models, the Ti-6Al-4V material properties as measured by AFRL/MLLN were used to model the actual plastic deformation of Ti-6Al-4V in uniaxial tension (4). In the simulation of the quasi-static chisel indentations, the final state of plastic strain created by the chisel remains after it is removed from the sample. This was accomplished by enforcing the measured chisel indentation



displacement as displacements applied to the model of the chisel, enforcing contact between the chisel and the specimen, finding the equilibrium state of the model, and then creating a second set of enforced displacements which removes the chisel from contact with the specimen. Values of the plastic strain were computed from the nodal displacements and plotted as various quantities with respect to the final position of the nodal locations. Figure 46 shows a plot of the deformed locations of the nodes in the model after the chisel is inserted and removed. The model captures the actual deformed shape of Ti-6Al-4V damaged this way, as can be seen in the inset photograph of a specimen. This faithful representation of the deformation caused by the chisel indentation indicates that the strains computed from the deformations are accurate also.

The reported strain values from ABAQUS are the values at the nodes. The node locations reported are the positions in the undeformed state. To locate the position of each node in the deformed state, each node's displacement must be recorded and added to the original coordinates. Figure 47 shows a typical plot of the plastic strain in the chisel displacement direction as a function of the depth into the specimen. In the figure, the von Mises' plastic strain is plotted, along with the absolute value of the tensorial strain value representing  $e_{p_{xx}}$ , the direct strain in the x direction, which is what is evaluated by the grain size measurements. Note how the normal compressive strain and von Mises effective plastic strains peak somewhat behind the surface. This corresponds to the location of maximum width of the plastic bulge through the thickness, which can be seen in Figure 46.

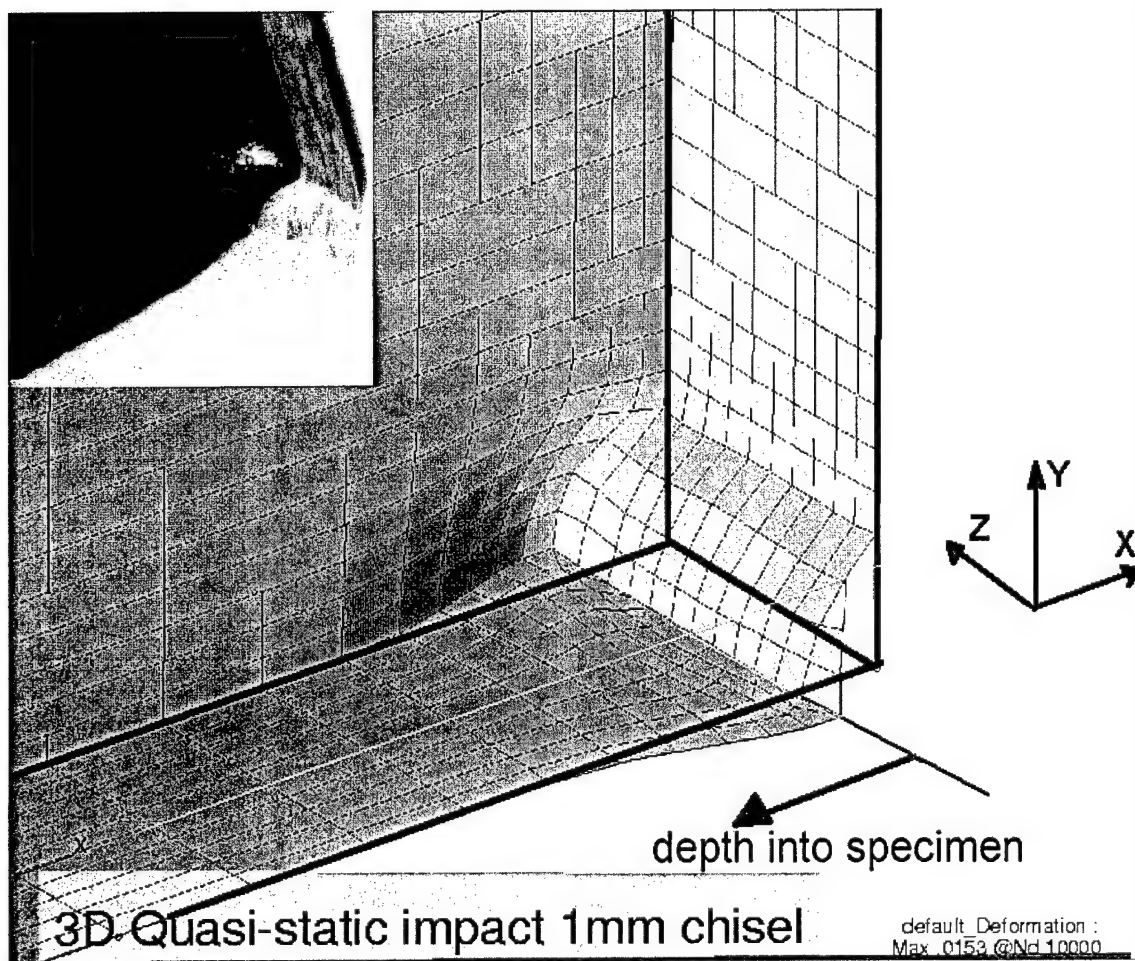


**Figure 46. Deformed Shape of 1 mm Diameter Chisel Indent.** This view shows the location of the nodes after moving a 1 mm chisel model 388  $\mu\text{m}$  into the specimen and then removing it. The solid dark lines show the undeformed shape. The inset shows specimen Scrap#02, which was indented 380  $\mu\text{m}$  with a 1 mm diameter chisel. Note how the model represents every important feature of the deformed shape.

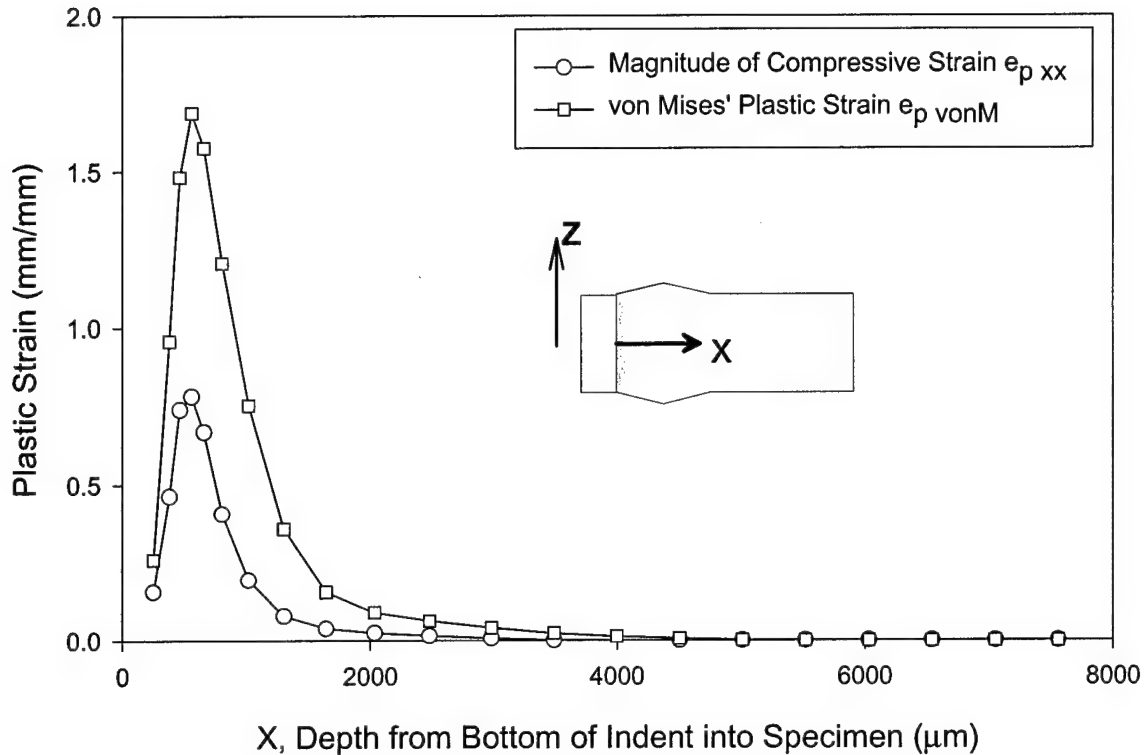


**Figure 47. Plastic Strain vs. Depth into Specimen from ABAQUS Model.** This graph plots the results of the 2 mm diameter chisel model. X increases as one goes deeper into the specimen as described in Figures 43 and 46.

In the case of the dynamic analysis of sphere impacts, MSC/Dytran was used to model the damage event. Fundamentally different in nature from ABAQUS (see Chapter II), Dytran had different options available for reporting results. The only plastic strain value available for output was the von Mises' plastic strain (referred to in the Dytran manual as EFFPLS), although the total strain in the x direction could be obtained. Further discussion of the relationship between EFFPLS and  $e_{p\ xx}$  follows in the section on the glass sphere impact damage. The values of strain at each node in the model were requested at time steps of 1 μsec. A typical plot of strain versus the

depth into the specimen (defined as in Figure 47) at a time step after the completion of the sphere impact event is shown in Figure 48.

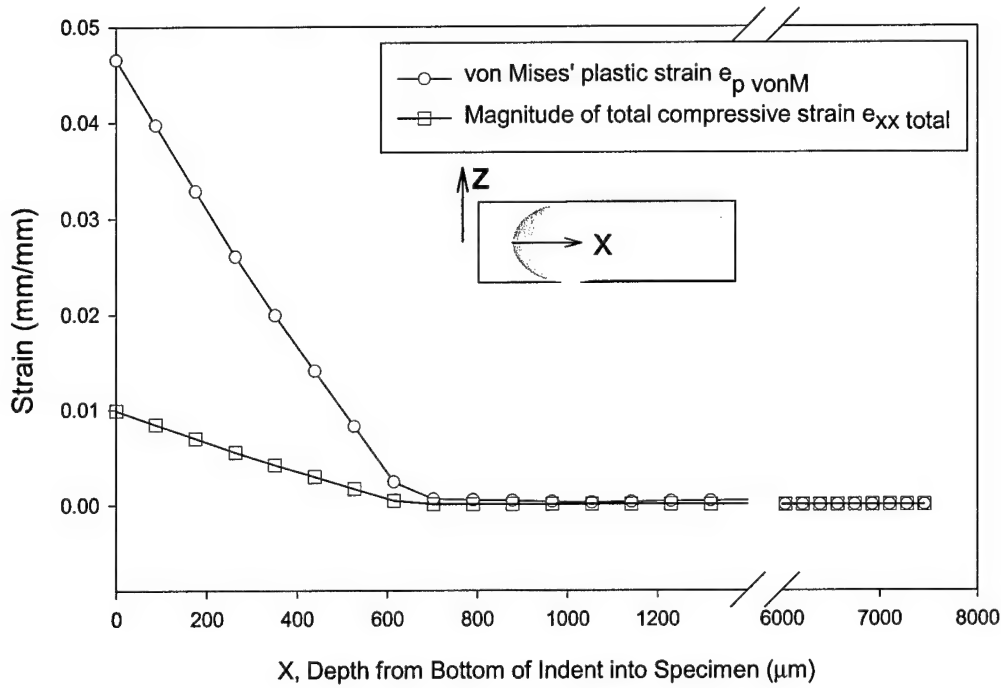


**Figure 48. Plastic Strain vs. Depth into Specimen from Dytran Model.**

The Dytran code provided von Mises' plastic strain and total normal strain. The graph plots this quantity along the centerline of the fracture surface from the bottom of the notch into the interior of the specimen.

In the following sections, the plastic zone size was estimated from FEM models which will be displayed as plastic strain values versus depth into the sample from the bottom of the indent. Wherever a grain size measurement was undertaken in the specimen, that will be plotted as well. From this comparison, it will be shown that at the distance into the specimens at which the deformation band was seen, the estimated plastic strain values from finite element analysis lie within a certain range. This range was found to be approximately 12% to 4% compressive plastic strain,  $e_{p_{xx}}$ ,

in the case of the quasi-static damage method, 6% to 4% effective plastic strain,  $e_{p\text{von Mises}}$ , for the dynamic steel sphere impact and 0.6% to 0.2%  $e_{p\text{von Mises}}$  in the case of the dynamic glass sphere impacts. The dynamic analyses use von Mises' effective plastic strain because the Dytran code could not compute normal plastic strains. This is shown as an example in Figure 49. When no grain size measurements are available for comparison with the FEM values,  $D_p$  will be taken to be the depth at which the strain values lie within the ranges mentioned above.

The large difference between the amounts of strain which corresponded to the deformation band locations may be a result of the dynamic nature of the sphere impacts. A fixed amount of energy, set by the sphere's mass and velocity, is available to deform the specimen during an impact event and this amount is larger for the steel sphere. The available energy is essentially infinite in a chisel indentation, since any amount of force necessary can be applied to displace the chisel. In addition, in the dynamic impact cases, strain rate hardening during deformation would allow the Ti-6Al-4V to resist the forces applied by the sphere at higher yield strengths, which would tend to decrease the residual plastic deformation. Also, animation of the dynamic impact cases, especially the 5 mm glass sphere, indicate that the eroded surface of the specimen is squeezed from the front and the eroded sides by the glass fragments. This provided high stresses on the eroded specimen surface in directions other than normal to the impact velocity. This may account for

the large discrepancy between the normal strain and the von Mises' effective strain because  $e_{p\text{von Mises}}$  is created mostly by the strain components other than  $e_{p_{xx}}$ , Figure 48.

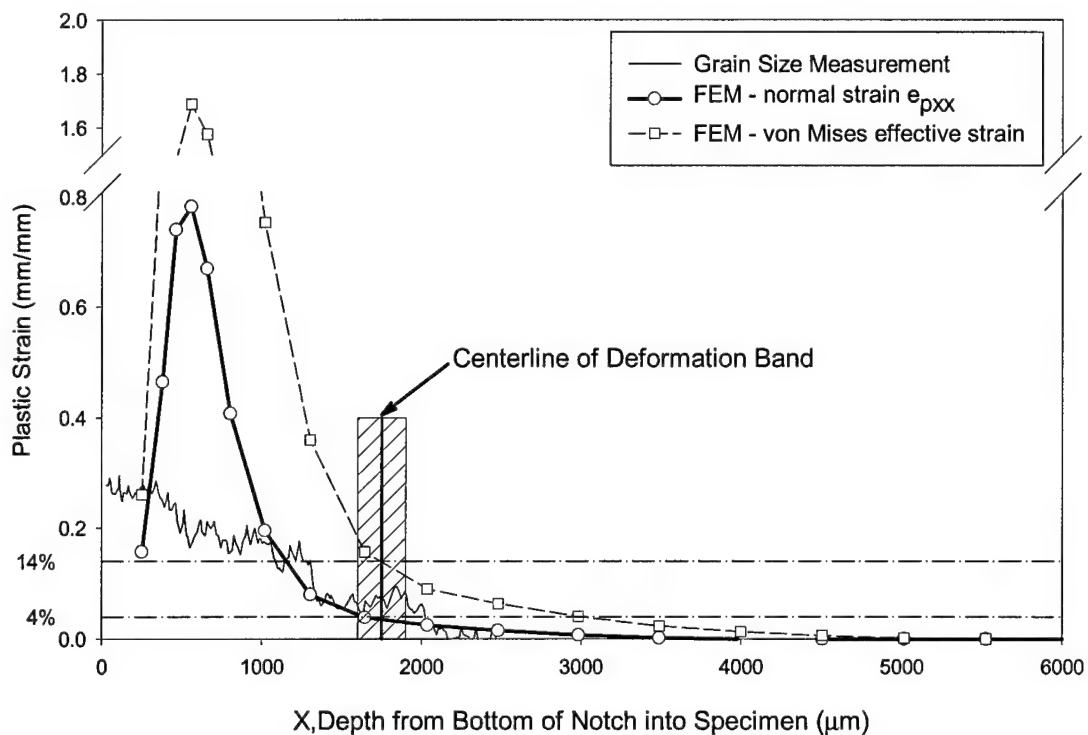


**Figure 49. Comparison of Damage Quantification Techniques.** The optical deformation band and grain size measurements from a cross-section near the centerline are shown for a 5 mm chisel indent. The ABAQUS results for von Mises' and normal plastic strain are also plotted. Note that the maximum strains are located in the vicinity of the maximum width of the bulge described in Figure 13c. At the location of the optical deformation band, ( $1750 \mu\text{m} \pm 150 \mu\text{m}$ ) the grain size measurement of strain lies between the FEM values for normal strain (4% - 3%) and von Mises' effective strain (15% - 13%). This location marks the maximum extent of the deformed region.

## Damage Mechanisms

For the four FOD simulation techniques described in Chapter III, seven distinct damage mechanisms were observed.

- 1) Glass sphere impacts without erosion
- 2) Glass sphere impacts causing erosion
- 3) Chisel indentations without chipping
- 4) Chisel indentations causing chipping
- 5) Steel sphere impacts without chipping
- 6) Steel sphere impacts causing chipping
- 7) Sheared notches using chisel in transverse direction

The following sections will describe details observed about each mechanism.

*Glass Sphere Impacts Without Erosion.* Since all glass sphere impacts were at  $305 \text{ m/s} \pm 22 \text{ m/s}$  ( $1000 \text{ fps} \pm 72 \text{ fps}$ ), the only distinction in damage energy was the mass difference among the three diameters. The impacts made by the smallest spheres (1 mm diameter) simply indented the specimens. No damage to the surface texture was observed (Fig. 50). The crater created by these impacts had the same surface texture as the undamaged surface as was about  $350 \text{ }\mu\text{m}$  in diameter and less than  $200 \text{ }\mu\text{m}$  deep, compared to the  $1000 \text{ }\mu\text{m}$  diameter of the sphere. On the rectangular specimens, the 1 mm diameter glass spheres did not create enough damage to initiate fatigue fracture at the damage site. All these specimens when tested failed at the test machine grip due to fretting initiated at the intersection of the roughened grip inserts and the free surface of the specimen (Fig. 26). Consequently, no fatigue strength data could be collected for this FOD simulating technique. No FEM analysis of this condition was therefore conducted.

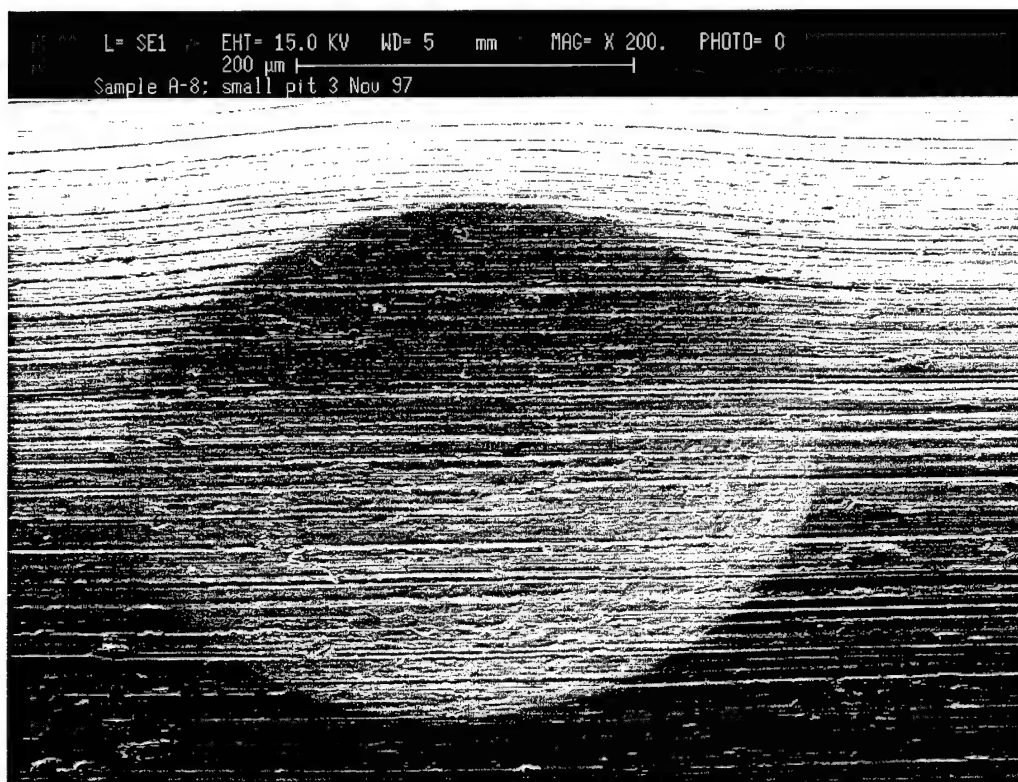


**Figure 50. Surface of Glass Impact Crater without Erosion.** A scanning electron microscope (SEM) image of a leading edge specimen is shown. Note the crater rim is smooth, and no pitting or erosion of the metal is evident.

*Glass Sphere Impacts Causing Erosion.* The two larger glass sphere impacts (2 mm and 5 mm diameter) were characterized by disintegration of the glass sphere immediately upon contact with the specimen. This is obvious from high speed photographs taken of the glass sphere impact event (Figs 16-17). As the sphere flies between the muzzle of the gas gun and the edge of the specimen where the contact will occur, the sphere's transparent nature is clear. In the first frame of film after contact, the texture of the sphere turns dull and opaque, indicative of broken fragments which diffuse the light by which it is filmed. From the first frame in which the sphere is broken, where it is still spherical, to the last frame in which the



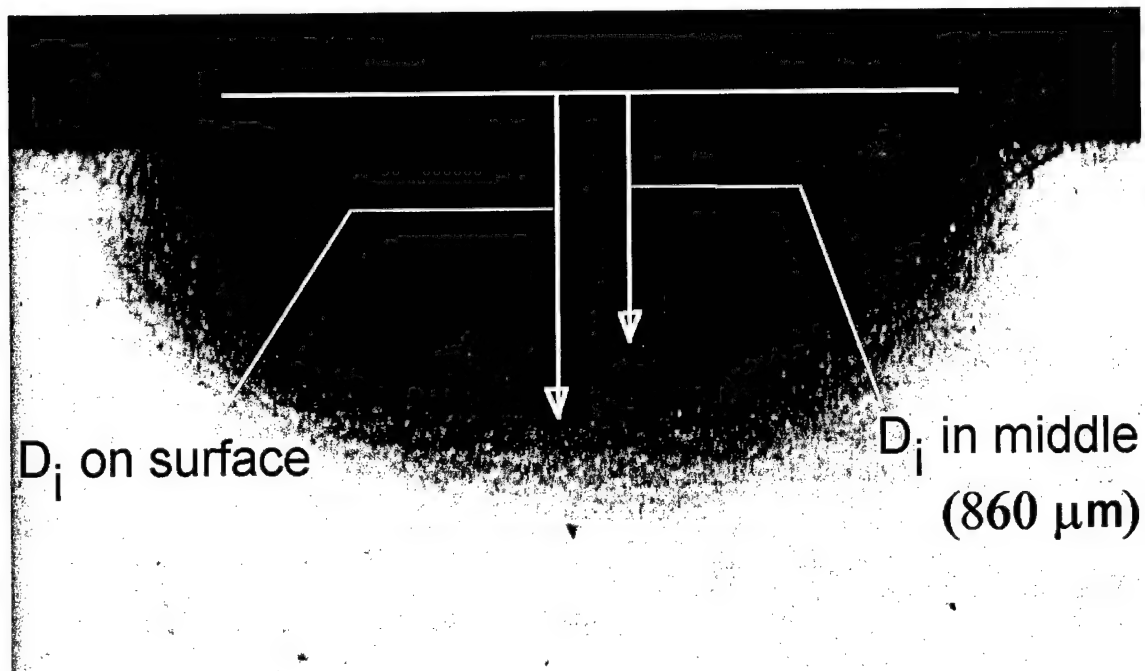
fragments can be observed, the cloud of fragments changes shape as it flows over the edge of the specimen.

After testing, the crater can be seen as rough and encrusted with glass fragments which have stuck to the surface (Fig. 51) . The crater's shape appears as a semicircular notch in this plane, although the crater is deeper on the surface faces of the specimen than it is at other points through the thickness (which runs perpendicular to the page in Figure 51). This is somewhat similar in shape to the notches ground into the teeth of a serrated knife blade. The minimum depth of the notch near the center of the thickness is the crater depth  $D_i$  recorded in Table 3. This variation in crater depth through the thickness is shown in Figure 15.

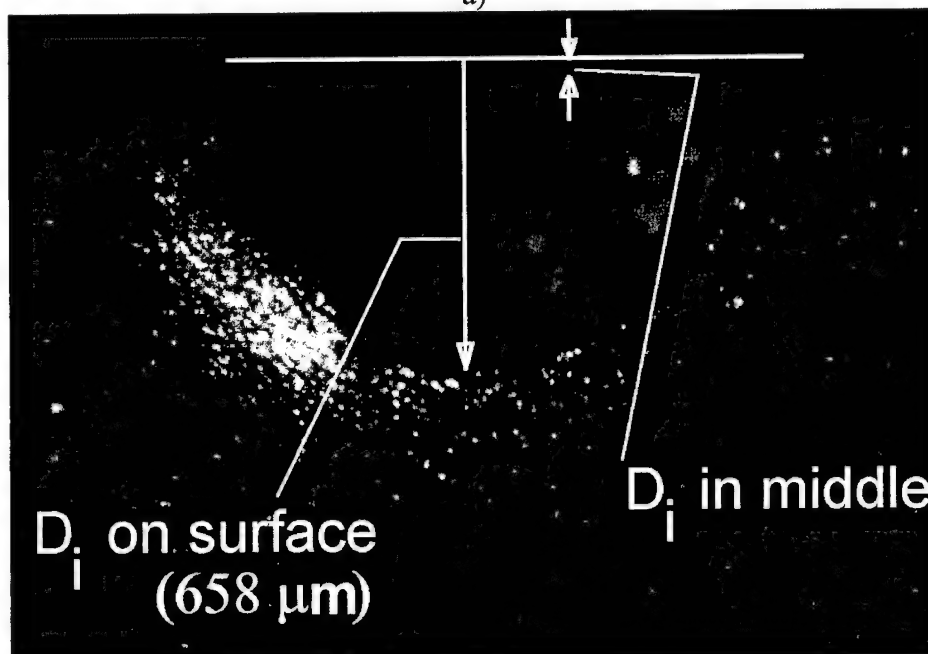
Note in Figures 51 and 52 the similarities and differences between the 2 mm diameter and 5 mm diameter craters. Keep in mind that the 2 mm diameter glass sphere is only slightly wider than the 1.27 mm thickness of the specimen, while the 5 mm diameter glass sphere is 4 times as wide. Both embed glass particles on the surface of the crater, but while the 5 mm craters uniformly erode the surface nearly symmetrically about the center of the thickness, the 2 mm diameter spheres did not always strike the center of the thin edge. Some specimens were hit by the 2 mm sphere such that the crater is much deeper on one face than another. As will be shown in Chapter VI, this had minimal impact upon the fatigue testing. In all cases, where one crater on the specimen was noticeably off center, the other crater on the same specimen was centered properly. Often the centered crater would be the site of

the fatigue crack initiation, but some specimens fractured from the off center crater. Optical observation indicated that the depth of damage in these cases was comparable to the damage depths which fractured the other specimens damaged by 2 mm diameter glass spheres. Figure 53 shows schematically how the damage mechanisms and different deformation bands for the glass sphere specimens appeared under examination of the fractured surface by optical microscope.

In Figures 54 and 55, the plastic strain is plotted as a function of depth from the bottom of the notch into the specimen. Note here that at the location of the optical deformation band, strains evaluated by FEM drop to less than 0.5%. The absolute value of strain from the grain size measurements, as mentioned previously, has a large amount of scatter and the location at which the grain size measurements indicate the extent of plastic deformation is uncertain. Also, the normal strain measurements plotted in Figures 54 and 55 are useful only in that the distance at which they vanish agrees with the other measurements. As described in the previous section on the finite element calculations of strain, Dytran cannot separate elastic and plastic strains as tensorial components, and the total strain contains a large amount of noise from the dynamic ringing in the model, and there are significant amounts of plastic strain other than the normal component contributing to  $e_{p \text{ von Mises}}$ . Finally, due to the nature of the failure algorithm, described in Chapter V, the elements with high compressive strain are removed from the calculation when they finally fail, leaving at the surface elements with lower normal strain values.

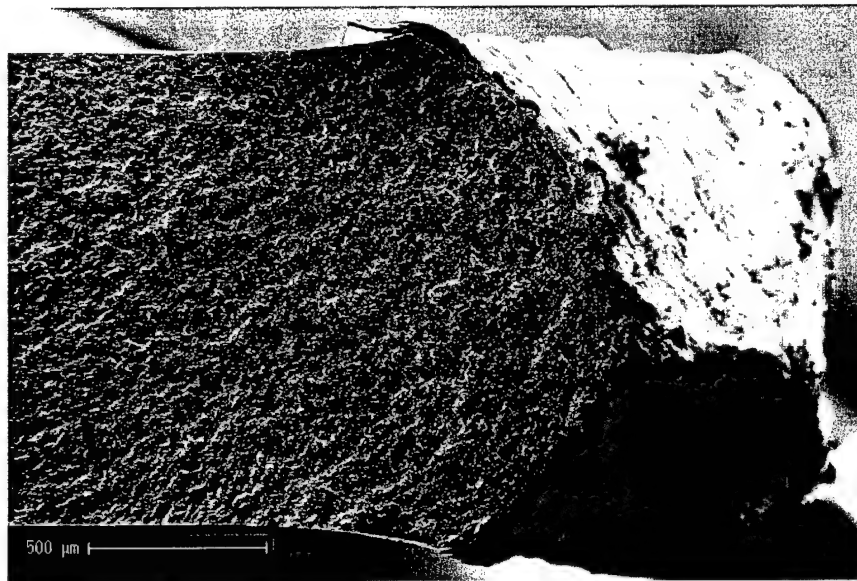


a)

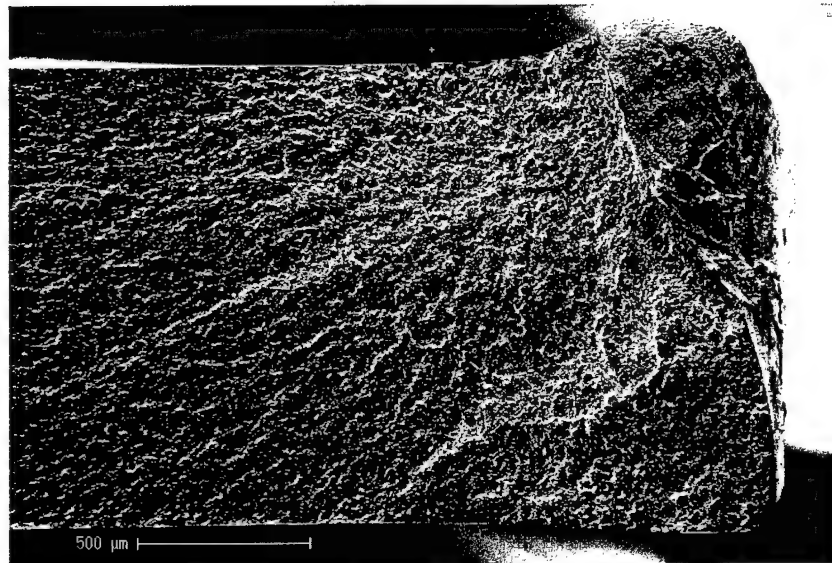


b)

**Figure 51. Crater from Glass Sphere Impacts with Erosion.** a) 98-B13 5 mm diameter. b) 98-B18 2 mm diameter. In this view the similarities of the damage can be seen. The crater surface is eroded, rough and encrusted with glass fragments. Near the specimen face,  $D_i$  of the crater is larger than at the center.



a)



b)

**Figure 52. Crater from Glass Sphere Impact with Erosion - cont'd.** a) 98-B09, a typical 5 mm diameter crater. The impact is slightly off center, however both sides of the crater eroded nearly equally. b) 98-B19, 2 mm diameter sphere. This impact was off center, eroded the top edge more than the bottom.

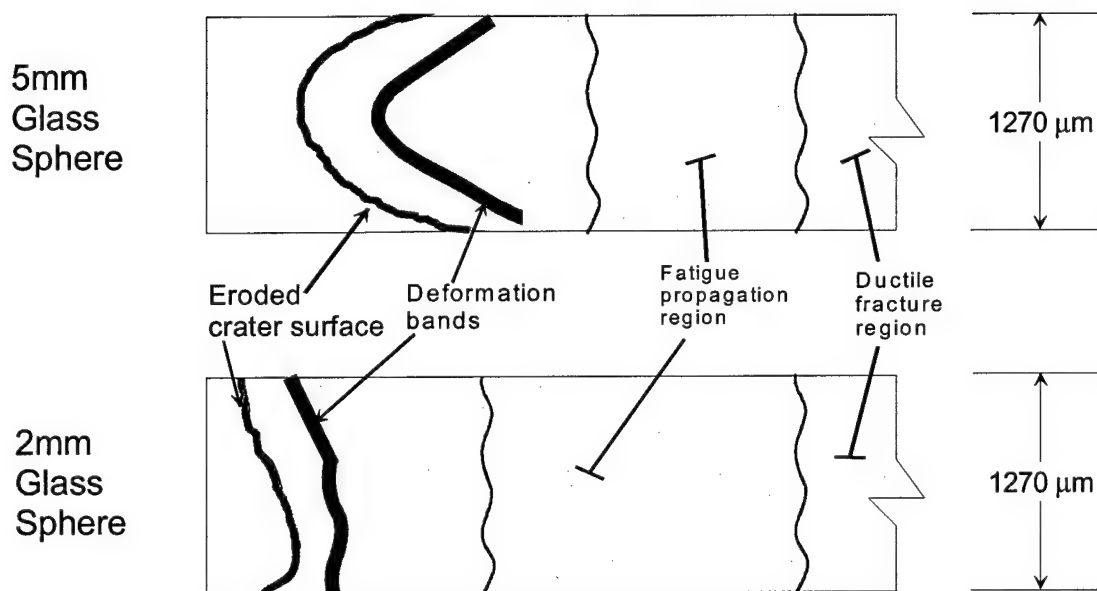


**Figure 53. Deformation Patterns for Glass Sphere Impacts.** The diagram shows qualitatively how the deformation patterns appear on glass sphere impacted specimens. Regions where the fatigue crack propagates across the specimen and where the specimen fails by ductile fracture in the remaining ligament are also shown.

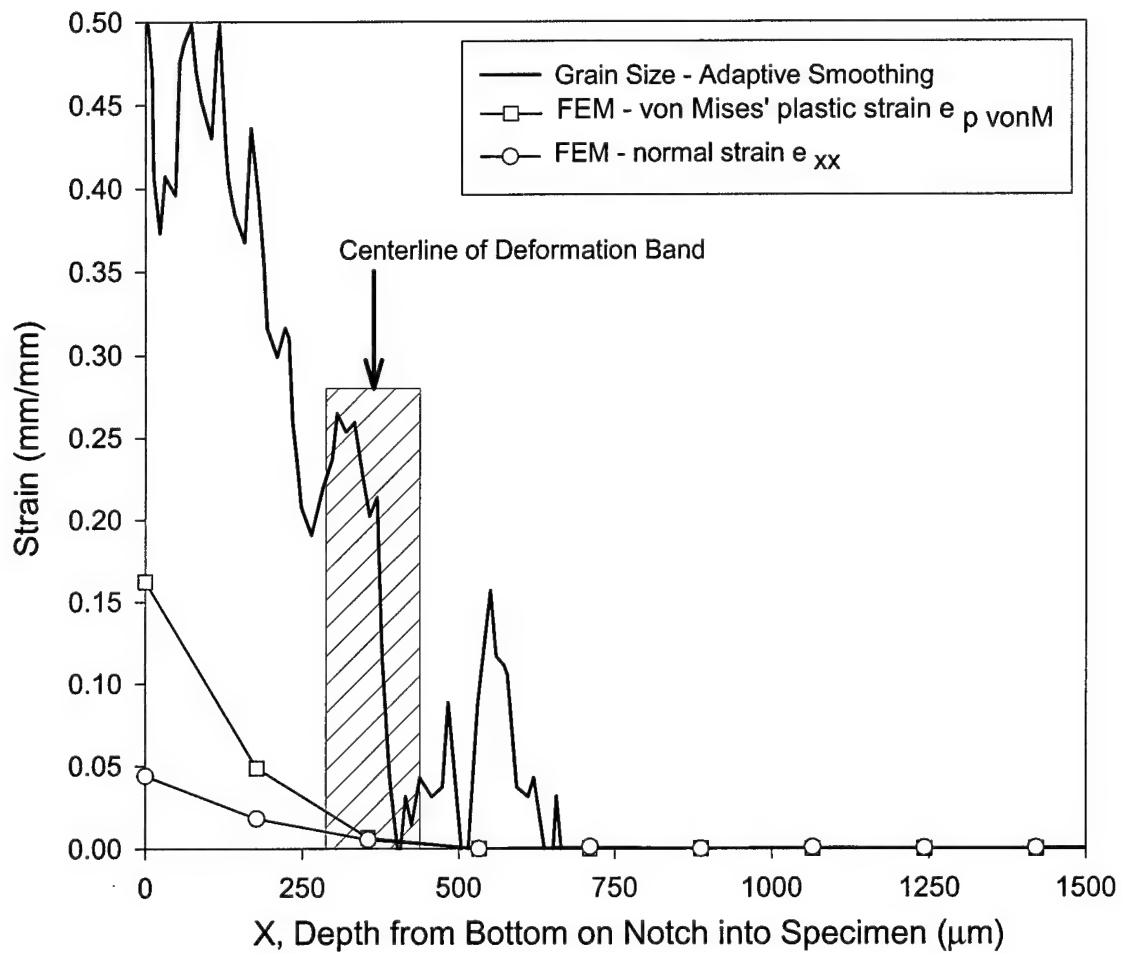


**Figure 54. Plastic Zone Size for 2 mm Glass Sphere.** Grain size measurement, FEM calculations and optical deformation band measurements are plotted together. The FEM calculations and optical deformation band location indicate similar plastic zone extent, but the grain size measurement is uncertain.

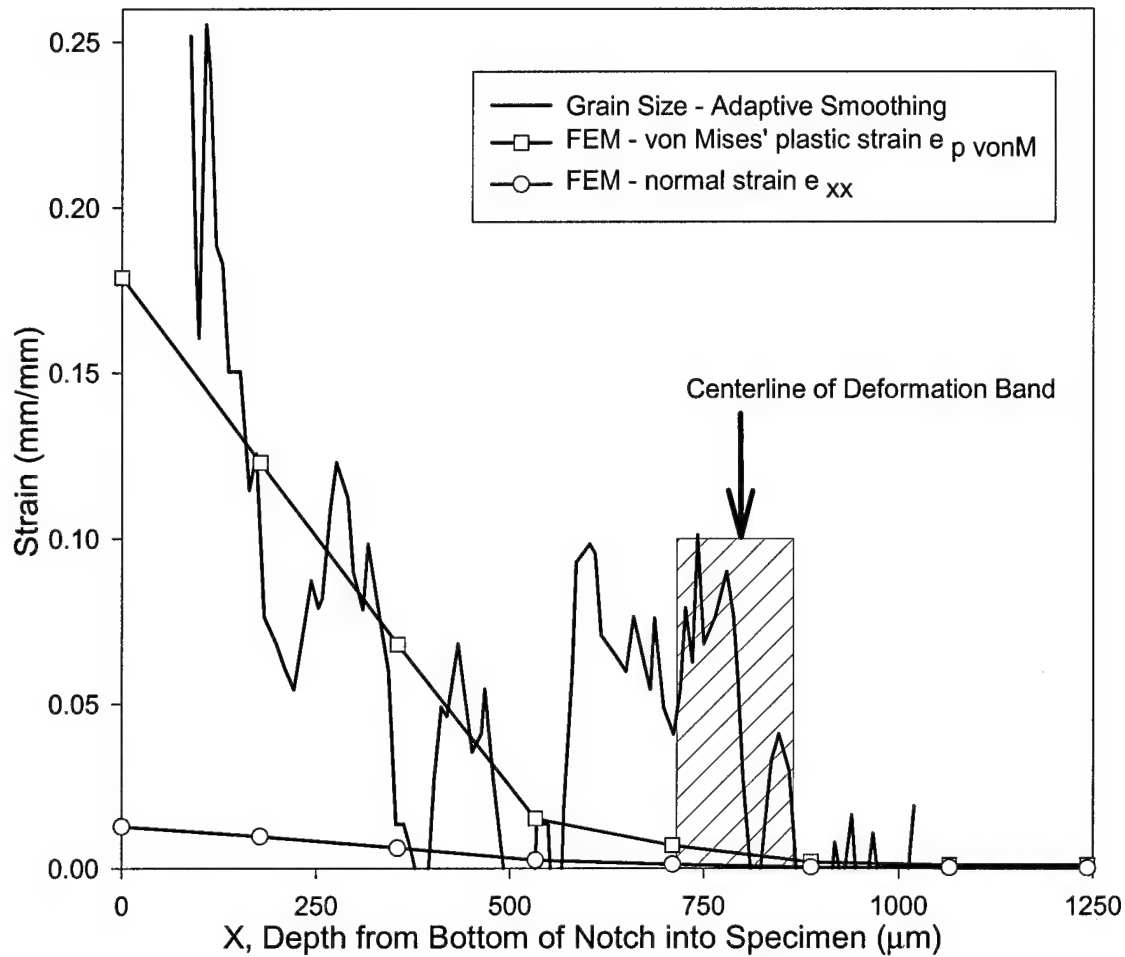


**Figure 55. Plastic Zone Size for 5 mm Glass Sphere.** Grain size measurement, FEM calculations and optical deformation band measurements are plotted together. As in Figure 54, the FEM calculations and optical deformation band location indicate similar plastic zone extent, but the grain size measurement is uncertain.

Figure 56 shows how the plastic zone size  $D_p$  increases with crater indent depth  $D_i$ .

$D_i$  was measured by the criteria described in Figure 13c. In Figure 56 and all subsequent figures plotting the plastic zone sizes, the vertical bars on the damage depth ordinates represent the uncertainty in determining  $D_p$ , i.e., the finite width of the deformation bands as described in the beginning of this chapter. For the FEM and grain size data, the bars represent the uncertainty in choosing where to denote the

end of plastic deformation. Note that the data for 2 mm and 5 mm glass spheres form a continuous trend. Even though the crater sizes for the two sizes of sphere are quite different, the plastic zone created directly behind the crater increases with increasing depth of the crater in the same manner for both sizes.

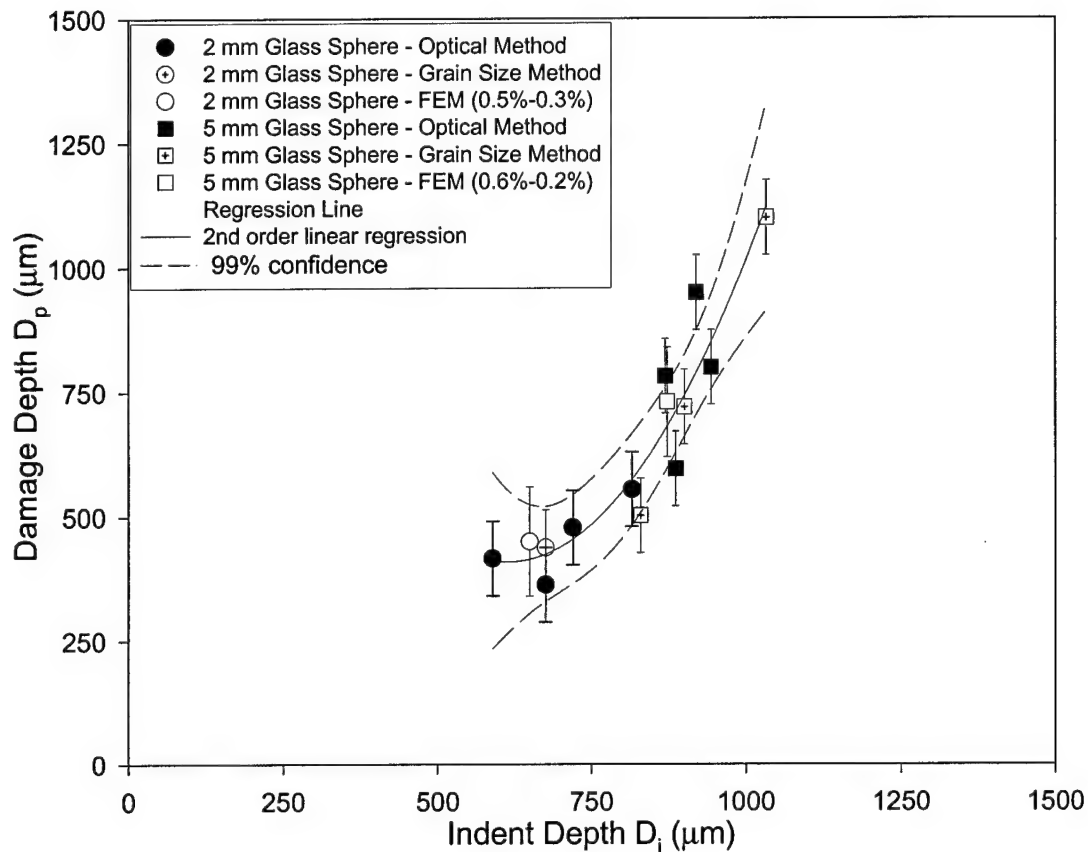


**Figure 56. Glass Sphere Damage Depth.** The FEM strain analysis, grain size measurements and optical observation values for  $D_p$  are plotted here against the crater depth  $D_i$  associated with the measurement.

*Chisel Indentations Without Chipping.* The 1 mm and 2 mm diameter chisel indentations left smooth surfaced round craters which bulged out of the plane of the specimen in a crescent shaped region behind the crater (Fig. 57). In the lower left of

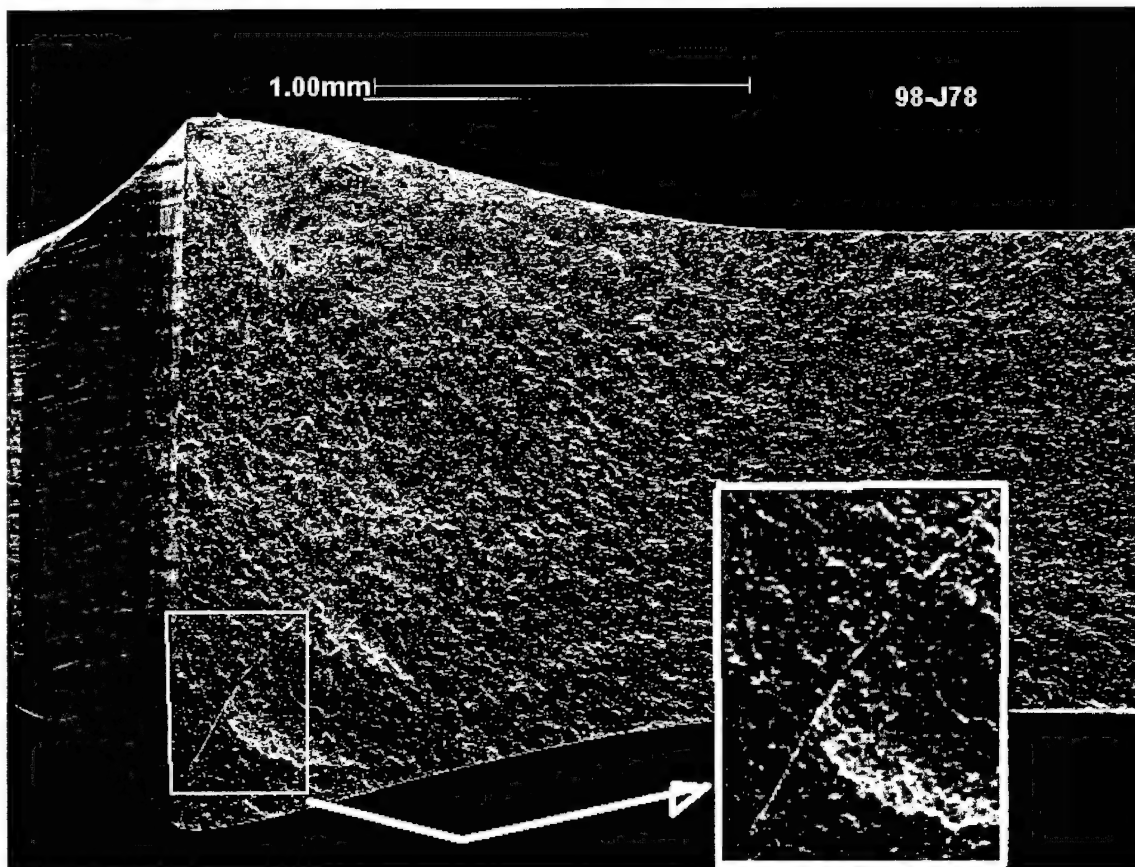


the fatigue fracture surface, evidence of cracking at 45 degrees to the direction of chisel insertion can be seen. These cracks are caused by the shear stresses in these regions, and lie in the half of the 'X' shape formed by the deformation bands that is closer to the notch (Figure 58). The other half of the 'X' is formed by the optical deformation bands described earlier. As the indent depth becomes larger, these cracks become more pronounced, as shown in Figure 59.

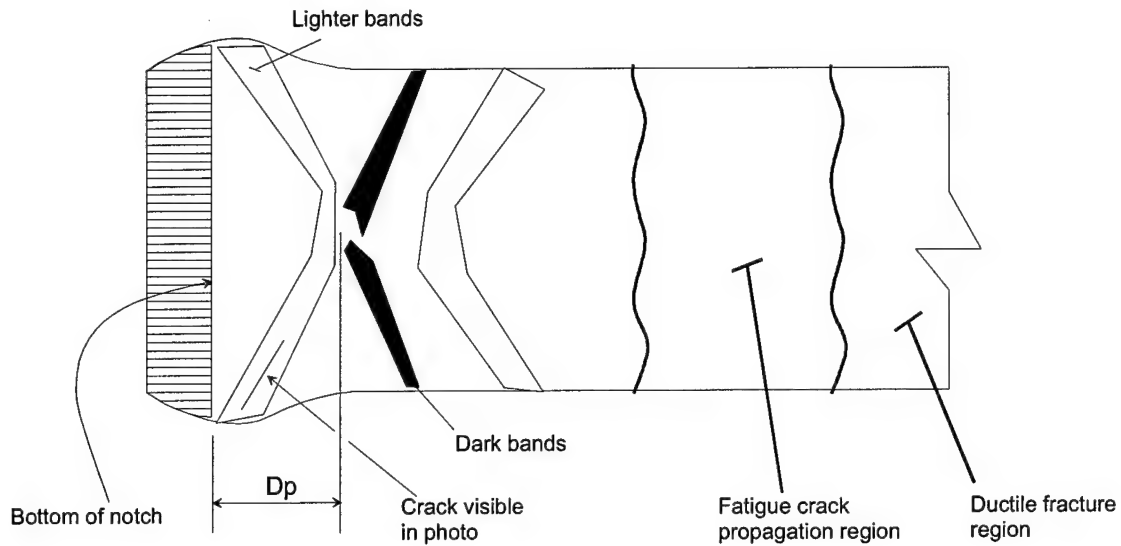
The region around the notch in the opposite edge of the specimen failed under tension with a marked difference in the shape of the fracture when the indentation depths were larger than about 500  $\mu\text{m}$ . In Figure 60a, the ductile fracture region around the notch opposite to the crack initiation site is shown for a specimen with a notch depth well below the critical depth of 500  $\mu\text{m}$ . Figure 60b shows a ductile fracture around a notch deeper than 500  $\mu\text{m}$ .

Figure 60a depicts a ductile fracture where the opposite notch was bypassed altogether by the fracture surface, indicating that as failure occurred, the propagating crack found no areas of particular weakness in the vicinity of the notch. Just the opposite is indicated by the highly irregular surface in Figure 60b. This fracture shows evidence of much higher levels of shear cracking damage, as seen in the shorter lengths over which the fracture surface runs in a straight line before turning at 45° to a different shear plane.

In Figure 61, these specimens with  $D_i$  values in excess of 500  $\mu\text{m}$  also tend to diverge from the trend exhibited by specimens with  $D_i$  less than 500  $\mu\text{m}$ . At the deeper notch depths ( $>500 \mu\text{m}$ ), the plastic zone is smaller than it would be if these specimens behaved as the others. Figure 61 also shows that like the previous case with glass spheres causing erosion, the 1 mm and 2 mm diameter chisel indentations show a consistent trend when the data with  $D_i > 500 \mu\text{m}$  are not considered. It should be noted that for specimens with  $D_i > 500 \mu\text{m}$ , shear cracking similar to Figure 59 was observed.



**Figure 57. 98-J78 Indentation from 2 mm Chisel without Chipping.** In the lower left, note the crack created by the shear stresses in the specimen. As shown in Figure 58, this crack coincides with the dark deformation bands in this region.



**Figure 58. Deformation Band Shape for Chisel Indentations without Chipping.** This schematic shows the general trend of the deformation bands observed on all chisel indented specimens which did not chip. Note that the center of the deformation band where the value of  $D_p$  was obtained is at the intersection of the darkest band and the lighter bands which complete the 'X' pattern.

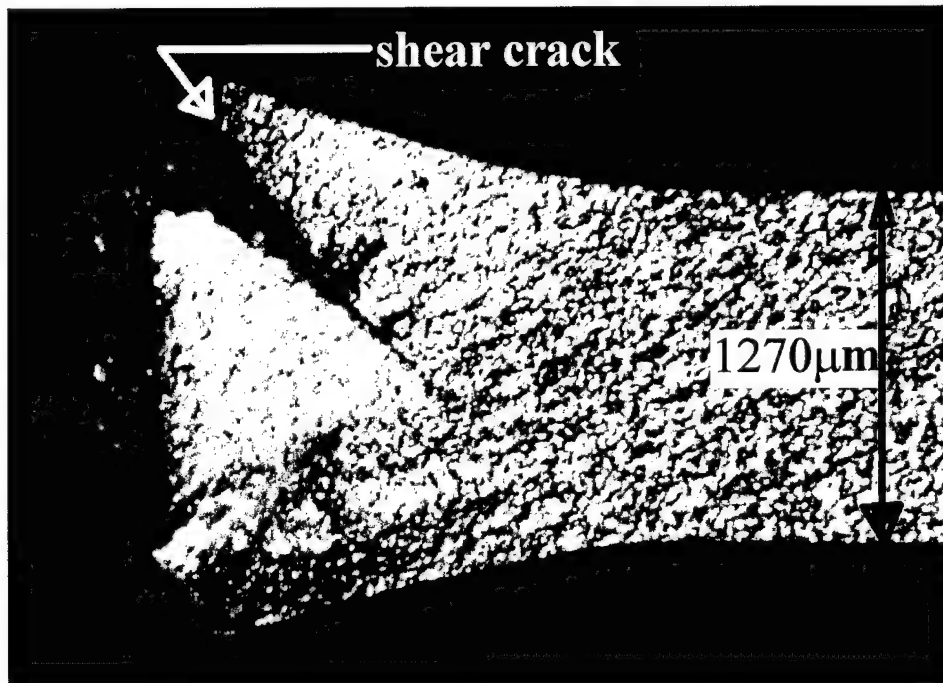
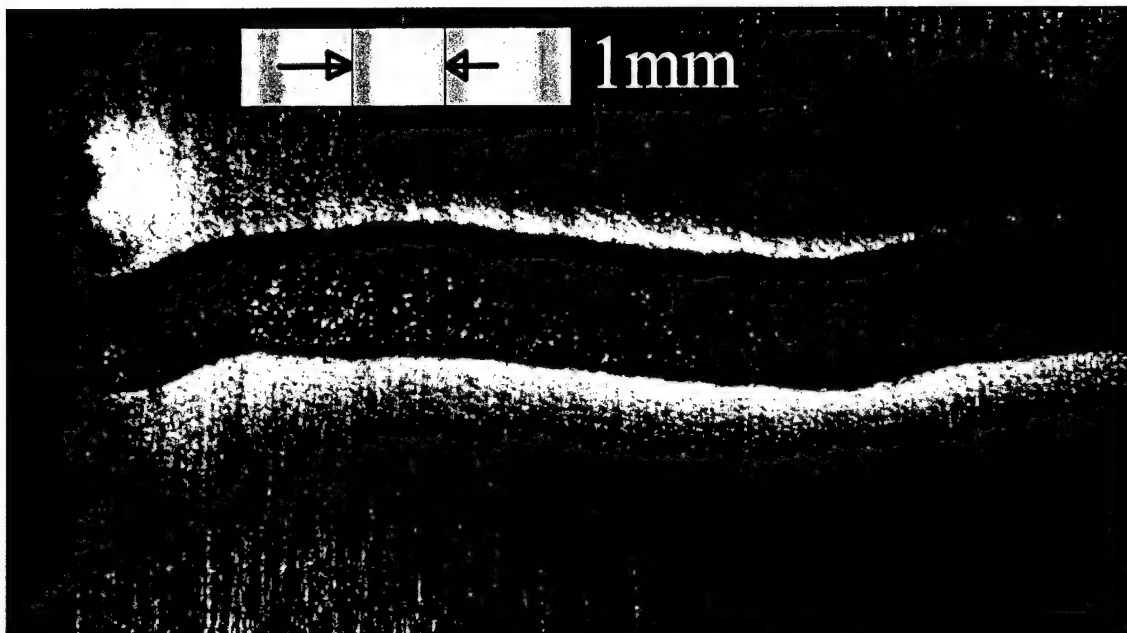


**Figure 59. Highly Developed Shear Cracking.** In this specimen, the shear cracking has progressed to the point where the fatigue crack follows the path of the shear cracks as it propagates through the damaged zone.

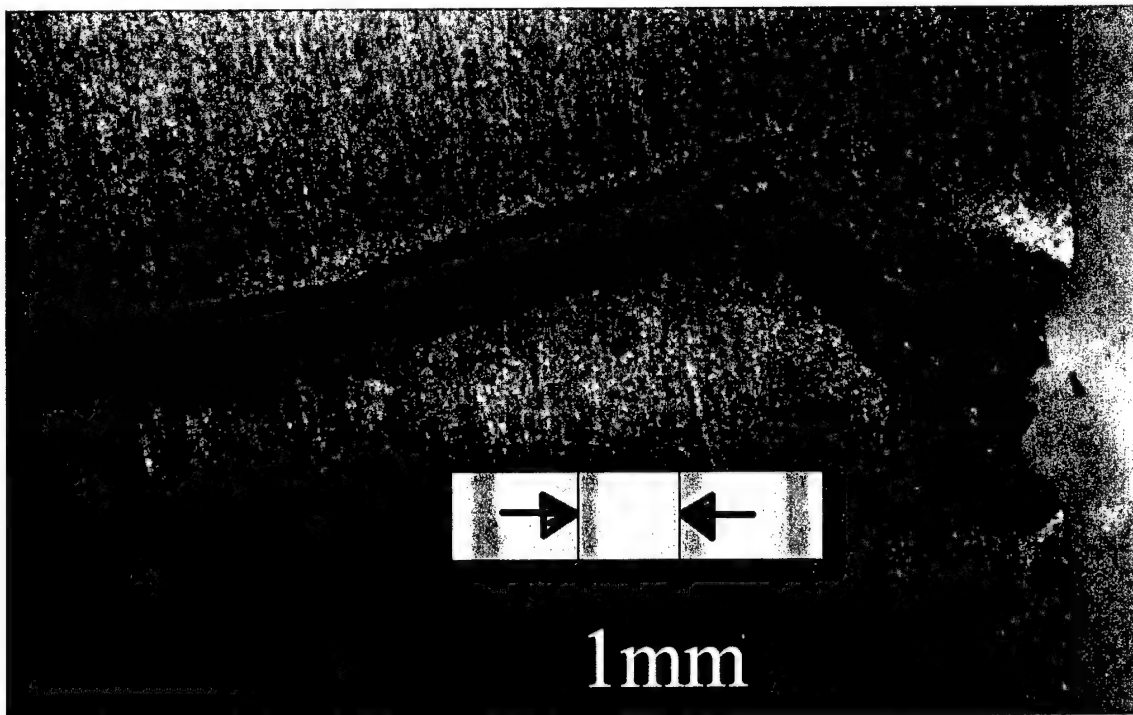


a)

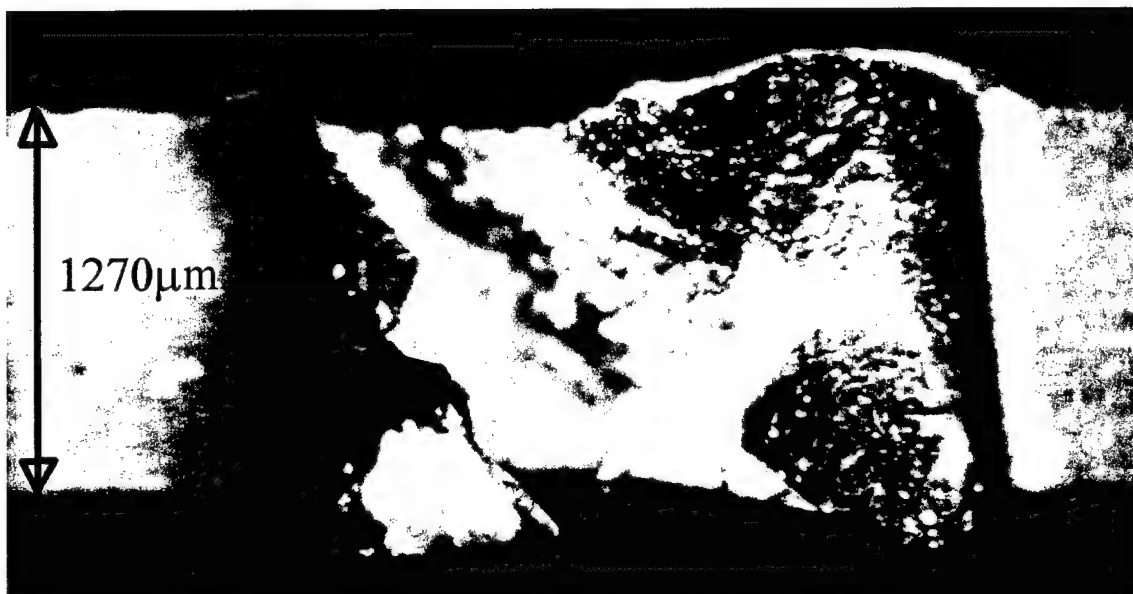


b)

**Figure 60. Ductile Fracture in Opposite Notch.** a) Side view. b) Edge-on view. In notches with  $D_i < 500 \mu\text{m}$ , the ductile failure, after crack propagation is finished, shows the type of  $45^\circ$  shear failure that would be expected in an undamaged specimen fractured by simple tension. The fracture surface crosses the unfatigued notch in a simple manner or bypasses it altogether, as shown here.



c)



d)

**Figure 60. Ductile Fracture in Opposite Notch (cont'd).** c) Side view. d) Edge-on view. When the unfatigued notch is indented more than 500  $\mu\text{m}$ , the shear cracking causes the fracture surface to follow the path of high damage.

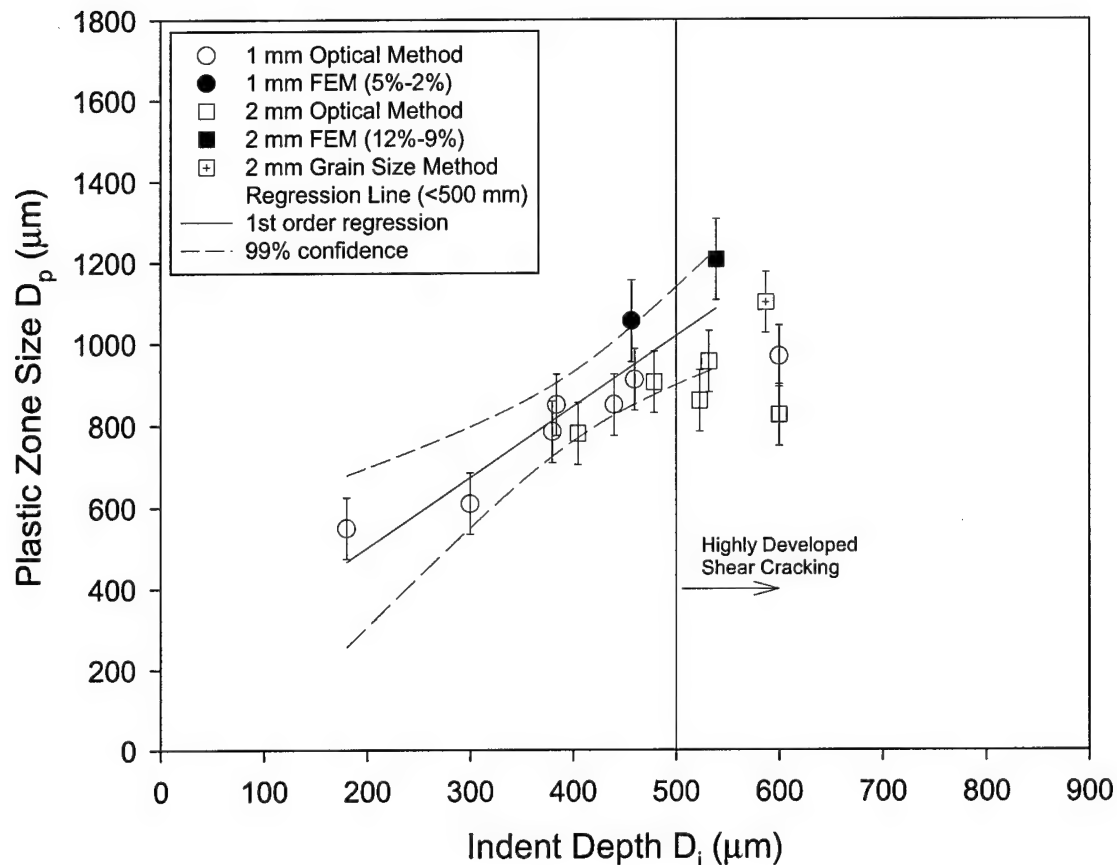


**Figure 61.  $D_p$  vs.  $D_i$  for Chisel Indentation without Chipping.** The FEM strain analysis, grain size measurement and optical method values for  $D_p$  are plotted against the crater depth  $D_i$ . The FEM model plotted here does not simulate the shear crack formation, and the predicted  $D_p$  continues along the monotonically increasing curve created by the data points below  $D_i = 500 \mu\text{m}$ .

*Chisel Indentations Causing Chipping.* The 5 mm chisel indentations which left craters less than 770  $\mu\text{m}$  deep were identical in nature to the 1 mm and 2 mm chisel indentations. In the case of indentations deeper than this, one leg or another of the shear cracking 'X' would grow through the thickness to the far free edge, and cause a chip of metal to be cleaved from the region of the crescent shaped bulge. Figure 62 shows an FEM simulation of a chisel bulged indentation, with the chipped region

highlighted. In this figure, the FEM model is half of the specimen, with symmetry about the XZ plane, which corresponds to the fatigue fracture surface (see Fig 12). As shown, the crescent chip begins in the notch root close to a free edge of the specimen where the chisel is in contact with the specimen. The chip progresses at a 45° angle through the thickness and meets the opposite free face at the location where the bulged region ends.

In Figures 63 through 65, this is shown in photographs of chipped and fractured specimens. While these figures show a specimen with the chip attached at one end of the crescent-shaped region, in many other specimens where the final indent depth was larger than about 770  $\mu\text{m}$ , the entire chip fell free during the indentation process. Figure 66 shows the fracture surface of such a specimen, where the complex shape of the cross section created by the chipping can be readily seen. In Figure 67, the location of the deformation bands and the manner in which  $D_p$  is measured in these specimens are shown.

For those specimens which had chips removed (either during the indentation or during the fatigue testing), the modified cross-sectional shape contained less material than it had previously where no chip formation occurred. This would cause a more complex stress distribution than that found in the specimens damaged by the other methods. As will be shown later, these specimens showed plastic zone sizes and fatigue strength reductions that were distinct from specimens tested with other damage conditions.

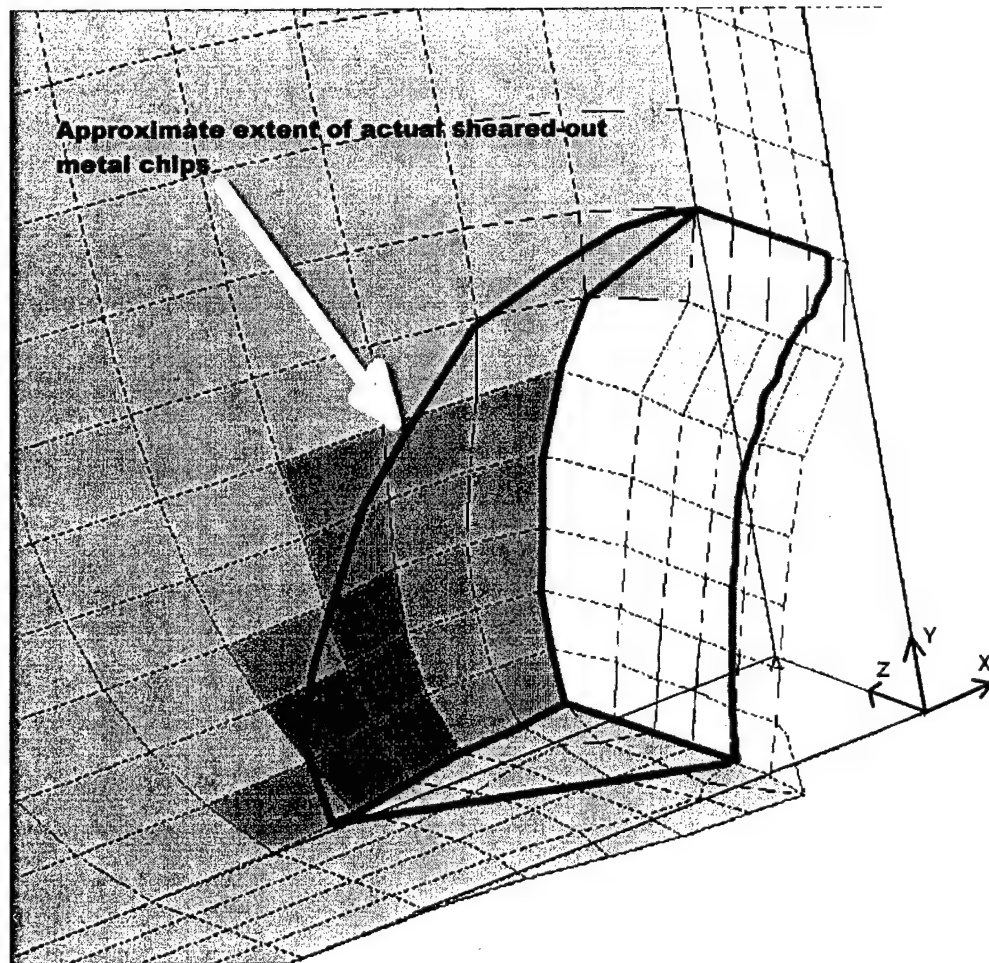


**Figure 62. FEM Simulation of Chipped Region.** An ABAQUS plot of deformed shape and outline of (half) a typical chip are shown. Compare to photograph of a chipped specimen in Figures 63 through 65.



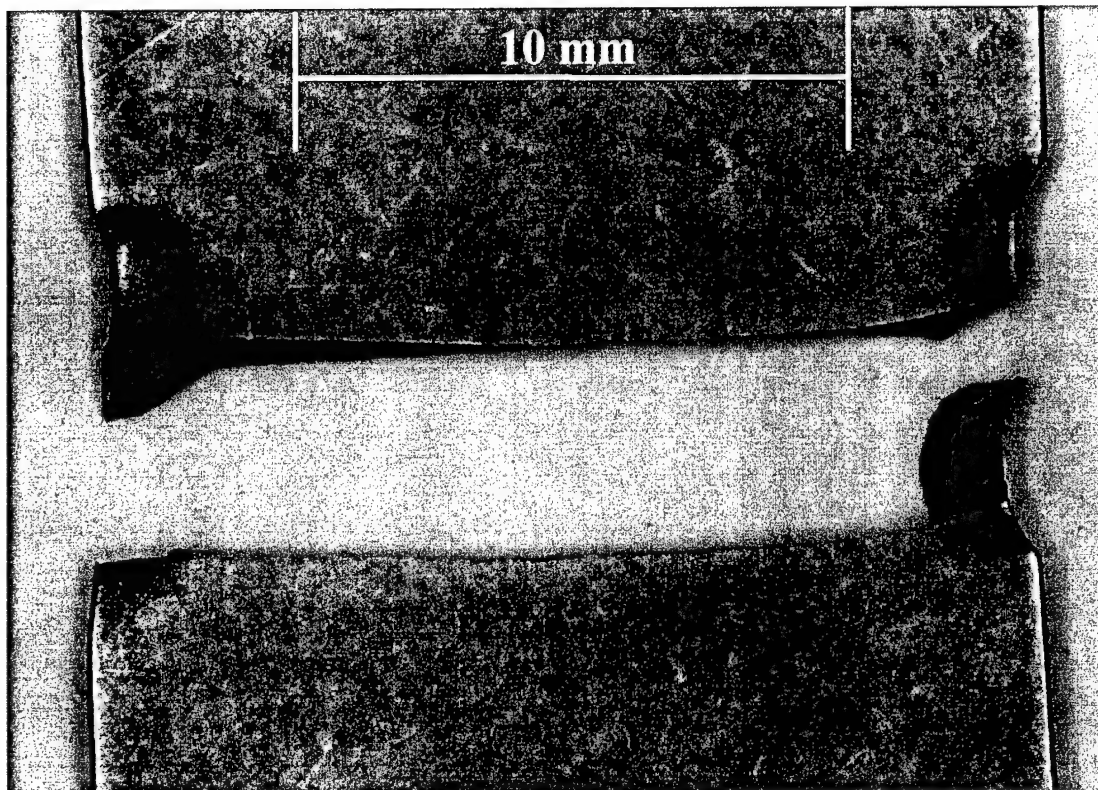


**Figure 63. Chipped Region from 5 mm Chisel Indentation.** Specimen 98-J60 is shown. The indent on the left did not create a chip. The one on the right hand side had a cracked chip which did not detach from the specimen. After the specimen was fatigue tested, the chip remained attached to the lower half.

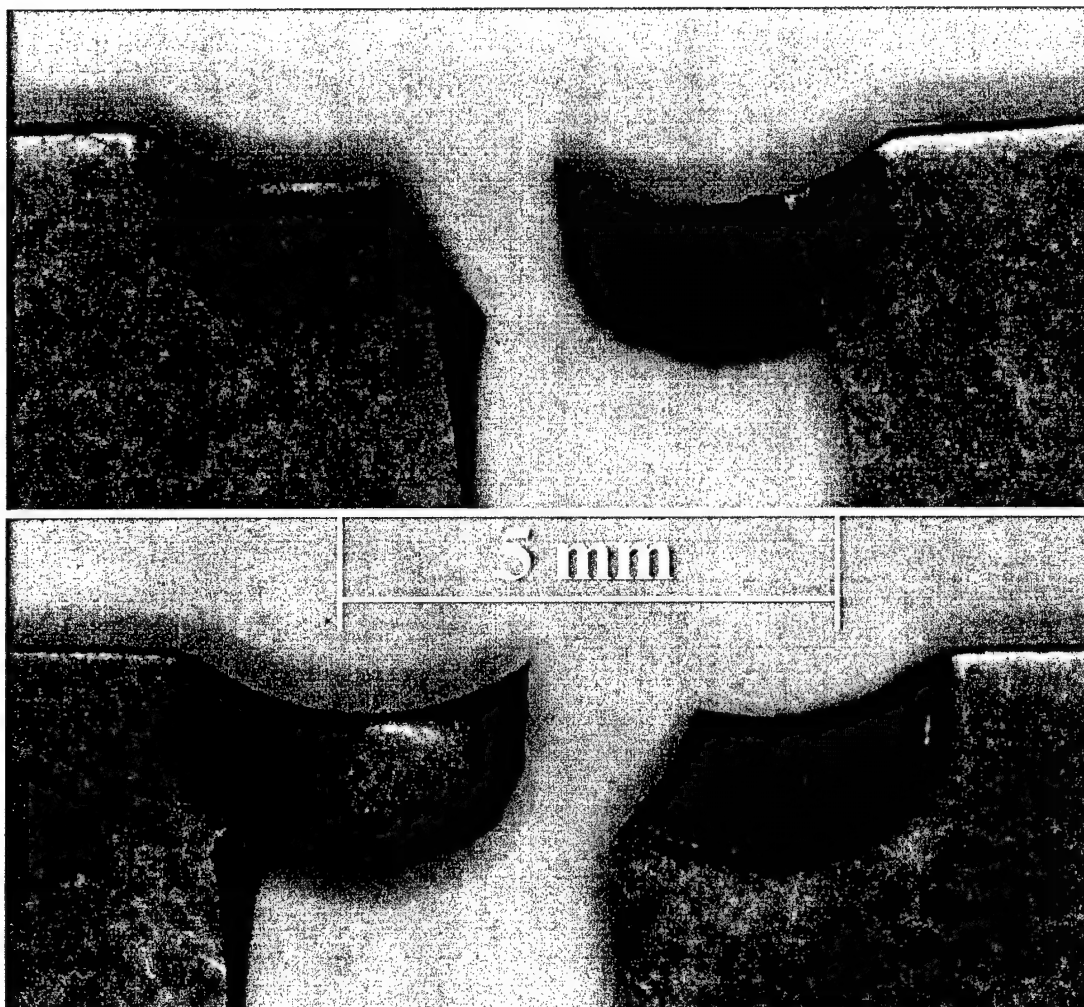


**Figure 64. Chipped Region from 5 mm Chisel Indentation - Close-up.**

Top - A closer view of the chipped indentation from Fig. 63 is shown. Bottom - The opposite face of the specimen.

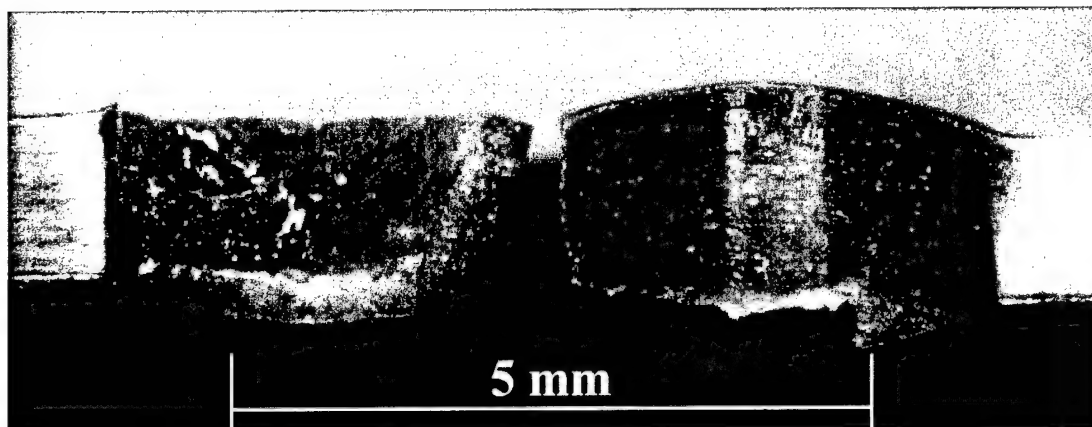


**Figure 65. Edge View of Chipped Specimen.** In this view, which is looking down from the top of Figure 64, the specimen edge that was deformed in direct contact with the tip of the 5 mm chisel, can be seen as the front face of the chip attached to the half of the specimen on the right. The left half of the specimen shows the cavity left behind by the chip's removal.

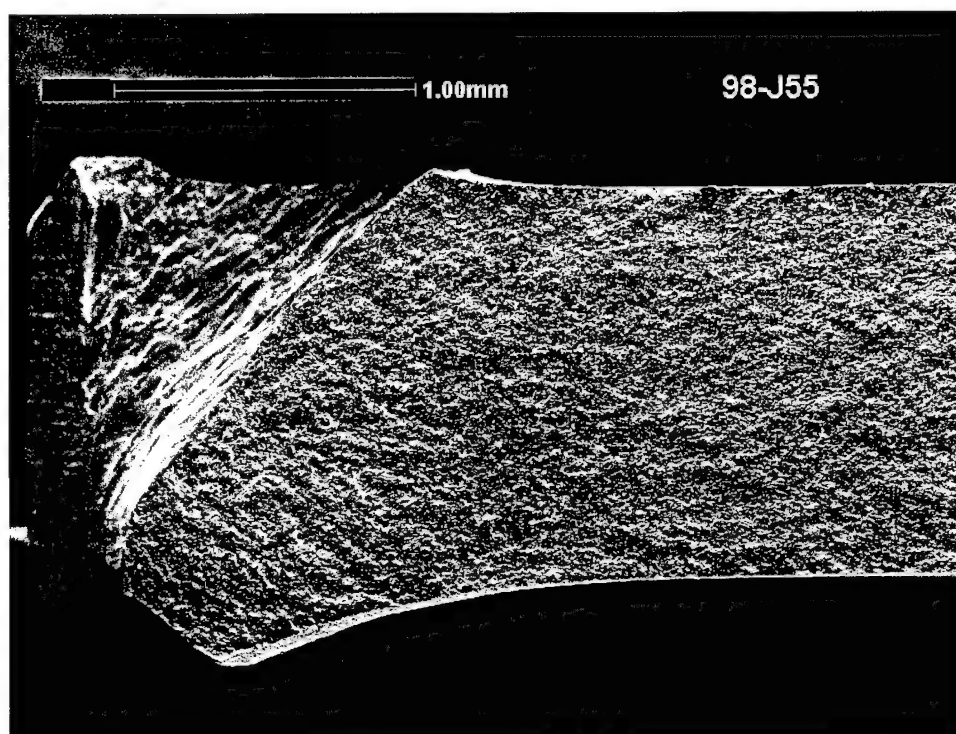


**Figure 66. Indentation from 5 mm Chisel with Chipping.** In specimen 98-J55, the entire chip came free. The cavity is the triangular region in the upper-left of the specimen cross-section.

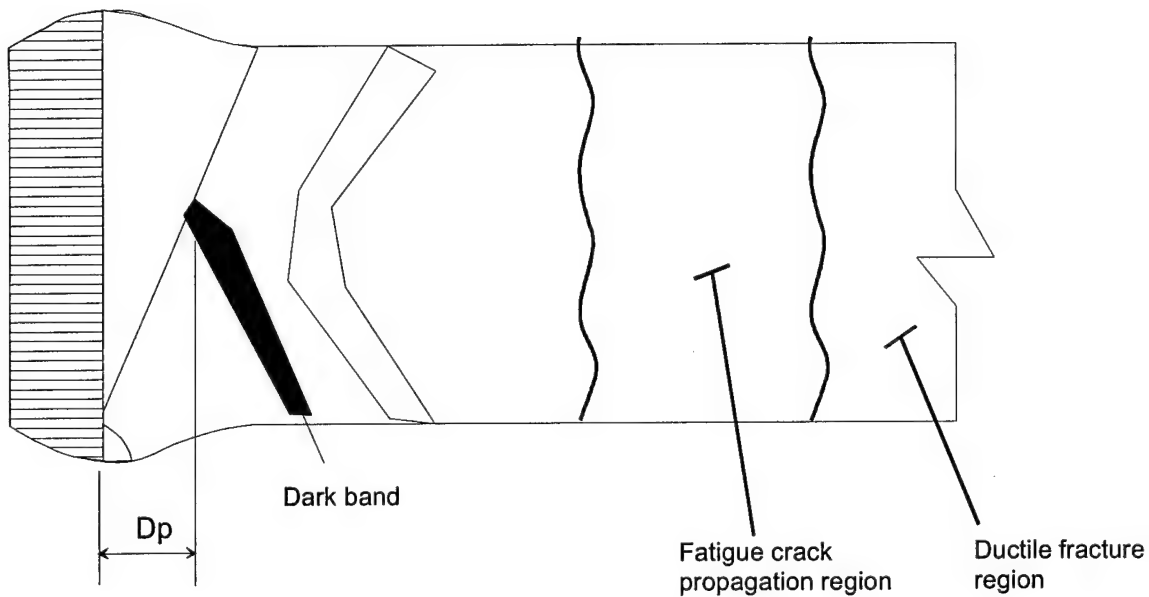


**Figure 67. Deformation Band Shape for Chisel Indentations with Chipping.** This schematic shows the general trend of the deformation bands observed on all chisel indented specimens which did chip. Note that there is no lighter band between the dark band at  $D_p$  and the notch root. This region is obliterated since the chip removed by shear failure cleaves along this path.

Finally, note in Figure 68, like the chisel indentations where chipping did not occur, there is a threshold  $D_i$  above which the trend of  $D_p$  to increase monotonically with  $D_i$  does not hold. In this case, the demarcation occurs when the indenter continues to be displaced past the point at which the chip falls free.

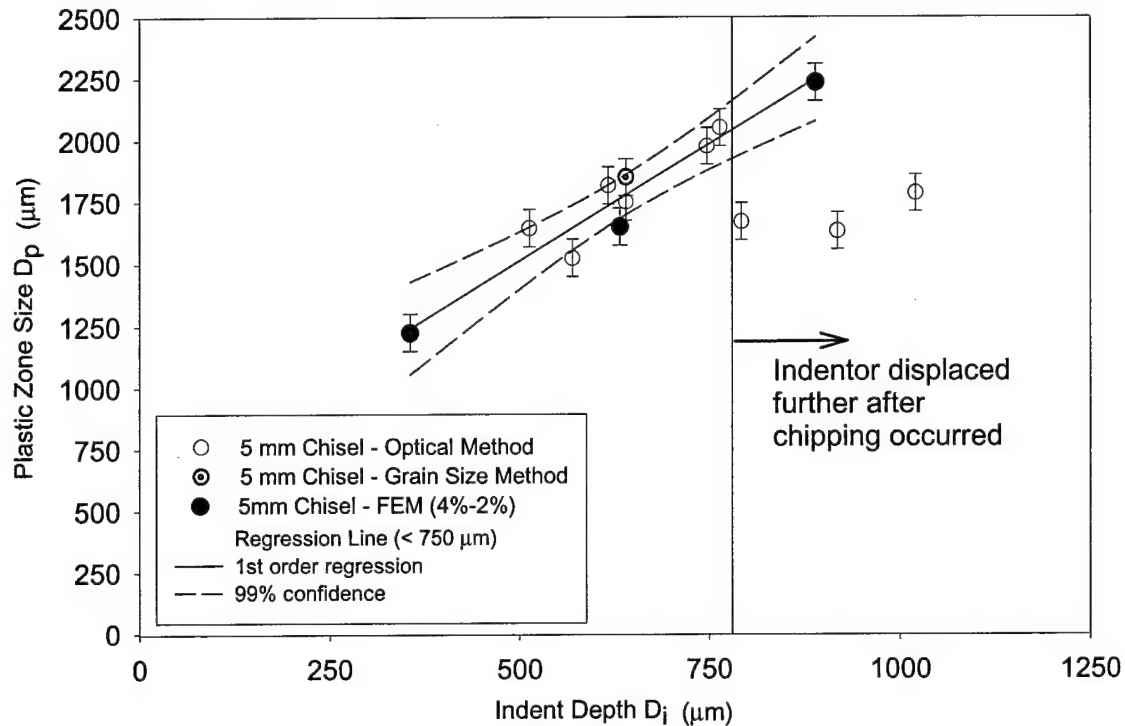
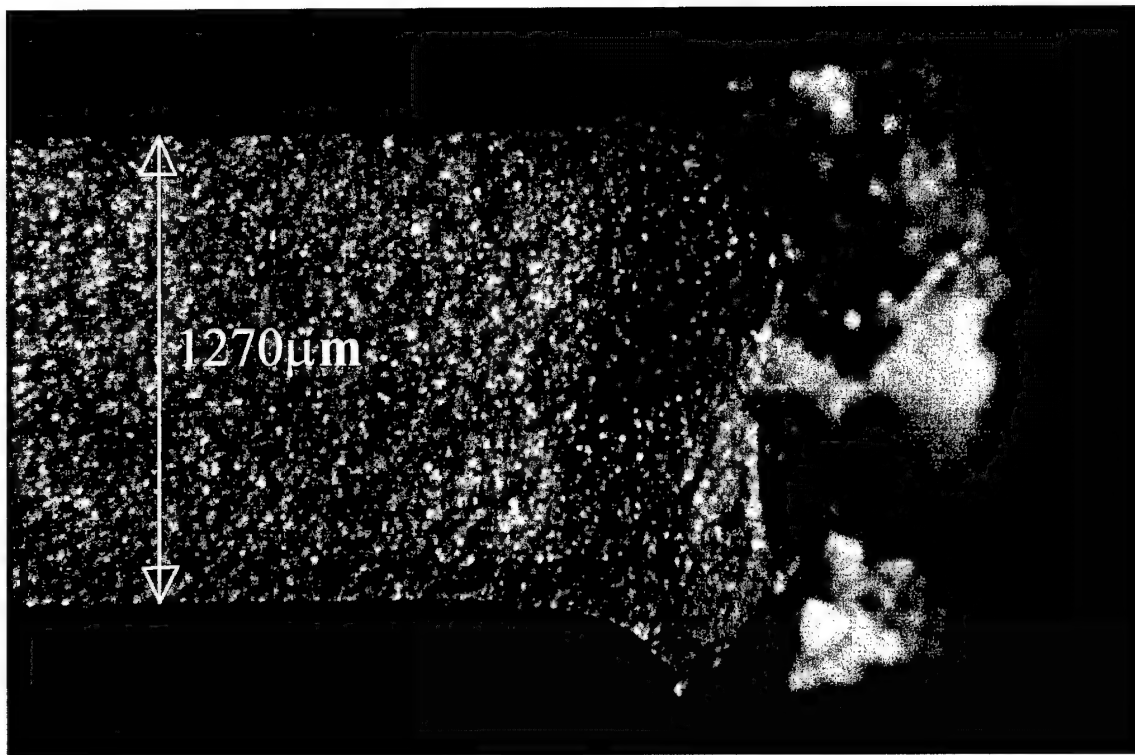


**Figure 68. Chisel Indentation with Chipping Damage Depth.** The FEM strain analysis, grain size measurement and optical method values for  $D_p$  are plotted against the crater depth  $D_i$ . As in Figure 61, the FEM model does not simulate the shear crack formation, and the predicted  $D_p$  continues along the curve created by the remaining data, whereas  $D_p$  measured optically falls off for specimens where the indenter continued to be displaced well after chip removal.

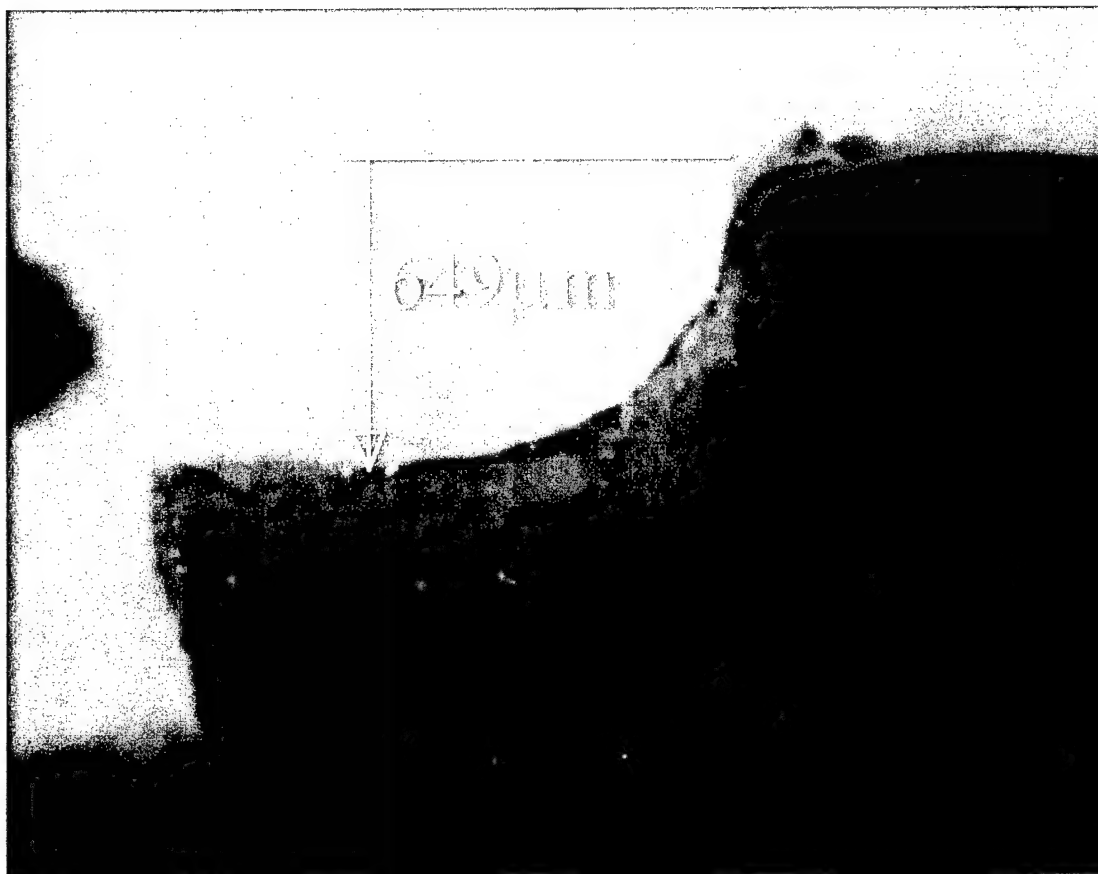
*Steel sphere impacts without chipping.* The 2 mm diameter steel sphere impacts created craters with characteristics similar to both glass spheres and chisels. Note in Figure 69a, the crater is deeper on the faces of the sample (top and bottom on the right in the figure) than it is in the center of the thickness. This is similar to the glass sphere samples and indicates that the steel sphere may be cleaving into two halves, causing the sphere to continue contact with the faces longer than it does in the center of the sample. However, like the chisel samples, the crater is nearly smooth, showing

no embedding of steel particles (Fig. 69b). In general, the 2 mm steel sphere craters were of comparable size to the 2 mm glass spheres in  $D_i$  and  $D_p$ .



a)

**Figure 69. Steel Sphere Impact without Chipping.** a) The fracture surface of specimen 98-Q17 is shown.



b)

**Figure 69. Steel Sphere Impact without Chipping (cont'd).** b) a side view of the crater.

Figure 70 shows schematically the major features of the fractured surfaces, especially the way the deformation bands follow the eroded crater contour. Figure 71 plots the plastic zone depth from optical observation and the Dytran finite element model.

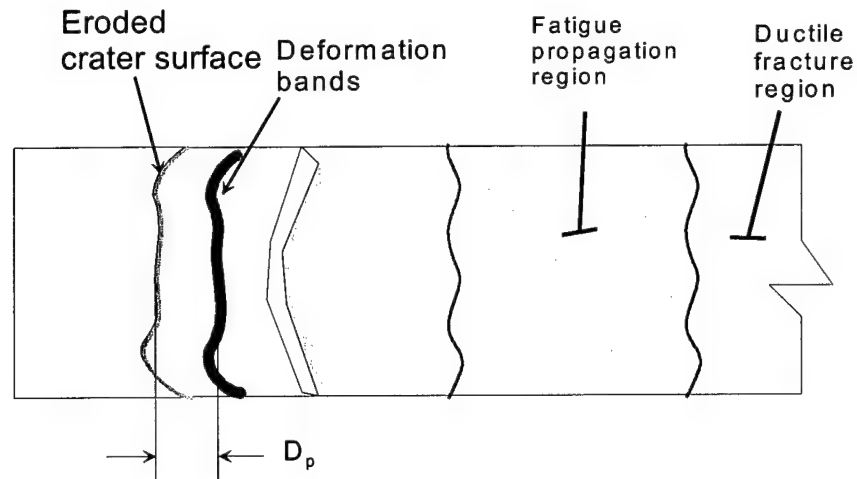


**Figure 70. Deformation Band Shape for Steel Sphere Impacts without Chipping.** This schematic shows the general trend of deformation bands observed on the steel sphere impacted specimens that did not chip.

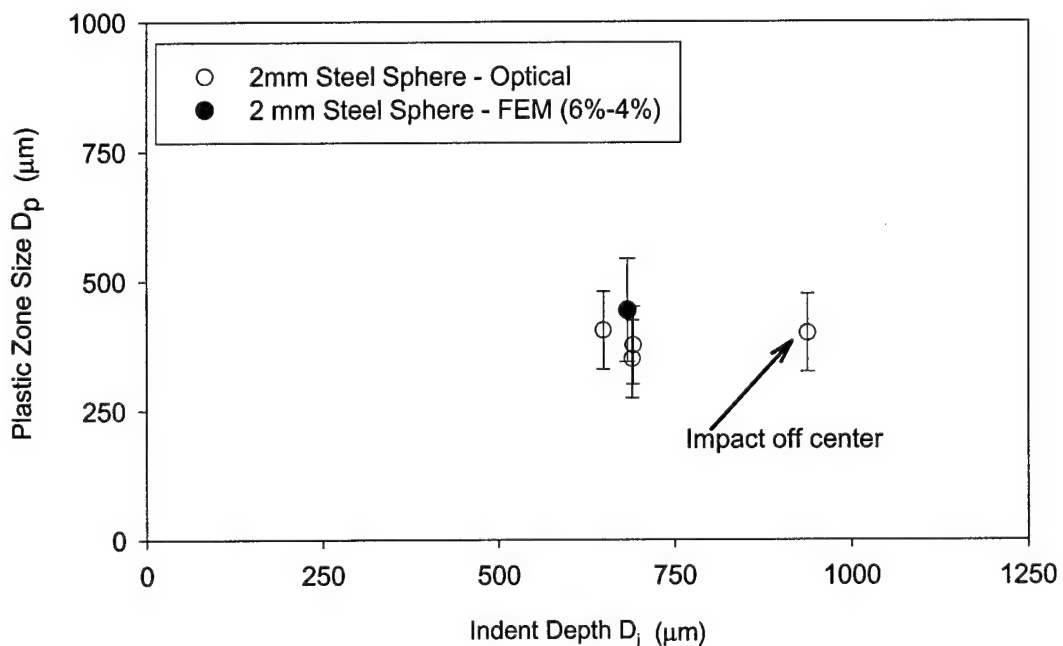


**Figure 71. Steel Sphere Impacts without Chipping Damage Depth.** The FEM strain analysis and optical observation values for  $D_p$  are plotted against the crater depth  $D_i$ . The indent and plastic zone depths were more consistent than the glass impacts.



*Steel sphere impacts causing chipping.* The impact from 4 mm diameter steel spheres created craters very similar to the 5 mm chisel indents with chipping. As shown in Figure 72, a 45° chipped region was removed past the root of the crater. The photographs in Figure 73 also illustrate this clearly.

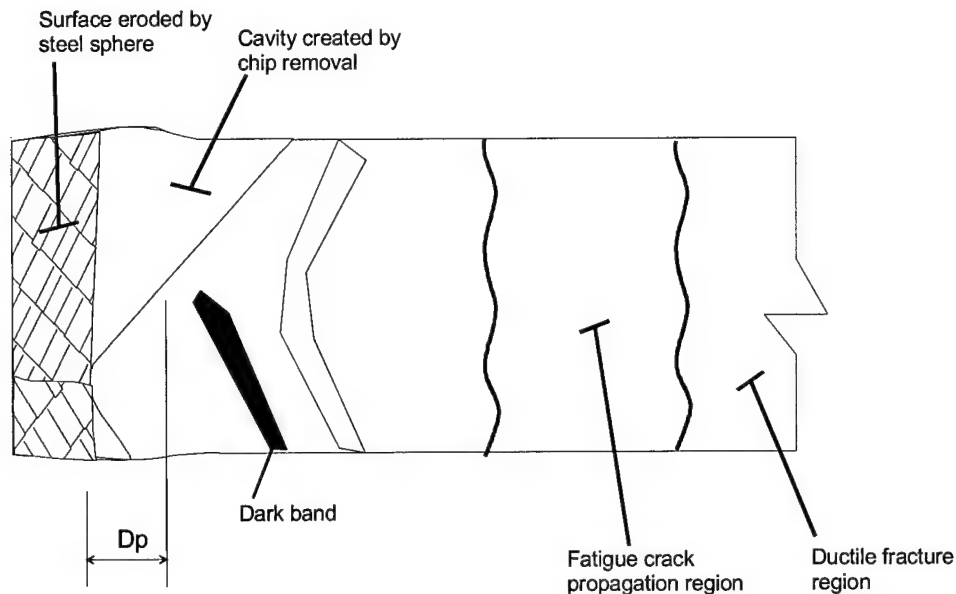
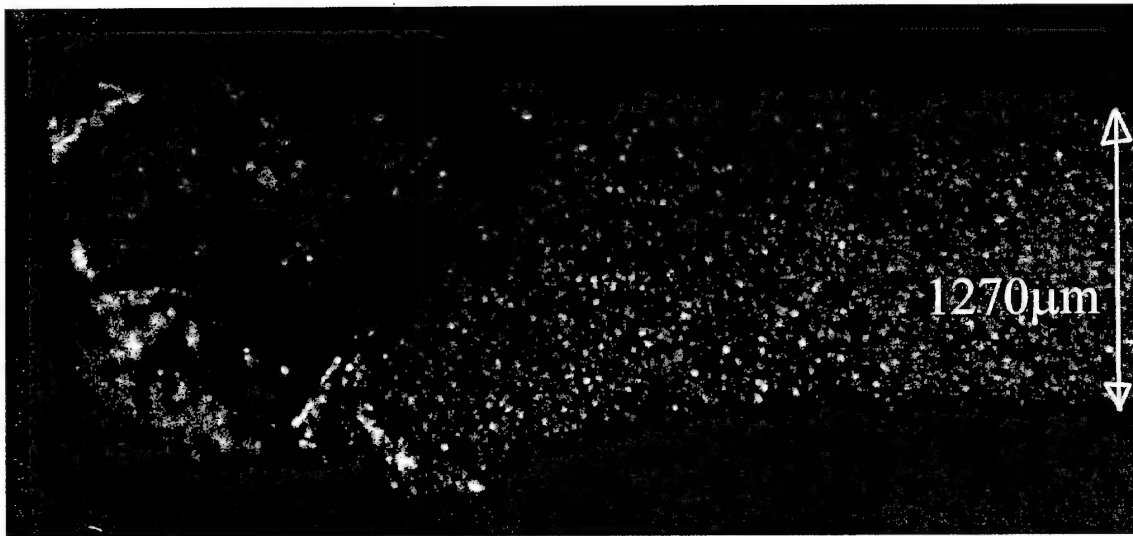


**Figure 72. Deformation Band Shape for Steel Sphere Impacts with Chipping.** This schematic shows the general trend of the deformation bands observed on all chisel indented specimens which did not chip.

Because of this shape and deformation similarity, the stress and strain distribution would be expected to resemble more that of the chisel chipped specimens. As will be shown in Chapter VI, the fatigue behavior of these specimens was more similar to the chisel indented specimens with chipping damage than to those with other forms of damage.

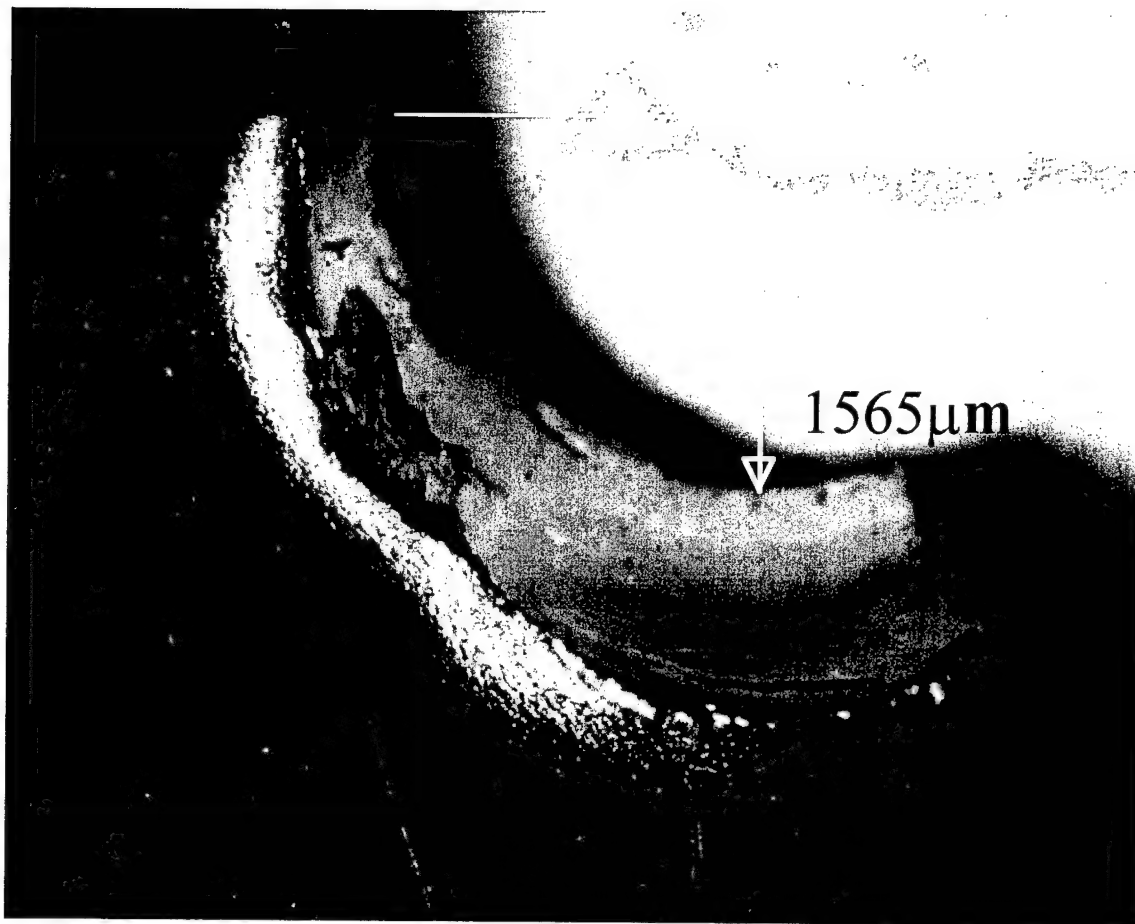
Only a few specimens were impacted by steel spheres, and at only one condition (see Table 2). Despite this, the indent depths varied by more than 500  $\mu\text{m}$  (Figure 74).

The plastic zone size as obtained by the optical measurement method was constant (within the uncertainty of measurement), making the total damage depth vary by  $\sim 500 \mu\text{m}$ .



a)

**Figure 73. Steel Sphere Impacts with Chipping** a) Fracture surface of 98-Q14. Note the strong similarity to Figure 66, the 5 mm chisel indentation with chipping.



b)

**Figure 73. Steel Sphere Impacts with Chipping (cont'd).** b) a side view of the chipped side of a crater from 98-Q14, damaged by a 4 mm steel sphere.

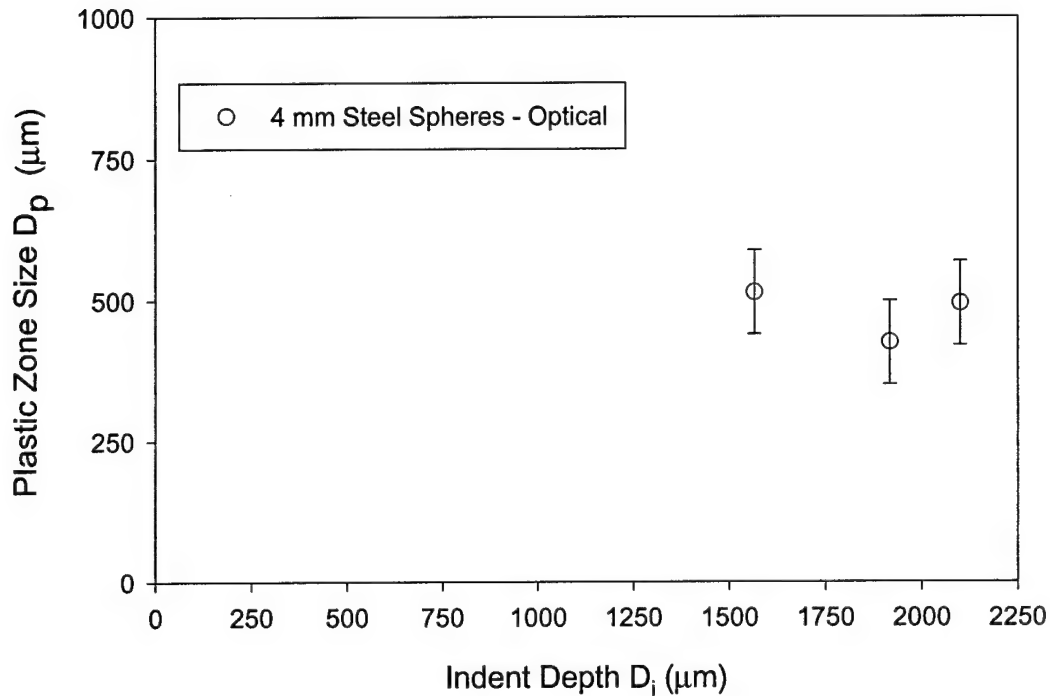


**Figure 74. Steel Sphere Impacts with Chipping Damage Depth.** Only optical observation values for  $D_p$  are available. Note the consistent plastic zone size over a rather large ( $\sim 500 \mu\text{m}$ ) range of indent depths.

*Sheared notches using chisel in transverse direction.* Several samples had notches sheared out by the transverse 2 mm diameter chisel. This method allowed precise control over the depth of the crater, but the plastic zone size was essentially identical on all specimens. The plastic zone resides behind the root of the sheared notch (Fig. 75). As mentioned previously, the optical indication of this region did not show up as a dark band. Rather the damage depth was taken to be the edge of a brighter zone which coincided with the out-of-plane displacement on the free face of the specimen opposite to the initial position of the chisel (Fig. 76a). The notch was smooth and uniform, looking nearly like a feature created by a machine tool (Fig. 76b).  $D_p$  evaluated by this criterion was nearly constant across the range of notch depths.

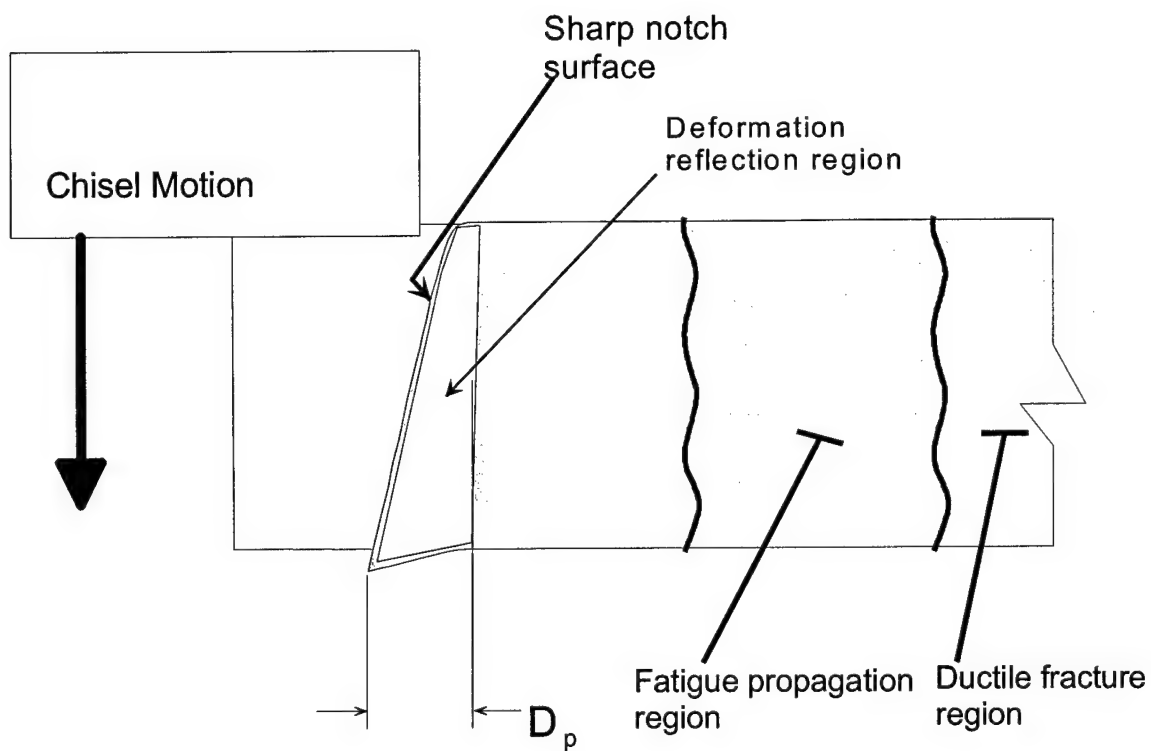
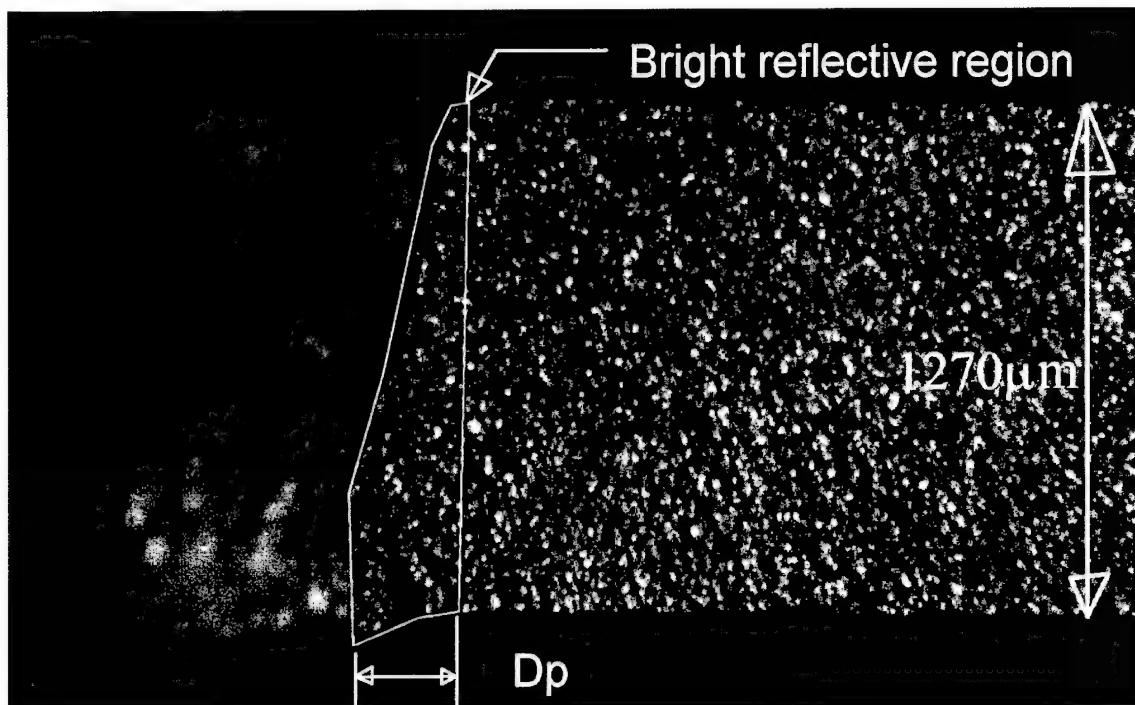
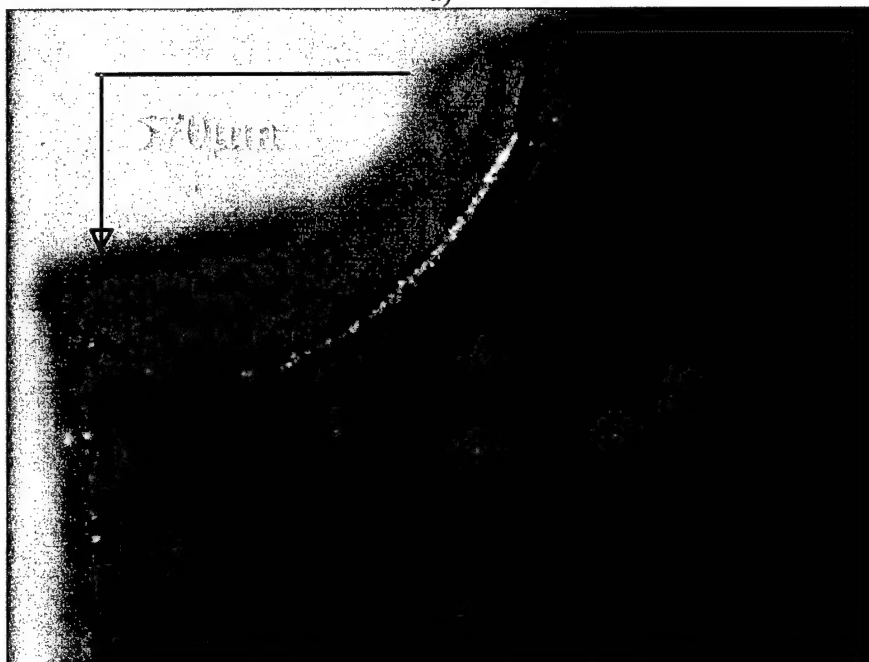


**Figure 75. Deformation Band Shape for Chisel Sheared Notches.** This schematic shows the general trend of the highlighted region observed on the specimens notched by the transverse chisel.



a)



b)

**Figure 76. Chisel Sheared Notch.** a) Fracture surface of 98-Q21. Note that the notch depth  $D_i$  is not uniform, but varies slightly across the thickness of the specimen. b) Side view of 98-Q21.

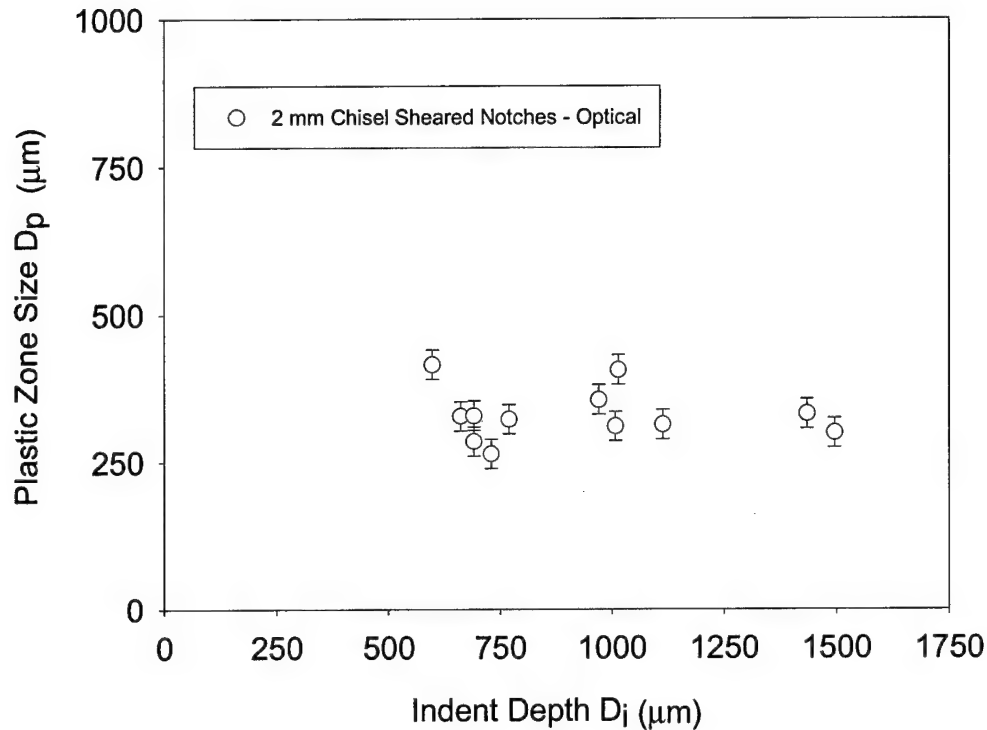


**Figure 77. Chisel Sheared Notches Damage Depth.** The optical observation values for  $D_p$  are plotted against the crater depth  $D_i$ . As one would expect, there is nearly no variation in  $D_p$ , which is essentially constant with the indent depth  $D_i$ . Note that the uncertainty band on  $D_p$  is less than that for the deformation band measurements.  $D_p$  for this mechanism is primarily based upon the intersection of the notch root with the out of plane bulging on the bottom face of the specimen, as shown in Figure 76.

### Summary

Seven distinct damage mechanisms were observed from the four FOD simulation techniques used in this study. The plastic zone depths which can be observed by optical or grain size measurement or predicted by FEM models of the damage are plotted in Figure 78a as a function of the visible notch depths where no chipping or extensive cracking occurred while Figure 78b shows all the cases inclusive of chipping or cracking. The relationships observed can be summarized as follows:

The transverse chisel shearing technique generated a uniform plastic zone size regardless of the depth of notch generated. This provided the ability to generate total damage depths  $D_t$  over a large range.

The chisel indentations created a plastic zone size which is essentially proportional to the indent depth. The 1 mm and 2 mm chisel indentations lie on a single curve. The 5 mm chisel indent data lie on their own curve with a different slope. Both curves show a critical point at which the plastic zone size ceases to increase with increasing indent depth. This point seems to coincide with a marked increase in the severity of the shear banding and/or cracking in the damaged region.

The glass sphere impacts had less variation in notch depth, which isn't surprising given that the impact energy available was fixed by the sphere weights and velocity. The variation in plastic zone size had more range, but the 2 mm and 5 mm glass spheres together create a single curve describing the increase in  $D_p$  with increasing  $D_i$ .

The steel sphere impacts that didn't cause shear chipping all had nearly the same value of  $D_i$  and  $D_p$ . These values lie within the curve for the 2 mm glass spheres.

The 4 mm steel spheres that did remove a sheared chip had a constant plastic zone depth, but indent depths varied more than 500  $\mu\text{m}$ . The appearance of these specimens has many similarities in shape and texture to the 5 mm chisel indentations.



Evaluating the plastic strain by measuring the change in average grain size was not demonstrated to work well for Ti-6Al-4V. By polishing and etching a surface within a highly strained specimen and measuring the distances at which the grain boundaries cross a path through the specimen from the plastically strained zone to an unstrained zone, the plastic strain was deduced as the average difference between the size of each strained grain and the average size of the unstrained grains in the same orientation. However, because of the large variation in grain sizes in the undeformed material used in this study, a large amount of uncertainty remained in the strain computed this way.

The surface exposed after fatigue fracture on specimens damaged by simulated FOD exhibited nonuniform reflectivity characteristics under highly polarized light. This reflectivity was developed into a novel method to directly observe the demarcation between the unstrained material and that material which was strained to a certain level of strain, as described in Table 5. This demarcation was found to coincide with shear bands created in the plane of the fracture surface. The distances to these bands were also compared to finite element models of the plastic strain distribution. The damage size obtained by all three techniques agreed within each measurement's limits. The distance from the surface of the specimen to this damage level was taken as the total damage depth.

Despite the wide range of damage mechanisms seen, the relationships between the notch depth and the size of the plastic damage zone fell into only a few trends. The

glass sphere impacts and the steel sphere impacts which did not cleave material from the notch resolved into a common monotonically increasing trend. The chisel indentations which did not cleave material from the specimens also share a common, nearly linear trend. Chisel indentations which do cleave material from the specimens also increase linearly when the indentation depth is less than 770  $\mu\text{m}$ . Above this, increasing depth affects plastic damage zone size less, and the trend follows a different, flatter slope. The notches sheared by the transverse chisel had a plastic damage zone size independent of the notch depth. The steel spheres which cleaved material from the specimens also appear to have a constant plastic zone size, although the number of data points for this mechanism is small.

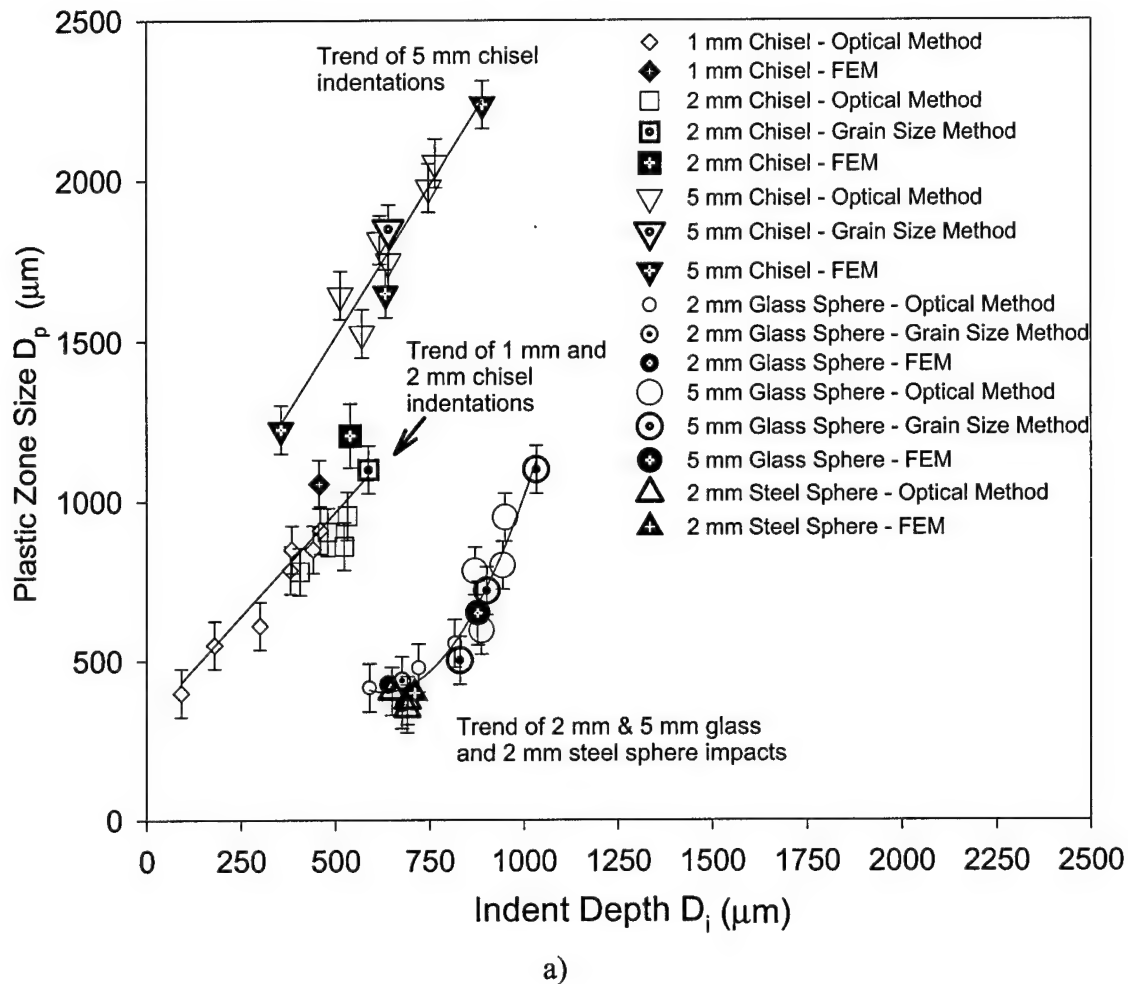
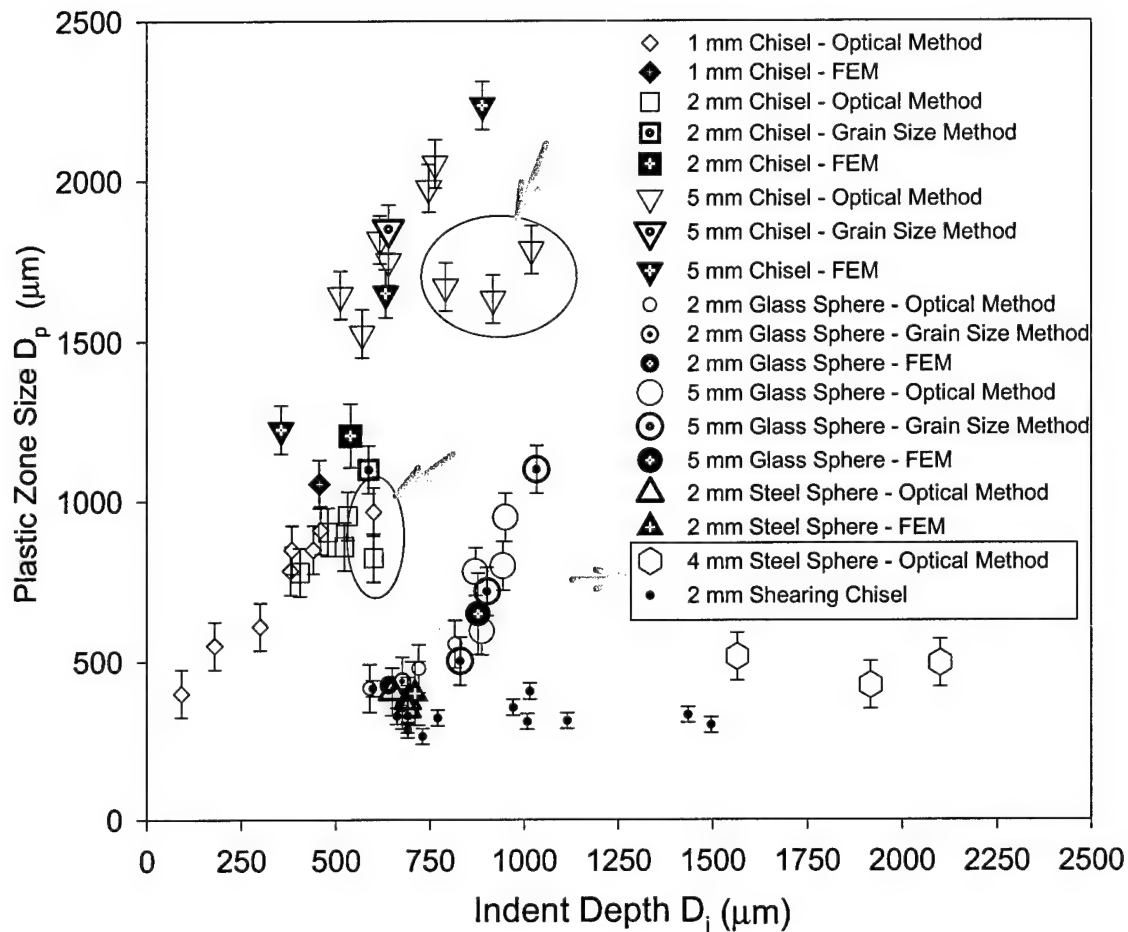


**Figure 78. Plastic Zone Size as a Function of Indent Depth.** a) Three distinct relationships can be discerned. The glass spheres which caused erosion and steel spheres which did not chip together create a concave up parabolic relationship. The chisel indentations create a plastic zone size which is essentially proportional to the indent depth, so long as the shear cracking/chipping threshold is not included at each chisel diameter. When this threshold is crossed, the plastic zone size is lower than the maximum  $D_p$  possible when the indent depth is just below the critical value.



b)

**Figure 78. Plastic Zone Size as a Function of Indent Depth (cont'd).** b) The gray arrows point to the data points filtered from Fig. 78a) because they exceeded the normal behavior for their damage mechanism. Another gray arrow points to the legend entries for the two damage mechanisms not included in Fig. 78a). These mechanisms are the shearing chisel and 4 mm steel spheres which created chipping. These two techniques created essentially constant plastic zone sizes behind the indent depth.

## ***V. FINITE ELEMENT ANALYSIS***

The damage created by the sphere impacting and chisel indentation FOD simulation techniques was modeled using finite element analysis. The shear failure behavior of Ti-6Al-4V under the conditions of the transverse chisel shearing damage mechanism is complex, and accurately modeling this damage mechanism was beyond the scope of this study.

To numerically simulate the impact and indentation damage, an appropriate model was made of the Ti-6Al-4V sample using material properties generated by AFRL/MLLN (4) and Allison Advanced Development Company (AADC) (78). Boundary conditions appropriate to the damage and fatigue loading were defined and initial conditions that represented conditions during the FOD simulation were applied. Application of these conditions, details of which follow in subsequent sections, created a state in the model which simulated the Ti-6Al-4V specimens' response to chisel indentations and impacts from glass and steel spheres. Next, the model was subjected to new loading conditions that represented the tensile loads applied to the specimens during HCF testing. This produced a new stress state in the specimen from which the material response could be predicted.

The FOD simulation conditions tested fall into two classes of events as far as FEM codes are concerned. The glass and steel sphere impacts are dynamic events, where the velocity with which the sphere travels can be assumed to play a significant part in

the interaction. The chisel indentations occur so slowly that dynamic effects may be assumed to play no role in the end state -- a condition referred to as 'quasi-static'.

These two distinct regimes are best treated differently numerically (15).

### **Material Models and Boundary Conditions**

The model of the specimen was made using the material properties listed in Table 6 and Figure 79, which shows a stress-strain curve for Ti-6Al-4V that is representative of those provided by AFRL/MLLN (4) and AADC (78). The points plotted on the curve show the discrete values entered into the FEM models of the specimen.

Figure 80 shows the mesh and symmetry used to model the specimen. Two planes of symmetry were introduced. The XZ plane is a plane of symmetry if the notch created by the chisels and spheres is assumed to be symmetric. The YZ plane is a plane of symmetry if the assumption is made that creating the two simulated FOD notches on each specimen at the same time is identical to creating them sequentially. This was obviously not quite correct in the case of the chisel indentations, as Figure 19 shows that only one-third of the specimen extended above the supporting plates. Similar discrepancies exist in this assumption for the sphere impacts. Preliminary cases of the numerical models indicated that the region of interest around the notches was localized enough that this boundary condition played no role in the response near the damaged notch, and since this symmetry is correct for the subsequent loading steps, the boundary conditions were kept the same during the entire simulation process. The models consisted of a  $\frac{1}{4}$  model of the Ti-6Al-4V sample, using the two planes of

symmetry, and a  $\frac{1}{2}$  model of the steel chisel or the sphere about the XZ plane. The center of the whole sample is the origin of the finite element model.

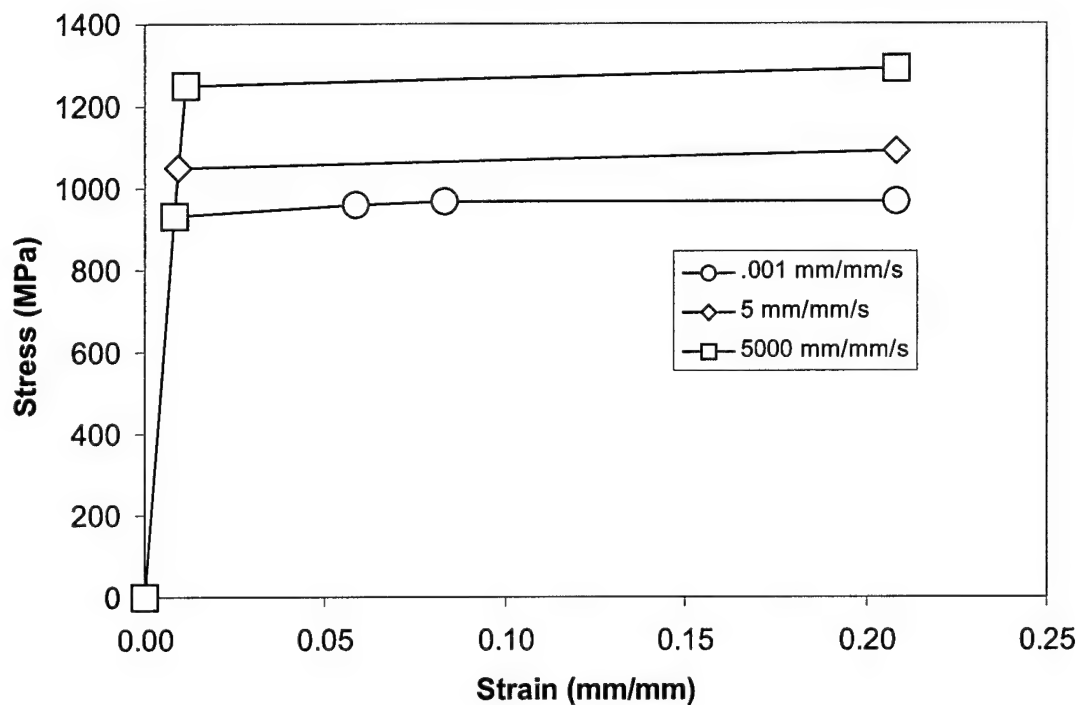
The elements used in the majority of the model were 8-noded linear hexahedrons (also known as 'brick elements') (1; 48; 47). The 4-noded tetrahedral elements were used to transition the fine mesh in the area of interest into the remainder of the specimen with a much coarser mesh.

Table 6. Material Property Inputs to FEM Codes

Property	Ti-6Al-4V (3; 70)	Steel (13)	Glass (13)
Young's Modulus (MPa)	1.125E+05	2.000E+05	7.400E+04
Plastic Behavior	See Figure 79	None	None
Poisson's ratio, $\nu$ (elastic)	0.33	0.3	0.20
Poisson's ratio, $\nu$ (plastic)	0.50*	Not Used	Not Used
Yield stress (MPa)	950	1620	999 (comp'n) 48 (tension)**
Ultimate strain (mm/mm)	0.2000	0.0600	0.0135 (comp'n) 0.0007 (tension)**
$\rho$ (kg/m <sup>3</sup> )	4,500	8,170	2,480
<p>* <math>\nu = 0.5</math> is assumed by the codes for plastic behavior and is not user adjustable if isotropic yielding is selected. It enforces the assumption that plastic deformation creates no volume change.</p> <p>** Glass is assumed to be brittle, and the ultimate stress is taken to be the same as the yield stress. Glass exhibits distinct fracture stresses in compression and tension.</p>			

The contact region had a mesh size that began at 254  $\mu\text{m}$  (0.01") between nodes and increased gradually to larger values far away. This size in the region of interest was

picked as a result of numerical tests conducted to determine the mesh refinement necessary to give good agreement for stress concentration factors (SCF) around smooth notches with tabulated theoretical SCFs. A nodal spacing of  $254\text{ }\mu\text{m}$  ( $0.01''$ ) was found to be adequate. The details are in Appendix F.



**Figure 79. Stress-Strain Curve for Ti-6Al-4V.** This data was generated by AFRL/MLLN at strain rates between 0.001 (mm/mm)/sec and 5 (mm/mm)/sec (4) and by AADC at higher strain rates (78). The 0.001 (mm/mm)/sec curve was used for the quasi-static models. The dynamic models used values interpolated from the three curves.



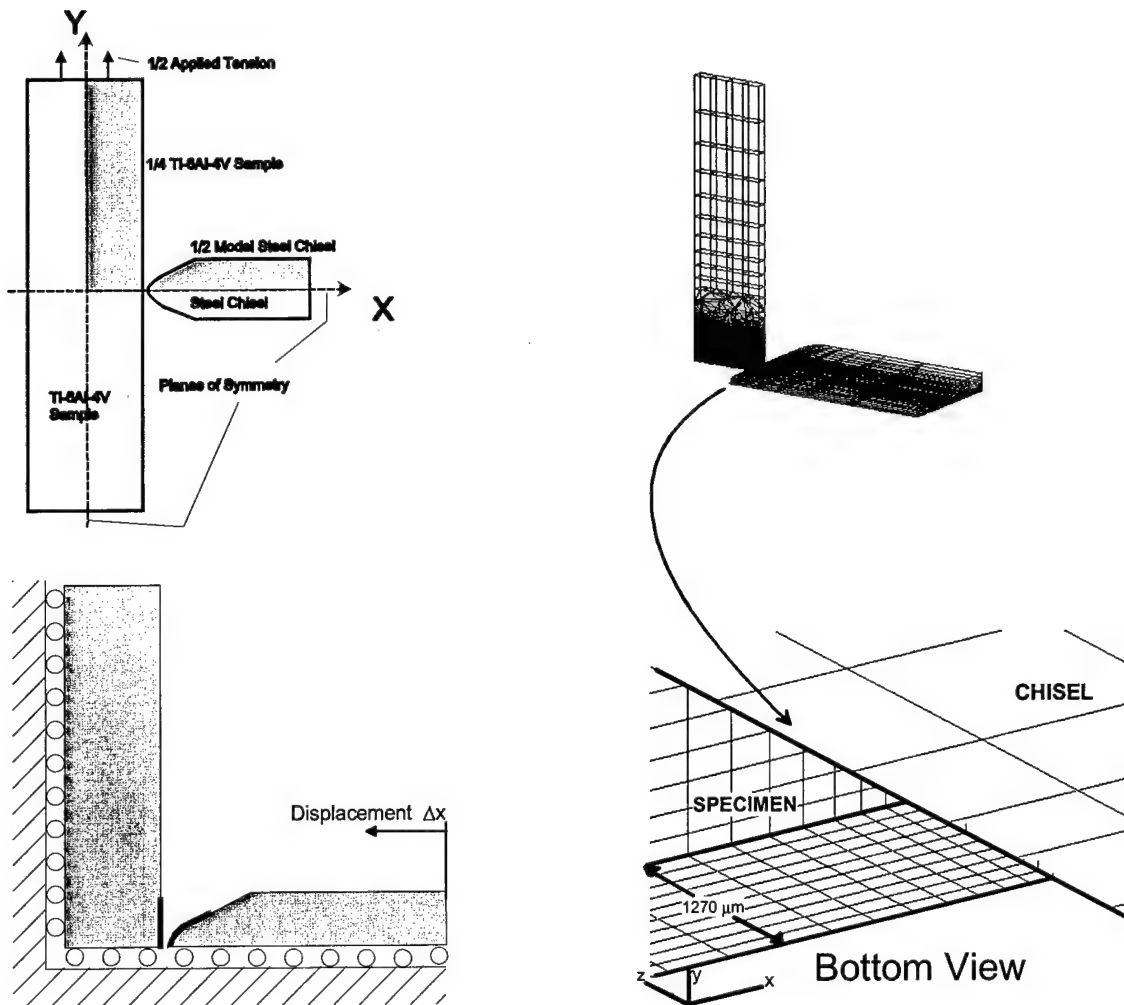


**Figure 80. Finite Element Model of Ti-6Al-4V Specimens.** In the upper left is a diagram of the specimen, showing the  $\frac{1}{4}$  region actually modeled and a  $\frac{1}{2}$  model of a chisel. In the lower left is a description of the boundary conditions used, and the region of contact is highlighted. On the right are views of the mesh used.

### Quasi-static Model

The quasi-static chisel indentations were modeled using the implicit commercial FEM package ABAQUS v5.8. ABAQUS was chosen because it was considered to be the most capable for handling large material and geometric nonlinearities (1; 10; 78). These nonlinearities occur both in the geometry of the chisel indentations and in the material properties of Ti-6Al-4V, which flows almost perfectly plastically.

Consequently, large deformation theory and an elastic-plastic material were used in the analysis. Full integration of the element stiffness matrices was used -- i.e., sufficient Gauss integration points were used to exactly integrate quantities in the undeformed elements (15:188; 47:14.1).

Experimental observation of the steel chisels used to indent the samples showed no signs of wear or deformation on chisel tips which had been properly quench hardened. Based upon this observation, a simple linear elastic model was chosen for the steel chisel. Three models of the steel chisel were made, one each with the equivalent of 1 mm, 2 mm and 5 mm diameters (Figs. 81-83). The same model of the sample was used in all three cases.

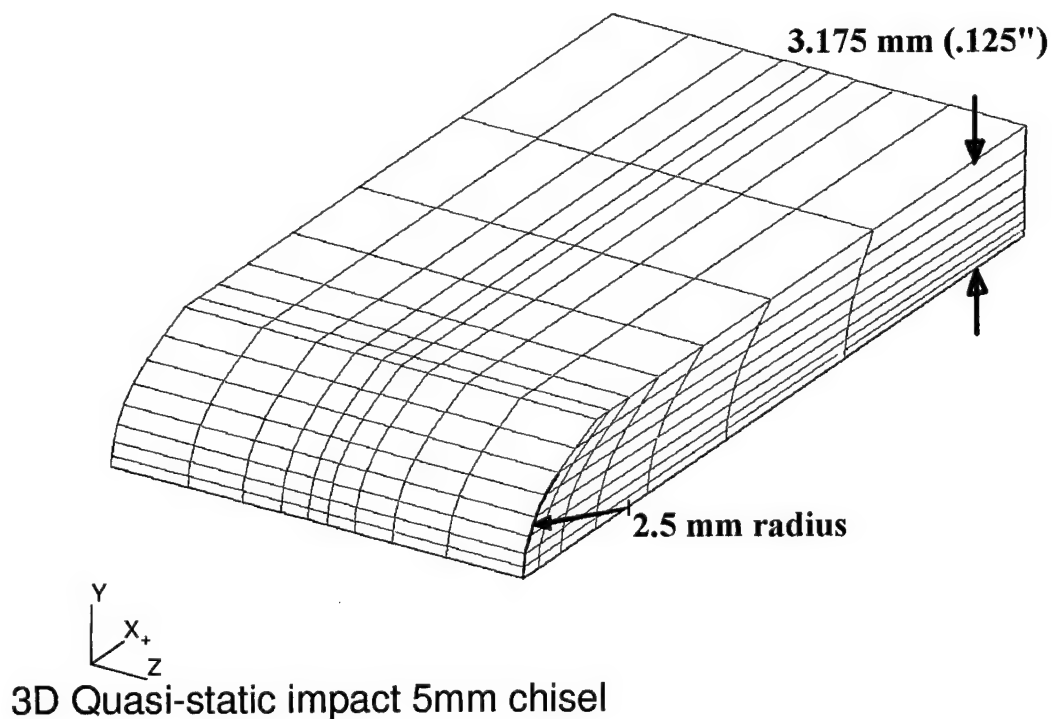


**Figure 81. FEM Model of 5 mm Chisel Indentor.** This indentor's relationship to the specimen model is shown in Fig. 80.

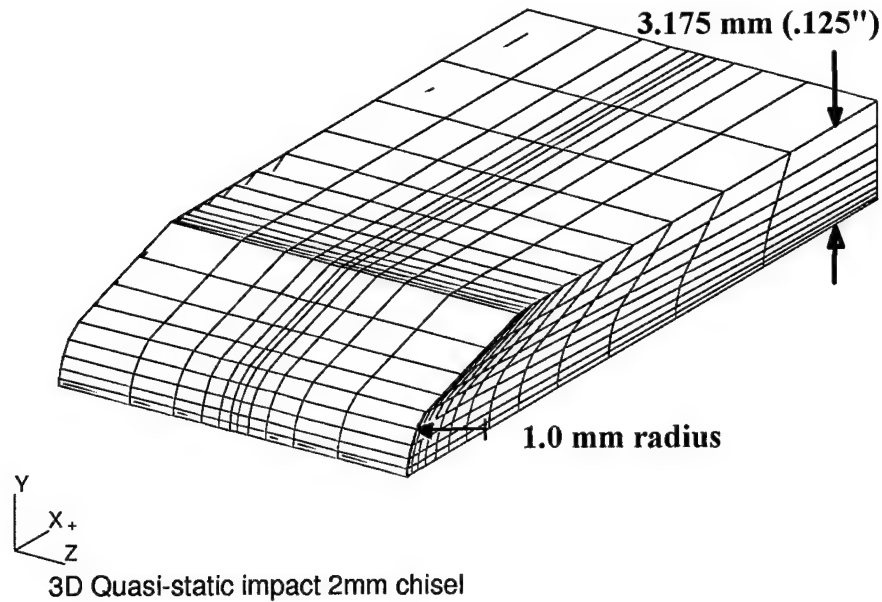


**Figure 82. FEM Model of 2 mm Chisel Indentor.** The Ti-6Al-4V specimen model is identical to that used with the 5 mm indenter model from Figure 81.

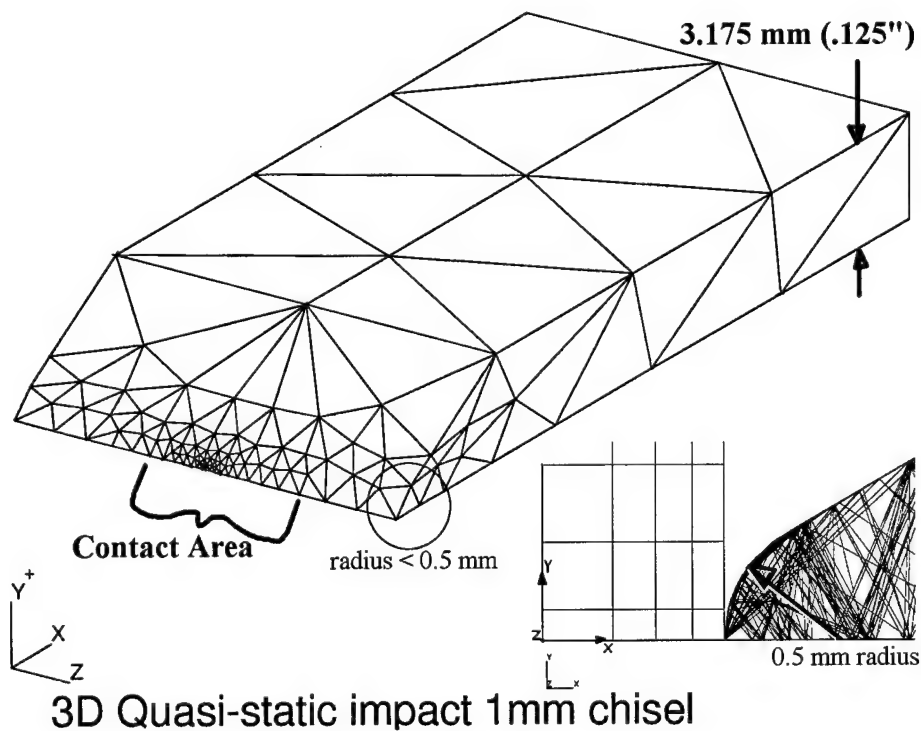


**Figure 83. FEM Model of 1 mm Chisel Indentor.** The Ti-6Al-4V specimen model is identical to that used with the 5 mm indenter model from Figure 81. Because of the small radius, the mesh grows coarser at the edges of the chisel. In the inset, a side view shows that the radius is matched in the middle contact area.

To determine the stress and strain distribution around the damaged area, a displacement approximately 11% larger than the indent desired is applied to the chisel nodes farthest away from the sample as the first step in the analysis (Fig. 84). This allows the contact event to partially take into account the deflection of the steel chisel. A typical case would be to apply a 991  $\mu\text{m}$  displacement to a 5 mm diameter chisel. After this maximum displacement is achieved, the nodes of the chisel are returned to their initial position in the 2nd step, which removes the chisel from contact with the sample. The indent depth remaining after recovering the elastic strain in the specimen is 907  $\mu\text{m}$ . This compares favorably with experimental data, in which the displacement of the crosshead carrying the chisel would be 1210  $\mu\text{m}$  (Fig. 19) and the final indent depth would be 917  $\mu\text{m}$ . The extra recovered displacement in the experimental case comes from the compliance of the test frame.

Contact surfaces are defined around the region where contact occurs, and ABAQUS automatically computes the nodes that are in contact and the forces resulting from the interaction. Friction between the two materials was fixed at a static coefficient of 0.7 and a dynamic coefficient of 0.5. Sensitivity analysis of this parameter indicated that it had a negligible effect on the Ti-6Al-4V's response. ABAQUS incrementally increases the displacement values from zero, inverting the stiffness matrix and solving the model at each increment. This allows the nonlinear Ti-6Al-4V material model to be approximated by a piecewise linear curve at each increment. As the strain in a element increased, the stress-strain relation moved along the curve shown

in Figure 79. Due to a lack of data at larger strain, at strains in excess of the last value, 20%, the last value of stress is maintained as yielding increased further.

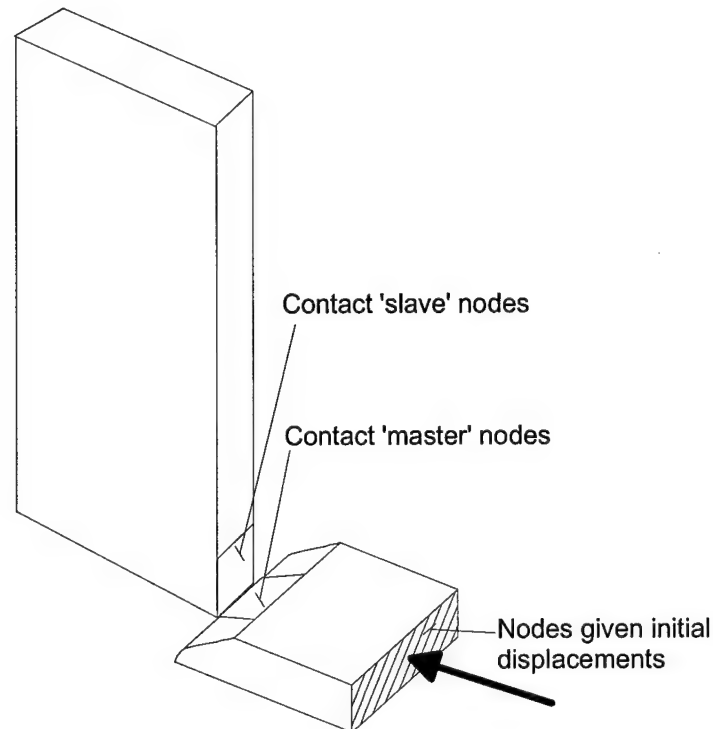


**Figure 84. Displacement and Contact for Quasi-static Model.** This schematic shows the contact regions and the nodes where the chisel displacements are enforced.

In the next four steps, a tension load is applied to the sample (Fig. 85). These four loads are equal to the  $\sigma_{\min}$  and  $\sigma_{\max}$  which caused failure at fatigue conditions at  $R=0.5$  and  $R=0.1$  during the HCF testing of specimens and had indents comparable to the modeled FOD (Fig. 86).

Analysis of the output results showed several areas in which the model reproduced several important qualities found in the tested specimens. As mentioned in the

section describing optical measurement of the plastic zone, on the fractured surface the deformation bands seen on the chisel indented specimens formed an 'X' shape. The relationship between this shape and the plastic deformation was investigated because initial FEM results showed just this shape when contours of plastic strain are plotted (Fig. 39).

The most obvious parameter to compare between experiments and analyses were the final deformed size and shape of the specimens. The section on plastic zone size measurement from grain sizes in Chapter IV compared the indentation depths directly. Table 7 lists quantitative comparisons of the deformed shapes predicted by ABAQUS and those seen from experiment (Fig. 87). All dimensions predicted by ABAQUS are within 10% of the actual experimental values.

Observation of the plastic strain results throughout the chisel contact and subsequent tension steps shows that the plastically deformed zone does not change after the chisel is removed. This means that during all four tension load levels applied after plastic deformation, the sample behaved linearly. This information leads to the assumption that the fatigue process which occurs after damage creation is indeed true HCF, in the sense that no further bulk plastic deformation is created by the fluctuating fatigue load being applied. Inertia effects were also ignored in this study. Although a frequency effect is known to exist in HCF, results on the undamaged fatigue strength of Ti-6Al-4V in Chapter VI will show this effect to be negligible at 350 Hz. This means that the stress state predicted by the static application of a fixed

load in the FEM can be assumed to be the state that exists in the specimen when the HCF load reaches the same level.

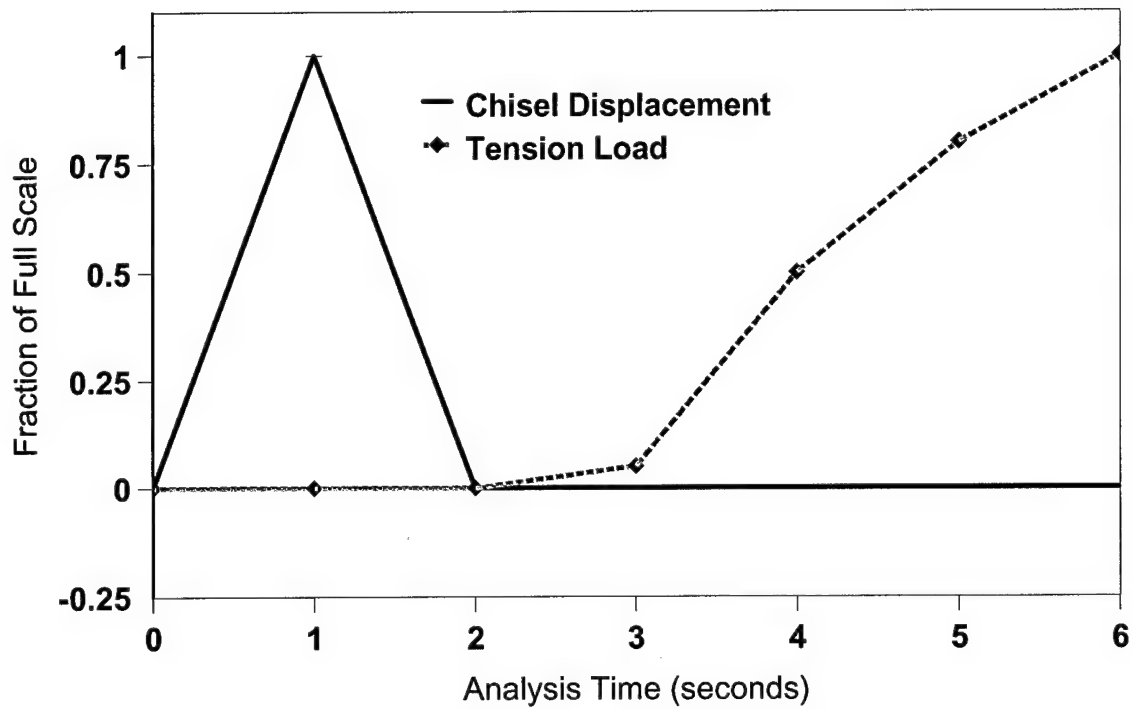


**Figure 85. Load Application Steps for Chisel Models.** As the ABAQUS models are quasi-static at each step, the time in seconds is simply a convenient parameter to discretize the increments.

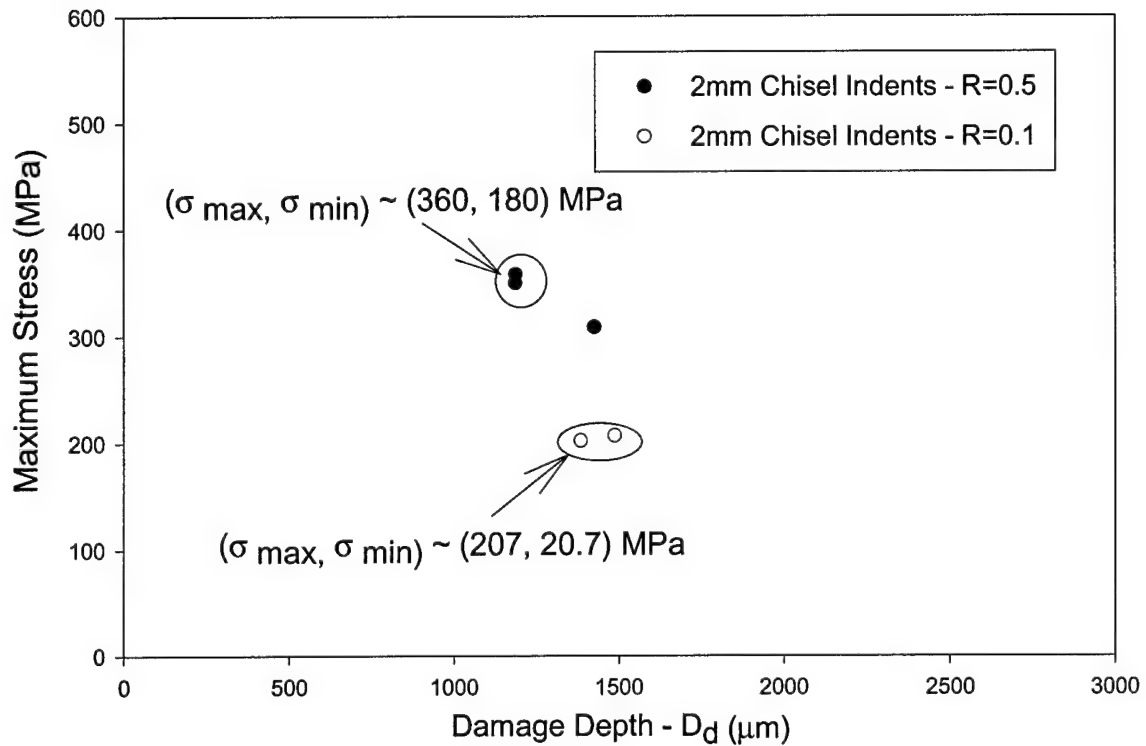


**Figure 86. Selection of Tension Loads During FEM.** For each condition modeled, the stresses applied were picked to represent the actual stresses seen by the specimens, as shown in this plot of fatigue strength for 2 mm chisel indentations. The circled points are the actual fatigue data which were averaged to obtain the loads to be applied to models. The uncircled point corresponds to a damage depth and fatigue strength combination which was not modeled.



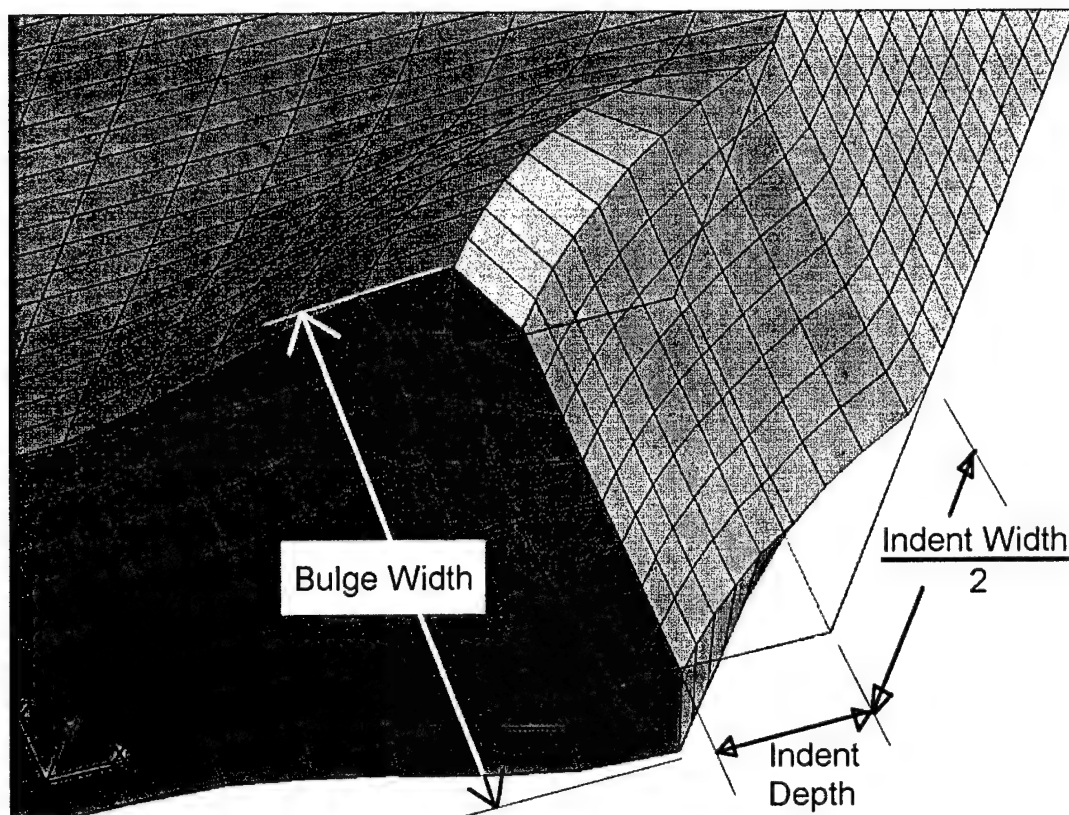


**Figure 87. Quasi-static Crater Dimensions.** This deformed plot of an ABAQUS run describes the dimensions compared in Table 7.

Table 7. Quasi-static FEM Notch Predictions

Chisel diameter (mm)	Indent Depth $D_i$ ( $\mu\text{m}$ )		Indent Width ( $\mu\text{m}$ )		Bulge width ( $\mu\text{m}$ )	
	FEM	Exp'l	FEM	Exp'l	FEM	Exp'l
1	462	460	1,118	1,136	1,814	1,836
2	539	532	2,555	2,484	1,935	2,050
5	907	918	3,810	3,679	2,057	2,270

Note: Indent depth  $D_i$  was enforced as an initial condition to match experimental conditions of interest. The indent and bulge widths indicate the accuracy of the model's response.

## Dynamic Model

The damage modeling of glass and steel sphere impacts occurs over much shorter time increments under dynamic loading conditions than those in the nonlinear static models described above. In this case, the commercial dynamic FEM code MSC/Dytran v4.0 was used. All solid continuum elements available in Dytran use reduced integration to compute elemental quantities. As in the quasi-static analysis, two planes of symmetry were used in the specimen model, although it wasn't an exact match to the damage conditions. Initial runs also indicated these boundary conditions were sufficiently accurate to model the damage. Figures 88 - 90 show the meshes used to model these three sphere impact events.

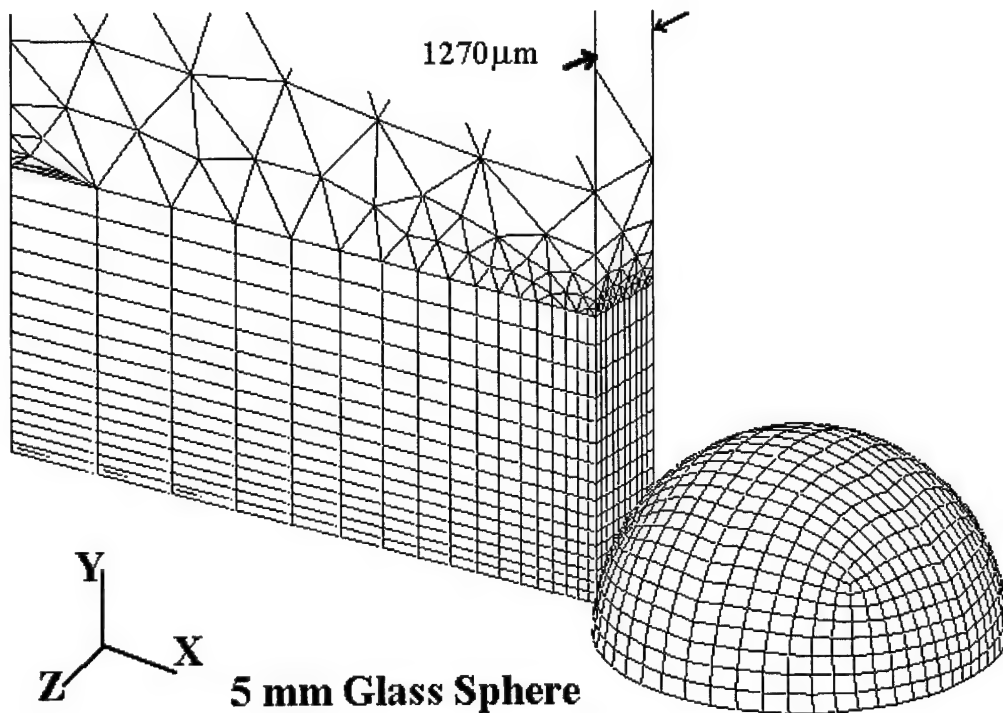
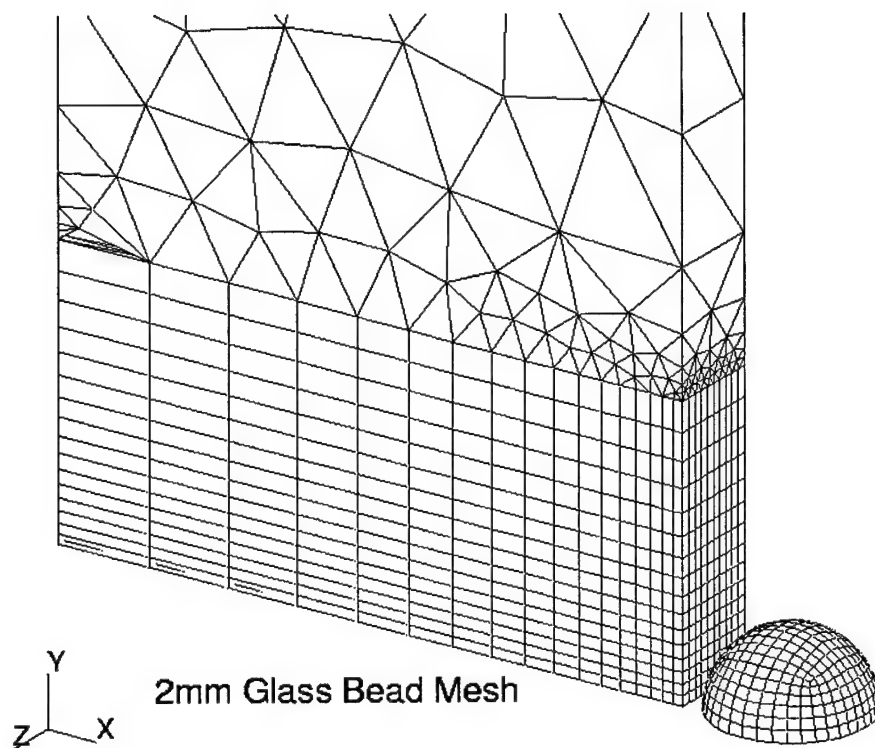
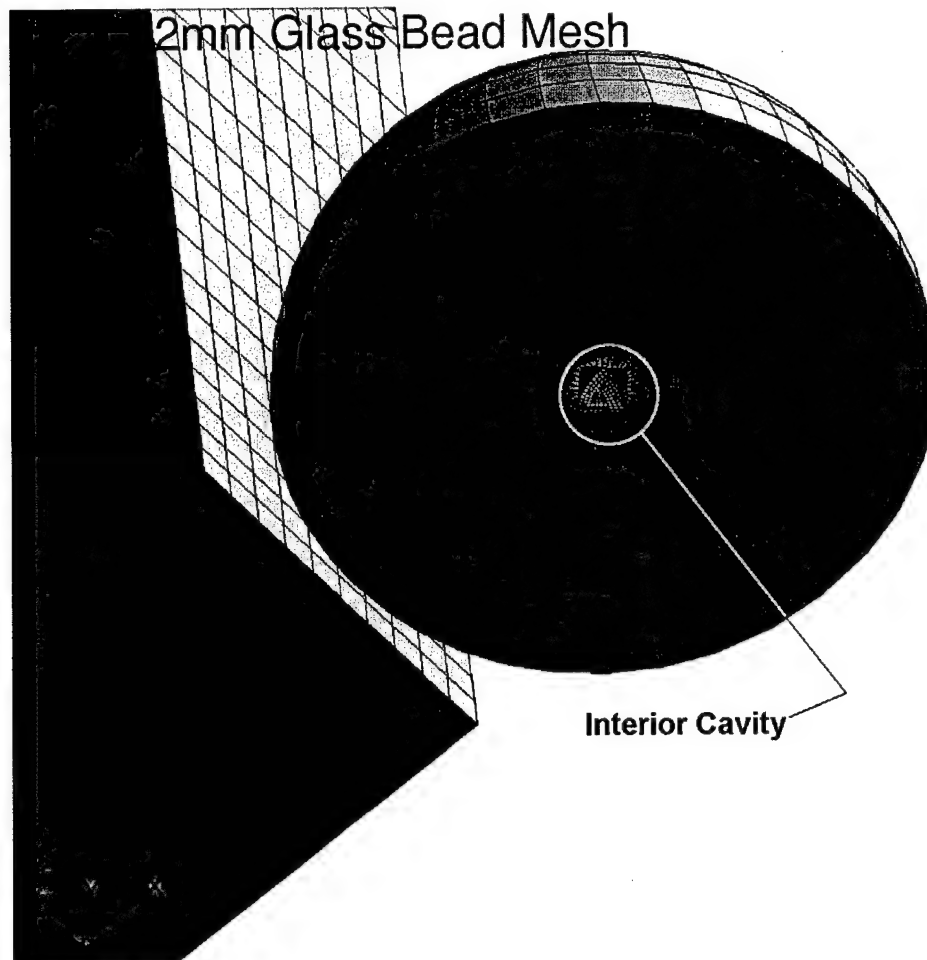


Figure 88. Dytran Mesh - 5 mm Glass Sphere



**Figure 89. Dytran Mesh- 2 mm Sphere.** The 2 mm glass and 2 mm steel spheres were both modeled by the same mesh. The material properties were changed in the Dytran input deck after mesh generation. The Ti-6Al-4V sample is modeled by the same mesh shown in Figure 87.



**Figure 90. Interior of Dytran Mesh- 2 mm Sphere.** The inside of the spheres (including the 5 mm glass model) had a small cavity at the center of the sphere. This was necessary to avoid a limitation on the automatic meshing in Patran, the preprocessor used to generate the nodes.

The initial velocity of the sphere is prescribed, and the calculation proceeds from this non-zero velocity at those nodes. Because the glass spheres are known to erode the Ti-6Al-4V, a more complex contact algorithm is used. Dytran was programmed to automatically compute which nodes are on the surface defined by the elements of the sphere. These surface nodes were assumed to be in contact with surfaces of the specimen if the gap between them were smaller than the specified contact tolerance.

Dytran automatically changed the definition of the surfaces that were in contact as these surfaces eroded. The surfaces erode because the elements were assumed to fail if they met a user defined failure criterion. In this study, elements in the specimen and spheres failed when the von Mises' plastic strain at every node in the element exceeded the failure strain. For the specimen, it was 20% -- the value at failure seen in tensile specimens (4). The steel sphere elements failed at 6% strain, and the glass sphere at 1.35% (the compressive value). When an element failed, the stiffness in it was set to zero and all associated nodes were removed from the contact algorithm.

Simulation of the tensile fatigue loads, which would be essentially a static force application such as was done in ABAQUS, is made in a significantly more complex manner due to the explicit nature of Dytran. Dytran is capable of modeling the 'ringing' (i.e., vibration) of the sample as it is excited by the glass or steel sphere impact. This level of dynamic detail is not needed here and is in fact a waste of computer time. However, discussions with experts in the transient analysis community (10) indicate that schemes to artificially damp out the ringing would interfere with the proper modeling of the interaction between the sphere and the sample. To avoid this, the Dytran models were allowed to run normally for the duration of the sphere impact event. This duration was determined by several initial runs used to refine the dynamic model and found to be less than 40  $\mu$ sec for all three spheres.

After the impact event was completely finished, an artificial damping coefficient ( $\beta$ ) was applied to the model, and the four tension load levels were applied as in the quasi-static chisel case. Appendix G describes the damping and how it was selected. Figures 91-93 show the loads and damping applied. The tensile stresses were applied as step loads. A time interval was allowed after each increment to allow the stress wave propagation throughout the model to equilibrate. Since the steady-state response of the model to these step loads was desired, the artificial damping parameter  $\beta$  caused the response of the model to die out to its steady-state value more quickly, otherwise the amount of computer time needed to model these steps would be prohibitive. Note in Figures 91-93 that  $\beta$  was not introduced into the equations until after the sphere impact event was completely finished. This is essential to ensure that the full kinetic energy of the sphere is transferred to the sample (10).

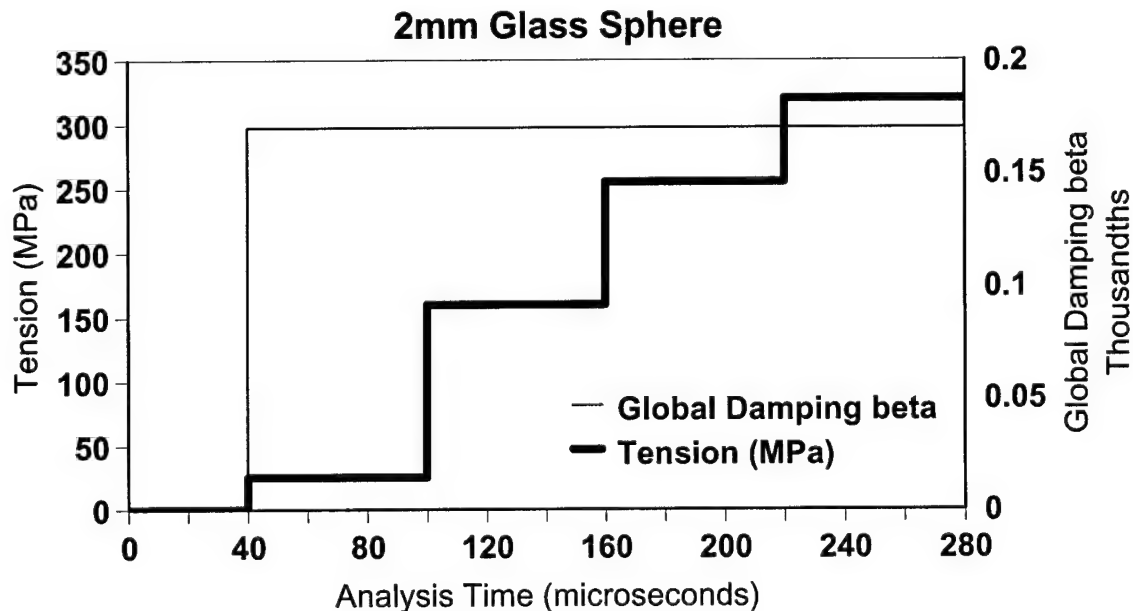


Figure 91. Damping and Loading Applied - 2 mm Glass Sphere

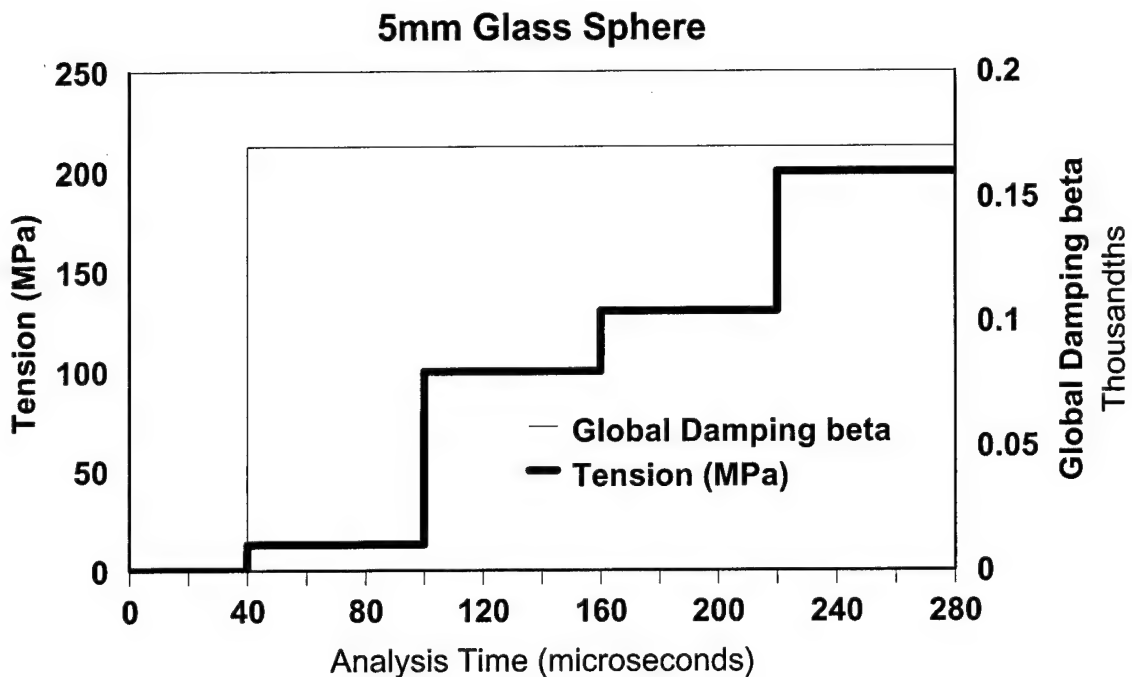


Figure 92. Damping and Loading Applied - 5 mm Glass Sphere

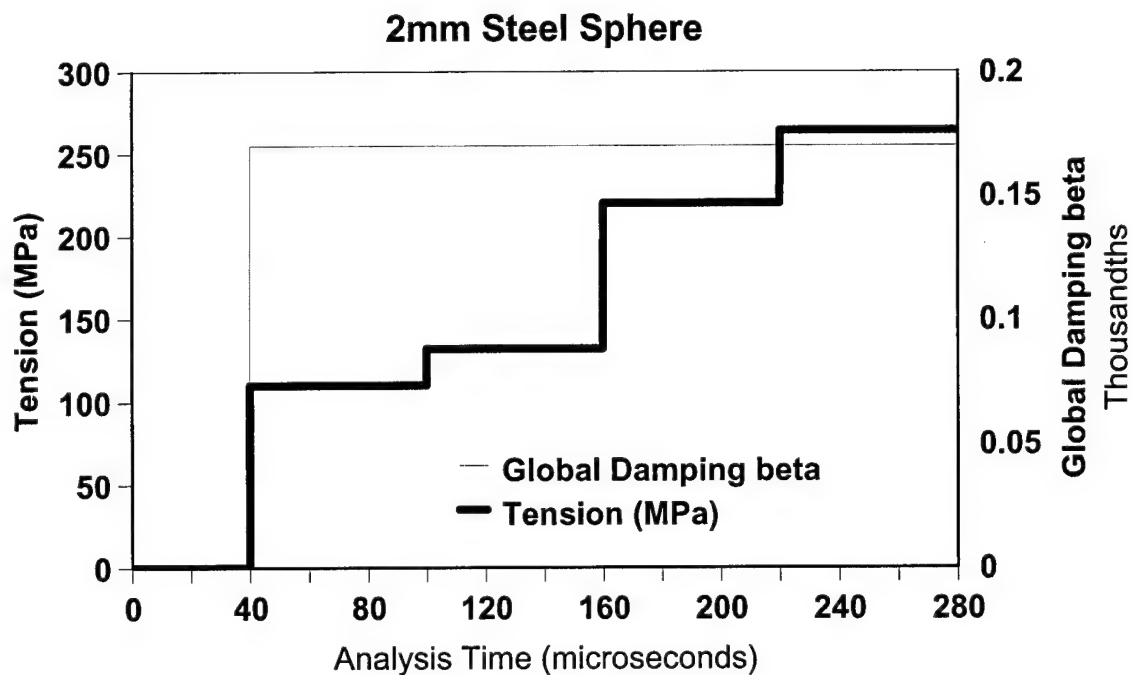
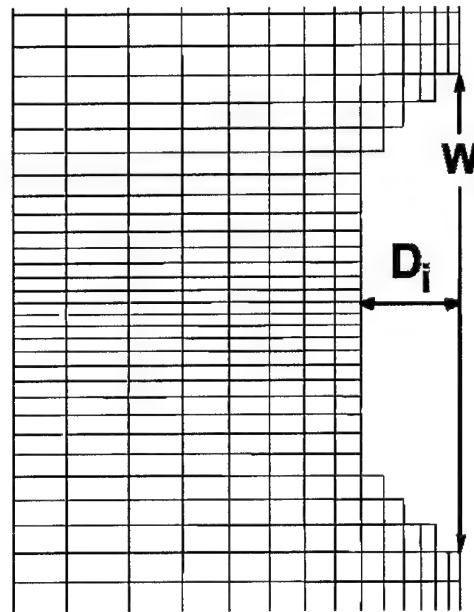


Figure 93. Damping and Loading Applied - 2 mm Steel Sphere

After the impact event is completed, the crater dimensions and plastic zone size have reached their final sizes. As in the quasi-static runs, it was observed that no further plastic strain was introduced into the model by the application of the tensile load steps. The Dytran predictions of the crater depths and widths (Fig. 94) are summarized in Table 8.



**Figure 94. Dynamic Crater Dimensions.** This plot of Dytran output describes the dimensions compared in Table 8.

Table 8. Dynamic FEM Notch Predictions

Sphere	Indent Depth $D_i$ ( $\mu\text{m}$ )		Indent Width $W$ ( $\mu\text{m}$ )	
	FEM	Experiment	FEM	Experiment
5 mm Glass	877	800	4,840	4,572
2 mm Glass	640	600	1,894	1,780
2 mm Steel	710	691	1,910	1,688



## Quasi-static Results

Based upon the reasonable agreement between the grain size measurements of strain and the strain distributions from ABAQUS (as shown in Chapter IV) as well as from the agreement in the physical dimensions of craters described in the first section of this chapter, it is reasonable to assume that the finite element models of the chisel indentations predict the stress states in the specimens accurately also. These stress distributions are described in this section. Figures 95 through 97 show perspective plots of stress contours at the maximum tension loads applied to each model.

Four stress states, corresponding to the four tensile loads used during fatigue tests (Fig. 86) are created at the four steps. The locations of the large tensile stresses are spread throughout the plastic zone and just behind it. In each case, there are two or more locations where the tensile stresses,  $\sigma_{yy}$ , reach the largest levels. To locate the maximum predicted stress, several locations must be compared. The centerline of the specimen located at  $y = z = 0$  always contains one of the larger stresses,  $\sigma_{yy}$ , as is the case in Figure 95, where the maximum stress is shown to be at the bottom of the notch. In Figures 96 and 97, the location of the largest stress is slightly above the bottom of the notch and at the far edge of the notch, respectively. Stresses at these locations as well as the centerline were examined to determine the maximum tensile stresses for each case.

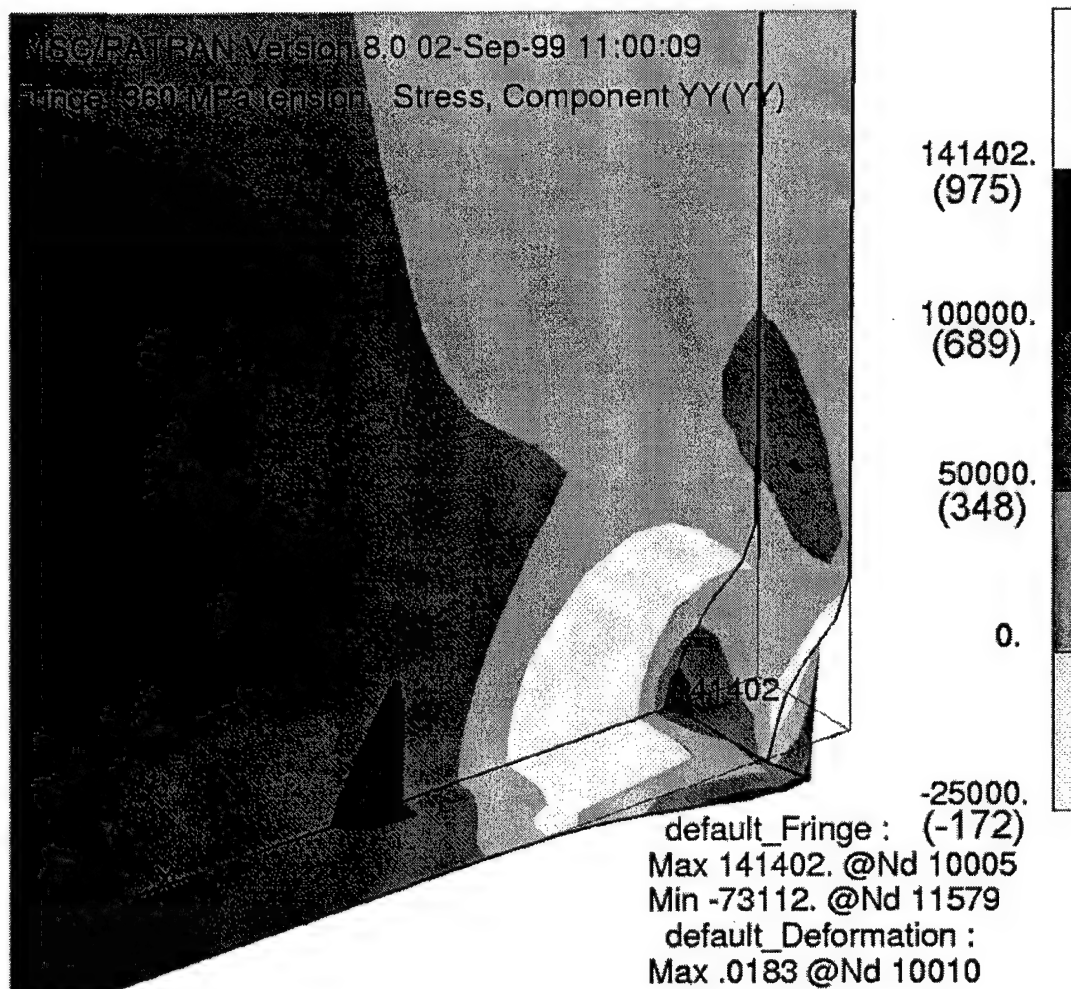


**Figure 95. ABAQUS Prediction of Tensile Stress; 1 mm Chisel Indent.**  
 The stress state for a nominal stress of 360 MPa is shown. This view shows only  $\frac{1}{2}$  of the damaged area, in order to expose the contours along the center plane  $z = 0$ . Note that the maximum tensile stress is located at the bottom center of the notch in this plot. Plots of stress values along the centerline  $y = z = 0$  are shown in Fig. 98. The scale is plotted in English units (psi and inches). Stresses in MPa are shown as annotations to the plot in parentheses.

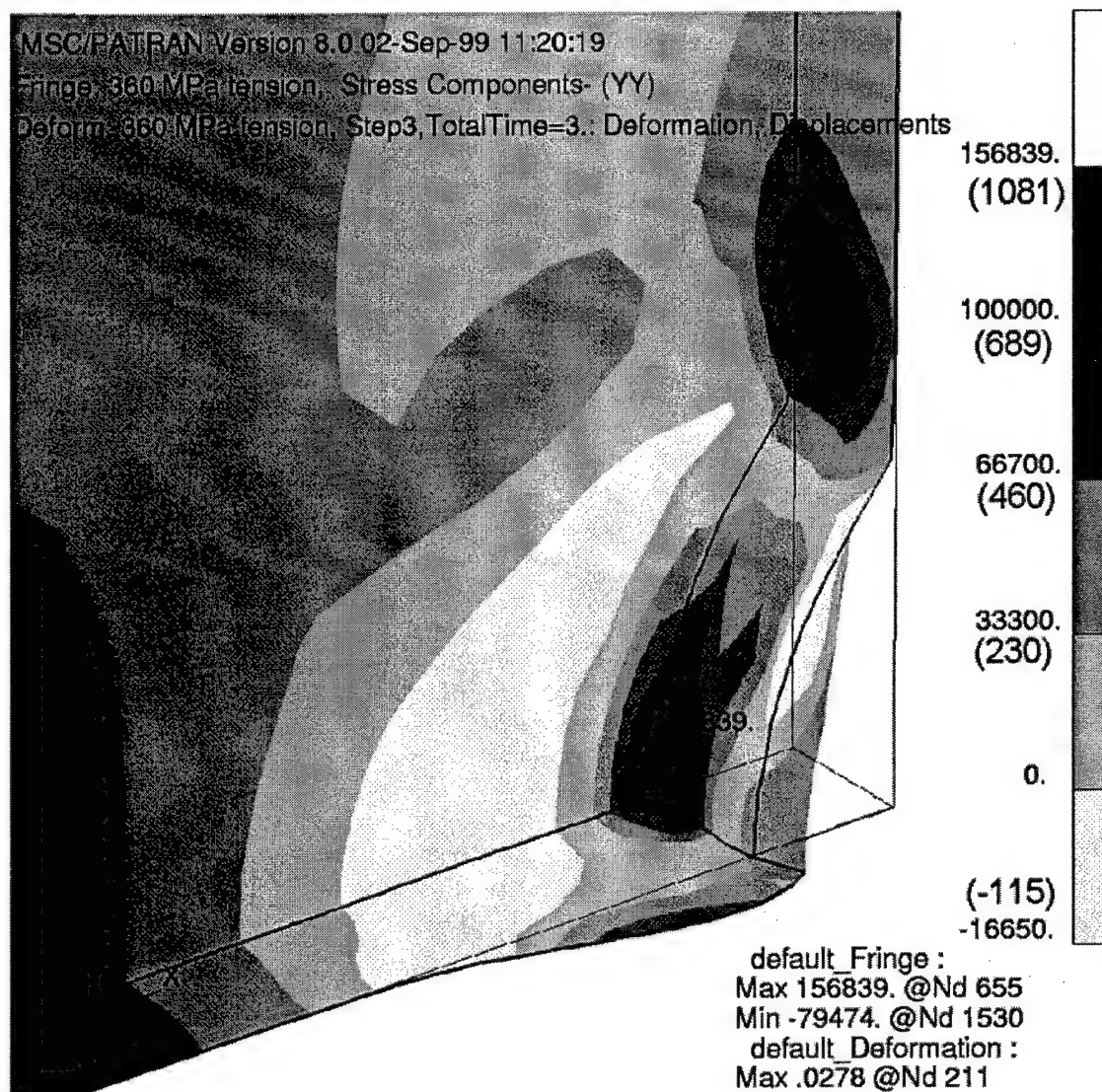


**Figure 96. ABAQUS Prediction of Tensile Stress; 2 mm Chisel Indent.**  
 The stress state for a nominal stress of 360 MPa is shown. This view shows only  $\frac{1}{2}$  of the damaged area, in order to expose the contours along the center plane  $z = 0$ . The maximum tensile stress is located slightly above the bottom center of the notch in this plot. Plots of stress values along the centerline  $y = z = 0$  are shown in Fig. 99. As in Fig. 95, English units are plotted with MPa in parentheses.

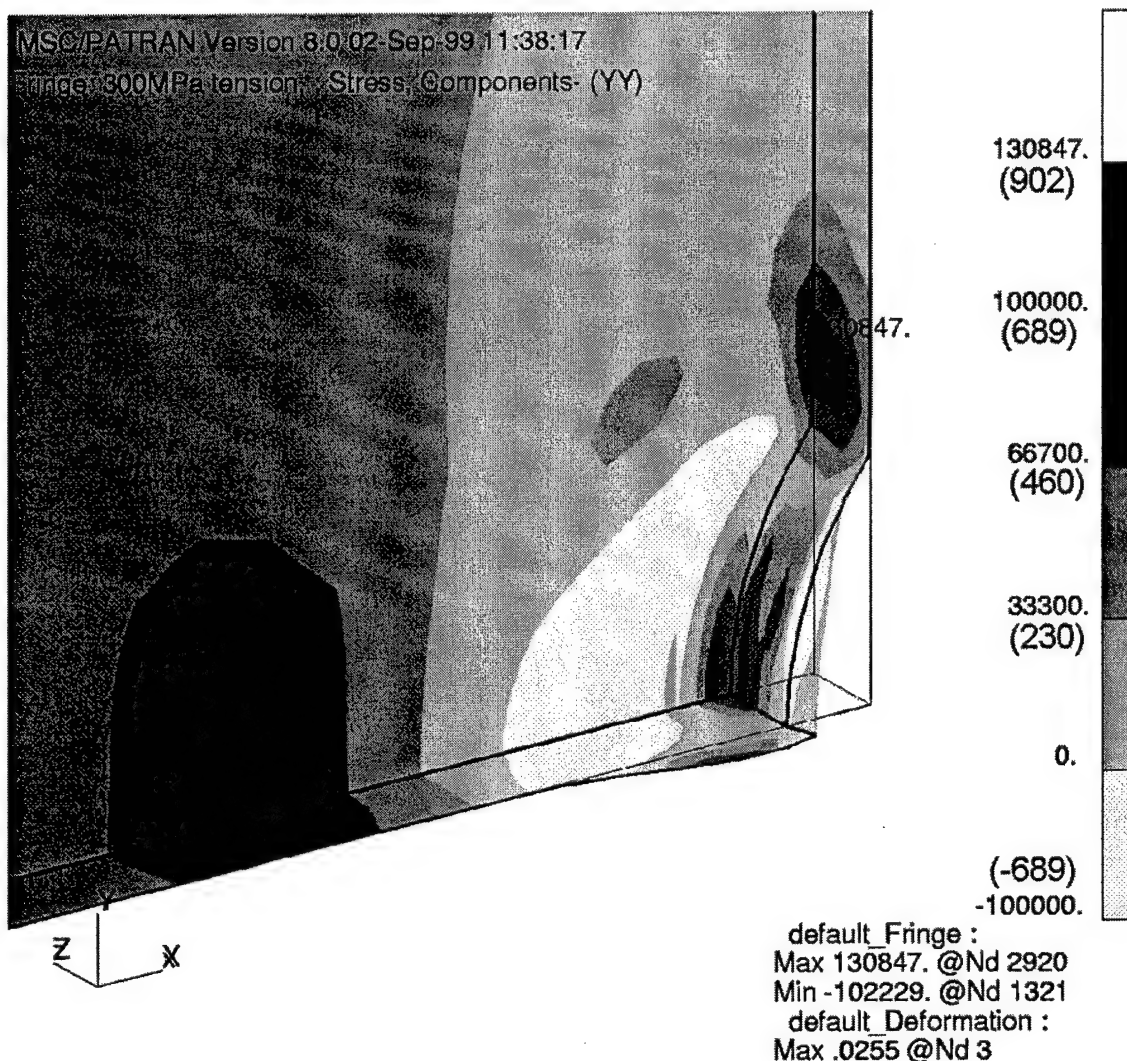


**Figure 97. ABAQUS Prediction of Tensile Stress; 5 mm Chisel Indent.**

The stress state for a nominal stress of 300 MPa is shown. This view shows only  $\frac{1}{2}$  of the damaged area, in order to expose the contours along the center plane  $z = 0$ . The maximum tensile stress is located at the top edge where the notch ends in this plot. Plots of stress values along the centerline  $y = z = 0$  are shown in Fig. 100. As in Fig. 95, English units are plotted with MPa in parentheses.

Plots of the tensile stresses,  $\sigma_{yy}$ , along the centerline of the specimen are given in

Figures 98 through 100. Note that at all tensile load levels, as the absolute value of the applied stresses increases, the region at which high stress locations are found stays the same. As the fatigue stresses increase and decrease under alternating

loading, the region at which the maximum stresses exist is unchanged. As the distance,  $x$ , increases into the interior of the sample from the notch root, the tensile stresses rapidly drop down and become compressive due to the plastically deformed zone. They then rise rapidly again before dropping to a constant value which continues into the middle of the sample and across the vertical plane of symmetry.

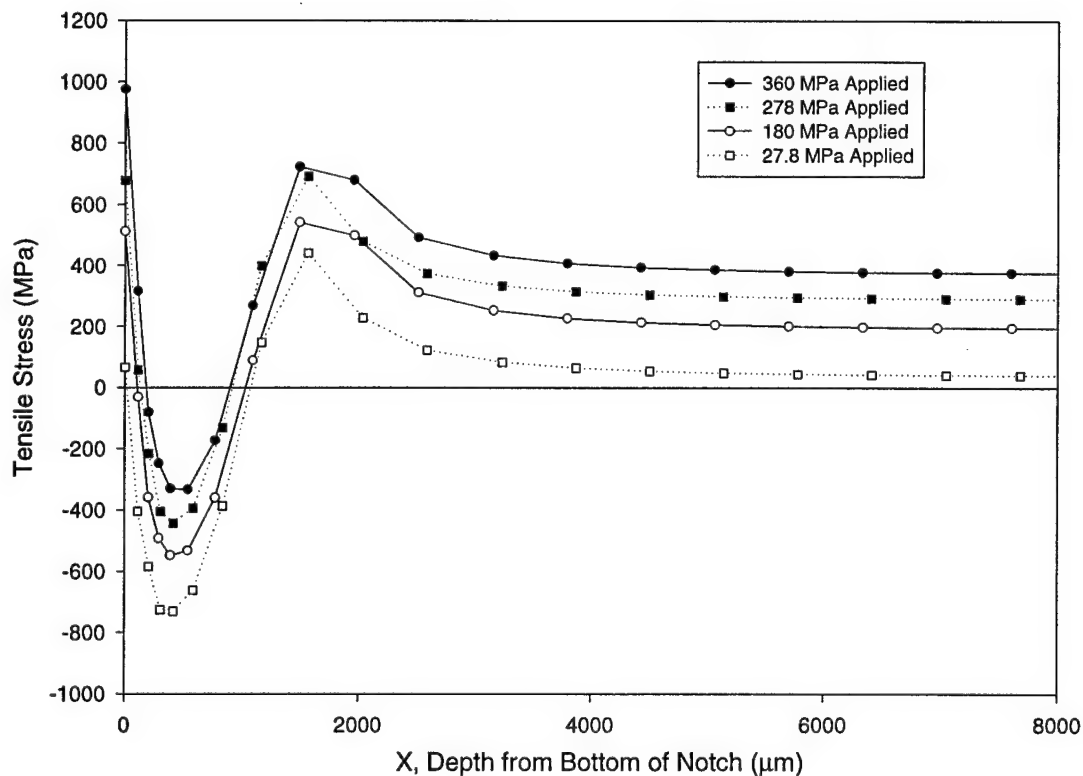


**Figure 98. Stress Distribution Due to Tensile Load; 1 mm Chisel Indent.**  
These stress values are plotted along the centerline  $y = z = 0$ .

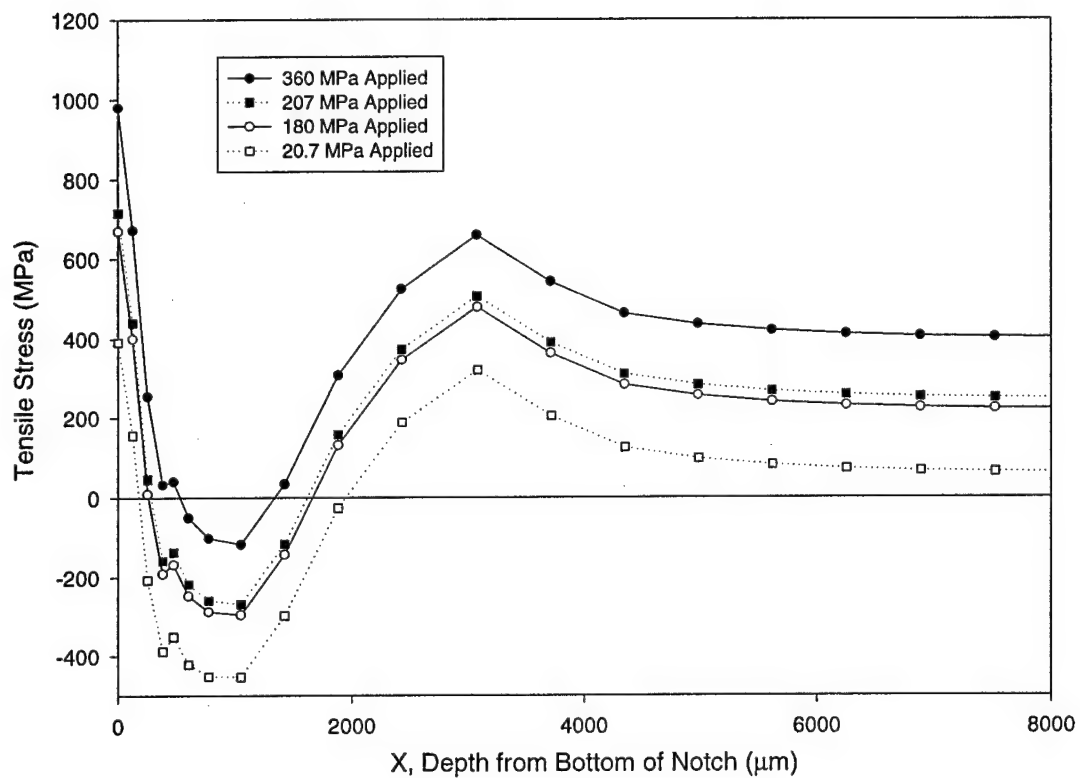


**Figure 99. Stress Distribution Due to Tensile Load; 2 mm Chisel Indent.**  
 These stress values are plotted along the centerline  $y = z = 0$ .

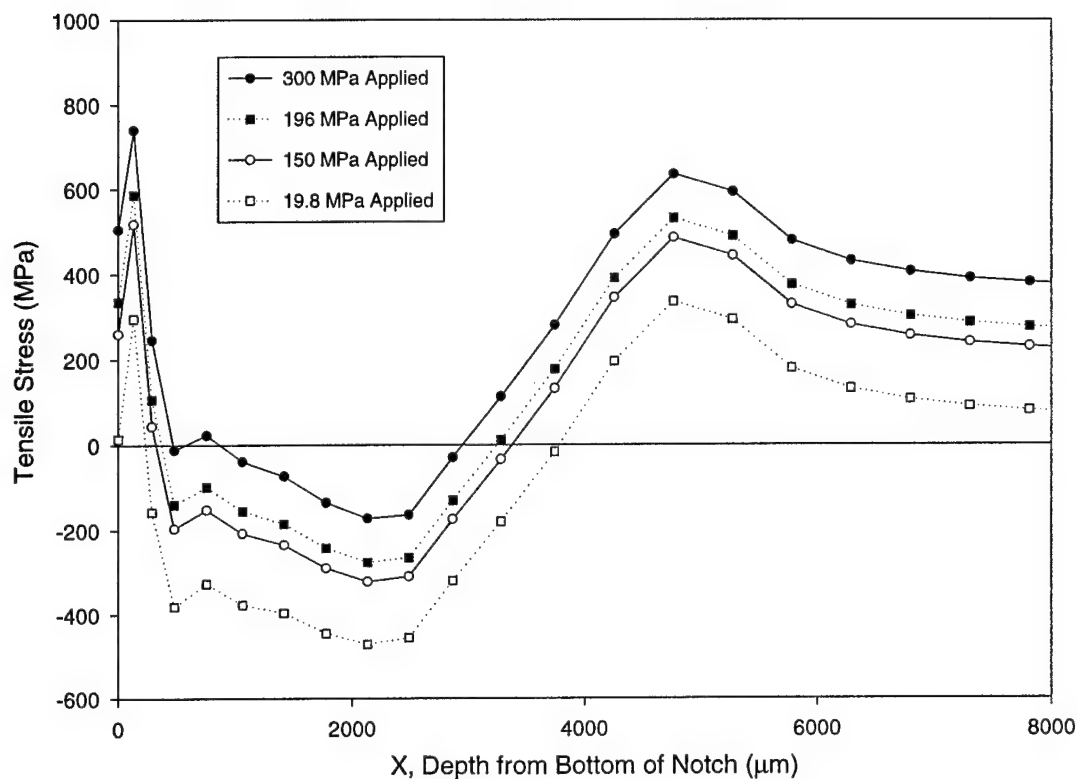


**Figure 100. Stress Distribution Due to Tensile Load; 5 mm Chisel Indent.** These stress values are plotted along the centerline  $y = z = 0$ .

By locating the peak stress for each load condition and finding the ratio of the largest stresses resulting from the applied loads representing the minimum and maximum fatigue loads applied, it was found that applied stress ratios of  $R=0.1$  and  $R=0.5$  yield true peak tensile stresses that have stress ratios from  $R=0.56$  to  $R=0.78$  in most cases (except one anomaly of  $R=0.09$ ) with higher mean stresses. As seen in Figures 98-100, one peak is located in the plastic zone, and another one nearly as large in the elastic region. These local stress ratios are listed in Table 9.

Table 9. Effective Stress States from Chisel Indentations

	Applied Stress (MPa)		Actual Peak Stress (MPa)			
Chisel diameter	R	$\frac{\sigma_{\min}}{\sigma_{\max}}$	In Elastic Zone		In Plastic Zone	
				Effective R		Effective R
1 mm	0.5	180	543	0.56	513	0.71
		360	975		723	
	0.1	28	441	0.64	66	0.09
		280	692		678	
2 mm	0.5	180	517	0.74	827	0.74
		360	696		1,117	
	0.1	20.7	359	0.66	758	0.71
		207	545		1,062	
5 mm	0.5	150	552	0.78	696	0.77
		300	703		910	
	0.1	19.6	414	0.69	534	0.72
		196	600		741	
Note: These maximum and minimum values are obtained by scanning along the whole specimen, and they may not necessarily agree with Figs. 98-100.						

### Dynamic Results

Like the quasi-static analyses, the dynamic analyses yielded the stress distribution in the specimen after damage and application of tensile loads. Figures 101 through 106 show contour plots of representative results from these analyses. As in the ABAQUS predictions, note that the plastic zone doesn't change after the impact event is finished (Figs. 107, 110, 113). In the case of the time-dependent dynamic calculations, the tension states are referred to by picking an analysis time at which the applied stress is at the level of interest. The applied stress and the computed peak stress at a certain point within the model are given as functions of time for all three



cases (Figs. 108, 111, 114). In these plots, the nominal applied stress is the stress at a node far from the impact region along the center of the specimen  $x = z = 0$ . This node is on the symmetric boundary as described in Figure 80.

The variation of  $\sigma_{yy}$  along the centerline of the specimen (i.e.,  $y = z = 0$ ) at four applied stress levels, corresponding to the  $R = 0.1$  and  $R = 0.5$  fatigue test condition, are shown in Figures 109, 112 and 115.

As in the quasi-static analyses, the peak stresses provided local stress ratios quite different from the applied stress states. These values are summarized in Table 10.

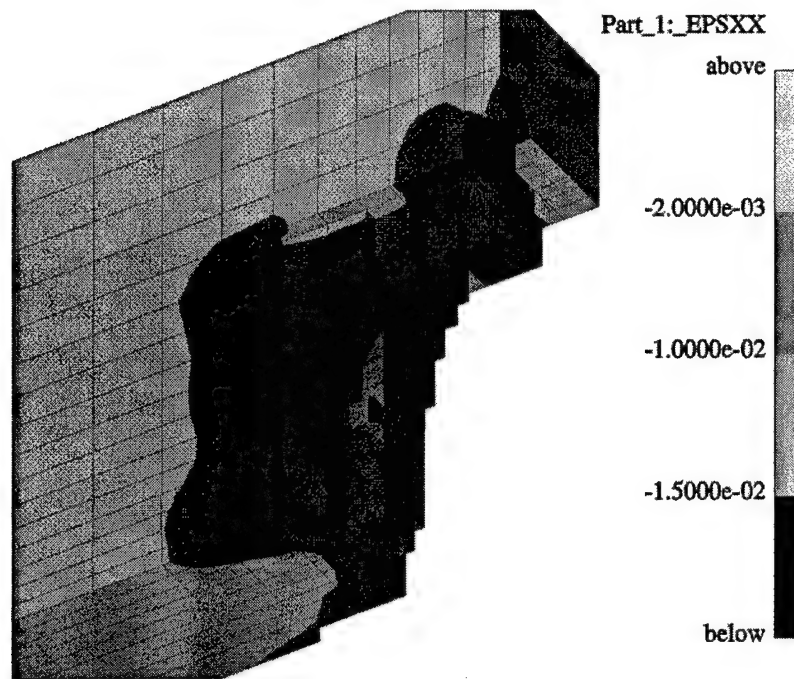


**Figure 101. Plastic Strain from 5 mm Glass Sphere Impact**

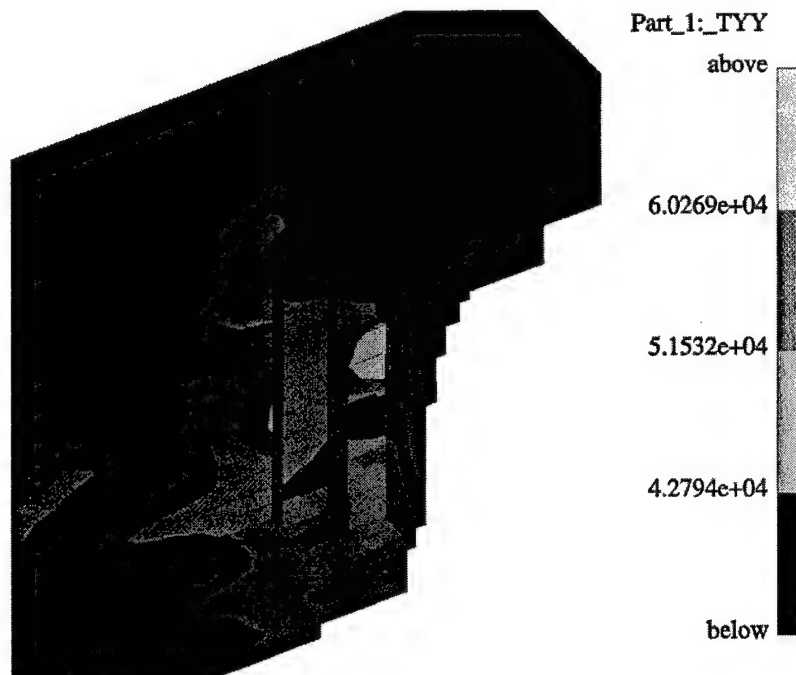


**Figure 102. Tensile Stress from 5 mm Glass Sphere Impact.** This stress state represents the maximum applied load, 200 MPa.

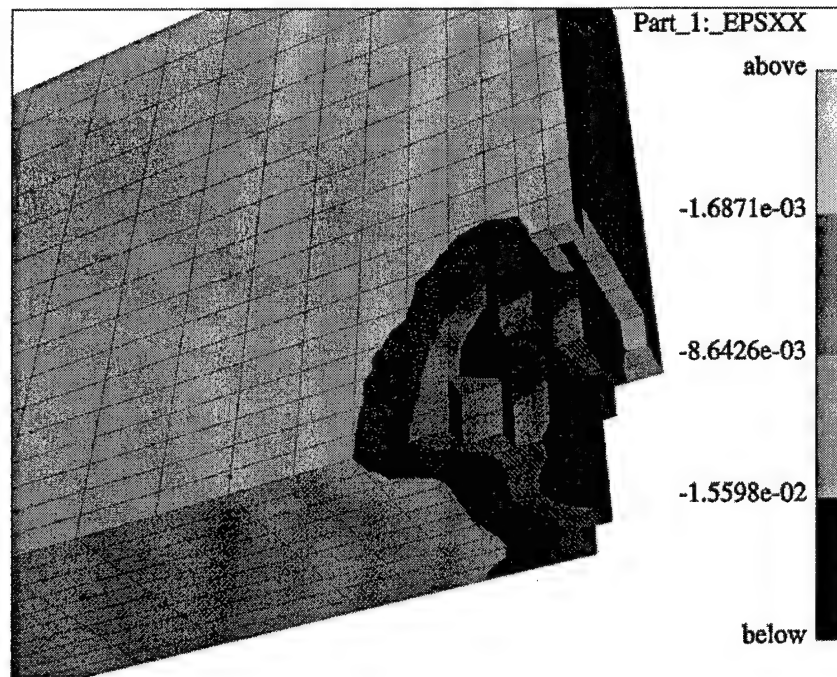


**Figure 103. Plastic Strain from 2 mm Glass Sphere Impact**

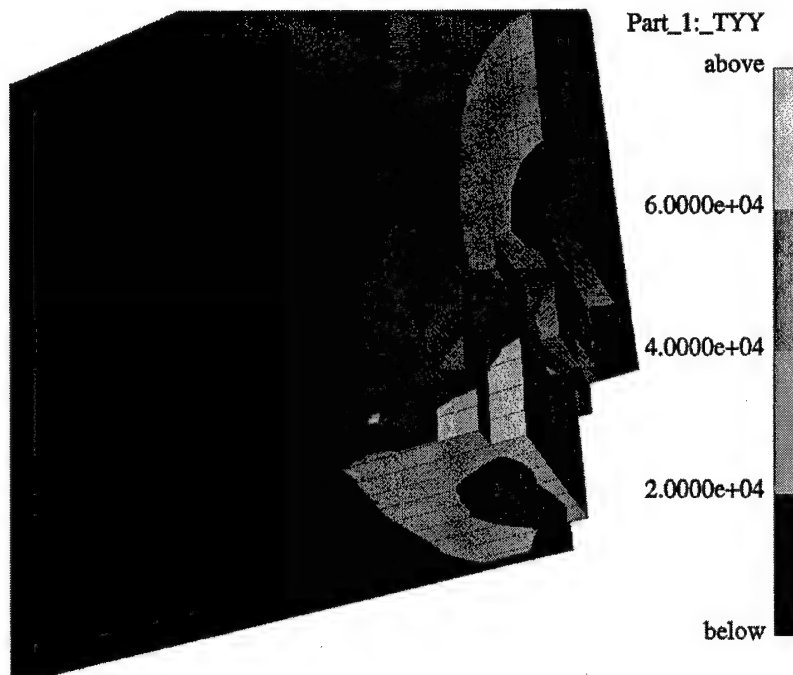


**Figure 104. Tensile Stress from 2 mm Glass Sphere Impact.** This stress state represents the maximum applied load, 320 MPa.

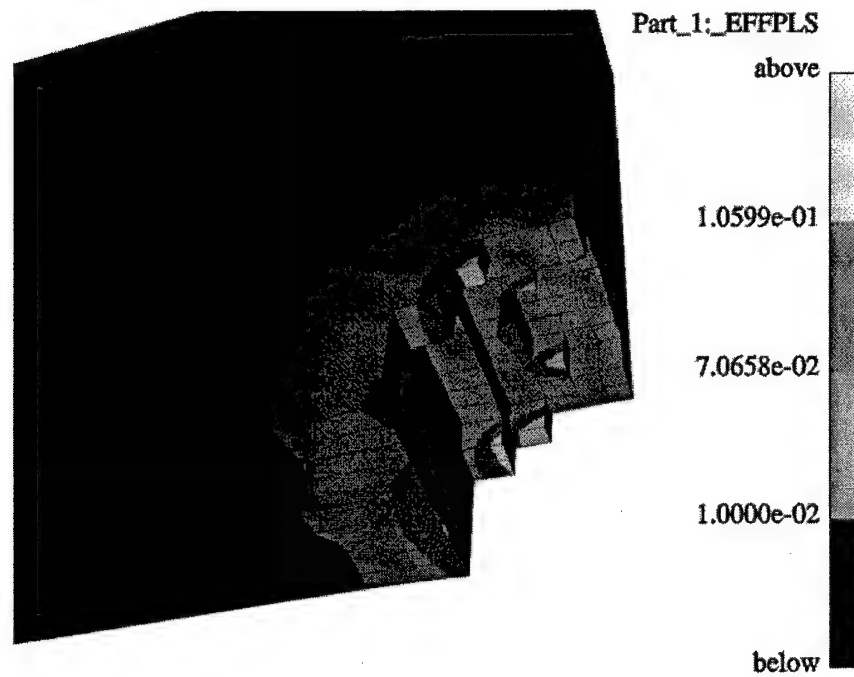


**Figure 105. Plastic Strain from 2 mm Steel Sphere Impact**

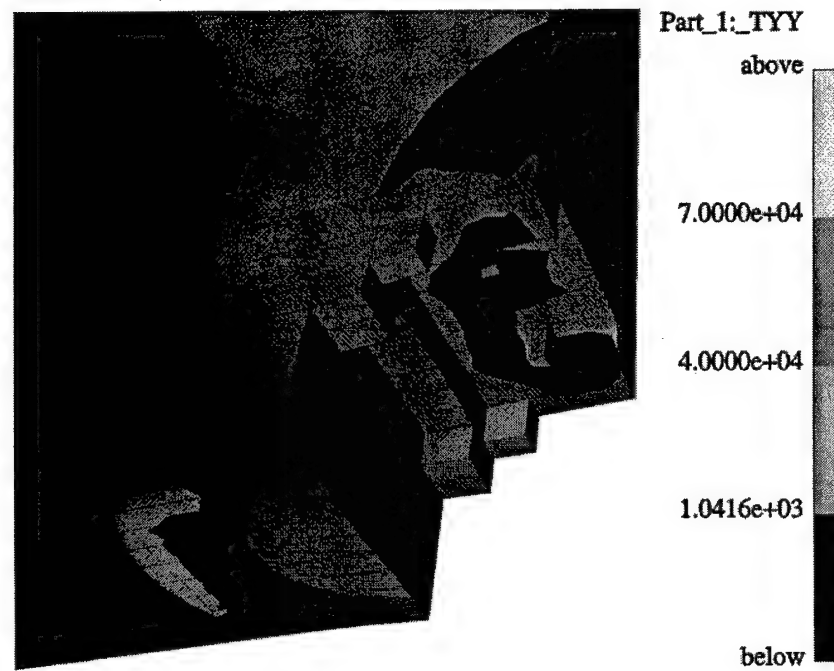


**Figure 106. Tensile Stress from 2 mm Steel Sphere Impact.** This stress state represents the maximum applied load, 250 MPa.

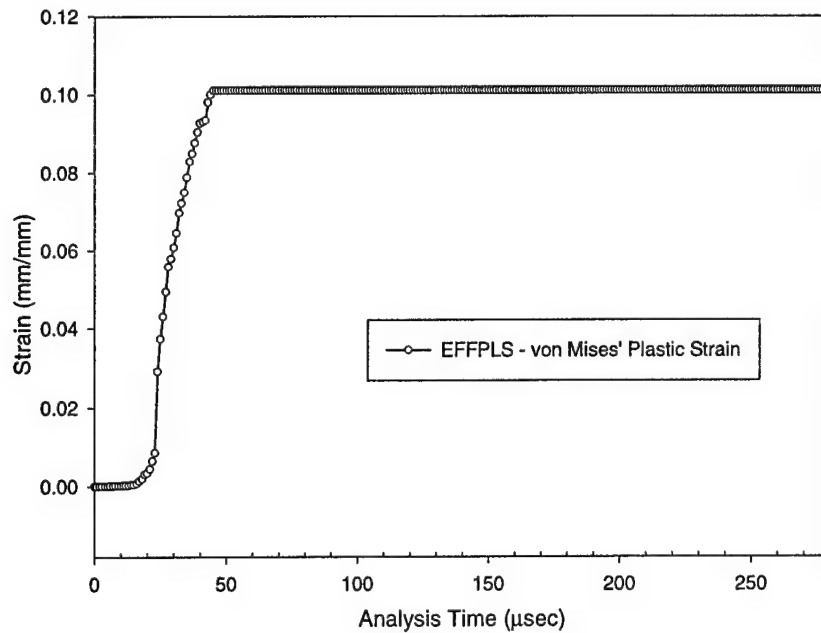


**Figure 107. Von Mises' Plastic Strain vs. Time; 5 mm Glass Sphere.** Notice that plastic strain does not change after the impact event. This plot and Figs. 109, 111 are at the notch root.

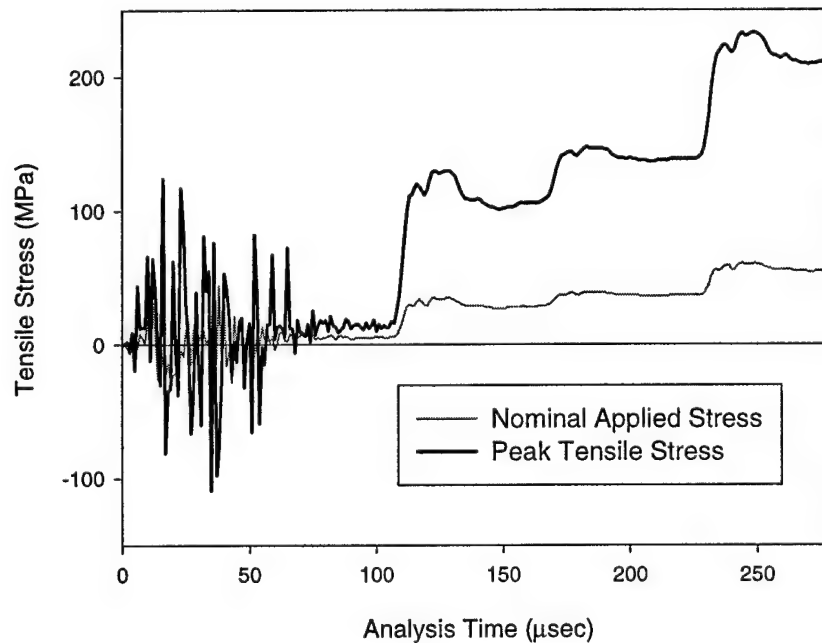


**Figure 108. Tensile Stress vs. Time; 5 mm Glass Sphere.** Nominal applied stress and peak stress are plotted over the time duration of the analysis.

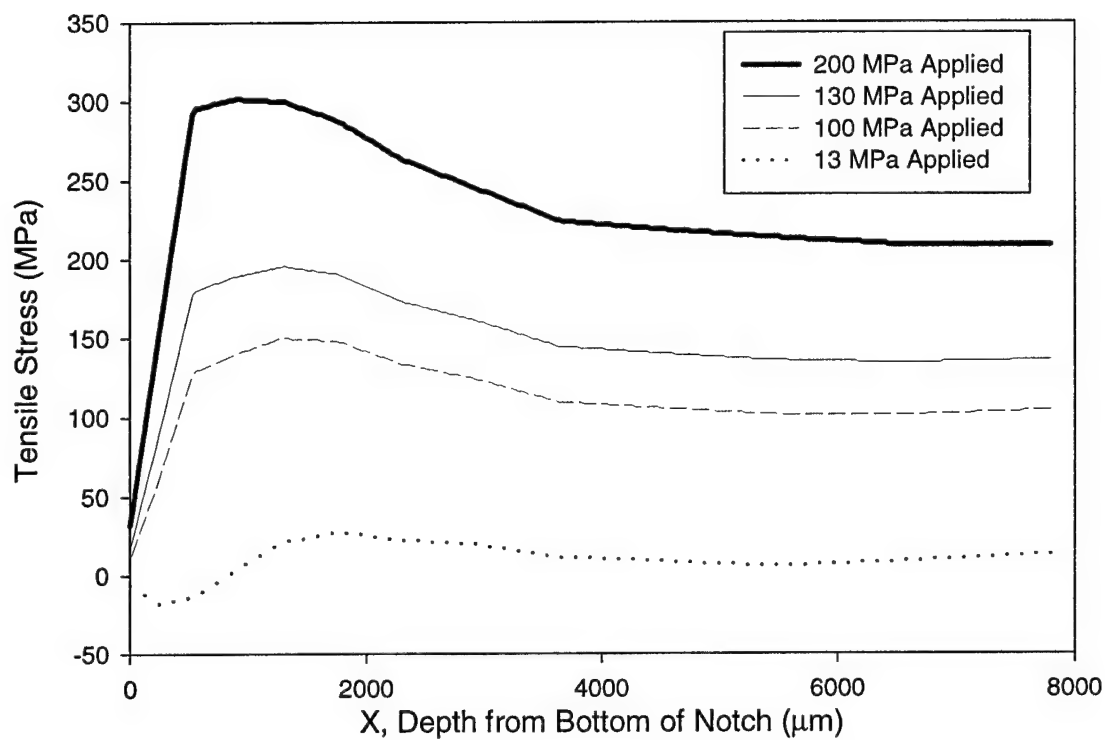


**Figure 109. Stress Distribution Due to Tensile Load; 5 mm Glass Sphere.** Stress  $\sigma_{yy}$  along  $y=z=0$  centerline associated with all applied load steps from Figure 108.

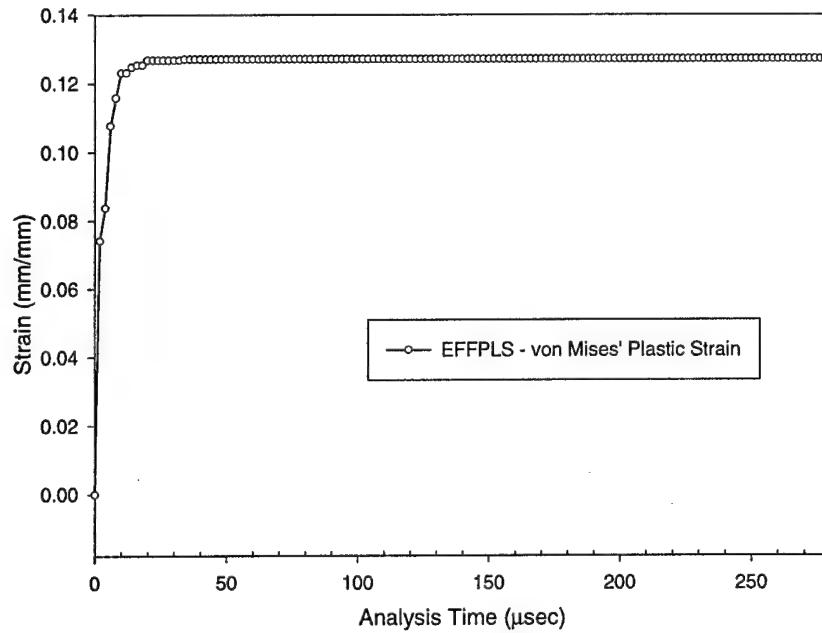


**Figure 110. Von Mises' Plastic Strain vs. Time; 2 mm Glass Sphere.** Again no further plastic strain occurs after the impact event.

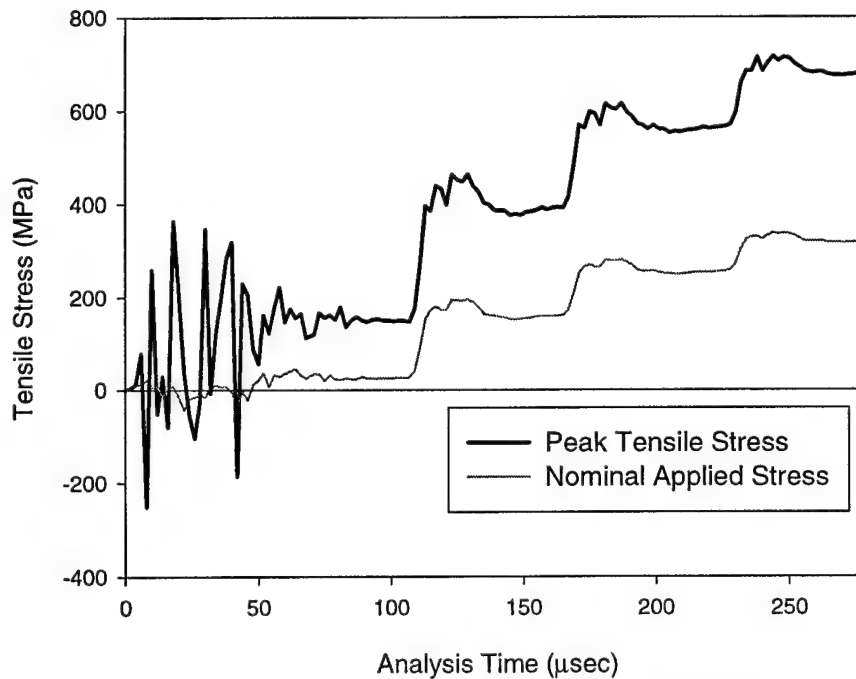


**Figure 111. Tensile Stress vs. Time; 2 mm Glass Sphere.** Nominal applied stress and peak stress are plotted over the time duration of the model.

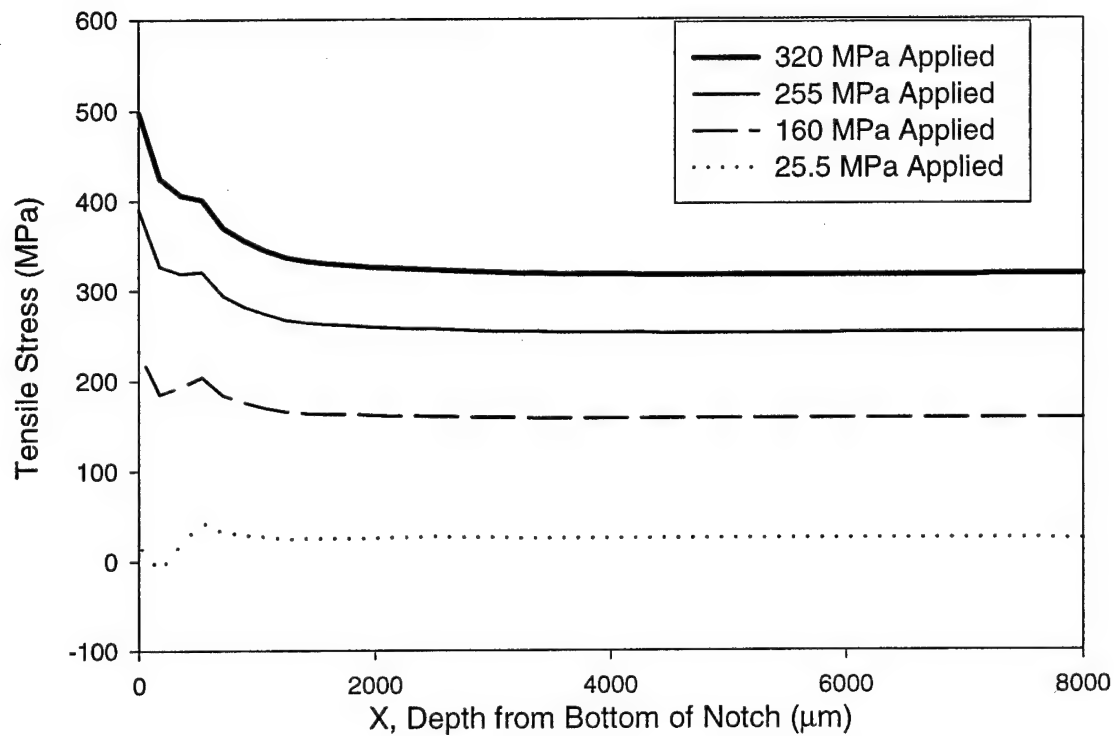


**Figure 112. Stress Distribution Due to Tensile Load; 2 mm Glass Sphere.** Stress  $\sigma_{yy}$  along  $y=z=0$  centerline associated with all applied load steps from Figure 110.



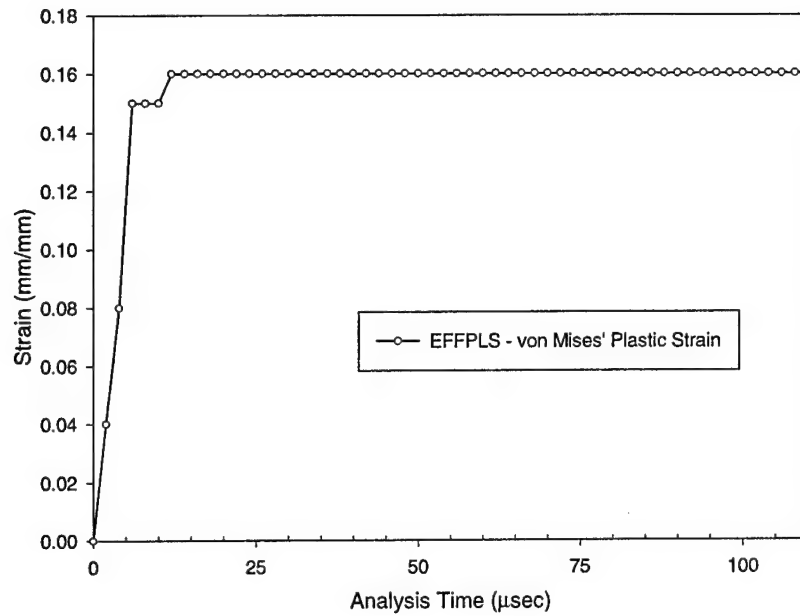


**Figure 113. Von Mises' Plastic Strain vs. Time; 2 mm Steel Sphere.**  
Again no further plastic strain occurs after the impact event.

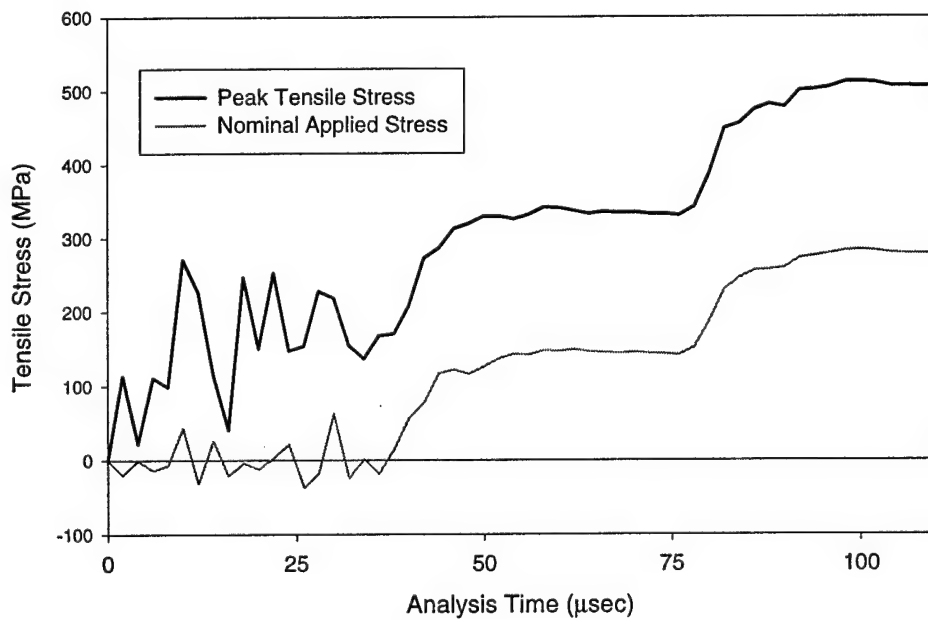


**Figure 114. Tensile Stress vs. Time; 2 mm Steel Sphere.** Nominal applied stress and peak stress are plotted over the time duration of the model.

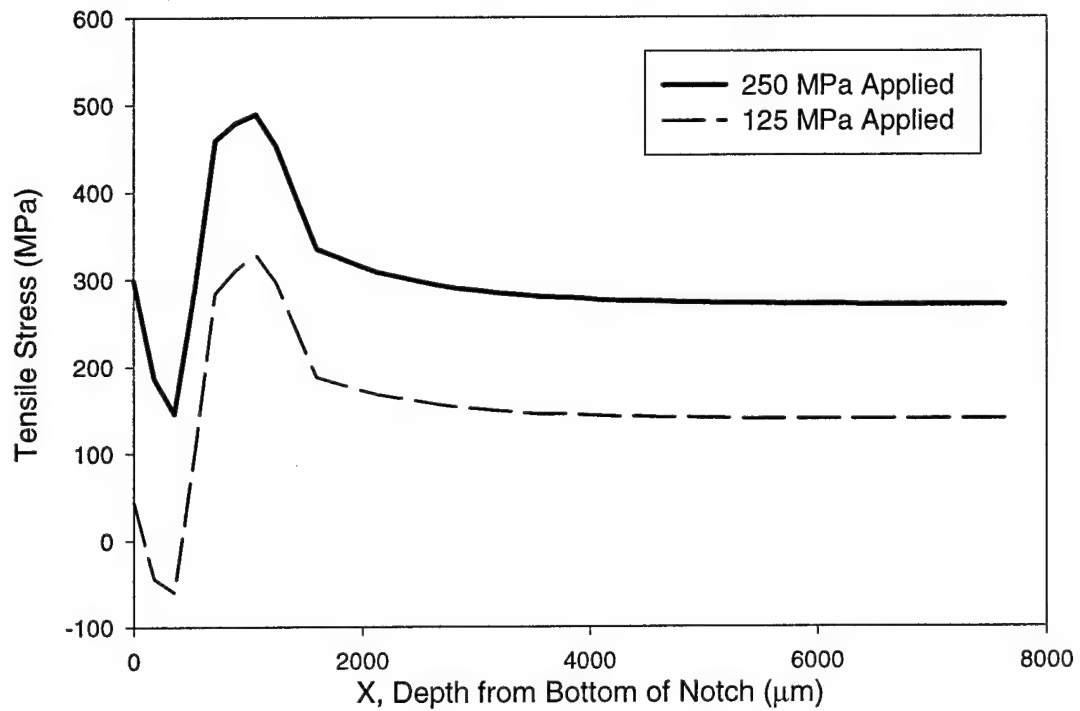


**Figure 115. Stress Distribution Due to Tensile Load; 2 mm Steel Sphere.** Stress  $\sigma_{yy}$  along  $y=z=0$  centerline associated with all applied load steps from Figure 112.

Table 10. Effective Stress States from Sphere Impacts

	Applied Stress (MPa)		Actual Peak Stress (MPa)	
	R	$\frac{\sigma \text{ min}}{\sigma \text{ max}}$		Effective R
5 mm Glass	0.5	100	284	0.51
		200	553	
	0.1	13	47	0.13
		130	366	
2 mm Glass	0.5	160	391	0.57
		320	681	
	0.1	25.5	148	0.26
		255	561	
2 mm Steel	0.5	125	343	0.66
		250	517	
	0.1	not tested		

## VI. FATIGUE STRENGTH OF SIMULATED FOD SPECIMENS

After creating the damage in the specimens, they were then subjected to accelerated fatigue strength testing as described earlier. The relationships plotted in Figure 78 between the damage quantity visible prior to fatigue testing,  $D_i$ , and those which could be found after the test,  $D_p$ , are summarized in Table 11.

Table 11. Damage Quantities Tested

Damage Type	Crater or Indent Depth ( $D_i$ ) - $\mu\text{m}^*$	Plastic Zone Depth ( $D_p$ ) - $\mu\text{m}^*$
1 mm chisel	180-600	550-1568
2 mm chisel	326-600	780-955
5 mm chisel	513-1020	1525-2053
2 mm glass sphere	701	453
5 mm glass sphere	833	782
2 mm steel sphere	742	383
4 mm steel sphere	1861	478
2 mm chisel shear	598-1500	264-416
* FOD mechanisms over which indent depth could be varied are shown as a range. FOD mechanisms where the damage was fixed by sphere velocity are shown as a single average.		

### Fatigue Strength Reduction.

The maximum stresses that Ti-6Al-4V can withstand under high cycle fatigue are obviously lowered by damage such as the simulated FOD studied in this effort.

Quantifying the amount of degradation begins by measuring the strength of undamaged Ti-6Al-4V.

*Undamaged Fatigue Strength.* Two independent variables need to be prescribed to describe a cyclic fatigue loading state. The most useful method for representing the undamaged fatigue strength in this case is the Haigh diagram described in Chapter II. The Haigh diagram in Figure 116 shows the fatigue strength of the undamaged Ti-6Al-4V used in this study. As mentioned in Chapter I, the batch of Ti-6Al-4V material researched in this effort is being studied by numerous investigators. Those results applicable to this study are plotted along with data collected in this study. They include results both at low frequency (50 to 60 Hz) (45; 54) and higher frequencies (350 to 400 Hz) (61).

In Figure 117, a 3rd order polynomial is fit by polynomial regression to the data from Figure 116. Prediction intervals about this line are also plotted. The band between these lines represents the region in which 99% of all future observations of undamaged fatigue strength would be expected to lie (64).<sup>5</sup>

*Effect of Chisel Indentation Damage.* Analysis of the fatigue strength data shows that the fatigue strength of the damaged Ti-6Al-4V correlates well with the total depth of damage measured by the location of the optical deformation band ( $D_d =$

---

<sup>5</sup> The regression and prediction limits were computed by SigmaPlot v4.00. The computations for confidence intervals assumed the data had a normal distribution of stress amplitude about the mean stress values. The SigmaPlot software package performed tests on the data to verify that this normal distribution assumption was valid.

$D_i + D_p$ ; see Fig. 58) but not with  $D_i$  or  $D_p$  individually as shown in Appendix H. In Figures 118 through 121, the maximum fatigue strength at which the specimens failed at a life of  $10^7$  cycles is plotted against  $D_d$ . This data is tabulated and plotted on a Haigh diagram in Appendix I.

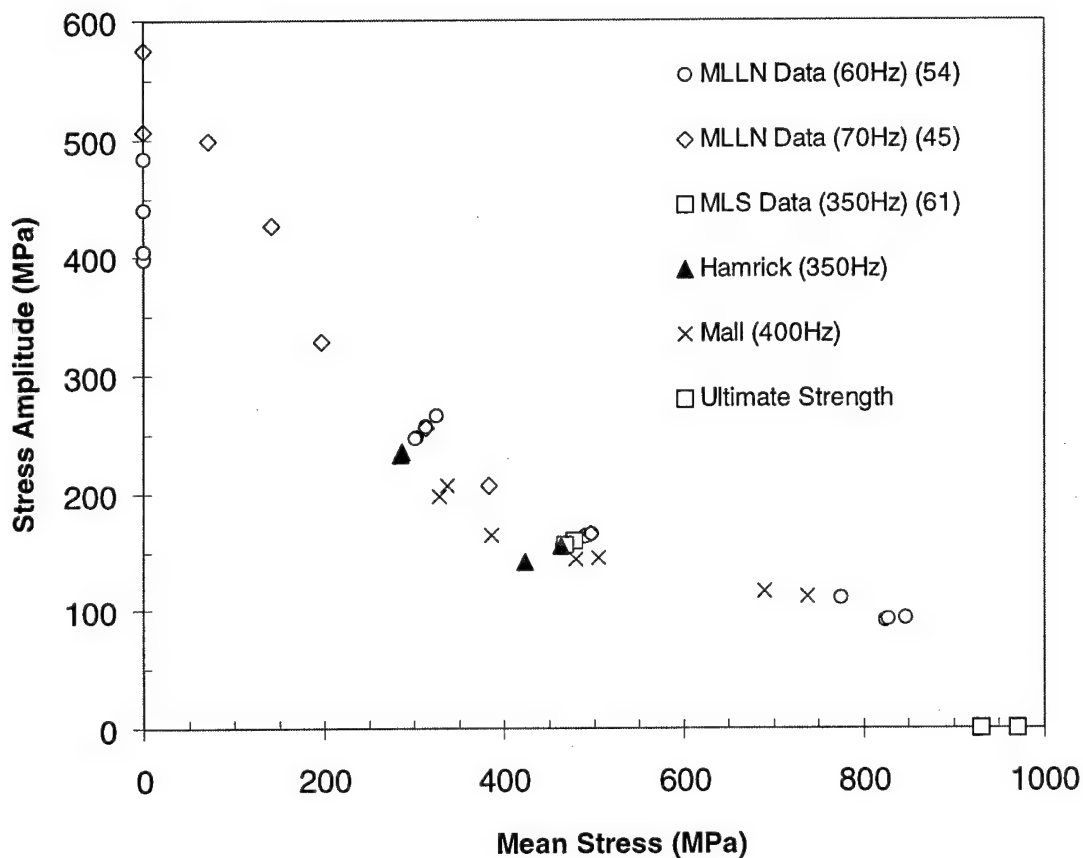


**Figure 116. Nicholas-Haigh Life Diagram - Undamaged Ti-6Al-4V.** This plot includes data generated by other investigators.

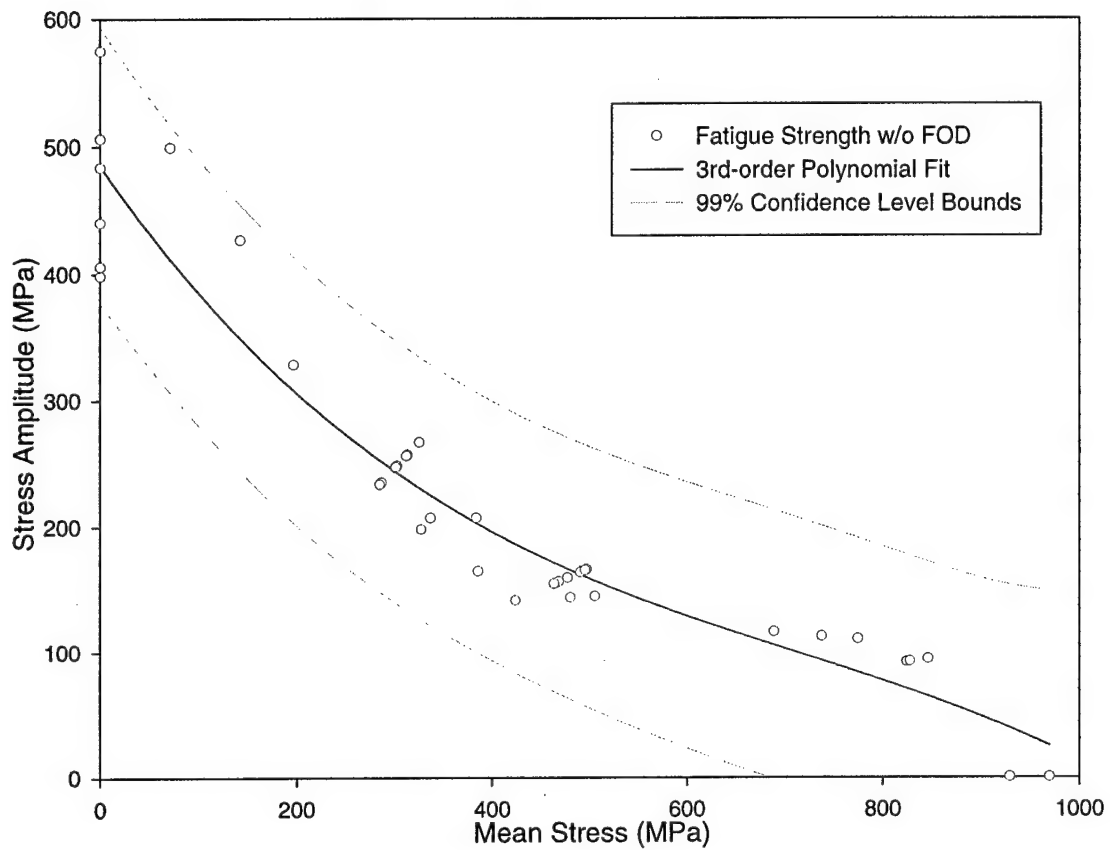


**Figure 117. Undamaged Ti-6Al-4V - 99% Prediction Interval.** The data from Figure 116 are plotted with bands representing the region in which 99% of future measurements would lie.

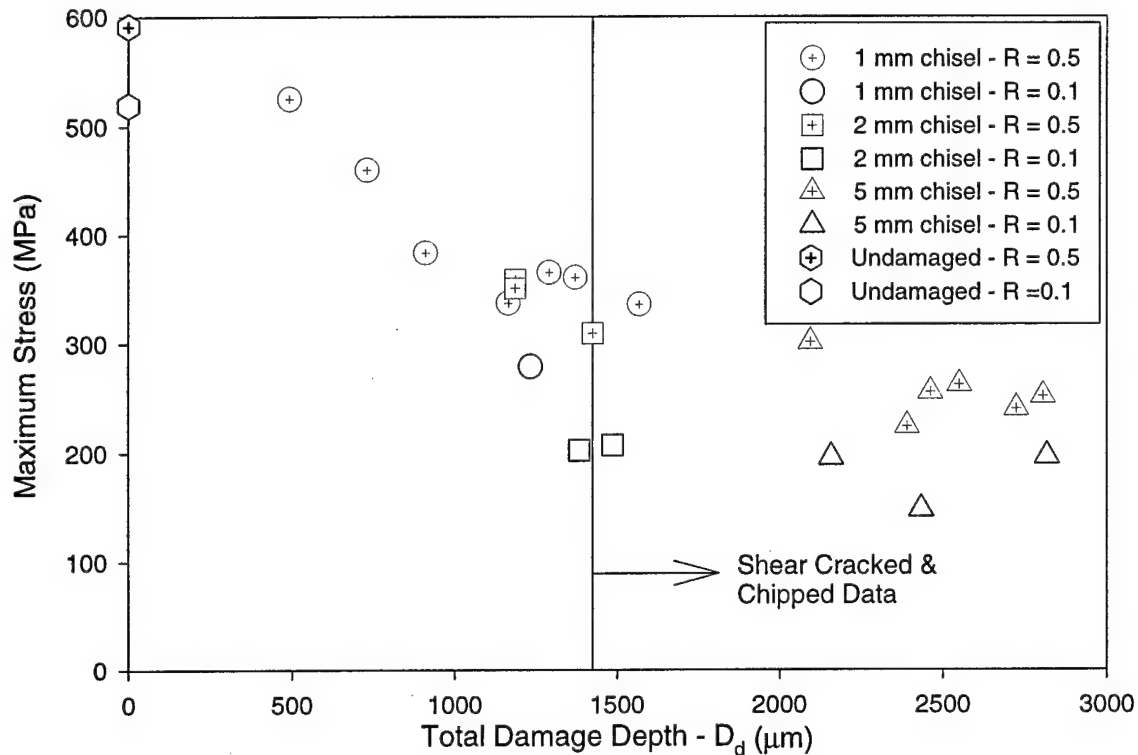


**Figure 118. Fatigue Strength vs.  $D_d$  for Chisel Indentations**

As expected, the 1 mm and 2 mm chisel indentations showed a decreasing fatigue strength with increasing damage depth. With a few exceptions noted below, this decrease is almost linear. What seems surprising at first is the limit reached by the 5 mm chisel indentations. For indentations with damage above 2000  $\mu\text{m}$ , increasing damage has little to no effect on the fatigue strength, which levels out at approximately 200 MPa  $\pm$  50 MPa. Also note that for the 1 mm and 2 mm diameter chisels, there is only slight dependence on the stress ratio, while the 5 mm chisels seem to form two thresholds, with the threshold for  $R = 0.1$  being about 50 MPa lower than that for  $R = 0.5$ .



The data at  $R = 0.5$  for the 1 mm chisel decrease with increasing  $D_d$  in a linear manner until  $D_d$  is about 1250  $\mu\text{m}$ , but data at larger damage depths rise above this line, seeming to form a new trend toward the 5 mm chisel data.

*Effect of Glass Sphere Damage.* The 2 mm and 5 mm diameter glass spheres show a far more linear correlation for the degradation in fatigue strength with increasing  $D_d$  than that seen in the chisel indentations (Fig. 119). Over the entire range of damage depth tested, a linear relationship with no discernible stress ratio effect is seen.

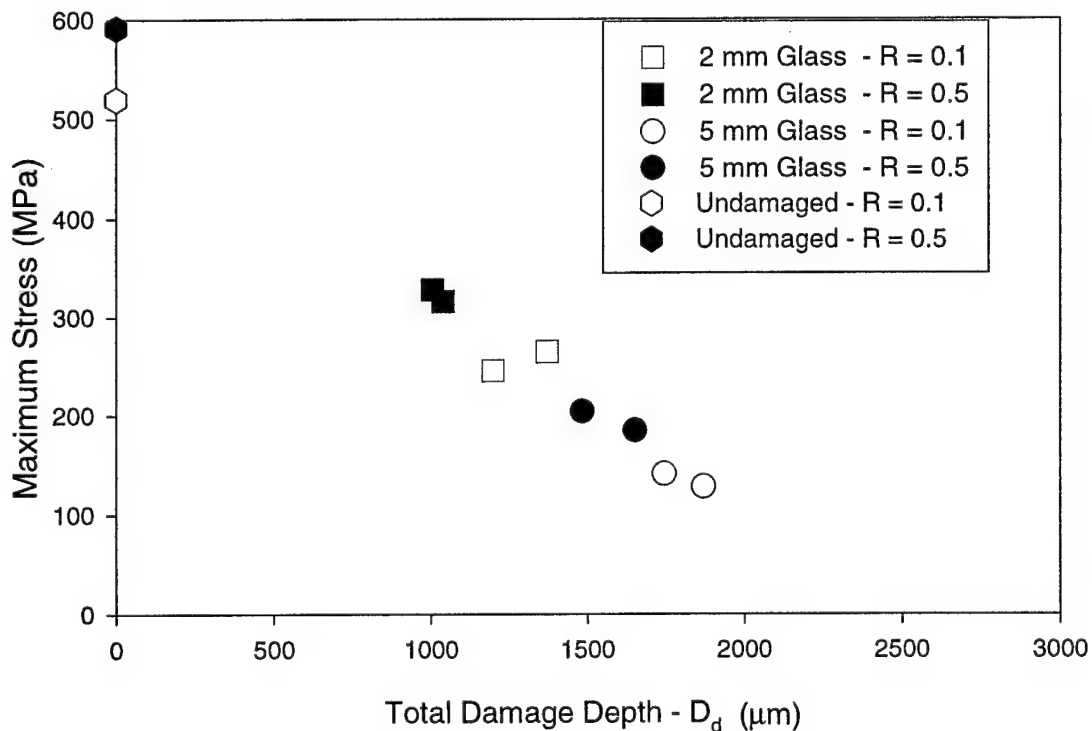


**Figure 119. Fatigue Strength vs.  $D_d$  for Glass Sphere Impacts.** A far more obvious linear trend appears here. No stress ratio dependence can be seen.

*Effect of Steel Sphere Damage.* Figure 120 shows the fatigue strength for the steel sphere damaged samples. The 2 mm sphere sample with the largest  $D_i$  did not survive for  $10^7$  cycles and is not plotted here. Consequently, there is no clear trend visible for 2 mm steel spheres when viewed by themselves. As will be shown later, however, these data points fall within the overall decreasing linear trend when plotted with all other damage data. The 4 mm steel spheres, which as it was shown in the last chapter exhibited chip shearing similar to 5 mm chisels, lie in the same region as the 5 mm chisel indents data.

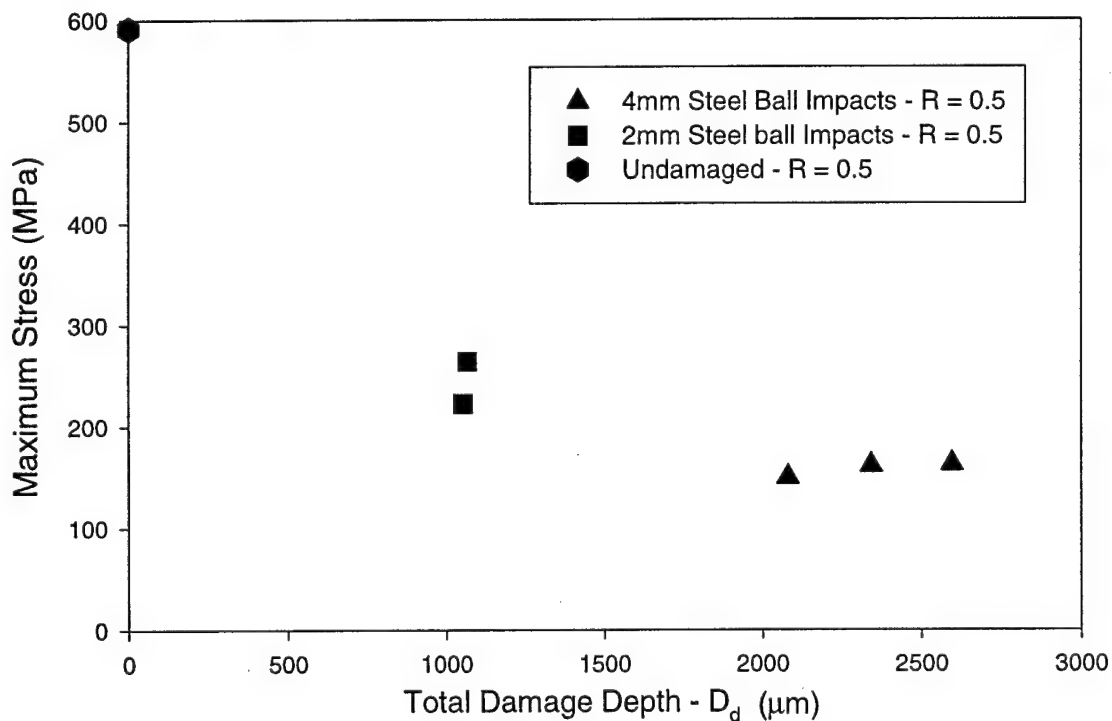


**Figure 120. Fatigue Strength vs.  $D_d$  for Steel Sphere Impacts**

*Effect of Chisel Sheared Notches.* Figure 121 shows again a decreasing trend of fatigue strength with increasing damage depth. Note that a clear stress ratio effect appears for depths less than 1500  $\mu\text{m}$ . The two data points larger than this damage depth are in the region in which chipped data from the 5 mm chisel lie. These data points coincided with sheared indents that extended past the point where the half-width of the notch was larger than the depth (Fig. 122). This may indicate a transition from one stress redistribution phenomena to another.

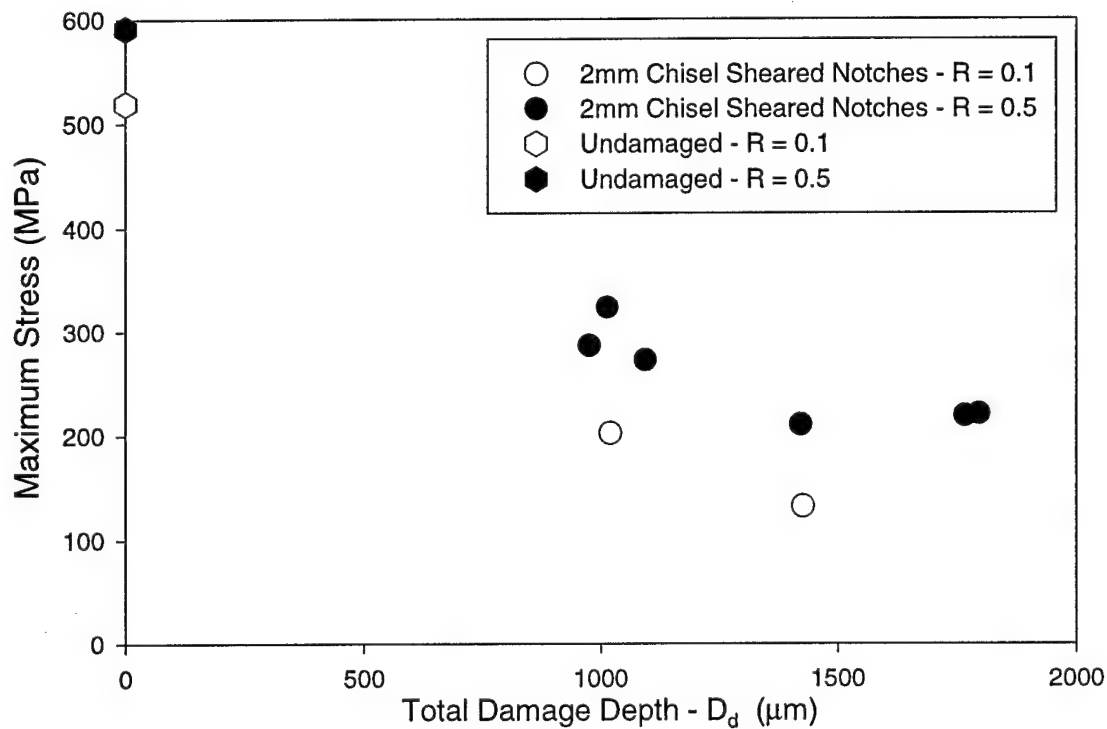


**Figure 121. Fatigue Strength vs.  $D_d$  for Chisel Sheared Notches.** From the plot of  $D_p$  vs.  $D_i$  (Fig. 77), the rightmost points resulted from a notch deeper than 1150  $\mu\text{m}$ . Figure 122 shows that this depth represents a change in the profile of the notch in this case from all other cases.

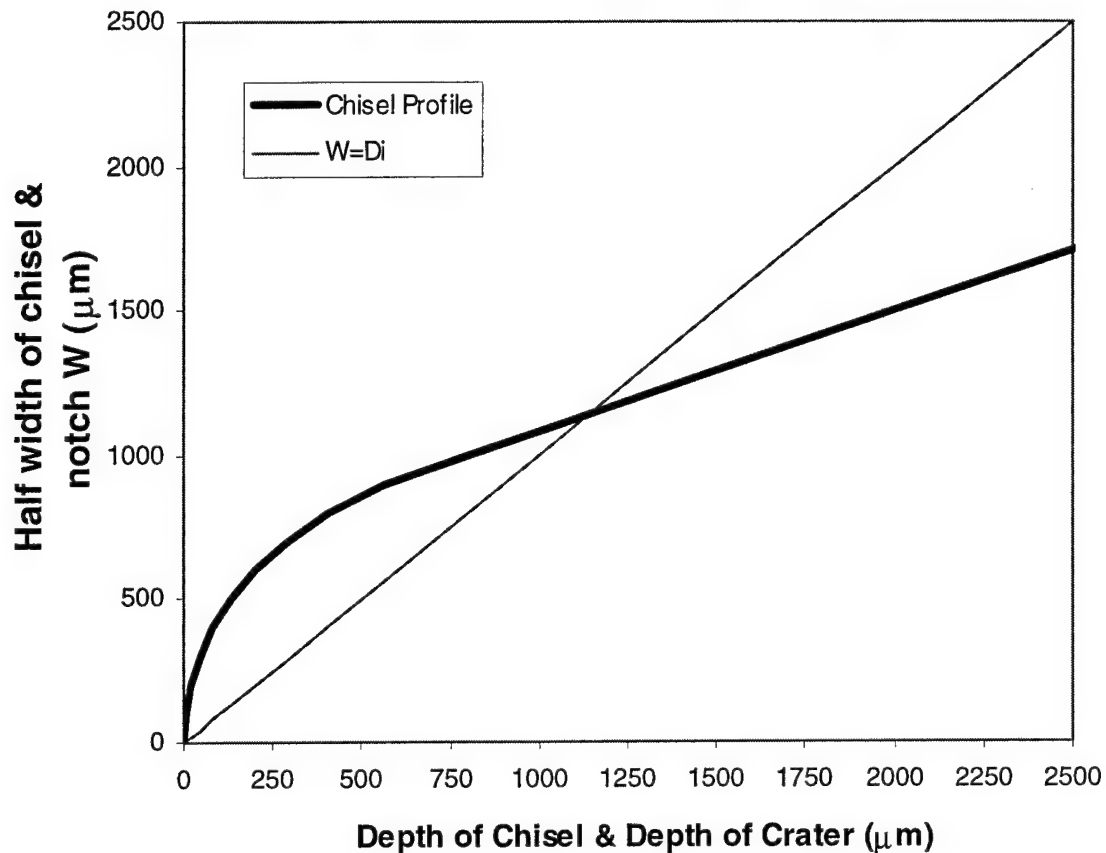


**Figure 122. 2 mm Chisel Profile.** The curved chisel profile represents the thickness of the 2 mm chisel versus the chisel length. The straight line represents those locations where the depth of chisel sheared notch equals the half-width of the notch. These two lines cross at 1150  $\mu\text{m}$ . The anomalous points in Figure 121 came from the notches created deeper than this.

### Analysis of Simulated FOD Effects

The individual trends shown in Figures 118 through 121 coalesce into a single trend for all simulated FOD types when all data are plotted together. No damage depths below 500  $\mu\text{m}$  were found to cause failure at the damage site; and at 500  $\mu\text{m}$  damage, the fatigue strength was within 11% of the undamaged value. A simple linear trend between the fatigue strength and depth appears between 500  $\mu\text{m}$  and 1750  $\mu\text{m}$ . This

trend encompasses all of the damage mechanisms tested except those that sheared loose discrete chips (5 mm chisel and 4 mm steel sphere). All other mechanisms - at both stress ratios 0.5 and 0.1 - can be expressed as a single line

$$\sigma_{\max} = c_0 + c_1 \cdot D_d \quad (19)$$

where  $c_0 = 629.7 \text{ MPa}$

$c_1 = -0.291 \text{ MPa}/\mu\text{m}$

The correlation coefficient computed by SigmaPlot (64) for this line is  $r^2 = 0.812$ .

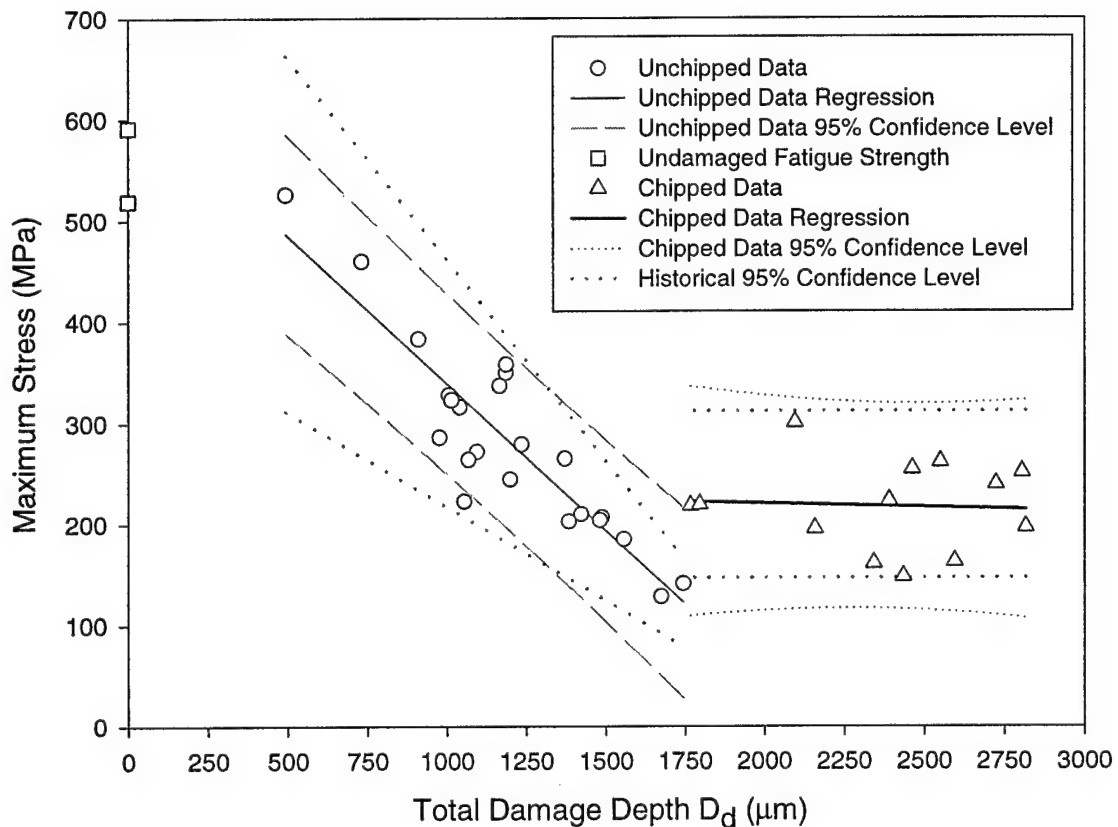


**Figure 123. Fatigue Strength vs.  $D_d$  for All Samples.** Here 95% confidence intervals are plotted for the two trends seen in the data. All damage mechanisms that did not create discrete chips fit a single line from  $D_d = 1750 \mu\text{m}$  down to the point where the simulated FOD data ends. The historical confidence level comes from multiple sources (26:308).

Along with the 95% confidence level for the data collected in this study, Figure 123 shows the variance in a large collection of historical fatigue strength data for Ti-6Al-4V. Fuchs and Stephens report a standard deviation (SD) in fatigue strength data equal to 18% of the mean value (26:308). The historical 95% confidence level plotted in Figure 120 represents  $\pm 2 \cdot \text{SD}$  about the line fit between  $D_d = 500 \mu\text{m}$  to  $1750 \mu\text{m}$  and about the average fatigue strength data above  $D_d = 1750 \mu\text{m}$ .

A slight stress ratio effect was seen when plotting the chisel indentation and chisel sheared data points separately. Figure 124 plots all data by stress ratio to investigate its effect on the overall trend. Here it can be seen that the stress ratio effects seen in Figs. 118 and 121 are smaller than the scatter in the overall data in the linear region described by Eqn. (19). The stress ratio effect can still be discerned in the transition region above  $D_d = 1750 \mu\text{m}$ , where the fatigue strength is essentially constant, and that constant is lower for  $R = 0.1$ .

Hudak et al. predicted a fatigue stress threshold below which fracture would not occur due to initiated cracks being unable to propagate (31). This threshold is based upon the geometric stress concentration factor from the notch alone, although they describe how the effects of residual stresses could be incorporated. A 'worst case notch' is hypothesized which could exist in a component subjected to fatigue, based upon recent work on the behavior of small fatigue cracks. That is, notches deeper than this worst case are predicted to fail by crack propagation, thus providing a threshold. Hudak et al. calculate this threshold to be about 160 MPa for notches

similar to the chipped data points above  $D_d = 1750 \mu\text{m}$  that are subjected to fatigue loading at  $R = 0.5$ . Figure 124 shows that indeed no specimens tested at  $R = 0.5$  failed at levels below this threshold.

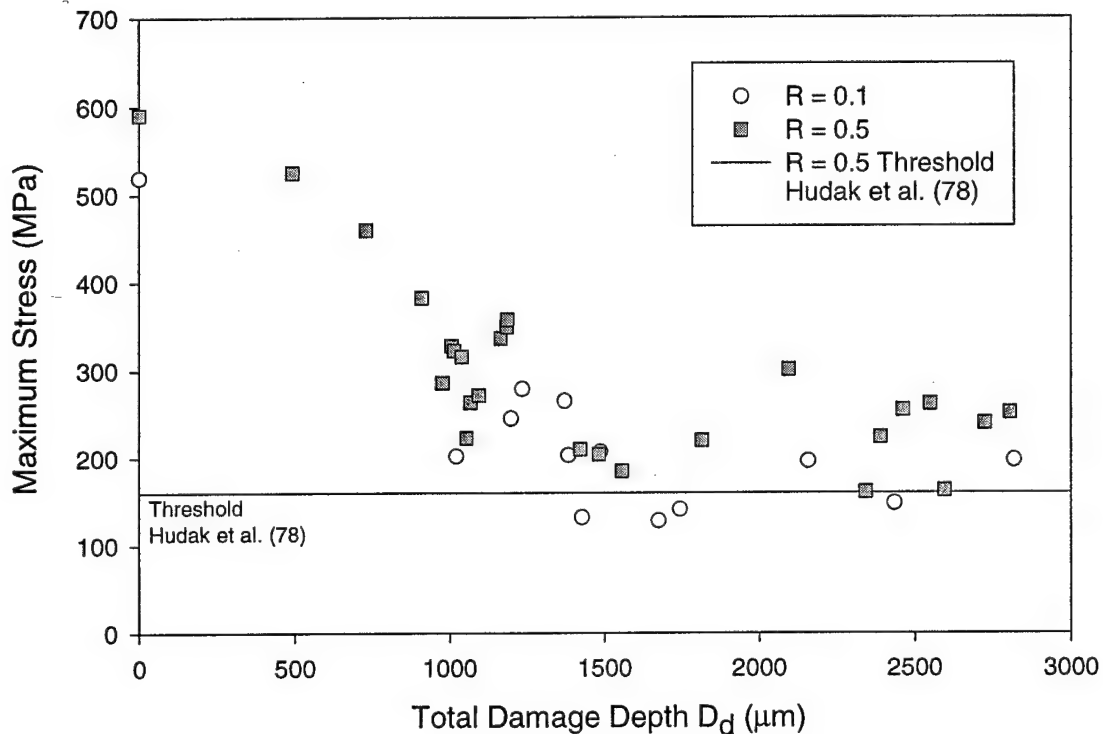


**Figure 124. Fatigue Strength Data Sorted by Stress Ratio.** When the data from Figure 123 is sorted by stress ratio, it can be seen that in the linear region stress ratio effects are minor. The undamaged fatigue strengths and the chipping dominated region above  $D_d = 1750 \mu\text{m}$  show a trend toward lower fatigue strengths for  $R = 0.1$ . Note the lower threshold stress for  $R = 0.5$  predicted by Hudak et al. (31).

Traditionally in the study of fatigue of notched members, the elastic stress concentration factor  $K_t$  or the fatigue notch factor  $K_f$  have been used to describe the effect of notches on the fatigue strength (17:399; 68:272). Texts on the subject always caution, though, that  $K_t$  ceases to be valid if large plastic deformation occurs in the notch vicinity (17). To verify that  $K_t$  is not valid in the case of simulated FOD,

the SCFs for the notches were computed, and the fatigue strengths predicted by this method compared to the actual data.

$K_t$  can be computed from the geometry of the notch. Reference (57) is an excellent source of tables compiling values of  $K_t$ . These tables used U-shaped notches with constant radii. This shape is the nearest representation to the physical shape of the notches created in this study. The SCFs computed this way are shown in Figure 125.

The relations between SCF and  $D_i$  from Figure 125 are used to plot the ratio (fatigue strength / SCF) as a function of  $D_i$ . If the SCF were sufficient to describe the degraded strength of the Ti-6Al-4V tested in this study, the data would lie along the lines plotted in Figures 126 and 127. At each stress ratio, three lines are plotted corresponding to the three radius cases as shown in Fig. 125. Note that 5 mm and 4 mm diameter data are grouped together. The data for damage at each radius would be expected to correlate to the line for that radius if the SCF were useful in describing the fatigue strength degradation.

The empirical relationships described above are intriguing and useful. They show that the fatigue life of a Ti-6Al-4V specimen can be predicted after suffering damage from any of the simulated FOD methods studied here by a simple relationship, which starts at the undamaged fatigue strength for Ti-6Al-4V. The predicted value proceeds along the line described by Eqn (19) down to the threshold limit seen for total damage more than 1750  $\mu\text{m}$ .



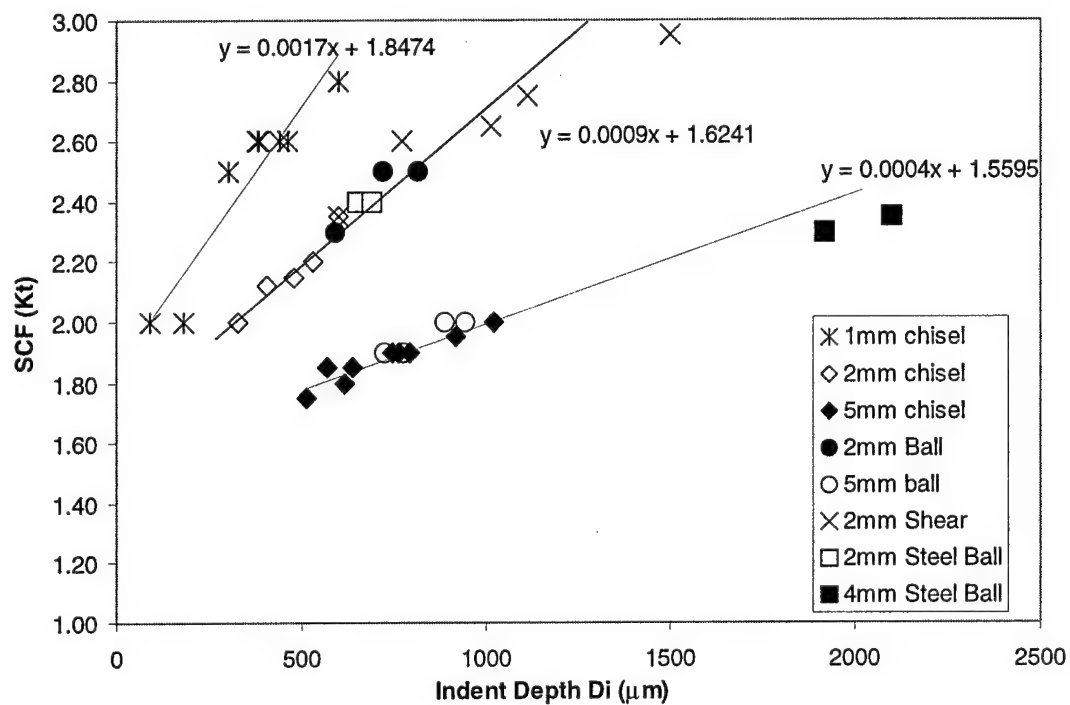


**Figure 125. Elastic SCF Measured from Notch Dimensions.** These values of  $K_t$  were determined from the physical dimensions of the notches using tables from (57:35-36). Notches of similar radius increased with depth  $D_i$  along a common line.

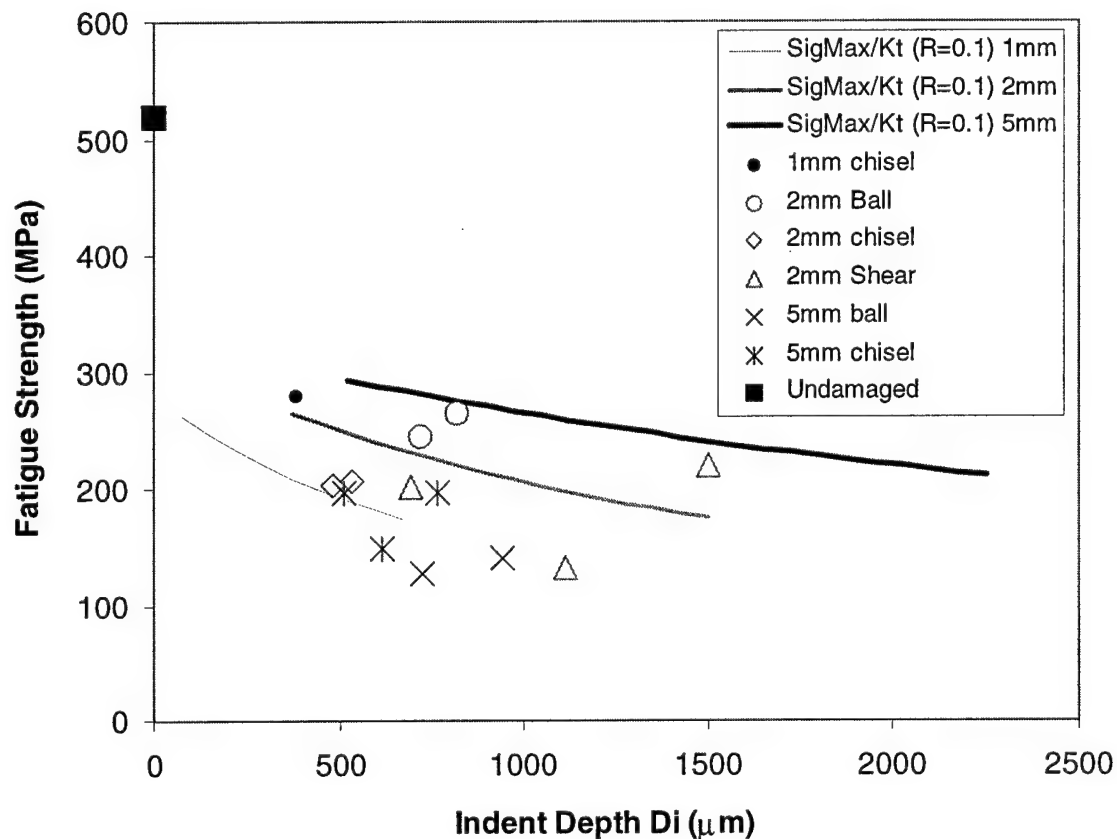


**Figure 126. Fatigue Strength vs.  $D_i$  with SCF -  $R = 0.1$ .** The SCF lines from Fig. 125 are used here to plot lines of  $\sigma_{\max}/K_t$  as a function of  $D_i$ . If the SCF described the crack initiation stresses in the simulated FOD, the lines for 1 mm radius damage should lie near the line of  $\sigma_{\max}/K_t$  for 1 mm, and so forth. They clearly do not.

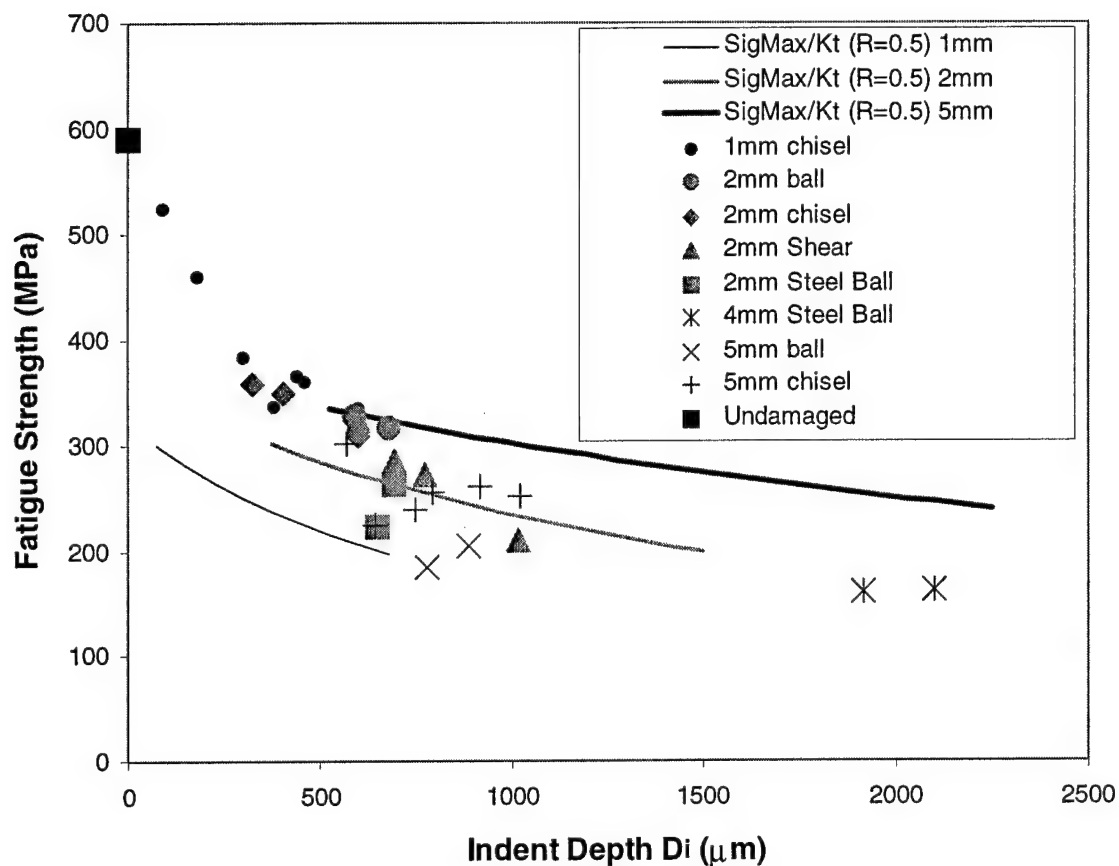


**Figure 127. Fatigue Strength vs.  $D_i$  with SCF -  $R = 0.5$ .** The SCF lines from Fig. 125 are used here to plot lines of  $\sigma_{\max}/K_t$  as a function of  $D_i$ . As in Fig. 126, the lines for 1 mm radius damage should lie near the line of  $\sigma_{\max}/K_t$  for 1 mm, and so forth. Again there is no clear relation between the data and SCF computed simply from the physical dimensions of the notch. Figs. 126 and 127 also indicate that there is no apparent correlation between the damaged specimens' fatigue strength and the indent depth  $D_i$ . This is contrasted with the linear decreasing - threshold trend seen in Figs. 123-124.

These fatigue data were also evaluated in a different manner by using the states of stress computed by finite element analysis. As described in the last chapter the

applied stresses create local stress states with different maximum values and stress ratios.

Back in Chapter V in Tables 9 and 10 the actual peak stresses predicted by finite element analysis of the chisel indentations and three of the four sphere impact cases are listed. When these peak stress states are plotted on a Haigh diagram along with the applied stresses that created them, these peak stresses move data points as shown in Figures 128-129. Most of these corrected points lie in the region corresponding to the fatigue strength of undamaged material plotted in Figures 116-117. Figure 128 plots both data sets from the peak stress states in the plastic zone and those from the peak stress in the elastic region of the chisel indentation models as described in Table 9. Figure 129 plots the peak stresses from the dynamic models as given in Table 10. The material in the damaged region has been severely strained, and may no longer have the same fatigue strength properties as those of undamaged Ti-6Al-4V. Future efforts to evaluate the fatigue strength of severely compressed Ti-6Al-4V are underway, although no results are available yet (54). Lacking the data at present, it will be assumed here that the fatigue strength shown in Figure 116 represents the behavior of the material in the damaged zone also.

These two figures indicate that the cause of crack initiation at any given applied stress for specimens with simulated FOD damage is the result of the creation of a state within the specimen where the peak stresses increase to the level which is

known to initiate cracks in Ti-6Al-4V. Most importantly, accurate predictions of these states can be accomplished by appropriate finite element analysis.

Finally, note that from Figures 95-97, 102, 104 and 106, the location of the maximum tensile stresses was not always the bottom of the notch. Appendix J describes the locations where the maximum stresses were most often seen, and lists the actual sites of the fatigue crack initiation seen in the experimental specimens.

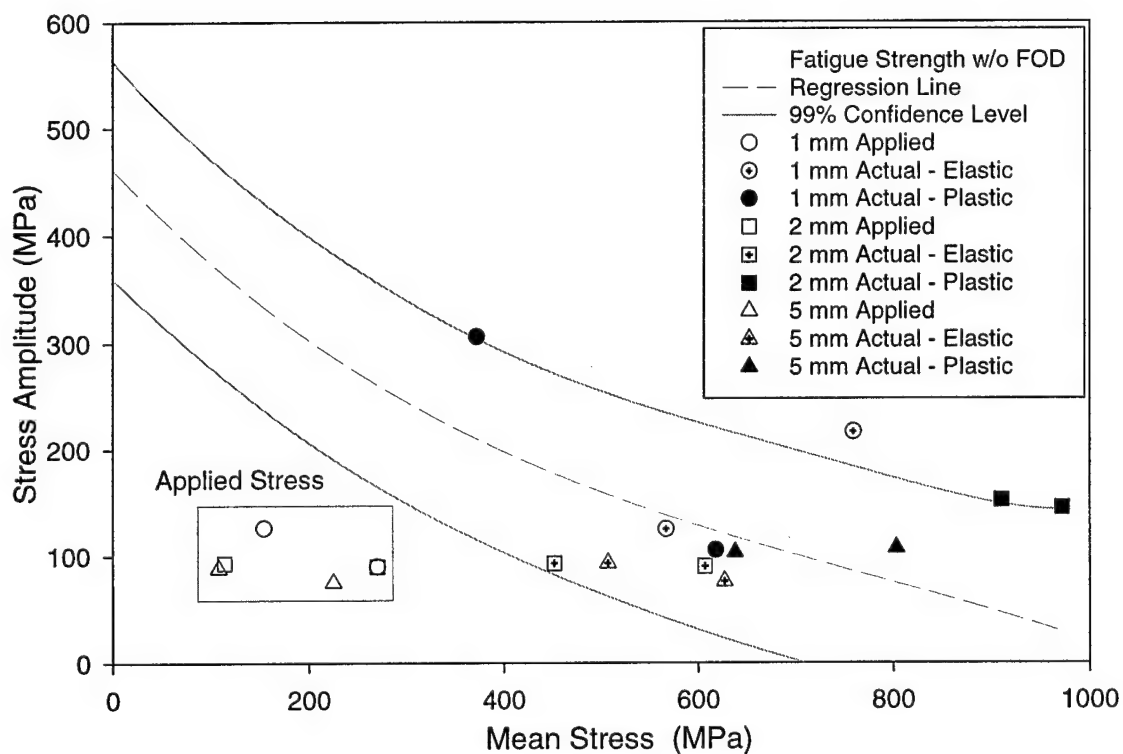


**Figure 128. Actual Tensile Stress State Shift - Chisel Indents.** The FEM conditions are plotted on a Haigh diagram along with the 99% prediction band for the actual undamaged Ti-6Al-4V data. The stress states in the box in the lower left are the representative loads applied to the finite element models. The remaining points are the peak stress states predicted to exist within the damage zone and just behind it from Table 9. The FEM model predicts that the nominal stresses which fractured the specimens all correspond to a stress state in the interior of the specimen which meets or exceeds the stress state known to initiate cracks in undamaged Ti-6Al-4V.

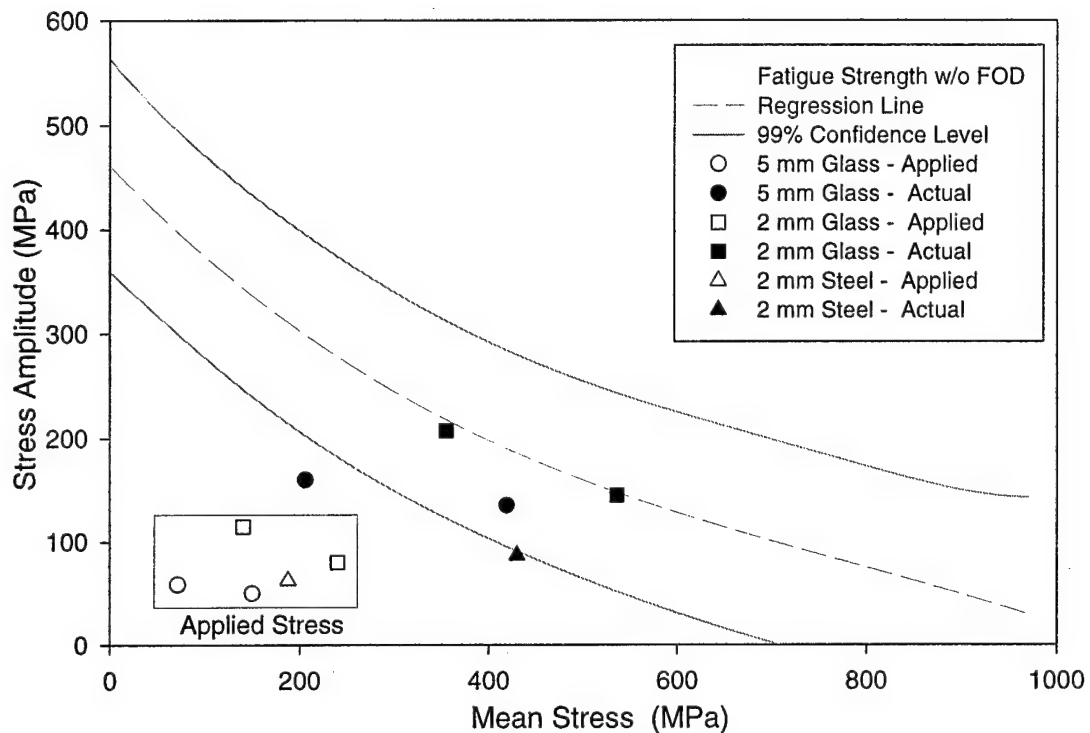


**Figure 129. Actual Tensile Stress State Shift - Sphere Impacts.** The FEM conditions are plotted on a Haigh diagram along with the 99% prediction band for the actual undamaged Ti-6Al-4V data. The stress states in the box in the lower left are the representative loads applied to the finite element models. The remaining points are the peak stress states predicted to exist within the damage zone and just behind it from Table 10. The peak stresses predicted by the dynamic model are slightly lower than those from the quasi-static model, but still lie in or near the predicted band for the stress states which fail undamaged Ti-6Al-4V.

## ***VII. SUMMARY***

The combined effect of foreign object damage (FOD) and high cycle fatigue (HCF) loading on engine blades is a major safety and reliability issue in aircraft turbine engines. An analytical approach to evaluate the FOD resistance of a component subjected to HCF loading is critical to the development of improved engines and proper maintenance of existing engines.

Prior to this study, several phenomena related to the mechanics of materials were suspected to play an important role in the reduction of the high cycle fatigue life of turbine engine components such as blades made from Ti-6Al-4V. These phenomena included the stress concentrations due to the geometry in the vicinity of a notch created by FOD. The change in stress due to the residual stress field created by the FOD damage was also believed to play a role in the high cycle fatigue behavior, but the exact contributions of these were uncertain. Finite element modeling of damage from FOD had not been proven to accurately represent these residual stress fields, and the ability to measure residual stresses on the scales needed to determine their role in HCF are still being developed. Different methods of simulating FOD for laboratory testing had not been compared with each other to determine if fatigue strength test results of specimens so damaged could be related to each other. This study has addressed these concerns by accomplishing the following tasks:

1) Investigated damage in flat rectangular specimens of Ti-6Al-4V by four different means of simulating FOD:

- from impact by 1 mm, 2 mm and 5 mm diameter glass spheres at 305 m/s (which has been considered the most faithful representation of real FOD from sand or gravel).
- from impact by 2 mm and 4 mm diameter steel spheres at 305 m/s (a good simulation of damage from rivets or other metallic objects).
- by quasi-statically indenting the specimen edges with steel chisels having tip radii of 0.5 mm, 1 mm and 2.5 mm.
- by shearing a notch from the specimen edges with a 1 mm radius chisel.

2) Quantified the damage by three different techniques:

- optical observation of the effects of shear straining on the fatigue fracture surface, an easy to apply method that has not been previously reported
- measuring the change in grain size through the plastically damaged zone
- finite element calculations of the plastic damage zone extent

3) Tested these specimens at 350 Hz to determine their fatigue strength at  $10^7$  cycles.

4) Analyzed the glass and steel sphere impacts and chisel indentations with three-dimensional elastic-plastic finite element models and verified the ability of these models to accurately describe the FOD event.

5) Used these finite element models to understand the effect of the residual stress state on the failure of the damaged specimens and determined a criterion to predict HCF failure of Ti-6Al-4V after damage by simulated FOD.

The conclusions from this study are summarized in the following:



## **Damage Quantification**

The four damage methods created seven distinct damage mechanisms. A summary of each mechanism are as follows:

- 1) Chisels with 1 mm and 2 mm diameter tips indented the Ti-6Al-4V specimens with circular cavities and transverse bulges from Poisson's effects. Shear stress induced cracking occurred in some cases at the larger indentation depths, but the cracks did not extend through the thickness of the specimens.
- 2) The 5 mm diameter chisels created shear cracks that generally extended through the thickness of the specimens. Many samples had chips of material cleaved completely from the specimen.
- 3) The 1 mm diameter glass spheres created no erosion of the specimens, merely indented the surface. The level of damage due to this method was not found to cause any failure at the damage site during fatigue testing.
- 4) The 2 mm and 5 mm diameter glass spheres eroded the specimen surface by hydrodynamic flow of small particles created by spallation of the spheres upon impact with the specimen. Although it was desired to hold the impact velocity constant, difficulty in doing so created a range of velocities, which led to a range of crater depths. The plastic zone sizes associated with the damage increased monotonically with crater depth.

- 5) The 2 mm steel spheres eroded semicircular craters similar to the 1 mm and 2 mm diameter glass spheres.
- 6) The 4 mm steel spheres also created semicircular craters, but past the root of the notch made by the crater, a chip of material identical to that made by the 5 mm chisel was removed.
- 7) The 2 mm diameter chisel used to shear the specimens created smooth surfaced notches with a damaged region of a uniform size over the entire range of notch depths tested.

Evaluating the plastic strain by measuring the change in average grain size was not demonstrated to work well for Ti-6Al-4V. The plastic strain was deduced as the average difference between the size of each strained grain and the average size of the unstrained grains in the same orientation. Because of the large variation in the size of the undeformed grains in the specimens tested in this study, the approximate strain values computed had large uncertainties associated with them.

The surface exposed after fatigue fracture on specimens damaged by simulated FOD exhibited nonuniform reflectivity characteristics under highly polarized light. This reflectivity was developed into a novel method to directly observe the demarcation between the unstrained material and that material that had suffered plastic deformation. The location of this border was found to correspond to the distance at which the strains computed by finite element analyses were equal to 12% to 2% compressive plastic strain in the case of the chisel indentation analysis, and 0.6 to

0.2% von Mises' effective plastic strain for the sphere impact analysis. This demarcation also was found to coincide with shear bands created in the plane of the fracture surface. The distances to these bands were also compared to finite element models of the plastic strain distribution. The damage size obtained by all three techniques agreed within each measurement's limits. The distance from the surface of the specimen to this damage level was taken as the total damage depth.

Despite the wide range of damage mechanisms seen, the relationships between the notch depth and the size of the plastic damage zone grouped together into a few trends. The glass sphere impacts and the steel sphere impacts that did not cleave material from the notch resolved into a common monotonically increasing trend. The chisel indentations that did not cleave material from the specimens also share a common, nearly linear trend. Chisel indentations that did cleave material from the specimens also increased linearly when the indentation depth is less than 770  $\mu\text{m}$ . Above this, increasing depth affected plastic damage zone size less, and the trend followed a different, flatter slope. The notches sheared by the transverse chisel had a plastic damage zone size independent of the notch depth. The steel spheres that cleaved material from the specimens also appeared to have a constant plastic zone size, although the number of data points for this mechanism was very limited.

Depending upon the method used to simulated FOD, there will be different sizes of plastic damage zones created, but this study verified three techniques for measuring

these damage zone sizes, and showed that simple relationships exist to infer the plastic zone size from the notch depth.

### **Finite Element Analysis**

Quasi-static and dynamic finite element analyses of three of the FOD simulation techniques were conducted. These models were created using known material properties of the bodies being simulated and appropriate boundary and initial conditions to model the FOD events. The models yielded accurate values for the physical dimensions and damaged zone sizes of the notches in the experimental specimens, thereby validating the models' ability to reproduce the damage events. The models of the damaged specimens were then subjected to tensile loading identical to the loading conditions that caused fatigue failure in the damaged experimental specimens.

The finite element calculations of the stress state created by these tensile loadings in the vicinity of the damage produced peak stresses different from those applied. The stress states were also different from the stresses that would be predicted by the elastic stress concentration factor associated with the notches. Local stress ratios produced by the actual stresses in this damaged zone were compared to the stress conditions known to cause fatigue failure in undamaged Ti-6Al-4V. This predicted fatigue limits of the damaged specimen from smooth bar fatigue data. This clearly indicates that by calculating the real stress state in Ti-6Al-4V that has been damaged by simulated FOD, the conditions under which it will fail from high cycle fatigue can

be predicted. This failure will occur when the stress state in the vicinity of the damage is as severe as the fatigue strength of undamaged Ti-6Al-4V. When data on the fatigue strength of damaged material would be available, this failure criterion should be even more precise.

### **Fatigue Strength**

The fatigue strength evaluated on undamaged Ti-6Al-4V in this study agreed very closely with data obtained by other investigators using this material. The variability in the fatigue strength values was well within established bounds seen in previous works.

The total depth into a specimen from its edge to the maximum extent of the plastically deformed zone ( $D_d$ ) was found to be a damage quantification parameter that yielded a simple empirical relationship with the reduction in fatigue strength. Simulating FOD in laboratory specimens cannot be accomplished using any method other than the expensive technique of impacting specimens with representative foreign objects if the depth and shape of the notch are the only quantities matched. It is clearly the size of the notch plus the size of the plastic damage zone together which reduces the fatigue strength of Ti-6Al-4V. But when the parameter  $D_d$  is used, damage created by all techniques investigated in this study produced identical reductions in fatigue strength, within the statistical variation.

The chisel indentations created a degradation in the fatigue strength with a monotonically decreasing relationship to the total depth of damage in the specimen.

A slight dependence upon the stress ratio at which the fatigue testing was conducted appeared in specimens damaged this way. Specimens with smaller amounts of damage showed a reduction in fatigue strength proportional to the damage. As the amount of damage increased, shear cracking began to appear. After the onset of this cracking, the fatigue strength decreased at a slower rate, eventually reaching a nearly constant value at the largest damage sizes.

The relation between fatigue strength and total damage depth for specimens damaged by both diameters of glass spheres was also linear, and did not show any stress ratio dependence. This included the 2 mm diameter steel sphere data as well. All these data points shared similar damage mechanisms, which were dominated by the erosion of the specimen as the spheres impacted.

The 4 mm diameter steel spheres showed a damage mechanism different from the 2 mm steel spheres. The 4 mm steel spheres not only eroded portions of the specimens, but a large portion of the notches were created by cleaving a chip of material from the specimen, just as the 5 mm diameter chisels. The fatigue strength data also coincided with the 5 mm diameter chisel fatigue strength data.

The notches sheared with the 2 mm diameter chisel showed the strongest indication of a stress ratio dependence of any technique. Like the chisel indentation damage, they showed a tendency for the fatigue strength at larger damage depths to increase above the level expected from the general trend of the data.

The smallest amounts of total damage that could be generated were about 500  $\mu\text{m}$  (92  $\mu\text{m}$  notch depth with 400  $\mu\text{m}$  plastic zone). At these levels of damage, the fatigue strength is nearly the same as undamaged Ti-6Al-4V. At greater damage depths, all damage mechanisms evaluated in this study show a linear decrease in fatigue strength with increasing damage depth until it reaches 1750  $\mu\text{m}$ . Although a stress ratio effect was seen in the chisel indentations and sheared notches when plotted separately, this effect on fatigue strength was smaller than the variation in the fatigue strength data from all damage types taken as a whole.

At damage depths larger than 1750  $\mu\text{m}$ , a threshold appeared below which no specimen failures occurred. The 5 mm chisel and 4 mm steel sphere impacts exhibited the lowest fatigue strengths seen in this study, although the levels were higher than would be predicted based upon the trend describing all the other data. This may be because these notches approach the 'worst case notch' conditions; i.e., notches with initial cracks that will not propagate at stresses below the threshold level.

The elastic stress concentration factor based upon physical notch dimensions had no relationship to the measured fatigue strength. The relationship between damage depth and fatigue strength results from the manner in which the plastic deformation behind the notch increases the actual peak stress in the specimen. The true peak stresses in the damage zone created in the specimens, as calculated by finite element

analysis, were found to be equal to the actual stress states that caused failure in undamaged Ti-6Al-4V.

Impacts by glass spheres between 2 mm and 5 mm in diameter and 2 mm diameter steel spheres at realistic FOD velocities can be simulated more economically by indentation techniques that use chisels of various radii to create damage so long as the total damage depth is matched, not the visible crater dimensions.

Although the leading edge specimens were not subjected to FOD and fatigue tested, the experimental and numerical work performed on the rectangular cross-sectioned specimens should be directly applicable. The total damage depth may be expected to increase with notch depth at a rate different from that seen in this study, but the total damage depths obtained in simulating FOD on leading edge specimens should still be the primary factor determining the reduction in fatigue strength. Modeling a leading edge specimen using the techniques described in this study should likewise predict the specimen's fatigue strength when the peak stresses computed exceed the criteria for failure of undamaged material as plotted on a Haigh diagram.

In summary, this study has contributed to four major aspects of the effects of FOD on HCF.

- 1) The validity of numerical modeling to compute the residual stress field created by FOD has been demonstrated, and the importance of the residual stresses on the fatigue strength of Ti-6Al-4V has been confirmed.



- 2) The existence of a threshold stress for Ti-6Al-4V that has suffered large amounts of damage is also indicated - a potentially very useful result for engine design.
- 3) A parameter was found by which the damage from four different FOD simulation techniques could be equated. It was determined that damage from one FOD simulation technique should not be correlated with damage created by another technique by merely creating notches with equal physical dimensions, but rather that the total damage consisting of the notch depth plus the size of the plastic damage zone is the quantity which must be matched.
- 4) Use of this total damage depth parameter will allow the use of inexpensive and easily controlled methods of simulating FOD to replace more difficult and expensive means.

## ***APPENDIX A: Processing of the HCF Program Ti-6Al-4V***

*(The entirety of this appendix is condensed from Summary of the Available Information on the Processing of the Ti-6Al-4V HCF/LCF Program Plates (21) by Daniel Eylon of the University of Dayton Graduate Materials Engineering Faculty. All table and figure numbers are those of the original source and not connected to the numbering scheme in this text.)*

---

The sources for this data summary include reports, memos and conversations with the following organizations: AlliedSignal, General Electric, Textron Turbine Engine Components, AFRL/MLLN and HCF/LCF program reviews.

### **PLATE PROCESSING**

#### **BILLET MATERIAL**

The forging stock material was a double VAR melted Ti-6Al-4V Heat No. TE01 2.50" diameter bar stock from Teledyne Titanium, produced in accordance with AMS4928.

It was supplied in random lengths of 10' to 14', in mill annealed condition: 1300F/2 Hr/AC, with no traceability of the bar segments to the location in the ingot. This is believed to be the practice in the gas turbine engine industry.

Chemistry was acceptable in accordance with AMS4928 and is reported in detail in Table 1.

Table 1: Chemistry of Teledyne Titanium Heat No. TE01						
Element	Ti	Al	V	Fe	O	N
Top	bal.	6.27	4.19	0.20	0.18	0.012
Bottom	bal.	6.32	4.15	0.18	0.19	0.014
AMS4928	bal.	6.50-6.75	3.50-4.50	0.30 max	0.20 max	0.050 max

Hydrogen measured on bar stock delivered was 0.0041%. Specs max is 0.015%.

The ingot beta transus temperature, from DTA: Top - 1814 °F; Bottom - 1837 °F.

Table 2: RT longitudinal tensile (5N) from 5 positions along the ingot				
	UTS (ksi)	TYS (ksi)	EL (pct)	RA (pct)
Average of 5	143.9	132.0	19.1	42.9
Minimum	142.8	130.9	18.4	41.8
Maximum	146.2	134.6	20.4	44.4

### 3.2. FORGING (1720F)

The 2.5" diameter segments, with random length, were cut into 200 16" long forging preforms. The forging was done on a 16" long closed-end channel-die, with the intended plate size of 16.0"x6.0"x0.80". This was intended to follow with a post forging heat treatment to produce a final microstructure consisting of 60% +/- 10% primary alpha for optimum fatigue properties. It was to be followed by a vacuum anneal at 1300F/2hr to stabilize microstructure and normalize hydrogen content that might have been picked up during the descaling stage.

The 16" plate length was determined by the die's closed-end length. The width was slightly short of 6", and because of die friction the plates were somewhat narrower at their ends. The average strain rate at impact (for plain strain case) was 8.6/sec.

Textron forged all 200 pieces in one campaign, with dies initially heated to 300F. Glass-lubricant coated bars were preheated to 1720F +/- 20F for 30 minutes in a continuous furnace and rapidly transferred to the press. After a one stroke forging, the pieces were simply air-cooled. This is the standard practice for both GE and P&W fan blade forging. Textron used plate #17 for microstructural, transus and heat treatment evaluation.

### 3.3. HEAT TREATMENT

Microstructural evaluation of #17 showed about 52% primary alpha that varied with location as a possible result of temperature gradients, and different levels of work. This justified the subsequent RA treatment, which is not an industry standard practice, to provide study material with no concern about location-to-location microstructural variations. As it will be later seen, actual forged fan blades, typically, undergo only 1300/2hr mill-anneal, leading to a more elongated primary alpha structure and possibly to a different crystallographic texture.

#### 3.3.1. Beta Transus Determination

In order to facilitate subsequent heat treatments to achieve the goal primary alpha content, a transus approach curve was established using. Textron cut #17 into several

pieces and soaked each for 60 minutes at temperatures below the reported beta transus. A summary of this work is in Figure 1.

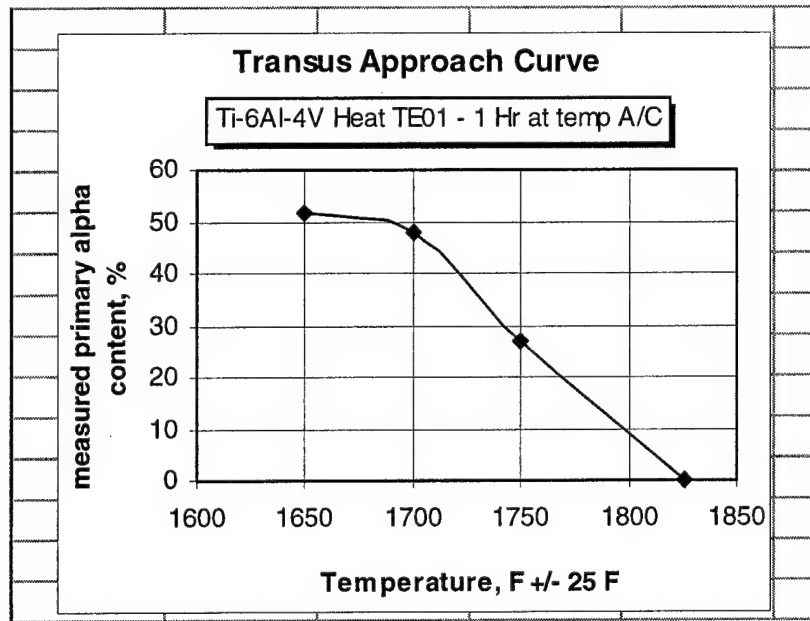


Figure 1. Beta transus approach curve for heat TE01. Three sub transus temperatures were used and combined with the average reported transus to produce this curve. The heat-treated samples were rapidly cooled from the solution temperature. Point intercept method was used on metallographically prepared samples for % primary alpha determinations.

### 3.3.2. Solution Treatment (1700F/1hr)

Based on a goals of the program: to achieve first a uniform primary alpha content and secondly a level near 60%, and considering the normal uncertainties in furnace temperature associated with large heat treatment lots, a solution temperature of 1710F was selected. From Figure 1 it appears as though this will yield about 45% which is expected to grow as a result of a lower cooling rate and during the subsequent 1300F vacuum anneal. Solution treatment was done in a Lindberg air furnace with 1710F +/- 25F surveyed uniformity. After set temperature was

achieved, furnace was adjusted to maintain 1700F at the lowest of the 4 recording TC's to assure minimum primary alpha vol% in all plates. A load-TC was embedded in a 1" diameter x 1.5" long Ti 6Al-4V bar, which was placed with the plates. The rack of forgings, heat treated on edge was rolled out of the furnace after one hour at temperature and fan air-cooled. The load time/temperature diagrams are available. I have measured from these charts a cooling rate from 1700 to 1000F of 6F/sec (3.3C/sec) [360F/min (200C/min)].

Solution treatment was accomplished in 4 lots with heat treat lot identification associated with each forging serial number. The heat treat batch-loading map for each lot is available for examination at Textron. Heat treat lots 44, 46, 48 and 50 were involved. As this heat treatment is presumed to be most important relative to traceability, Table 3 indicates the distribution of forgings for each lot.

Table 3: Solution heat treatment distribution by heat treat lot

Lot number	44	46	48	50
Forging #s	1-16, 18-57	58-109	110-165	166-200

### 3.3.3. Cleaning

All of the solution treated forgings were cleaned of glass lubricant; oxide and alpha case using caustic and acid baths as well as grit blasting. Such processes may increase the level of hydrogen near the surface, leading to lower mechanical behavior.

### 3.4. Vacuum Anneal (1300F)

The cleaned forgings were vacuum annealed at 1300F for 2 hours at temperature.

The vacuum annealing was done in two lots. Lots 1449 (pieces 110-200) and 1451 (pieces 1-16, and 18-109). This was done to reduce the cooling stresses from the solution treatment, to stabilize the microstructure and reduce the hydrogen level at the surface.

## 4. POST-TREATMENT PLATE CHARACTERIZATION

To detect die heating effects on the microstructure, plates #4, 7, 100, and 200 were designated for characterization by ML. A most extensive work was done on plate #7 to statistically determine the primary alpha vol%, possible microstructural directionality, location-to-location variations, end-of-plate morphology, longitudinal and transverse tensile, location-to-location tensile, and strain rate effects on tensile behavior.

### 4.1 MICROSTRUCTURE

Based on the extensive metallographic examination it was determined that:

Microstructure was found to be the same for the ST, SL and LT orientations.

Microstructure is a duplex structure with 60vol% of equiaxed primary alpha. This precisely matches the program-planning goal.

The microstructures of Plates #4 and 7 were very similar, indicating no die heating effects.

Some forging related surface cracks were detected on the die-contact plate surfaces. However, these cracks were only one or two grains deep and any specimen machining practice will have them removed.

There were no significant differences in the microstructure of the plate middle sections and the far-end zones. Therefore, there is no need to be careful about the test specimen locations in the plates. The microstructure was judged to be very uniform throughout the entire plate volume, with only minimal location-to-location variations.

As the initial forging bar stock had a highly elongated primary alpha-structure, it is expected that the forged plate will have some crystallographic texture.

#### 4.2 TENSILE RESULTS

The tensile results of Plate #7 are shown in Table 4.

The tensile results of the edge vs.. center show almost no difference, indicating microstructural and textural uniformity.

T results have higher modulus and strength than L, indicating a crystallographic texture.

Higher strain rate results have higher strength (OK) and higher modulus (???)

The tensile property data referenced in the report are summarized in Table 1 of this report.



## ***APPENDIX B: Gas Gun Impacting Procedure***

The high speed impact of glass and steel spheres was accomplished by placing the spheres in a sabot, a plastic cylinder sized to fit in the bore of the gas gun shown in Figure 127 below. A hemispherical cavity in the sabot keeps the sphere in place. The sabot and sphere are propelled down the barrel of the gas gun by bursting a disk placed across the barrel between the sabot and an accumulator charged with high pressure helium or other gas. When the sabot and sphere leave the barrel, a screen with a hole large enough for the sphere but smaller than the sabot strips it from the sabot. The sphere goes through two timing screens which measure the time at which the sphere passes, allowing the speed to be determined.

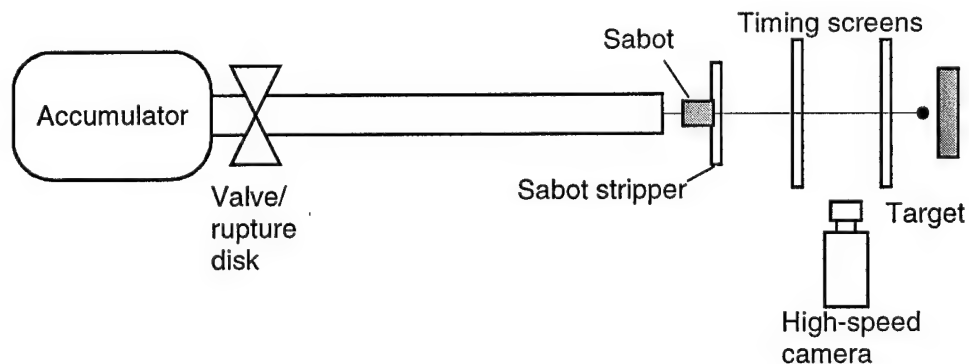


**Figure 130. Schematic of Gas Gun Used for Sphere Impact Tests**

Table 12. Glass Sphere Impact Raw Data

UDRI Shot #	Specimen #	Projectile Radius (mm)	Projectile Weight (g)	Impact Angle (deg)	Impact Velocity(ft/s)
3-0213	98-878	0.5	0.0018	30	1024
3-0215	98-879	0.5	0.0014	30	1037
3-0217	98-881	0.5	0.0011	0	1024
3-0219	98-882	0.5	0.0014	0	1070
3-0221	98-883	0.5	0.0017	0	1024
3-0223	98-884	0.5	0.0019	0	1024
3-0225	98-885	0.5	0.0017	0	1095
3-0227	98-886	0.5	0.0018	30	961
3-0229	98-887	0.5	0.0019	30	961
3-0231	98-888	0.5	0.0015	30	1002
3-0233	98-889	0.5	0.0016	30	961
3-0235	98-890	0.5	0.0014	30	1024
3-0237	98-891	0.5	0.002	30	1047
3-0239	98-892	0.5	0.0011	30	1024
3-0241	98-893	0.5	0.0019	30	1024
3-0243	98-894	0.5	0.0015	60	981
3-0245	98-895	0.5	0.0015	60	1047
3-285	98-B11	0.5	0.0017	0	1013
3-286	98-B11	0.5	0.0019	0	1047
3-287	98-B11	0.5	0.0022	0	1035
3-288	98-B11	0.5	0.0023	30	1047
3-289	98-B11	0.5	0.0019	30	1035
3-290	98-B11	0.5	0.0019	30	1002
**3-282	98-B12	0.5	0.0022	0	992
**3-283	98-B12	0.5	0.0017	0	981
**3-284	98-B12	0.5	0.002	0	951
**3-291	98-B12	0.5	0.0021	30	1024
**3-292	98-B12	0.5	0.002	30	992
**3-293	98-B12	0.5	0.0022	30	1024
3-0307	98-A95a	1.0	0.0098	0	950
3-0308	98-A95b	1.0	0.0098	0	946
3-0309	98-A95c	1.0	0.0098	30	985
3-0310	98-A95d	1.0	0.0098	30	981
3-0354	98-B18	1.0	0.0098	0	969
3-0355	98-B18	1.0	0.0098	0	1006
3-0356	98-B19	1.0	0.0098	0	1031
3-0357	98-B19	1.0	0.0098	0	1004
3-0358	98-B20	1.0	0.0098	0	1000
3-0359	98-B20	1.0	0.0098	0	1002
3-0360	98-B21	1.0	0.0098	0	1011
3-0361	98-B21	1.0	0.0098	0	992
3-0366	98-B22	1.0	0.0098	0	1004
3-0367	98-B22	1.0	0.0098	0	996
3-0368	98-B23	1.0	0.0098	0	985
3-0369	98-B23	1.0	0.0098	0	1015
3-0378	98-J44	1.0	0.0098	0	1022
3-0379	98-J44	1.0	0.0098	0	1020

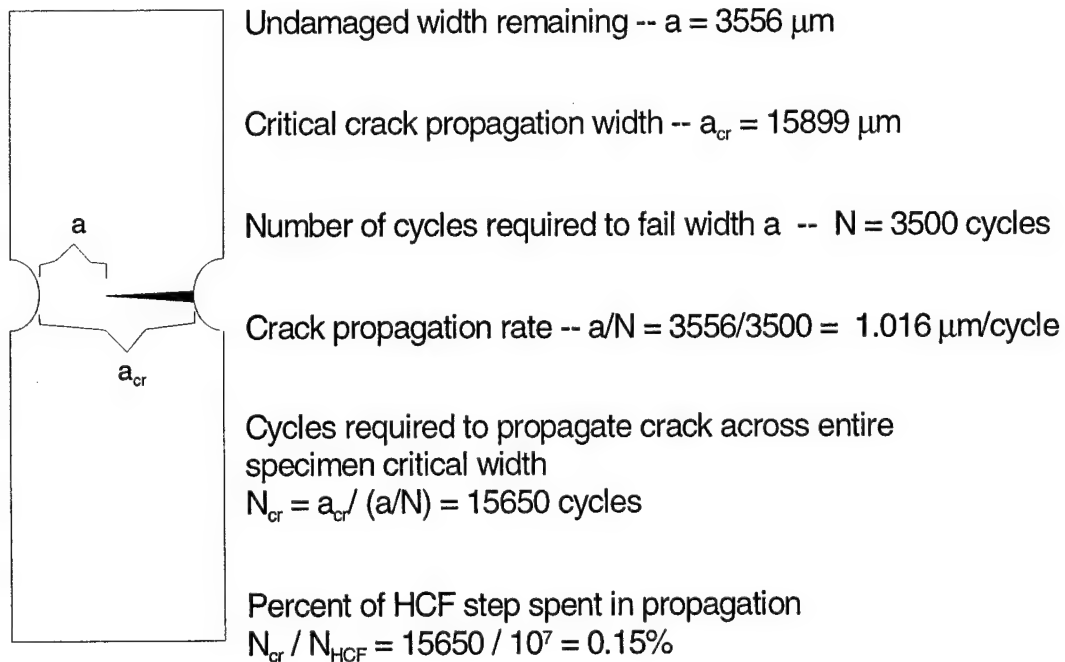
Table 12. Glass sphere impact data (cont'd).

UDRI Shot #	Specimen #	Projectile Radius (mm)	Projectile Weight (g)	Impact Angle (deg)	Impact Velocity(ft/s)
3-0380	98-J45	1.0	0.0098	0	1002
3-0381	98-J45	1.0	0.0098	0	994
3-0382	98-J46	1.0	0.0098	0	1022
3-0383	98-J46	1.0	0.0098	0	1035
3-0384	98-J47	1.0	0.0098	0	1008
3-0385	98-J47	1.0	0.0098	0	1008
3-0312	98-B09	2.5	0.16	0	953
3-0313	98-B09	2.5	0.16	0	953
3-0314	98-B10	2.5	0.16	0	957
3-0315	98-B10	2.5	0.16	0	950
**3-296	98-B12	2.5	0.16	30	991
**3-297	98-B12	2.5	0.16	30	1002
**3-298	98-B12	2.5	0.16	30	1002
**3-299	98-B12	2.5	0.16	0	1002
**3-300	98-B12	2.5	0.16	0	1013
**3-301	98-B12	2.5	0.16	0	1024
3-016	98-B13	2.5	0.16	0	946
3-017	98-B13	2.5	0.16	0	957
3-018	98-B14	2.5	0.16	0	961
3-019	98-B14	2.5	0.16	0	957
3-020	98-B15	2.5	0.16	0	961
3-021	98-B15	2.5	0.16	0	957
3-022	98-B17	2.5	0.16	0	977
3-023	98-B17	2.5	0.16	0	938
3-0338	98-J48	2.5	0.16	0	946
3-0339	98-J48	2.5	0.16	0	953
3-0340	98-J49	2.5	0.16	0	994
3-0341	98-J49	2.5	0.16	0	953
3-0342	98-J50	2.5	0.16	0	961
3-0343	98-J50	2.5	0.16	0	957
3-0344	98-J51	2.5	0.16	0	973
3-0345	98-J51	2.5	0.16	0	953
3-0346	98-J52	2.5	0.16	0	981
3-0347	98-J52	2.5	0.16	0	981
3-0348	98-J53	2.5	0.16	0	977
3-0349	98-J53	2.5	0.16	0	977

\*\* These samples had multiple impacts made so that the impact regions could be destructively evaluated. These samples were not fatigue tested.

### APPENDIX C: Approximate Crack Growth Rate

The assumption that crack initiation consumes the majority of fatigue life under the conditions tested was verified by the serendipitous capture of several specimens in a state of partial crack propagation. The high frequency testing machine had a switch located on the electromagnetic armature to shut down the machine if the displacement grew too large. On four specimens, the added compliance created by the propagating crack allowed this switch to shut down the testing machine before failure. Upon restarting the machine, the number of cycles necessary to continue the crack to failure was measured. A typical result is given below for specimen 98-J53 which was found to have 3556  $\mu\text{m}$  of width left after being stopped by the displacement switch. It failed after 3500 additional cycles.



## ***APPENDIX D: Verification of the Step Loading Technique***

In order to investigate the validity of the step loading technique to establish the fatigue life behavior of Ti-6Al-4V at various cyclic stress ratios, several experiments were conducted to compare two different ways of step loading a sample. The first way to achieve this is the method used in this research effort, which is to increase the maximum stress and the alternating stress together in a manner as to maintain a constant stress ratio  $R$ .

The other way to increase the loading is to maintain a constant maximum stress and increase the minimum stress in such a way as to gradually increase the stress ratio  $R$ .

If the step loading technique is valid then fatigue data generated by both means should give identical results.

Figure 131 plots two curves representing specimens which were step load tested by both means during this study. The upper curve represents the fatigue behavior of Ti-6Al-4V from undamaged samples. Both data from the constant- $R$  method and the constant maximum stress methods are plotted together. The lower curve plots data collected on samples notched with a circumferential groove of constant radius which created a stress concentration factor of approximately 2.5. Again this curve has data collected by both step loading techniques.

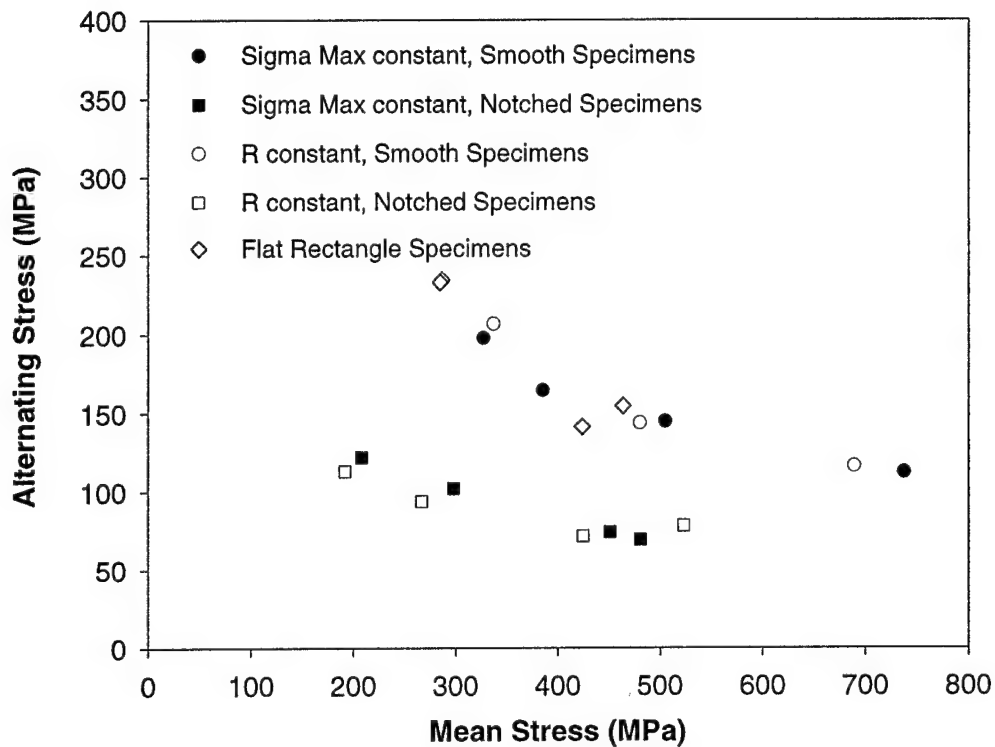


**Figure 131. Step Loading Variation Results**

It can be seen by the close agreement between the curves generated by both methods that for undamaged Ti-6Al-4V it makes no difference if a step-loading test is conducted at constant R, increasing  $\sigma_{\max}$  or constant  $\sigma_{\max}$  and increasing R. A small increase in load can be seen in the notched specimens when loaded at constant  $\sigma_{\max}$ . These differences, listed in Table 13, are less than 12%. This compares favorably with the random scatter of fatigue data collected on nominally identical specimens in the remainder of this report.

Table 13. Variations Between Step Loading Techniques (Notched Specimens)

	Sigma Mean		Percent Change
Approximate R range	Using Constant R	Using Constant SigmaMax	
0.25	191.67	208	8.5%
0.49	266.9	297.98	11.6%
0.71	422	450.98	6.9%
	Sigma Max		Percent Change
R	Using Constant R	Using Constant SigmaMax	
0.25	304.7	330	8.3%
0.49	360.7	400	10.9%
0.71	492.1	537.5	9.2%

In the Figure 132, S-N data for undamaged specimens tested at  $R=0.5$  and 5 mm glass sphere damaged specimens at both stress ratios are plotted on semi-log axes. On the same plot is fatigue life data collected by the step loading technique. The extrapolation of the S-N data to a life of  $10^7$  cycles agrees with the step loading data within the scatter of repeated measurements.

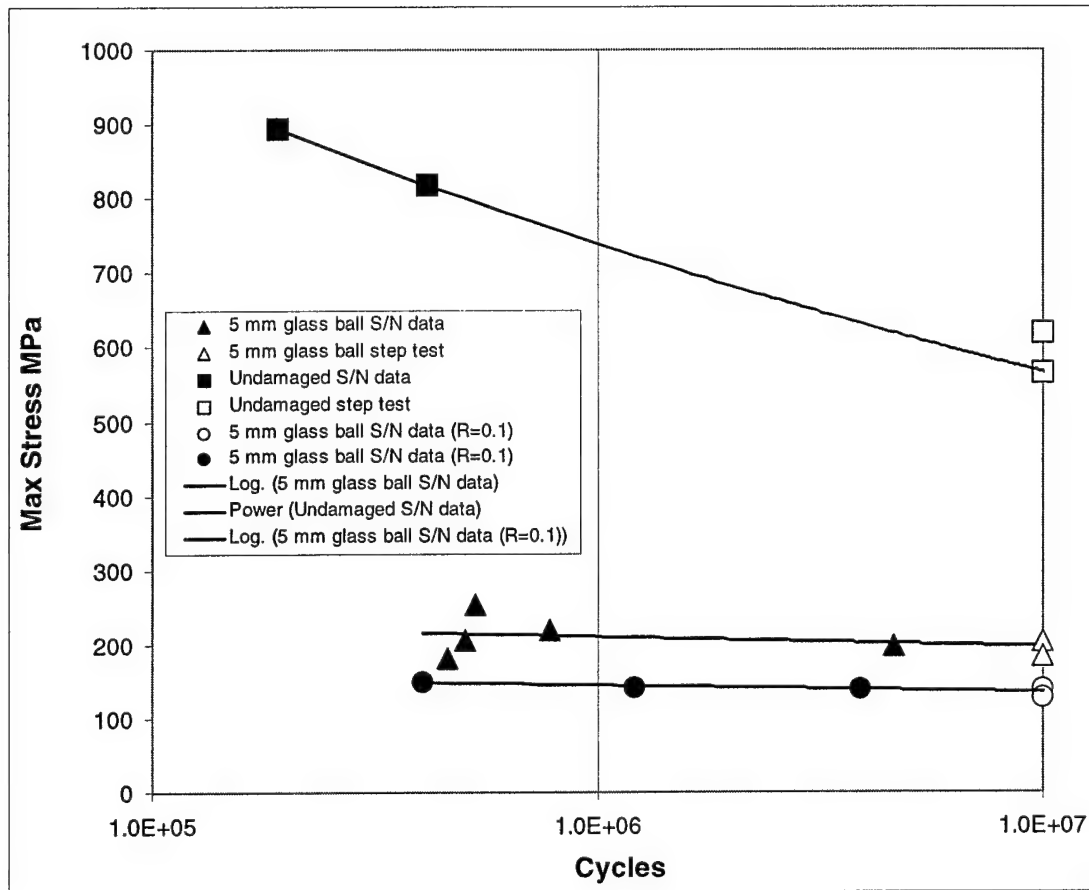


**Figure 132. S-N Data and Step Loading Comparison.** 5 mm glass spheres at R = 0.1 and R = 0.5 are plotted on semi-log axes, along with R = 0.5 data from undamaged specimens.



## ***APPENDIX E: Example HCF Testing Machine Output***

An example data file is shown below. (Note: for the non-rectangular cross section samples, specimen thickness and specimen width values are input that multiply to the same cross sectional area as the sample. This is to ensure that the load and stress values computed will be the same.)

---

MATE METEST log file - MATE version 2.53F

DATE: 12/15/1997 TIME: 16:03:32

CURRENT TEST PARAMETERS:

SPECIMEN ID: HAMRICK FOD D-9

SPECIMEN TYPE: Rect

SPECIMEN THICKNESS: 2.5400 mm

SPECIMEN WIDTH: 7.3406 mm

MATERIAL/COATING: Ti-6-4

TEST TEMPERATURE: 23.0 C

TEST ENVIRONMENT: Lab Air

HF LOAD RANGE: 20.000 kN

LF LOAD RANGE: 20.000 kN

AUX RANGE: .00025

MAJOR WAVEFORM: HF ONLY (STATIC MEAN

MINOR FREQUENCY: 350. Hertz

MINOR LOAD RATIO: .500  
 MAJOR FREQUENCY: .0050 Hertz  
 MAJOR LOAD RATIO: .9900  
 HOLD LOAD: 10.00 %  
 TEST TYPE: Incremental P(N)

SMPL	CYCLES	MAX	LOAD	Px-Hi	Px-Lo	Aux 1	Aux 2	ET
NMBR		LOAD	RATIO	kN	kN			
		kN						SEC
****	*****	*****	*****	*****	*****	*****	*****	*****
1	3158.	14.030	.508	14.026	.014	.000	.000	7.
2	631956.	14.166	.500	14.218	13.988	.000	.000	1810.
3	1262099.	14.144	.498	14.233	14.007	.000	.000	3613.
4	1892012.	14.169	.503	14.225	13.997	.000	.000	5415.
5	2520845.	14.117	.501	14.216	14.052	.000	.000	7218.
6	3149681.	14.100	.498	14.226	14.029	.000	.000	9020.
7	3779633.	14.096	.498	14.220	14.036	.000	.000	10822.
8	4409547.	14.130	.502	14.212	13.972	.000	.000	12625.
9	5038385.	14.101	.502	14.218	14.045	.000	.000	14427.
.								
.								
.								
52	30004080.	16.172	.505	16.161	11.999	.000	.000	172334.
53	30009010.	16.172	.510	16.190	1.537	.000	.000	172346.
54	30637730.	16.317	.497	16.428	15.331	.000	.000	174148.

## ***APPENDIX F: Mesh Refinement Analysis***

This appendix describes the ABAQUS runs used to determine the mesh size necessary for useful reproduction of stress states in Ti-6Al-4V.

Table 14 gives the SCF tabulated by Peterson for the notch sizes analyzed.

Table 14. Stress Concentration Factors (57)

Notch Diameter (mm)	Notch depth (mm)	SCF
6.1	11.4	2.00
3.3	14.0	2.45

Figures 134 and 135 show the tensile stress versus distance from notch results from ABAQUS. Based upon the runtime performance for the computers at the Air Force's Major Shared Resource Center (MSRC) for various mesh sizes used in preliminary runs, the mesh size of 254  $\mu\text{m}$  (0.01") was chosen as the best trade off between accuracy and speed.

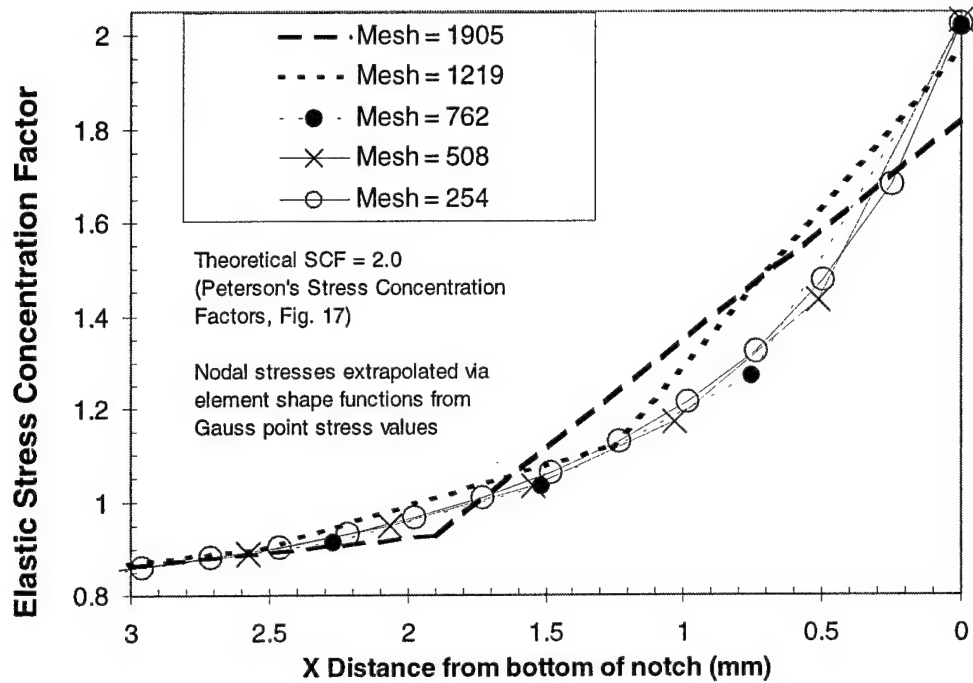


Figure 133. ABAQUS Predicted Stresses for Notch with SCF of 2.00

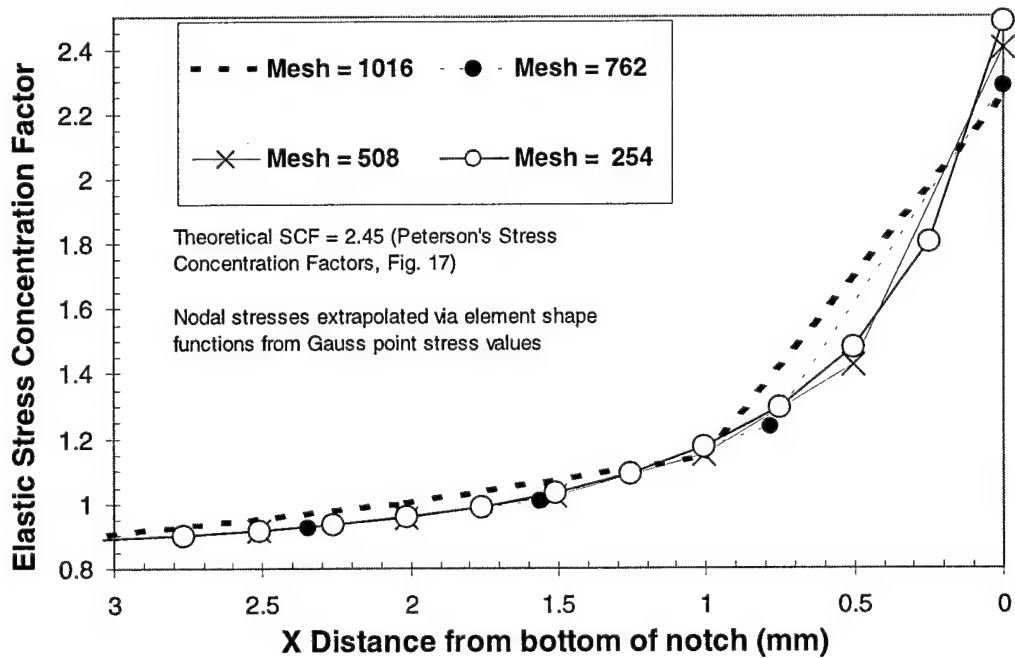


Figure 134. ABAQUS Predicted Stresses for Notch with SCF of 2.45

## ***APPENDIX G: Calculation of Damping for Dynamic Model***

The critical damping parameter  $\beta$  is an artificial ratio applied to velocity terms in the explicit time integration used by Dytran (48). Also known as a dynamic relaxation parameter,  $\beta$  is used to create a damping matrix  $C = (2\beta/\Delta t)M$  for the equation of motion (17). Inclusion of  $C$  in Eqn. (17) reduces the velocities of the nodes at each time step. This increases the speed at which the steady-state values of the dynamic models are reached.

A typical procedure used to estimate  $\beta$  is to watch the system's kinetic energy as it rises in the first initial time integration steps. The time for the kinetic energy to rise to a maximum is taken as  $\frac{1}{4}$  of the period of the fundamental frequency. This can be seen in the first few iterations, so that damping can be estimated and applied to subsequent runs without spending large times on the undamped cases (10).

In this effort, an initial estimate of  $\beta$  was made by assuming a longitudinal displacement mode (the displacement in the direction of the applied tension load of interest) and the stiffness of the sample was assumed to be  $k=EA/l$  where  $E$  is the modulus of Ti-6Al-4V,  $A$  is the cross-sectional area, and  $l$  the length.

The estimate given in the Dytran manual (48) for damping is then given as  $\beta = \omega_n \Delta t$  where  $\omega_n = \sqrt{k/m}$  with  $m$  being the sample mass. In this case,  $\Delta t$  is the time step of the iterations. These quantities combined to give an initial estimate for  $\beta = 8.85 \times 10^{-6}$ .

Runs made with this value showed underdamped behavior. But from these runs, the period of the underdamped response could be used to get a better estimate of the natural frequency from  $\omega_n = 2\pi/T$  . This new estimate was eventually refined to the 0.00017 value shown in the text.

## APPENDIX H: Fatigue Strength versus Indent Depth

The total damage depth proved to be a better indication of the fatigue strength degradation than the indent depth. In Figure 136 the fatigue strength is plotted both as a function of indent depth  $D_i$  and of total damage depth  $D_d$ . 95% confidence levels are shown for both relations. When  $D_i$  is used as the independent variable, the correlation coefficient ( $r^2$ ) of the line fit to the data is 0.698 and the confidence bands are 270 MPa apart. Using  $D_d$  as the independent variable,  $r^2 = 0.840$  and the bands are only 180 MPa apart, 33% closer.

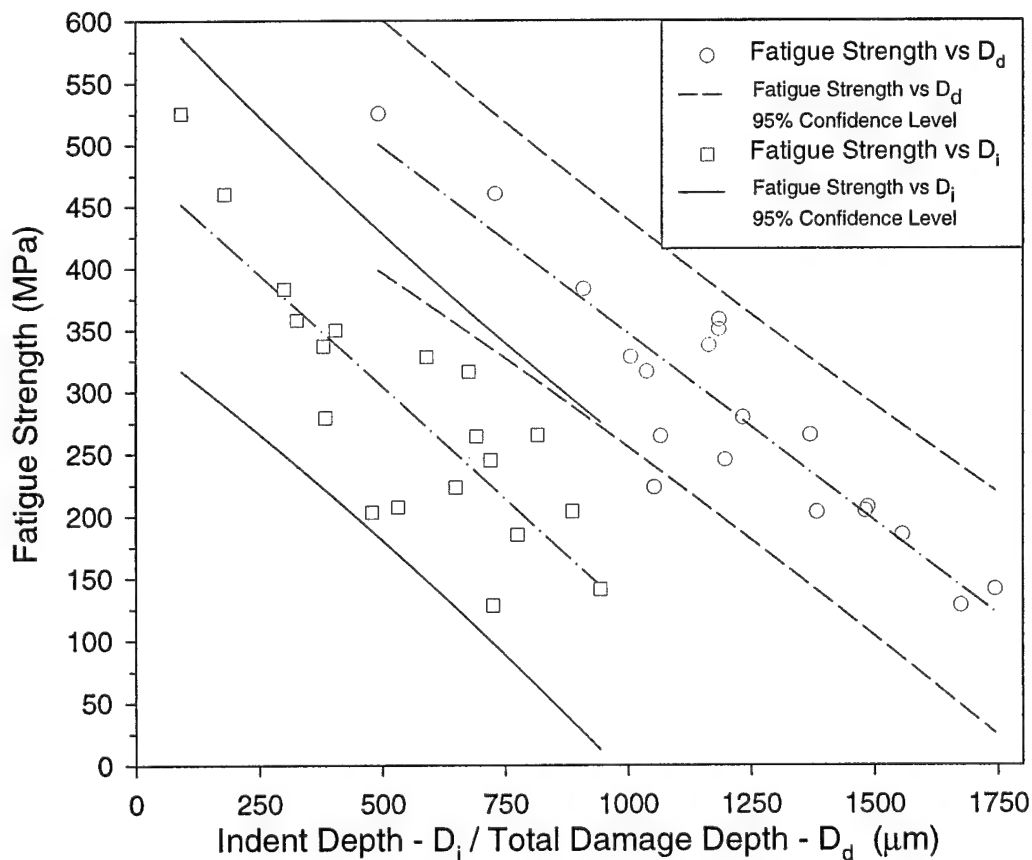
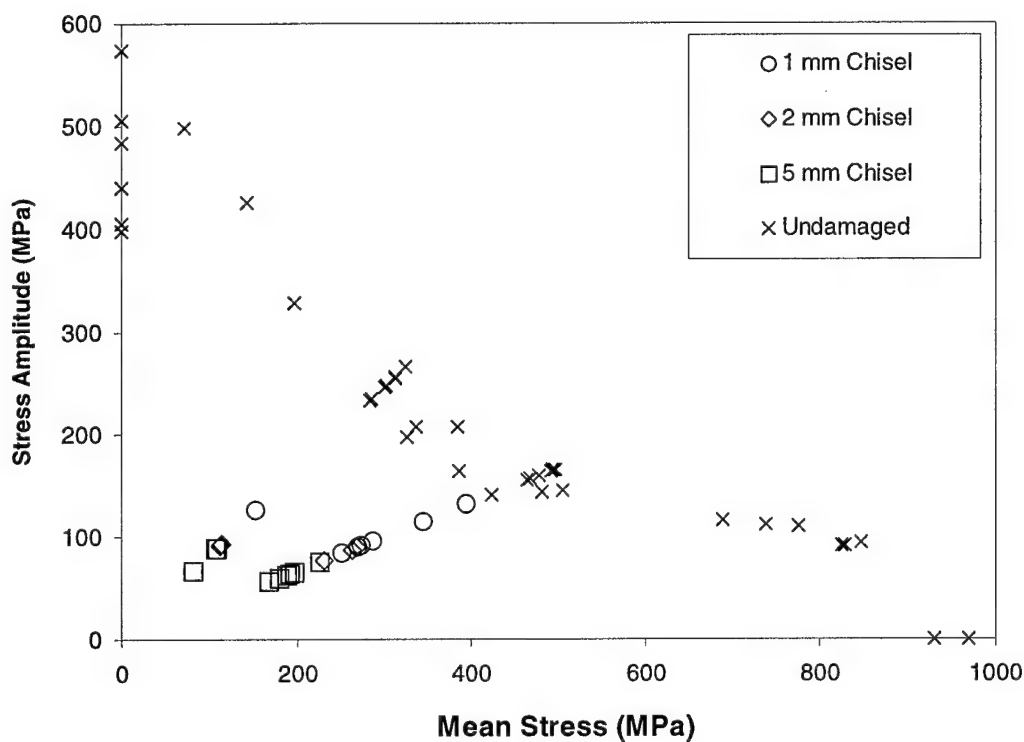


Figure 135. Fatigue Strength vs.  $D_i$  and  $D_d$

## APPENDIX I. Fatigue Strength Data

The data from which the fatigue strength graphs are drawn are given in Table 15 as the mean stress and stress amplitude which resulted in a life of  $10^7$  cycles. The chisel indentation data are plotted in Figure 136 and the remaining cases in Figure 137.



**Figure 136. Stress Amplitude vs. Mean Stress - Chisel Indentations.** The fatigue strengths shown are for a life of  $10^7$  cycles.



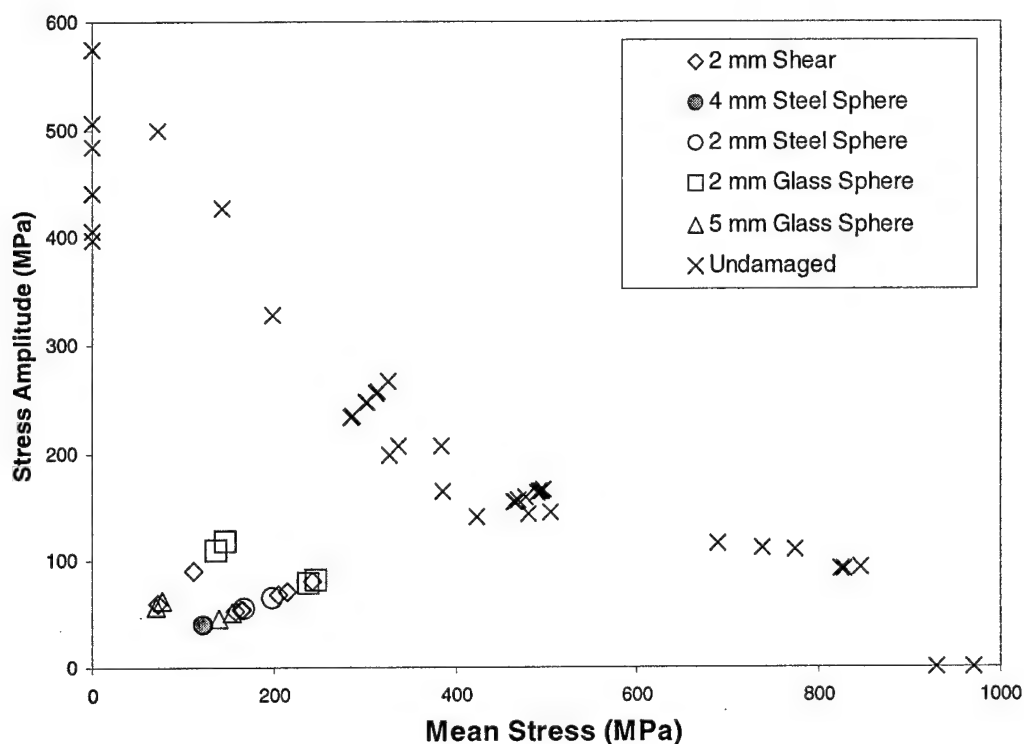


**Figure 137. Stress Amplitude vs. Mean Stress - Spheres and Sheared Notches.** The fatigue strengths shown are for a life of  $10^7$  cycles.

Table 15. Fatigue Strength of Simulated FOD Specimens

Specimen	FOD Simulation Method	Di (μm)	Dp (μm)	Dd (μm)	R	Mean Stress (MPa)*	Stress Amplitude (MPa)*
Scrap#7	2 mm Shear	662	328	990	0.1	#N/A	#N/A
98-Q21	2 mm Shear	691	329	1,021	0.1	111.1	90.9
Scrap#9	2 mm Shear	971	356	1,327	0.1	#N/A	#N/A
Scrap#8	2 mm Shear	1,008	311	1,319	0.1	#N/A	#N/A
Scrap#10	2 mm Shear	1,114	314	1,427	0.1	72.71	59.49
Scrap#4	2 mm Shear	598	416	1,014	0.5	242.55	80.85
Scrap#6	2 mm Shear	691	285	976	0.5	214.8	71.6
Scrap#5	2 mm Shear	730	264	994	0.5	#N/A	#N/A
98-Q22	2 mm Shear	770	323	1,094	0.5	204.3	68.1
Scrap#3	2 mm Shear	1,015	407	1,422	0.5	157.5	52.5
Scrap#12	2 mm Shear	1,435	332	1,767	0.5	163.95	54.65
Scrap#11	2 mm Shear	1,496	299.5	1,796	0.5	165.18	55.06
98-Q12	4 mm Steel Sphere	2,100	495	2,595	0.5	122.18	40.73
98-Q13	4 mm Steel Sphere	1,917	425	2,342	0.5	121.05	40.35
98-Q14	4 mm Steel Sphere	1,565	515	2,080	0.5	#N/A	#N/A

Table 15. Fatigue Strength of Simulated FOD Specimens (cont'd)							
Specimen	FOD Simulation Method	Di (μm)	Dp (μm)	Dd (μm)	R	Mean Stress (MPa)*	Stress Amplitude (MPa)*
98-Q18	2 mm Steel Sphere	938	400	NA		#N/A	#N/A
98-Q15	2 mm Steel Sphere	690	350	1,040		#N/A	#N/A
98-Q16	2 mm Steel Sphere	691	376	1,067	0.5	198.3	66.1
98-Q17	2 mm Steel Sphere	649	405	1,054	0.5	166.95	55.65
98-J46	2 mm Glass Sphere	816	555	1,371	0.1	145.64	119.16
98-J45	2 mm Glass Sphere	720	478	1,198	0.1	134.97	110.43
98-B19	2 mm Glass Sphere	590	416	1,006	0.5	245.85	81.95
98-B18	2 mm Glass Sphere	676	363	1,039	0.5	236.93	78.97
98-B15	5 mm Glass Sphere	944	800	1,744	0.1	77.33	63.27
98-B17	5 mm Glass Sphere	950	950	1,675	0.1	70.29	57.51
98-B10	5 mm Glass Sphere	887	596	1,482	0.5	152.85	50.95
98-B14	5 mm Glass Sphere	870	782	1,557	0.5	138.38	46.13
98-B05	1 mm Chisel	92	400	492	0.5	393.94	131.32
98-Q03	1 mm Chisel	384	850	1,234	0.1	153.23	125.37
98-B06	1 mm Chisel	180	550	730	0.5	344.85	114.95
98-A98	1 mm Chisel	300	610	910	0.5	287.4	95.8
Scrap#2	1 mm Chisel	380	785	1,165	0.5	252.45	84.15
98-Q06	1 mm Chisel	440	850	1,290	0.5	273.75	91.25
98-Q05	1 mm Chisel	460	911	1,371	0.5	270.38	90.13
98-Q09	1 mm Chisel	600	968	1,568	0.5	251.55	83.85
98-J78	2 mm Chisel	479	905	1,384	0.1	111.43	91.17
98-J75	2 mm Chisel	532	955	1,487	0.1	114.02	93.28
98-J68	2 mm Chisel	405	780	1,185	0.5	262.8	87.6
98-J69	2 mm Chisel	523	860	1,186	0.5	268.8	89.6
98-J67	2 mm Chisel	600	825	1,425	0.5	231.9	77.3
98-J62	5 mm Chisel	513	1,645	2,158	0.1	107.75	88.16
98-J60	5 mm Chisel	617	1,817	2,434	0.1	81.34	66.56
98-J61	5 mm Chisel	764	2,053	2,817	0.1	108.08	88.42
98-J59	5 mm Chisel	570	1,525	2,095	0.5	225.68	75.22
98-J54	5 mm Chisel	640	1,750	2,390	0.5	168.07	56.02
98-J56	5 mm Chisel	747	1,977	2,724	0.5	180.07	60.02
98-J55	5 mm Chisel	792	1,670	2,462	0.5	191.47	63.83
98-J57	5 mm Chisel	918	1,632	2,550	0.5	196.5	65.5
98-J58	5 mm Chisel	1,020	1,785	2,805	0.5	188.78	62.92
* #NA refers to specimens which failed in less than one loading step and therefore no fatigue strength can be determined.							

## ***APPENDIX J. Fatigue Crack Initiation Sites***

In Figure 138, the locations where the peak tensile stresses were found in the finite element models are shown. Figure 139 describes the locations of the fatigue fracture initiation sites on the surfaces of the glass sphere impacted and chisel indented specimens. Table 16 lists which of the locations in Figure 139 contained the crack initiation sites by specimen number when that location could be determined. The table also locates the initiation site with respect to the peak stress locations shown in Figure 138.

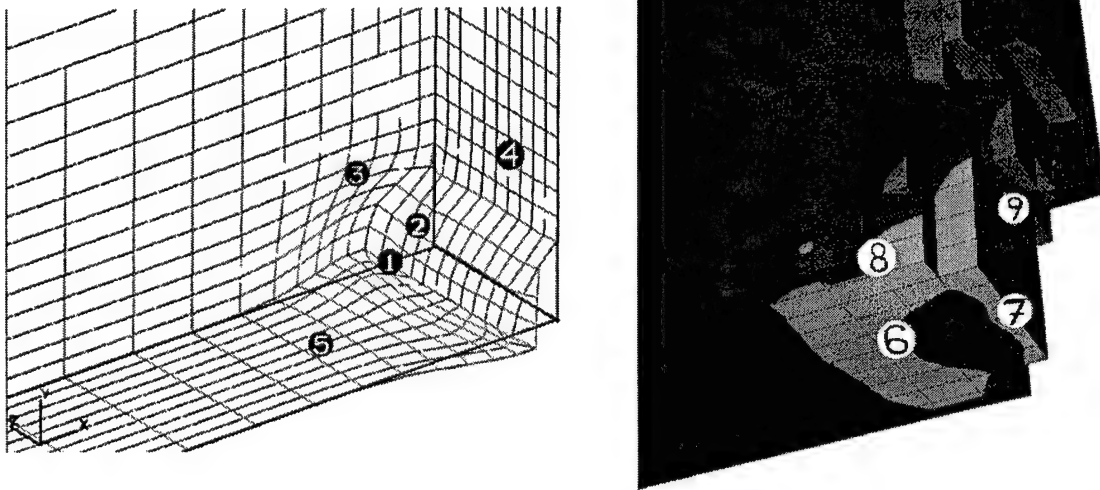


**Figure 138. Peak Tensile Stress Locations**

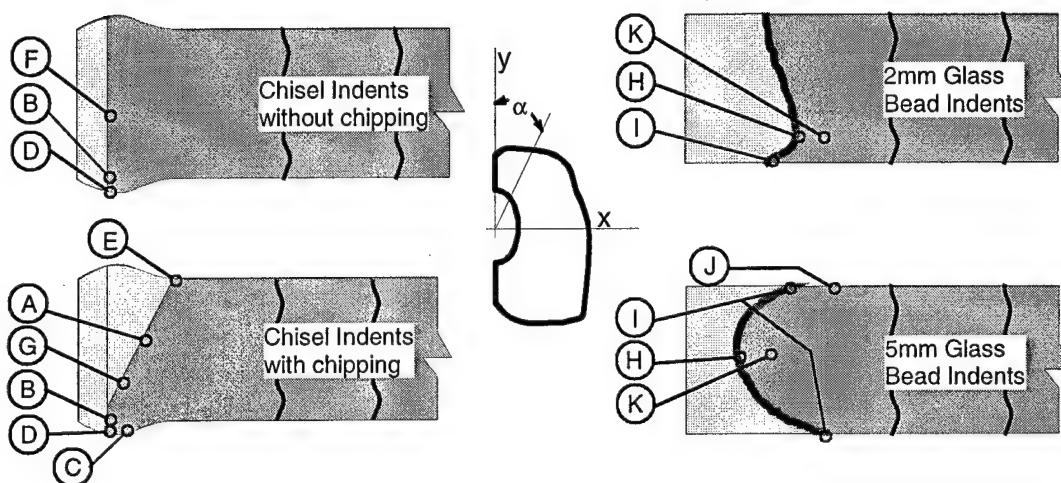


**Figure 139. Fatigue Crack Initiation Sites.** The letters marking the locations correspond to Table 15. The diagram in the center is a side view of a notch, depicting the angle used to refer to the location with respect to the y axis of the specimen at which crack initiation occurred.

Table 16. Locations of Crack Initiation Sites

Damage/Stress Type	Specimen ID	Location on Surface	Angle (degrees)	Location in Damage Zone
2mm Ball R0.5	98-B19	H	45	9
5mm ball R0.5	98-B09	H	90	7
5mm ball R0.5	98-B10	H	80	7
5mm ball R0.5	98-B13	H	U	-
5mm ball R0.5	98-J49	H	90	7
2mm Ball R0.1	98-J44	H or K	90	7
5mm ball R0.5	98-B14	H or K	85	7
2mm Ball R0.1	98-J46	I	85	8
5mm ball R0.1	98-B17	I	90	8
5mm ball R0.1	98-J51	I	90	8
5mm ball R0.5	98-J48	I	60	O
5mm ball R0.1	98-J52	J	70	8
2mm Ball R0.1	98-J45	K	90	6
2mm Ball R0.1	98-J47	K	90	6
2mm Ball R0.5	98-B18	K	90	6
5mm ball R0.1	98-B15	K	70	O
2mm chisel R0.1	98-J72	A	30	O
2mm chisel R0.1	98-J75	A	U	-
2mm chisel R0.5	98-J65	A	U	-
5mm chisel R0.5	98-J58	A	U	-
5mm chisel R0.1	98-J61	A or B	5	4
2mm chisel R0.1	98-J76	A or G	U	-
2mm chisel R0.5	98-J66	A or G	25	2
5mm chisel R0.5	98-J55	B	60	3
5mm chisel R0.5	98-J59	B	65	3
5mm chisel R0.5	98-J56	C	45	3

Table 16. Locations of Crack Initiation Sites (cont'd)

Damage/Stress Type	Specimen ID	Location on Surface	Angle (degrees)	Location in Damage Zone
5mm chisel R0.5	98-J57	D	60	3
5mm chisel R0.1	98-J60	E	45	O
2mm chisel R0.5	98-J64	G	25	2
2mm chisel R0.5	98-J67	G	U	-
5mm chisel R0.1	98-J62	G	90	1
5mm chisel R0.5	98-J54	G	60	3
2mm chisel R0.1	98-J71	A	75	O
2mm chisel R0.1	98-J73	A	40	O
2mm chisel R0.5	98-J70	A or B	70	3
2mm chisel R0.1	98-J74	B	30 - 85	3
2mm chisel R0.1	98-J77	B	U	-
2mm chisel R0.5	98-J63	B	45	3
1mm chisel R0.5	98-Q05	B	90	1
1mm chisel R0.1	98-Q04	D	0	4
2mm chisel R0.1	98-J78	F	90	2
2mm chisel R0.5	98-J68	F	90	2
1mm chisel R0.5	SCRAP#2	F	70	2
1mm chisel R0.1	98-Q03	F or D	90	1
2mm chisel R0.5	98-J69	G	70	3
Angle: 'U' = Uncertain Location: 'O' = Other				

## ***BIBLIOGRAPHY***

1. *ABAQUS v5.8 Theory Manual*. Pawtucket, RI (USA): Hibbit, Karlsson & Sorensen, Inc. 1998.
2. Abdel-Raouf, H., D. L. DuQuesnay, T. H. Topper and A. Plumtree. "Notch-size effects in fatigue based on surface strain redistribution and crack closure," *International Journal of Fatigue*, 14(1): 57-62, 1992.
3. Air Force Research Laboratory/MLLN. Grain structure data collected on Ti-6Al-4V in support of HCF Science and Technology program. Wright-Patterson AFB OH: AFRL/MLLN, October 1997.
4. Air Force Research Laboratory/MLLN. Strain rate sensitivity data collected on Ti-6Al-4V in support of HCF Science and Technology program. Wright-Patterson AFB OH: AFRL/MLLN, October 1997.
5. Atzori, B., P. Lazzarin and R. Tovo. "Stress distributions for V-shaped notches under tensile and bending loads," *Fatigue and Fracture of Engineering Materials and Structures*, 20(8):1083-1092, 1997.
6. Baratta, F. I. "Comparison of various formulae and experimental stress-concentration factors for symmetrical U-notch plates," *Journal of Strain Analysis*, 7(2):84-86, 1972.
7. Boyce, B.L. et al. "Measurement of Residual Stresses in Impact-damaged Ti-6Al-4V", Proceedings of the 4th National Turbine Engine High Cycle Fatigue (HCF) Conference, Monterey CA, 9-11 February, 1999.
8. Boyer, Howard E., editor. *Atlas of Fatigue Curves*. Metals Park OH: American Society for Metals, 1986.
9. Brockenbrough, J. R., et al. *Microstructurally Based Model of Fatigue Initiation and Growth*. Alcoa Technical Center Report 94-11376, Alcoa Center PA: ALCOA, 07 April 1994, AD-A278198.
10. Brockman, Robert. University of Dayton Research Institute. Personal Conversations. 1 October 1997-15 July 1999.

11. Broek, David. *Elementary Engineering Fracture Mechanics* (Fourth revised edition). Dordrecht: Martinus Nijhoff, 1987.
12. Burns, Joseph. HCF Program Materials Damage Tolerance Action Team Chair, AFRL/MLLN, Wright-Patterson AFB OH. Personal Conversations. 1 October 1997- 1 January 1998.
13. Carlson, R. L. and G. A. Kardomateas. *An Introduction to Fatigue in Metals and Composites*, London: Chapman & Hall, 1996.
14. Chen, Qiye and T. H. Lin. "High-Cycle Fatigue Crack Initiation of Intermetallic Compounds," *Fatigue '93*:1043-1050, 1993.
15. Cook, Robert D. et al. *Concepts and Applications of Finite element Analysis 3rd Ed.* New York: John Wiley & Sons, 1989.
16. Department of Defense. *Engine Structural Integrity Program (ENSIP)*. MIL-STD-1783 (USAF). Wright-Patterson AFB OH: ASD/ENES, 30 November 1984.
17. Dowling, Norman E. *Mechanical Behavior of Materials*. Prentice Hall, New Jersey: 1993.
18. Duggan, T. V. "Influence of notch-geometry on fatigue threshold," *Fatigue Thresholds-Fundamentals and Engineering Applications Volume II*:809-826, Eds. J. Backlund et al. London: Chameleon Press, 1982.
19. Du-yi, Ye and Wang De-jun. "A new approach to the prediction of fatigue notch reduction factor  $K_f$ ," *International Journal of Fatigue*, 18(2):105-109, 1996.
20. El Haddad, M. H. et al. "Prediction of Non Propagating Cracks," *Engineering Fracture Mechanics*, 11:573-584, 1979.
21. Eylon, D. "Summary of the Available Information on the Processing of the Ti-6Al-4V HCF/LCF Program Plates". University of Dayton, Dayton OH 45469-0240, Unpublished report. 1998.
22. Eylon, D. and C. M. Pierce. "Effect of Microstructure on Notch Fatigue Properties of Ti-6Al-4V," *Metallurgical Transactions A*, 7A:111-121, January 1976.
23. Flynn, P. D. and A. A. Roll. "A comparison of stress-concentration factors in hyperbolic and U-shaped grooves," *Experimental Mechanics*, 272-275, June 1967.



24. Flynn, P. D. and A. A. Roll. "A re-examination of stresses in a tension bar with symmetrical U-shaped grooves," *Experimental Mechanics*, 93-98, February 1966.
25. CSAF General Fogelman, 1 November 1995, cited in briefing to AFRL/MLLN personnel, 6 November 1997.
26. Fuchs, H. O. and R. I. Stephens. *Metal Fatigue in Engineering*. New York: John Wiley & Sons, 1980.
27. Gravett, Phillip et al. "The Foreign Object Damage Project of the PRDA V HCF Materials and Life Methods Program", Proceedings of the 4th National Turbine Engine High Cycle Fatigue (HCF) Conference, Monterey CA, 9-11 February, 1999.
28. Hammouda, M. M. and K. J. Miller. "Elastic-Plastic Fracture Mechanics Analyses of Notches," *Elastic-Plastic Fracture*, ASTM STP 668, p.703-719, American Society for Testing and Materials, 1979.
29. Harding, Trevor S. and J. Wayne Jones. "The Characterization of Impact Damage and its Effect on the Fatigue Properties of Gamma TiAl Alloys," Vugraph presentation, n. pag. WWWeb, <http://titan.mems.cmu.edu/97Review/C4/>. 9 March 1998.
30. Hudak, Stephen J. et al. "A Damage Tolerance Approach to FOD Based on the Worst Case Notch Concept", Proceedings of the 4th National Turbine Engine High Cycle Fatigue (HCF) Conference, Monterey CA, 9-11 February, 1999.
31. Harkegard, G. "An effective stress intensity factor and the determination of the notched fatigue limit," *Fatigue Thresholds-Fundamentals and Engineering Applications Volume II*: 867-879, Eds. J. Backlund et al. London: Chameleon Press, 1982.
32. Klesnil, M. and P. Lukas. *Fatigue of Metallic Materials* (Second revised edition - Materials Science Monographs, 71), Amsterdam: Elsevier, 1992.
33. Lanning, David et al. "Notch Size Effects and LCF/HCF Interactions in Ti-6Al-4V", Proceedings of the 4th National Turbine Engine High Cycle Fatigue (HCF) Conference, Monterey CA, 9-11 February, 1999.
34. Lazzarin, P., R. Tovo and G. Meneghetti. "Fatigue crack initiation and propagation phases near notches in metals with low notch sensitivity," *International Journal of Fatigue*, 19(8-9):647-657, 1997.

35. Lemaitre, Jean. *A Course on Damage Mechanics*, Berlin: Springer-Verlag, 1992.
36. Lewis, J. A. "Absolute fatigue thresholds in metallic materials," *Fatigue* 87:801:808, 1987.
37. Liebowitz, H., H. Vanderveldt, and R. J. Sanford. "Stress concentrations due to sharp notches," *Experimental Mechanics*, 7:93-98, February 1966.
38. Lin, T. H. *Final Technical Report - Fatigue Crack Initiation*, N000-14-86-K-0153, University of California, Los Angeles: 10 September 1991, AD-A240196.
39. Lin, T. H. *Mechanics of Localized Deformation of Solids Under Cyclic and Thermal Loadings*. AFOSR-TR-97-0055, Air Force Office of Scientific Research, 23 September 1996, AD-A319999.
40. Lucas, J. J. and P.P. Konieczny. "Relationship between Alpha Grain Size and Crack Initiation Fatigue Strength in Ti-6Al-4V," *Metallurgical Transactions*, 2:911-912, March 1971.
41. Lukas, P. "Near-threshold fatigue," *Fatigue* 87:719-738, 1987.
42. Lukas, P. "Utilisation of threshold values for characterisation of fatigue notch sensitivity," *Fatigue Thresholds-Fundamentals and Engineering Applications Volume II*:737-758, Eds. J. Backlund et al. London: Chameleon Press, 1982.
43. Lukas, P. and L. Kunz, "Notch Size Effect in Fatigue," *Fatigue Fracture of Engineering Materials and Structures*, 12(3):175-186, 1989.
44. Lukas, P., et al. "Non-Damaging Notches in Fatigue," *Fatigue Fracture of Engineering Materials and Structures*, 9(3):195-204, 1986.
45. Maxwell, D. C. and T. Nicholas. "A Rapid Method for Generation of a Haigh Diagram for High Cycle Fatigue," *Fatigue and Fracture Mechanics*, 29, ASTM STP 1321. Eds. T. L. Panontin and S. D. Sheppard. American Society for Testing and Materials, 1998 (in press).
46. Mazumdar, P. K., W. C. Chen, and F. V. Lawrence, Jr. "An analytical study of the fatigue notch size effect," *Fatigue Thresholds-Fundamentals and Engineering Applications Volume II*:845-865, Eds. J. Backlund et al. London: Chameleon Press, 1982.
47. *MSC/ABAQUS v5.6 User's Manual Vols. I-III*. Los Angeles: MacNeal-Schwendler Corp., 1996.

48. *MSC/DYTRAN v4.0 User's Manual*. Los Angeles: MacNeal-Schwendler Corp., 1997
49. Murakami, Y. "Fundamental aspects of fatigue threshold of metals containing small defects, small cracks and nonmetallic inclusions - a unified quantitative evaluation and its applications," *Basic Mechanisms in Fatigue of Metals* (Materials Science Monographs, 46), Eds. P. Lukas and J. Polak. Amsterdam: Elsevier, 1988.
50. Murakami, Y., Y. Tazunoki, and T. Endo. "Existence of the coaxing effect and effects of small artificial holes on fatigue strength of an aluminum alloy and 70-30 brass," *Metallurgical Transactions A*, 15A:2029-2038, November 1984.
51. Murakami, Yukitaka and Masahiro Endo. "Quantitative evaluation of fatigue strength of metals containing various small defects or cracks," *Engineering Fracture Mechanics*, 17(1):1-15, 1983.
52. Nicholas, T. and J. R. Zuiker. "On the use of the Goodman diagram for high cycle fatigue design," *International Journal of Fracture*, 80:219-235, 1996.
53. Nicholas, T., Barber, J.P., and Bertke, R.S. "Impact Damage on Titanium Leading Edges from Small Hard Objects", *Experimental Mechanics*, 20(10), October 1980.
54. Nicholas, T. HCF Program Materials Damage Tolerance Action Team Technical Advisor, AFRL/MLLN, Wright-Patterson AFB OH. Personal Conversations. 1 October 1997- 1 January 1998.
55. Nihei, M., P. Heuler, Ch. Boller, and T. Seeger. "Evaluation of mean stress effect on fatigue life by use of damage parameters," *International Journal of Fatigue*, 8(3):119-126, 1986.
56. Peters, M., A. Gysler, and G. Lutjering. "Influence of texture on fatigue properties of Ti-6Al-4V," *Metallurgical Transactions A*, 15A:1597-1605, August 1984.
57. Peterson, R. E. *Stress Concentration Factors*. New York: John Wiley & Sons, 1974.
58. Ritchie, R. O. "Small Cracks and High-Cycle Fatigue," *Proceedings of the ASME Aerospace Division*, AMD-Vol. 52:321-333. New York NY: ASME, 1996.
59. Roder, O. et al. "Influence Of Simulated Foreign Object Damage on the High-Cycle Fatigue Properties Of Ti-6Al-4V for Gas Turbine Blades",

Proceedings of the 4th National Turbine Engine High Cycle Fatigue (HCF) Conference, Monterey CA, 9-11 February, 1999.

60. Roder, O., A. W. Thompson and R. O. Ritchie. "Simulation of Foreign Object Damage of Ti-6Al-4V Gas-Turbine Blades," Presentation to 3rd National Turbine Engine High Cycle Fatigue Conference, San Antonio TX, 3-5 February 1998.
61. Rushau, John J. et al. "Influence of Simulated Foreign Object Damage (FOD) on the Fatigue Life of Ti-6Al-4V", Proceedings of the 4th National Turbine Engine High Cycle Fatigue (HCF) Conference, Monterey CA, 9-11 February 1999.
62. Schutz, Walter. "The prediction of fatigue life in the crack initiation and propagation stages - a state of the art survey," *Engineering Fracture Mechanics*, 11(2):405-421, 1979.
63. Sheppard, S. D. "Field effects in fatigue crack initiation: long life fatigue strength," *Transactions of the ASME*, 113:188-194, June 1994.
64. SigmaPlot for Windows v4.00 online help. SPSS Inc., San Rafael CA, 1997.
65. Smith, R.A. and K.J. Miller. "Prediction of Fatigue Regimes in Notched Components," *International Journal of Mechanical Sciences*, 20:201-6, 1978.
66. Steif, Paul and Matt Rubal. "Damage Due to Small Particle Impacts on Gamma TiAl," Vugraph presentation, n. pag. WWWeb, <http://titan.mems.cmu.edu/97Review/C3/>. 9 March 1998.
67. Stewart, I.F. et al. "The Effect and Assessment of Foreign Object Damage to Aero Engine Blades and Vanes", Proceedings of the 4th National Turbine Engine High Cycle Fatigue (HCF) Conference, Monterey CA, 9-11 February, 1999.
68. Suresh, S. *Fatigue of Materials*. Cambridge, UK: Cambridge University Press, 1991.
69. Szolwinski, M. P., et al. "Comparison of Fretting Fatigue Crack Nucleation Experiments to Multiaxial Fatigue Theory Life Predictions," *Proceedings of the ASME Symposium on High Cycle Fatigue*, AD Vol. 55:445-457. Dallas TX: ASME, 1997.
70. Takemoto, T., et al. "The importance of surface layer on fatigue behavior of a Ti-6Al-4V alloy," *Metallurgical Transactions A*, 14A:127-132, January 1983.

71. Tanaka, K. and Y. Akiniwa. "Notch-geometry effect on propagation threshold of short fatigue cracks in notched components," *Fatigue* 87:739-748, 1987.
72. Taylor, D., et al. "Notch Fatigue Behaviour in Cast Irons Explained Using a Fracture Mechanics Approach," *International Journal of Fatigue*, 18(7):439-445, 1996.
73. Teng, N. J., et al. "Effect of Elastic Anisotropy on Fatigue Band in Polycrystalline Solids," *Numerical Methods in Structural Mechanics*. AMD-Vol. 204, p.151-160, American Society for Testing and Materials, 1995.
74. Timothy, S. P. and I. M. Hutchings. "Influence of Adiabatic Shear Bands on the Fatigue Strength of a Titanium Alloy," *Fatigue of Engineering Materials and Structures*, 7(3):223-227, 1984.
75. Ting, Jason C. and Frederick V. Lawrence, Jr. "A crack closure model for predicting the threshold stresses of notches," *Fatigue and Fracture of Engineering Materials and Structures*, 16(1):93-114, 1993.
76. Topper, T. H. and M. H. El Haddad. "Fatigue strength prediction of notches based on fracture mechanics," *Fatigue Thresholds-Fundamentals and Engineering Applications Volume II*:777-798, Eds. J. Backlund et al. London: Chameleon Press, 1982.
77. Walls, D. P., et al. "Damage Tolerance Based Life Prediction in Gas Turbine Engine Blades Under Vibratory High Cycle Fatigue," *Journal of Engineering for Gas Turbines and Power*, 119:143-6, January 1997.
78. Weeks, Craig. Allison Advanced Development Company, Telephone conversations, 12-31 August 1999.
79. Weixing, Yao, Xia Kaiquan, and Gu Yi. "On the fatigue notch factor,  $K_f$ ," *International Journal of Fatigue*, 17(4):245-251, 1995.
80. Williams, J. F. and D. C. Stouffer. "An estimate of the residual stress distribution in the vicinity of propagating fatigue crack," *Engineering Fracture Mechanics*, 11(3):547-557, 1979.
81. Wilson, I. H. and D. J. White. "Stress-concentration factors for shoulder fillets and grooves in plates," *Journal of Strain Analysis*, 8(1):43-51, 1973.
82. Xiaopeng, Zhao. "The effects of stress ratio on fatigue threshold," *International Journal of Fatigue*, 12(2):127-130, 1990.

83. Xin-lu, Yu, Yan Yong-Nian, and Zheng Chu-Hong. "The intensity of stress field method - a new criterion of fatigue design," *Fatigue Life: Analysis and Prediction*. Ed. V. S. Goel. American Society for Metals, 1986.
84. Xu, R. X., T. H. Topper, and J. C. Thompson. "Mode I stress intensity factor equations for cracks at notches and cavities," *Fatigue and Fracture of Engineering Materials and Structures*, 20(9):1351-1361, 1997.
85. Zahavi, Eliahu and Vladimir Torbilo. *Fatigue Design - Life Expectancy of Machine Parts*. Boca Raton: CRC Press, 1996.
86. Zhi-zhong, Hu and Cao Shu-zhen. "Relationship between fatigue notch factor and strength," *Engineering Fracture Mechanics*, 48(1):127-136, 1994.

## ***VITA***

Major Joseph L. Hamrick, II was born on 19 June 1963 in Elkins, West Virginia. He attended Tucker County High School until he was accepted as an early admission student in the Honors Program at the University of Delaware in Newark, Delaware. He graduated with Bachelor of Science degree in Mechanical Engineering in June 1984. He was commissioned through AFROTC Detachment 128 at the University of Delaware, where he was the recipient of a two-year scholarship.

His first assignment was at the Air Force Weapons Laboratory at Kirtland AFB, New Mexico where he studied the vulnerability of rocket boosters to directed energy weapons. In June 1988 he attended the Air Force Institute of Technology where he received a Masters of Science degree in Aeronautical Engineering in December 1989. He was then assigned to Aeronautical Systems Division, Wright-Patterson AFB, Ohio where he led the integrated product team responsible for the F-22 canopy. In June 1993 he was assigned to the Defense Intelligence Agency and served on the Joint Staff Directorate for Intelligence in the Pentagon as chief of the Targeting Requirements section. In June 1996, he again entered the Air Force Institute of Technology as a candidate for a Doctor of Philosophy degree in Aeronautical Engineering. Upon graduation he will be assigned to Propulsion Directorate, Air Force Research Laboratory, Edwards AFB, California.

Permanent Address:     519 Main Street  
                                 Parsons, WV 26287

REPORT DOCUMENTATIONPAGE			Form Approved OMB No. 0704-0188	
Public reporting burden for this collection of information is estimated to average 1 hour per response, including the time for reviewing instructions, searching existing data sources, gathering and maintaining the data needed, and completing and reviewing the collection of information. Send comments regarding this burden estimate or any other aspect of this collection of information, including suggestions for reducing this burden, to Washington Headquarters Services, Directorate for Information Operations and Reports, 1215 Jefferson Davis Highway, Suite 1204, Arlington, VA 22202-4302, and to the Office of Management and Budget, Paperwork Reduction Project (0704-0188), Washington, DC 20503.				
1. AGENCY USE ONLY (Leave blank)		2. REPORT DATE September 1999		3. REPORT TYPE AND DATES COVERED Final 01 July 1996 - 30 Sept 1999
4. TITLE AND SUBTITLE EFFECTS OF FOREIGN OBJECT DAMAGE FROM SMALL HARD PARTICLES ON THE HIGH-CYCLE FATIGUE LIFE OF Ti-6Al-4V			5. FUNDING NUMBERS PE 61102F PR 2302 TA DW WU 1F	
6. AUTHOR(S) Joseph L. Hamrick, II				
7. PERFORMING ORGANIZATION NAME(S) AND ADDRESS(ES) Air Force Institute of Technology (AFIT/ENY) 2950 P Street Wright-Patterson Air Force Base, OH 45433-7765			8. PERFORMING ORGANIZATION REPORT NUMBER  AFIT/DS/ENY/99-02	
9. SPONSORING/MONITORING AGENCY NAME(S) AND ADDRESS(ES) Dr Theodore Nicholas Air Force Research Laboratory (AFRL/MLLN) Wright-Patterson Air Force Base, OH 45433-7817 (937) 255-1347 DSN 785-1347			10. SPONSORING/MONITORING AGENCY REPORT NUMBER  AFIT/DS/ENY/99-02	
11. SUPPLEMENTARY NOTES Faculty Advisor: Dr Shankar Mall (937) 255-3636 x4587 DSN 785-3636 x4587 Shankar.Mall@afit.af.mil				
12a. DISTRIBUTION AVAILABILITY STATEMENT Approved for public release; Distribution unlimited			12b. DISTRIBUTION CODE	
13. ABSTRACT (Maximum 200 words) Thin rectangular samples of Ti-6Al-4V were damaged by four methods to represent foreign object damage found in turbine engine blades: 1) impact with 2 mm and 5 mm diameter glass spheres at 305 m/s, 2) impact with 2 mm and 4 mm diameter steel spheres at 305 m/s, 3) quasi-static displacement controlled indentation using steel chisels with 1 mm, 2 mm and 5 mm diameter tips and 4) shearing notches with a 2 mm diameter chisel point under a quasi-static loading condition. Finite element analysis was used to study the relationship between the stress state created by the plastic damage and the fatigue strength. A new method of quantifying the amount of plastic damage from multiple methods was developed. The fatigue strength required for crack initiation at 10E7 cycles was found to be a function of the total depth from the edge of the undeformed specimen up to the end of the plastically deformed zone. For damage depths less than 1750 $\mu$ m, the reduction in fatigue strength is proportional to the depth of total damage. For more than 1750 $\mu$ m, there appears to be a threshold value of fatigue strength.				
14. SUBJECT TERMS Fatigue Life, Fatigue Tests, High Strength Alloys, Titanium Alloys, Impact, Foreign Object Damage, Finite Element Analysis			15. NUMBER OF PAGES 268	
			16. PRICE CODE	
17. SECURITY CLASSIFICATION OF REPORT UNCLASSIFIED	18. SECURITY CLASSIFICATION OF THIS PAGE UNCLASSIFIED	19. SECURITY CLASSIFICATION OF ABSTRACT UNCLASSIFIED	20. LIMITATION OF ABSTRACT UL	